

High-fidelity microwave control of single-atom spin qubits in silicon

Juan Pablo Dehollain Lorenzana

A thesis in fulfilment of the requirements for the degree of
Doctor of Philosophy



UNSW
AUSTRALIA

School of Elec. Eng. and Telecom.
Faculty of Engineering

July 8, 2014

Abstract

As classical computers begin to reach their fundamental performance limits, quantum computers will be an invaluable tool for the advance of science and technology. The trillion dollar silicon electronics industry sets the perfect stage for the evolution of quantum computation, yet it has so far proved to be a tough challenge to implement all the elements needed to build a scalable quantum computer in silicon.

This thesis presents the first experimental demonstration of the full operation of single-spin qubits in Si. Our qubits consist of the electron and nuclear spins of a single phosphorus atom, implanted in a Si substrate, and controlled by a gated nanostructure. We describe an experimental setup tailored to minimise electron temperature and perform real-time data acquisition, analysis and instrument control. We present modeling, simulation and characterisation of a novel nanoscale coplanar antenna for spin control, designed to work at frequencies up to 50 GHz. These tools have allowed us to demonstrate the first ever single-atom spin-qubits in natural silicon, leading the way to demonstrating record qubit performances in isotopically purified ^{28}Si : an electron spin qubit with measurement and control fidelities $> 97\%$ and coherence times of 0.5 seconds; and a nuclear spin qubit with fidelities $> 99.99\%$ and a record single-spin coherence of 30 s. We have performed noise spectroscopy in our system and concluded that decoherence is currently limited by magnetic noise originating from our broadband antenna. We also describe a methodology towards the demonstration of electron-nuclear entanglement in a single atom, through density matrix tomography. Finally, we present the experimental demonstration of one of the key milestones towards implementing two-qubit gates in our system: single-shot readout and relaxation measurements of the singlet-triplet states of coupled electrons from a P donor pair in $^{\text{nat}}\text{Si}$; finding agreement of our observed J and T_1 to previous theoretical predictions for P dimers in Si.

The results presented in this thesis have catapulted silicon qubits onto the main stage of quantum computing systems, and pave the way to the exciting future experiments, that should see two-qubit gates and qubit transport become a near-term reality.

Acknowledgements

This thesis marks the close of an amazing chapter in my life, possibly the most rewarding I will have in my pursuit of professional happiness. I have been lucky enough to share this ride with some awesome people. If I mention you in these next paragraphs, you deserve a big THANK YOU for having been a huge influence in my professional and personal life.

To my lecturer, supervisor, mentor and friend, thank you Andrea. You are one of the smartest and most optimistic people I know. Your passion for science is incredibly contagious and it drives people to push the limits of achievement. Thank you most of all for the huge boost of professional self esteem you have given me, through the confidence you have shown in me both through words and through actions. To my co-supervisor, thank you Andrew for showing so much appreciation for our work. I always look forward to your reactions to new data, they fill me with joy but most importantly, fill me with confidence and motivation. Andrea and Andrew, you both are a credit to academia and fully deserve all the accolades you have received and the many more to come.

Thank you to all the colleagues who shared a part of this journey with me. My Finnish partner in lab crime Juha, I had a great time running these measurements with you and learning from you. Arne, Raj, Jarryd, Fahd, Sol, Gui, Alex, it has been amazing to work and play with you. We really are a privileged group. Floris, I really appreciate your friendship and all the great advice you have given me. Alex V.B., thank you for nudging me into research and starting this PhD. James and Tony, for giving me my first taste of research. Fay and Kuan, thanks for making our beautiful devices. Dave, Rod and Bob, you are the unsung heroes in the lab, thanks for having the patience to do all the dirty work that no one else ever wants to do. I'll try to list everyone else whose interactions were all influential in this work: Alessandro, Henry, Wee-Han, Kok-Wai, Nay-Shan, Menno, Jason, Anne, Joost, Joe, Holger, Bent, Martin, Matt, Tom, Sam, Suddo, André, Stephanie, thanks for being a part of this ride.

To my family and friends, you are the foundation of my life and my main source of happiness. I wish the world was smaller so we would not have to be so far apart. Marcos, Paula, Mami, Papi, I am so lucky to have grown up in such an educated, humble, fun, loving family. Ana, thanks for sharing your life with me and for never letting me keep my balance, the best card that life has dealt me was the one with your picture in it.

The work in this thesis was funded by the Australian Research Council Centre of Excellence for Quantum Computation and Communication Technology (Project No. CE110001027) and the U.S. Army Research Office (Contract No. W911NF-13-1-0024); and supported by the Australian National Fabrication Facility.

This thesis was accepted after reviews and recommendations
from Prof.Dr. Jörg Wrachtrup from Universität Stuttgart and
Prof. Mark Eriksson from The University of Wisconsin-Madison.

Publications

Peer reviewed journal articles

J.P. Dehollain, J.T. Muhonen, K.Y. Tan, A. Saraiva, D.N. Jamieson, A.S. Dzurak, A. Morello. “Single-shot readout and relaxation of singlet/triplet states in exchange-coupled ^{31}P electron spins in silicon”. *Physical Review Letters* vol. 112, no. 236801 (2014).

A. Laucht, R. Kalra, J.T. Muhonen, **J.P. Dehollain**, F.A. Mohiyaddin, F.E. Hudson, J.C. McCallum, D.N. Jamieson, A.S. Dzurak, A. Morello. “High-fidelity adiabatic inversion of a ^{31}P electron spin qubit in natural silicon”. *Applied Physics Letters* vol. 104, no. 092115 (2014).

J.P. Dehollain, J.J. Pla, E. Siew, K.Y. Tan, A.S. Dzurak, A. Morello. “Nanoscale broadband transmission lines for spin qubit control”. *Nanotechnology* vol. 24, no. 1, 015202 (2013).

J.J. Pla, K.Y. Tan, **J.P. Dehollain**, W.H. Lim, J.J.L. Morton, F.A. Zwanenburg, D.N. Jamieson, A.S. Dzurak, A. Morello. “High-fidelity readout and control of a nuclear spin qubit in silicon”. *Nature* vol. 496, no. 7445, pp. 334-338 (2013).

J.J. Pla, K.Y. Tan, **J.P. Dehollain**, W.H. Lim, J.J.L. Morton, D.N. Jamieson, A.S. Dzurak, A. Morello. “A single-atom electron spin qubit in silicon”. *Nature* vol. 489, no. 7417, pp. 541-545 (2012).

Other articles submitted for publication

J.T. Muhonen, **J.P. Dehollain**, A. Laucht, F.E. Hudson, T. Sekiguchi, K.M. Itoh, D.N. Jamieson, J.C. McCallum, A.S. Dzurak, A. Morello. “Storing quantum information for 30 seconds in a nanoelectronic device”. arXiv:1402.7140 [cond-mat.mes-hall]. Submitted to *Nature Nanotechnology* (2014).

M. Veldhorst, J.C.C. Hwang, C.H. Yang, A.W. Leenstra, B. de Ronde, **J.P. Dehollain**, J.T. Muhonen, F.E. Hudson, K.M. Itoh, A. Morello, and A.S. Dzurak. “Gate addressable quantum dot qubit with high fidelity in a nuclear-spin-free environment”. Submitted to *Nature Nanotechnology* (2014).

Presentations

J.P. Dehollain, J.T. Muhonen, F.E. Hudson, K.M. Itoh, D.N. Jamieson, A.S. Dzurak, A. Morello. “Single-donor spins in isotopically purified silicon: a new benchmark for solid-state qubits”. Presented at:

-2014 International Conference on Nanoscience and Nanotechnology. Adelaide, Australia (Oral)
-2013 International Symposium on Nanoscale Transport and Technology. Atsugi, Japan (Poster)
-2013 UNSW Faculty of Engineering Dean’s Award for Research Excellence. Sydney, Australia (Poster)

J.P. Dehollain, J.T. Muhonen, K.Y. Tan, A. Saraiva, D.N. Jamieson, R. Kalra, A. Laucht, C.D. Hill, A.S. Dzurak, A. Morello. “Observed T_1 degradation in a high- J ^{31}P dimer and proposal for low- J two-qubit gate”. Presented at:

-2014 Centre for Quantum Computation and Communication Workshop. Sunshine Coast, Australia (Poster)

J.P. Dehollain, J.T. Muhonen, F.E.Hudson, K.M. Itoh, D.N. Jamieson, A.S. Dzurak, A. Morello. “High fidelity quantum control of a phosphorous qubit in isotopically purified ^{28}Si ”. Presented at: -2013 Centre for Quantum Computation and Communication Workshop. Sunshine Coast, Australia (Oral)

J.P. Dehollain, J.T. Muhonen, F.E.Hudson, K.M. Itoh, D.N. Jamieson, A.S. Dzurak, A. Morello. “The next generation of ^{31}P single-atom spin qubits”. Presented at: -2013 Silicon Quantum Electronics Workshop. Villard de Lans, France (Poster)

J.P. Dehollain, J.J. Pla, E. Siew, K.Y. Tan, A.S. Dzurak, A. Morello. “Nanoscale broadband transmission lines for spin qubit control”. Presented at:

-2013 S3NANO Winter School. Windsor, UK (Poster)

-2012 20th Australian Institute of Physics Congress. Sydney, Australia (Poster)

-2012 CST Australian User Group Meeting. Sydney, Australia (Oral)

-2012 Silicon Quantum Electronics Workshop. Sydney, Australia (Poster)

-2011 IEEE Technologies of the Future Poster Competition. Sydney, Australia (Poster)

-2011 Silicon Quantum Electronics Workshop. Denver, USA (Poster)

Awards

Best poster of research theme and overall runner-up at 2013 UNSW Faculty of Engineering Dean’s Award for Research Excellence, research theme: “Digital World”.

Winner at 2011 IEEE Technologies of the Future Poster Competition, research theme: “Towards Miniaturisation”.

Abbreviations

#D	#-dimensional
A	Hyperfine coupling
B₀	Static magnetic field
B₁	Oscillating magnetic resonance field
CPMG	Carl-Purcell-Meigboom-Gill
CPS	Coplanar stripline
CPW	Coplanar waveguide
D	Drain
D⁰⁽⁺⁾	Donor in the neutral(ionised) state
DD	Dynamical decoupling
DG	Donor gate
E_c	Charging energy or addition energy
E_F	Fermi energy
E_Z	Zeeman energy
EP	Empty pulse
ESR	Electron spin resonance
F_c	Intrinsic control fidelity
F_{ce}	Effective control fidelity
F_i	Initialisation fidelity
F_m	Measurement fidelity
FWHM	Full width at half maximum
J	Exchange coupling
LB	Left barrier
LP	Load pulse
MW	Microwave
NMR	Nuclear magnetic resonance

P	Phosphorus
PM	Pulse modulation
ΦM	Phase modulation
QC	Quantum computing
QND	Quantum nondemolition
RB	Right barrier
RF	Radiofrequency
RP	Read pulse
RT	Room temperature
S	Source
S_{ij}	Scattering parameter of transmission from port j to port i
SET	Single electron transistor
Si	Silicon
SRD	Spin readout device
T₁	Spin lifetime or spin-lattice relaxation time
T₂[*]	Free induction decay time
T₂^S	Decoherence time using pulse sequence S
T_{el}	Electron temperature
TG	Top gate
TL	Transmission Line
UNSW	University of New South Wales

Contents

Abstract	ii
Acknowledgements	iii
Publications	v
Abbreviations	vii
1 An introduction to spin-based quantum computing	6
1.1 Motivation: Building a quantum computer	7
1.2 Our qubit of choice: P-Si single-spins	9
1.2.1 The qubit	11
1.2.2 Qubit control	13
1.2.3 Qubit measurement and initialisation	14
1.2.4 Two-qubit gates	16
1.2.5 Qubit transport	17
1.2.6 Our physical implementation	17
1.3 Basic concepts in RF transmission lines	23
1.4 Low temperature	25
1.5 Important spin qubit characteristics	26
1.5.1 Spin lattice relaxation time	26
1.5.2 Linewidths and coherence times	26
1.5.3 Fidelities	30
1.6 Putting some numbers in the equations	32
1.7 Thesis Outline	33
2 Experimental Methods	34
2.1 Introduction	35
2.2 Fabrication overview	35
2.3 Low temperature setup	37
2.3.1 Filter response measurements	42
2.3.2 Electron temperature measurements	42
2.4 Room-temperature setup	44
2.4.1 Noise	44
2.4.2 Instrument control	46

2.4.3	The superconducting magnet	48
2.5	Relevant qubit experiments	49
2.5.1	Qubit readout and control	49
2.5.2	Qubit fidelities	53
2.5.3	T_1 measurement	58
2.5.4	Fitting functions	58
2.6	Conclusions	60
3	Controlling qubits with microwaves	61
3.1	Introduction	62
3.2	Design guidelines for the optimal planar loop	62
3.2.1	Topologies of planar transmission lines	64
3.2.2	Choice of simulation methods for tapered structures	67
3.3	General model characteristics	69
3.4	Simulation Results	69
3.4.1	Electric and magnetic fields along the transmission line	70
3.4.2	Performance comparison between CPS/CPW topologies	71
3.4.3	Further optimization	73
3.5	Operating the first single spin qubits in Si	76
3.5.1	Electron qubit	76
3.5.2	Nuclear qubit	78
3.6	Benchmark of antenna simulations with experiments	81
3.6.1	Stub resonance of the on-chip CPW/CPS balun	81
3.6.2	Oscillating magnetic field at the spin qubit	81
3.6.3	Electric field radiated to the spin readout device	83
3.7	Conclusions	84
4	Qubits in isotopically purified ^{28}Si	85
4.1	Introduction	86
4.1.1	From bulk to a gated nanostructure	86
4.1.2	A new generation	87
4.2	The electron qubit	88
4.2.1	ESR spectrum	88
4.2.2	Coherent measurements	89
4.2.3	T_1 measurements	91
4.2.4	Fidelities	92
4.3	Nuclear qubit	93
4.3.1	Measurement fidelity and lifetimes	93
4.3.2	Coherent measurements and control fidelity	93
4.3.3	Nuclear initialisation using real-time feedback	95

CONTENTS

4.3.4	High-precision spectrum characterisation	96
4.4	In search of the sources of decoherence	97
4.4.1	B_1 source <i>on-off</i> ratio	97
4.4.2	Noise spectroscopy using DD	98
4.5	An unlikely accident	105
4.6	Towards electron-nuclear entanglement	105
4.6.1	Basic theory	107
4.6.2	Density matrix tomography in the P-Si system	107
4.6.3	Experimental considerations	111
4.7	Conclusions and future work	111
5	Readout of coupled electrons in P-Si	114
5.1	Introduction	115
5.2	Experiment background	115
5.2.1	Initial readout measurements	116
5.3	Spins and valleys in exchange coupled P-Si donors	117
5.4	Exchange coupling estimation	118
5.5	Tunnel-rate selective readout	119
5.6	Relaxation measurements	121
5.7	Conclusions	126
6	Conclusions and future work	127
6.1	Summary of achievements	128
6.2	Chapter 2 - Experimental methods	128
6.3	Chapter 3 - Microwave control of qubits	129
6.4	Chapter 4 - Qubits in isotopically purified Si	129
6.5	Chapter 5 - Readout of J -coupled P donors	130
6.6	Future work and outlook	130
References		132

List of Figures

1.1	Bloch sphere	8
1.2	2D QC architecture with Kane's device	10
1.3	Spin energy levels and transitions of the electron-nuclear system	13
1.4	Magnetic resonance driving a spin rotation	14
1.5	Elements needed for qubit measurement	15
1.6	Qubit device schematic with main components	18
1.7	Basic operation of the SET	20
1.8	Spin resonance spectrum and Rabi oscillations	23
1.9	RF transmission lines	24
1.10	Coherence times measurements	28
1.11	Isotopical purification of Si	30
2.1	Device substrates and gate layouts	36
2.2	Low temperature components	38
2.3	Frequency response (S_{21}) of components in our filter boxes	39
2.4	Schematic of the low temperature setup	41
2.5	Schematics of different S_{21} measurement techniques used for different frequency ranges	43
2.6	Electron temperature extraction	44
2.7	Schematic of the instrument setup	45
2.8	Charge detection, electron spin readout and control	50
2.9	Control sequence diagrams	52
2.10	Electron qubit initialisation and measurement fidelities	55
3.1	Broadband antenna model	63
3.2	Four planar loop designs	65
3.3	Conventions for the dimensions of coplanar TLs	66
3.4	Tetrahedral mesh used for simulations	68
3.5	Characterization of the planar transmission lines	70
3.6	Simulation results comparing antenna designs	72
3.7	Comparison of S_{11} parameters for different bond wire lengths and types	73
3.8	Qubit placement inside or outside the loop	74

LIST OF FIGURES

3.9	Improved performance for new device architecture	75
3.10	Importance of ground bridges at discontinuities	75
3.11	Qubit device and electron spin qubit operation	77
3.12	Measurement fidelity histograms for e and N qubits	79
3.13	Operation of the nuclear spin qubit	80
3.14	S ₁₁ measurements	82
3.15	Power-dependence of the electron Rabi frequency	82
3.16	SET island coulomb peak broadening with applied signals to the spin resonance antenna	83
4.1	Device schematic	87
4.2	Direct measurement of electron spin resonance linewidths	89
4.3	Electron qubit coherence	90
4.4	Field dependence of the electron lifetimes	91
4.5	Electron fidelity measurements	92
4.6	Nuclear readout and lifetimes	93
4.7	Nuclear control and coherence times	94
4.8	Nuclear initialisation with feedback	95
4.9	Effects of the signal generator <i>on-off</i> ratio	98
4.10	The filter function	99
4.11	Measured noise spectra in our devices	101
4.12	Noise spectrum analysis	103
4.13	Damaged antenna measurements	106
4.14	Density matrix tomography simulations	111
5.1	Device layout and initial measurements	116
5.2	Exchange coupling estimation	119
5.3	TR-RO readout scheme and fidelities	120
5.4	Relaxation measurements and fits	122
5.5	Relaxation in different B_0 -field regimes	125

Chapter 1

An introduction to spin-based quantum computing

“We’re all just protons, neutrons, electrons that rest on a Sunday, work on a Monday”

-The Cat Empire

The objective of this thesis is to establish silicon spin qubits as front-runners for the future of quantum computing. We will present the experimental realisation of a qubit with unprecedented fidelity and coherence characteristics. We will present the design of a nanoscale broadband spin resonance antenna which proved to be one of the cornerstones of the success of this project; we will describe in detail all the non-trivial experimental techniques used to successfully operate our qubits; and we will present detailed results of our qubit operation, along with some analysis on how they can be improved further; finally, we will provide an outlook for future work and present experiments that show some encouraging results for the next generation.

For readers who did not understand many words in the last paragraph, this chapter will present a general introduction to quantum computing, including some of its history, its importance and the physics behind it. This will lead the way into a description of our approach at implementing a quantum computer, followed by an introduction to all the necessary concepts that need to be learned in order to understand the rest of this thesis. This introduction is intended to be written in accessible language and for a general audience with interest in science. We introduce very general and basic concepts of quantum physics and magnetic spin resonance, which will be expanded upon as they become relevant in the following chapters.

1.1 Motivation: Building a quantum computer

In the early 1980s the myriad of potential applications for computers was very well established. It was only a matter of time before a physicist asked himself if computers could ever be used to simulate quantum systems (i.e. systems that need to be described by quantum mechanics, such as complex interactions between atoms). In doing so, Richard Feynman realised that the task required a whole different type of processor, where bits do not behave like discrete switches, but exhibit quantum behaviour [1].

A classical computer processes information using bits. These can only have one of two values (0 or 1) and can be put together in arrays to make a binary number (e.g. 1001 = 9); computers can then perform arithmetic and other operations on these numbers to process information. The quantum behaviour in Feynman's information processor comes from the use quantum bits or *qubits* [2], consisting of a quantum two-level system. Quantum two-level systems have two measurable energy *eigenstates*, which we define as $|0\rangle$ and $|1\rangle$. This binary measurement output is much like the output of a classical CPU, but that is where the similarities end. Unlike classical bits, qubits can be prepared in a *quantum superposition* state described by $|\psi\rangle = \alpha|0\rangle + \beta|1\rangle$, where $\alpha, \beta \in \mathbb{C}$ and $|\alpha|^2 + |\beta|^2 = 1$. What this means is, before measuring it, the qubit is in a combination of both states (e.g. Schrodinger's cat in the closed box is dead and alive at the same time). A quantum superposition state cannot be measured directly, only the eigenstates can be observed (e.g. when we open the box, the cat is either dead or alive). A measurement of $|\psi\rangle$ will result in either $|0\rangle$ with probability $|\alpha|^2$ or $|1\rangle$ with probability $|\beta|^2$. Measurements cause the qubit state to *collapse* to the measured eigenstate, meaning that immediately after

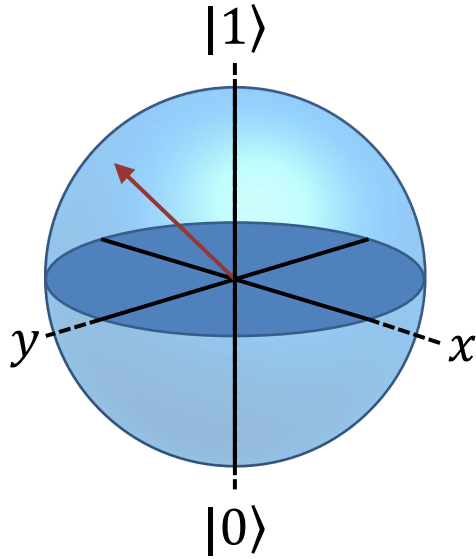


Figure 1.1: Bloch sphere. The state of the qubit is represented by the direction of the unit vector.

measurement, the qubit is no longer in its previous superposition state. A qubit can be visualised as a unity length point vector in three-dimensional space (Figure 1.1). All the possible vector directions form the surface of a unity radius sphere, known as the *Bloch sphere*. A measurement projects the vector to the axis hosting the eigenstates, by convention we will use the z axis.

Another important property of qubits is the possibility to prepare *entangled* states with two or more coupled qubits. When two qubits are entangled, the state of one can be described relative to the state of the other. This means that a measurement of one qubit will determine the state of the other. The effect of measuring one qubit appears instantly on the other, no matter how far apart they may be. Section 4.6 provides further detail on quantum entanglement and its relevance to the work presented in this thesis.

A massive spark of interest in quantum computing came in 1994, when Peter Shor discovered a way to use a quantum computer to efficiently find the prime factors of any integer [3]. This task can also be performed by a classical computer, but Shor discovered that as the numbers to be factored become very large, a quantum computer can perform the task exponentially faster than a classical computer. The products of large prime numbers are the foundation of most cryptographic algorithms; in general, the larger the prime number used, the harder it is to break the encryption of a message. Shor's algorithm gave quantum computing an immediate information security application, which was the incentive the field needed to start taking off. Since then, many more useful quantum algorithms have been surfacing, such as searching unsorted databases [4], determining if all elements in a list are distinct [5] and solving linear systems of equations [6]. Furthermore, the significance of quantum simulations has been highlighted with proposals that they could be used to calculate molecular properties from first principles [7], and to simulate drug-protein interactions for drug design [8]. These tasks are known to be

extremely hard to perform on classical computers.

Quantum two-level systems and therefore qubits, can be found in a countless range of physical systems. So far the ones that have attracted most interest from researchers are based on photons, trapped ions, nuclear magnetic resonance, superconductors, quantum dots and dopants in semiconductors [9]. Several issues need to be considered in order to attempt to judge the viability of a physical system as a means to implement a quantum computer. There are six main ingredients that every quantum computer must have: [10]

A scalable system with well characterised qubits The system must have a viable way to increase the number of working qubits, with all the qubits being clearly describable by an equation of energy or *Hamiltonian*.

Qubit initialisation Every operation should start from a well defined known value.

A universal set of quantum gates The system must have a set of available operations between two or more qubits, and the whole set of operations must be able to implement the required quantum algorithms.

A large ratio of coherence time to gate operation time One of the main challenges of working with quantum systems, is that the states can get “lost” easily. Noise in the environment where qubits live will cause us to lose track of the position of the qubit in the Bloch sphere. This is known as quantum *decoherence*, and will be one of the main subjects of study throughout this thesis.

Qubit measurement A mechanism must exist to allow to measure any specific qubit that might be needed at any point in time.

Qubit transport A realistic quantum computing architecture will have different regions of qubit interactions physically separated from each other. A type of qubit system must exist to allow coherent transport of qubit states between these different regions.

Every attempted qubit system implementation has strengths and weaknesses in different sets of these ingredients [9], so far there is no definite answer on what systems and components future quantum computers will be made up of.

1.2 Our qubit of choice: P-Si single-spins

The last 6 decades have seen the silicon microelectronics industry evolve to turn science-fiction into reality. Every electronic device found in our homes, offices, cars, pockets contains a brain made up of silicon transistors. Naturally, the trillion-dollar industry and sixty years of technological knowledge makes silicon a prime candidate to underpin the quantum electronics of the future. Many research groups have taken interest in using Si to host devices for quantum

1.2. Our qubit of choice: P-Si single-spins

computing and spintronics, with great progress having been made in implementing these in the past few years [11].

Australia sparked a massive interest in quantum computing from 1998, when Bruce Kane — while working at UNSW — proposed a method to implement a quantum computer using the nuclear spin of single phosphorus donors in silicon, controlled by a gated nanostructure [12]. This proposal exposed the viability of making spin qubits in silicon. A few years later, an architecture was developed for the implementation of a two-dimensional scalable universal quantum computer, based on spin-qubits from donors in semi-conductors [13]. The ingredients and recipe for silicon quantum computing are there, the time has come to build it. This thesis presents several important achievements in the task of building a silicon based quantum computer.

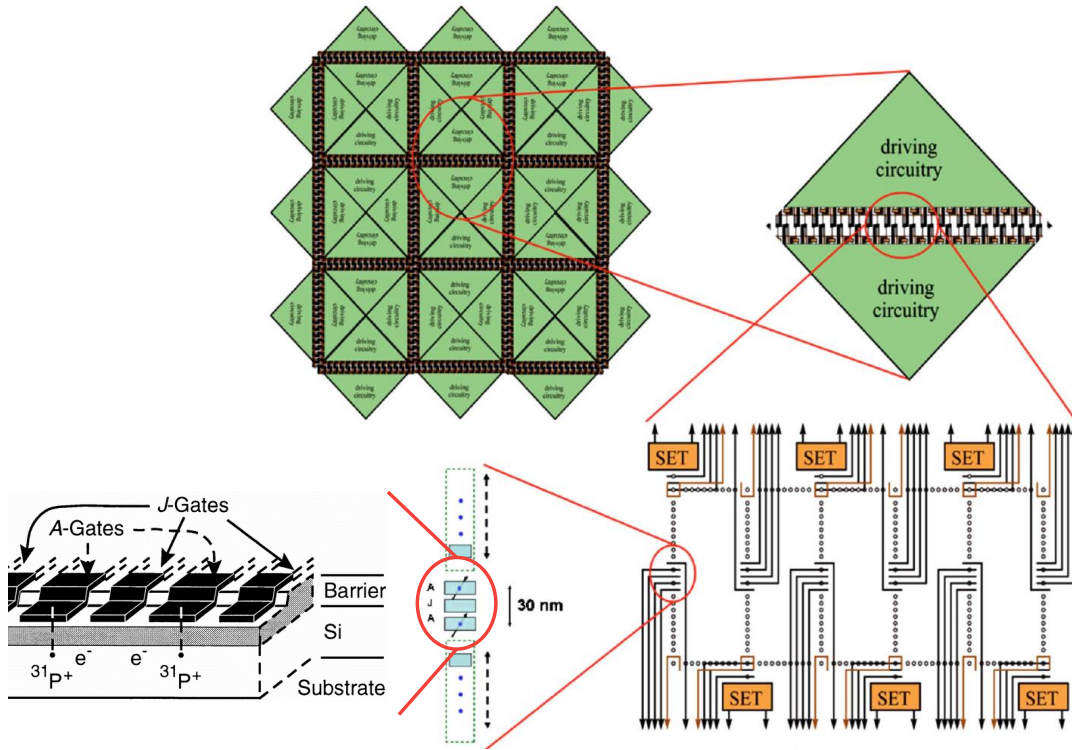


Figure 1.2: 2D QC architecture with Kane’s device. Figures extracted from References [12] and [13]. The large scale quantum computer will be composed of many interconnected qubit devices, such as the ones that will be presented in this thesis.

Each of the elements in the quantum computing architecture (qubits, control, measurement, transport) can be implemented in a wide variety of ways. The following subsections describe the main ingredients of this quantum computer, along with some sample implementation possibilities (sections 1.2.1–1.2.5). We also describe in Subsection 1.2.6, all the elements of the device we have been using to operate our single spin qubits.

1.2.1 The qubit

Spin is an intrinsic quantum mechanical property that describes how elementary particles and atomic nuclei react to magnetic fields (analogous to mass describing how particles react to force, or charge describing how particles react to electric fields). Particles have an intrinsic spin quantum number $s = \frac{n}{2}$ where $n \in \mathbb{N}_0$. The projection on a measurement axis of the spin is quantised, having $2s + 1$ possible values.

Spins from electrons and nuclei in semiconductors [14] are known to be the most natural and practical candidates for physical implementation of qubits [15]. Phosphorus is a donor in silicon, which means that a P atom bound to a Si lattice has an extra valence electron weakly bound to its nucleus. This is a very convenient system to study, because a donor atom in a semiconductor can be analysed in the same way as a hydrogen atom in vacuum (one of the most studied systems in quantum mechanics), with energy levels normalised by the effective mass and the dielectric constant of the semiconductor [16]. We will work with this P atom in two different charge states: *neutral* (D^0), when the extra valence electron is present; or *ionised* (D^+), when the electron is stripped, leaving the bare nucleus in the Si lattice. Electrons and the P nucleus are both spin- $\frac{1}{2}$ ($s = \frac{1}{2}$), which means their spin projection can take 2 values ($\pm\frac{1}{2}$) which we will call *up* (\uparrow) and *down* (\downarrow) in this thesis.

Unperturbed, spin states are *degenerate* (they share the same energy), but when perturbed by a magnetic field, the spin states split in energy due to the *Zeeman effect*. The Zeeman hamiltonian is:

$$\mathcal{H}_Z = \gamma B_0 \mathbf{S}_z$$

Here, γ is the spin's gyromagnetic ratio, B_0 is the component of magnetic field along the measurement axis z , and \mathbf{S}_z is the projection of the angular momentum along z . The eigenstates of this hamiltonian are just the spin up and down projection states $|\uparrow\rangle$ and $|\downarrow\rangle$; and solving the eigenvalues gives us two distinct energies corresponding to each of the spin states. The difference between the energies — or *energy splitting* — is the Zeeman energy $E_Z = \gamma B_0$. A spin- $\frac{1}{2}$ perturbed by a magnetic field is a quantum two-level system, therefore it can be used as a qubit.

Our quantum computer architecture utilises two types of spin-qubits: one from the bound electron and another from the nucleus, of a single P atom in a Si lattice. Both qubits are useful for different purposes because the timescales of coherence and operation are very different. Owing to its much larger magnetic moment, the electron can be operated much faster than the nucleus, but it's more susceptible to noise; therefore the electron qubits will be used to perform fast operations [17], while the nucleus provides an option for qubit storage [18].

The electron-nucleus system

The *hyperfine interaction* (A) is an intrinsic interaction between the electron and nuclear spins in an atom, which adds some complexity to the rather simple treatment of our spin-qubit. This interaction plays an important role in the control of both qubits and measurement of the nuclear qubit, so it is appropriate to describe it in more detail. The hyperfine interaction adds a term to the system's hamiltonian $A\mathbf{S} \cdot \mathbf{I}$, where \mathbf{I} and \mathbf{S} correspond to the nuclear and electron spin respectively, and A is the isotropic hyperfine interaction. The full spin hamiltonian of the electron-nucleus system is then given by the sum of the Zeeman terms of electron and nucleus with the hyperfine term:

$$\mathcal{H}_{\text{Si:P}} = \gamma_e B_0 \mathbf{S}_z - \gamma_N B_0 \mathbf{I}_z + A \mathbf{S} \cdot \mathbf{I} \quad (1.1)$$

Using the high-field approximation $\gamma_e B_0 \gg A > \gamma_N B_0$, which is accurate for our experimental conditions, the eigenstates of the hamiltonian are the equal to the tensor products of the individual qubit projection states [19]: $|\downarrow\uparrow\rangle = |\downarrow\rangle \otimes |\uparrow\rangle$, $|\downarrow\downarrow\rangle$, $|\uparrow\downarrow\rangle$ and $|\uparrow\uparrow\rangle$; the thin and thick arrows corresponding to the electron and nuclear spin projections respectively. [Figure 1.3](#) shows the resulting four-level system, with energies given by:

$$\begin{aligned} E_{\downarrow\uparrow} &= \frac{-\sqrt{(\gamma_e B_0)^2 + A^2} - A/2}{2} \\ E_{\downarrow\downarrow} &= \frac{-\gamma_e B_0 + A/2}{2} \\ E_{\uparrow\downarrow} &= \frac{\sqrt{(\gamma_e B_0)^2 + A^2} - A/2}{2} \\ E_{\uparrow\uparrow} &= \frac{\gamma_e B_0 + A/2}{2} \end{aligned}$$

Here, $\gamma_{\pm} = \gamma_e \pm \gamma_N$.

The electron and the nuclear spins can still work as single qubits, by fixing the state of one and addressing the corresponding two levels of the other (e.g. the electron qubit can be addressed by fixing the nucleus at $|\uparrow\rangle$, leaving a two-level system with $E_{\downarrow\uparrow}$ and $E_{\uparrow\uparrow}$). There are four sets of two-level transitions available ([Figure 1.3](#)), we use the subscript e and N for the electron and nuclear qubit transitions respectively:

$$\nu_{e\uparrow} = E_{\uparrow\uparrow} - E_{\downarrow\uparrow} = \gamma_e B_0 + A/2 \quad \nu_{e\downarrow} = E_{\uparrow\downarrow} - E_{\downarrow\downarrow} = \gamma_e B_0 - A/2 \quad (1.2)$$

$$\nu_{N\uparrow} = E_{\uparrow\uparrow} - E_{\uparrow\downarrow} = A/2 - \gamma_N B_0 \quad \nu_{N\downarrow} = E_{\uparrow\downarrow} - E_{\downarrow\downarrow} = A/2 + \gamma_N B_0 \quad (1.3)$$

The nuclear spin can also be used as a qubit while the nucleus is ionised with $\nu_N = \gamma_N B_0$.

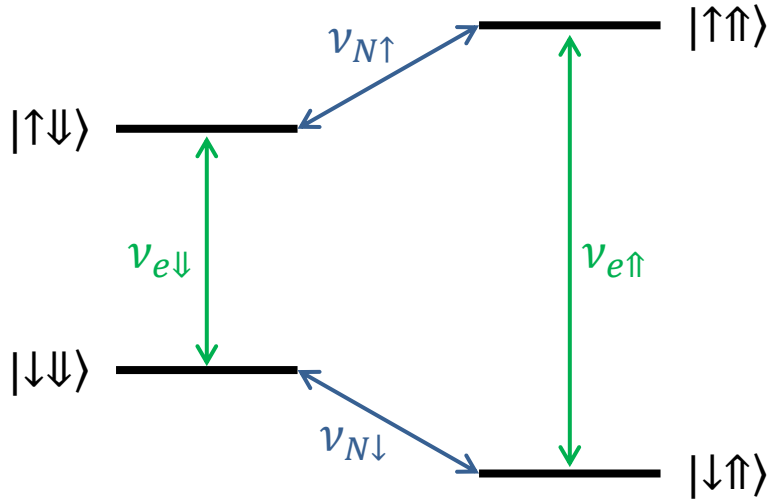


Figure 1.3: Spin energy levels and transitions of the electron-nuclear system.

1.2.2 Qubit control

Spin qubits are controlled using a technique which has been used to study the physical and chemical properties of matter for over 60 years, known as *magnetic resonance* [20]. When we explained the Zeeman effect in the previous section, we purposefully expressed the energy splitting in frequency units. We did this in order to simplify the visualisation of the Zeeman splitting, as a precession of the spin around the axis of magnetisation (the z axis), this is known as the *Larmor precession*. In order to control our qubits, we need a source of magnetic field oscillating at the exact frequency of the Larmor precession of the qubit we want to control. Under this resonant condition, the spin appears to be static in the reference frame of the oscillating source, this is known as the *rotating frame*. The spin will react to a magnetic field from this oscillating source, by precessing around the axis on which the field is applied (the *control axis*); if this axis is perpendicular to z , and assuming the spin is initialised to one of the eigenstates ($|↓\rangle$ or $|↑\rangle$), the spin will describe a circumference on the Bloch sphere which crosses the eigenstates — these spin rotations are known as *Rabi oscillations*. Furthermore, by applying the oscillating field over two different axes perpendicular to z (e.g. x and y), we gain access to the entire Bloch sphere. The Rabi oscillation frequency $f_{\text{Rabi}} = \gamma B_1$ — where B_1 is the amplitude of the oscillating magnetic field — tells us how fast we can position the spin about the Bloch sphere, therefore it is a measure of the qubit gate operation times.

Throughout this thesis, we will extensively use the term *nπ pulse*, to refer to a magnetic resonance pulse that rotates the spin by an angle $n\pi$ (in radians), where n can be any fraction (Figure 1.4 shows an example of a $\pi/2$ rotation). When appropriate, we will also use the notation $n\pi_\phi$ to refer to $n\pi$ pulses along the ϕ axis.

Magnetic resonance experiments are traditionally performed on macroscopic ensembles of

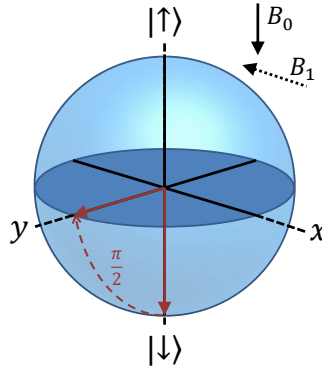


Figure 1.4: Magnetic resonance driving a spin rotation. The rotation is perpendicular to the axis of the applied oscillating field.

atoms or molecules. In those systems, the oscillating magnetic fields are generated using centimetre size coils or resonators at the tip of a magnetic resonance probe. Performing magnetic resonance on a single-spin requires the oscillating fields to be localised to the nanometre scale, and integrated with ultra-sensitive measurement techniques; this is one of the main challenges for the successful implementation of our qubit system. Single spin manipulation using magnetic resonance has been demonstrated in a number of occasions, using a range of techniques for delivering the oscillating magnetic fields, from small coils [21, 22] and waveguides [23] to nanofabricated coplanar striplines (CPS) [24] and coplanar waveguides (CPW) [25]. In Chapter 3 we will describe our approach to this challenge, with a novel nanoscale broadband antenna design capable of delivering microwave fields.

1.2.3 Qubit measurement and initialisation

Electronic systems operate by applying and measuring currents and voltages. In our common classical computing systems, the value of a bit is obtained by measuring a low-voltage (0) or high-voltage (1) at the terminals of a transistor. In order to measure our spin-qubits, we need to find a mechanism to translate spin states into measurable currents or voltages.

For our electron spin qubit, this translation is a two-step process: *spin to charge conversion* and *charge detection* (Figure 1.5). The latter involves devices that output a current which is very sensitive to movements in charge around their environment, such as the addition or removal of an electron to a nearby charge centre. *Quantum point contacts* [26, 27] and *single electron transistors* [28] are the devices commonly used in charge sensing experiments. Section 1.2.6 provides more detail on how one of these charge sensors operate.

Spin to charge conversion is a mechanism through which a charge is allowed to move into or away from a charge centre, depending on its spin state. To understand this mechanism, we need to define some basic terms. When an electron is added or leaves a charge centre, it requires some energy to be absorbed or dissipated respectively. This energy is the charge

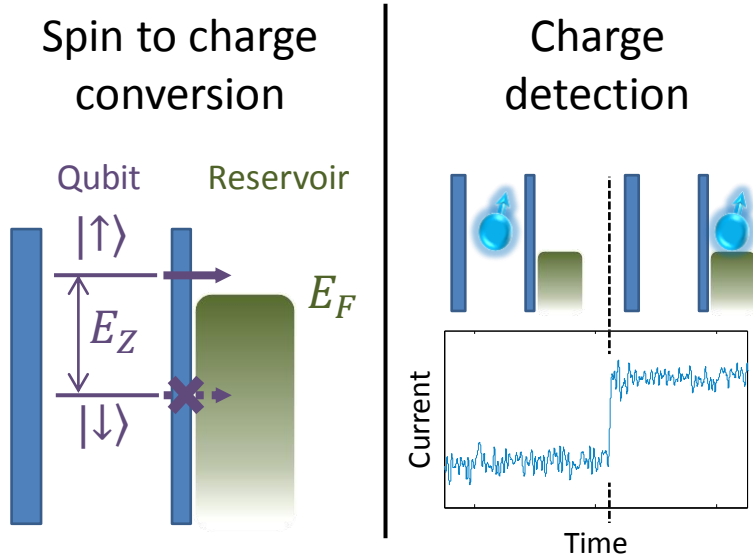


Figure 1.5: Elements needed for qubit measurement. The first step is to have tunneling from the donor to the reservoir, conditioned on its spin state. The second step involves a device that outputs different current levels, conditioned on the charge occupation of the donor.

centre's *electrochemical potential* (μ_E , where E is the energy state — e.g. an electron number or a spin state). An electron can move from e.g. charge centre 1 to charge centre 2, through a process called *quantum tunneling*, which is only allowed if $\mu_1 > \mu_2$. A spin qubit will have two distinct electrochemical potentials (μ_\uparrow and μ_\downarrow) split by the Zeeman energy. In contrast, a many electron system (such as a 2D electron reservoir), can receive an extra electron at almost the same energy cost (the *Fermi energy* E_F), independent of the spin [29]. Spin to charge conversion can be realised by tunnel coupling an electron spin qubit to a 2D electron reservoir, and tuning the potentials such that $\mu_\uparrow > E_F > \mu_\downarrow$. In this regime, the electron can only tunnel when its in $|\uparrow\rangle$, and the spin to charge conversion process is done. A nearby charge sensor will alert us when there is a tunneling event, allowing to discriminate between $|\uparrow\rangle$ and $|\downarrow\rangle$. This same mechanism is used for qubit initialisation, as the empty single electron charge centre will only be allowed to receive a $|\downarrow\rangle$ electron after measurement. This method has been successfully applied to perform single-shot readout of single electron spins in quantum dot [30] and P donor [31] systems.

The *energy-selective* spin to charge conversion technique described here is the most commonly used in this thesis and the most appropriate for single spin readout. Another spin to charge conversion technique, known as *tunnel-rate-selective* readout [32], discriminates spin states which have a large asymmetry in their rate of tunneling to the reservoir. This technique is used and will be described in further detail in Chapter 5.

Measurement of the nuclear spin qubit is achieved through a sequence of control and mea-

surement of the electron spin. As described [Subsection 1.2.2](#), the hyperfine interaction splits the electron spin resonance into two frequencies ([Equation 1.2](#)), one for each nuclear spin state. This can be exploited to measure the nuclear spin state through a measurement of the electron spin, using the following procedure, which we define as the *nuclear readout sequence*:

1. Initialise the electron spin $|\downarrow\rangle$
2. Apply an ESR π pulse using the frequency $\nu_{e|\uparrow\rangle}$. The electron will flip only if the nuclear spin state is $|\uparrow\rangle$
3. Measure the electron spin. The result of the electron spin measurement is equal to the nuclear spin state.

Notice that this measurement preserves the physical integrity of the nuclear spin. Additionally, in the high-field regime the hyperfine interaction is well approximated by $A\mathbf{S}\cdot\mathbf{I}$, which commutes with the nuclear hamiltonian. This constitutes a *quantum nondemolition measurement* [[33](#)]. In contrast, when we measure a $|\uparrow\rangle$ electron, it leaves the donor site and is later replaced by a different electron from the reservoir.

1.2.4 Two-qubit gates

A complete set of gates for a universal quantum computer contains single-qubit gates as well as at least one two-qubit gate [[34](#)]. Two-qubit gates require qubits to interact with each other, and there should be some level of control of the interaction. Several different methods to implement a controllable interaction between spin-qubits have been proposed. The simplest form of interaction — known as the *exchange interaction* — arises from the overlap of the wavefunctions of two nearby spins [[35](#), [36](#)]. The interaction can be controlled through any mechanism that distorts the electron wavefunction, such as an electric field from a nearby gate (labeled J in [Figure 1.2](#) from Kane’s proposal [[12](#)]). Other methods for generating interaction between spin qubits include the use of magnets [[37](#)] and microwave photons [[38](#)], these however are suited for spatially separated spins, making them more appropriate for spin transport (see next section).

Under a large exchange interaction, the eigenstates of the two-qubit system are:

$$\begin{aligned} |T_+\rangle &= |\uparrow\uparrow\rangle \\ |T_0\rangle &= \frac{1}{\sqrt{2}}(|\uparrow\downarrow\rangle + |\downarrow\uparrow\rangle) \\ |T_-\rangle &= |\downarrow\downarrow\rangle \end{aligned} \tag{1.4}$$

$$|S\rangle = \frac{1}{\sqrt{2}}(|\uparrow\downarrow\rangle - |\downarrow\uparrow\rangle)$$

The first three are known as the *triplet* states; they have total spin 1, are degenerate unperturbed and Zeeman split under static magnetic fields, with $|T_0\rangle$ remaining at the same energy, while

$|T_+\rangle(|T_-\rangle)$ increase(decrease) by E_Z . The remaining *singlet* state has a total spin 0. The energy difference between $|T_0\rangle$ and $|S\rangle$ is the exchange coupling (J).

Two-spin systems with controllable exchange have been realised with double quantum dots in GaAs [39] and Si [40]; furthermore, there are proposals and great experimental efforts to implement a quantum computing architecture using these double quantum dot systems as qubits [41]. Exchange interaction between pairs of donors in silicon has been observed in bulk spin resonance experiments [42] and — very recently — by electron transport experiments through a donor molecule [43]. However, dynamical control and instantaneous measurement of the quantum state has not been demonstrated. Nevertheless, there is a recipe available for implementing a two-qubit system compatible with our P-Si devices [44], the details of which are beyond the scope of this thesis. However, we will present in [Chapter 5](#), experimental results on the first ever time-resolved readout and lifetime measurements of the singlet-triplet states of two coupled electrons from a pair of P donor in Si.

1.2.5 Qubit transport

Most quantum computer architectures require a method for shuttling qubits coherently to different regions around the system. Under realistic experimental conditions, qubit states will need to be coherently transferred over distances in the order of hundreds of nanometres. This is a particularly tough challenge with semi-conductor qubits, due to the static nature of the particles in solid state. Hollenberg's architecture [13] proposed to use a method called *coherent transfer by adiabatic passage* [45]. This method requires dynamic coupling of the origin and destination charge centres to a chain of strongly coupled charge centres. By controlling the coupling to the chain in a clever way, an electron can be transferred from origin to destination, without occupying any of the charge centres in the chain. Other proposals for spin transport based on similar concepts of making chains of spin centres include *spin bus* [46, 47] and *resonant adiabatic passage* [48]. A slightly different approach involves using a large quantum dot, instead of a chain of single spins, as a medium to couple distant qubits, through a mechanism called *RKKY coupling* [49]. Another possibility is to couple the physically separated qubits through a planar microwave resonator, using a technique called *cavity quantum electrodynamics* [50].

1.2.6 Our physical implementation

All of the measurements described in this thesis were performed using a qubit device architecture designed to readout and manipulate the spins from a single P atom, buried near the surface of a Si substrate [29]. A simplified schematic of the device is shown on [Figure 1.6a](#) and a real device image taken using a scanning electron microscope (SEM) is shown in [Figure 1.6d](#) for reference. The following subsections describe the main components of the device.

1.2. Our qubit of choice: P-Si single-spins

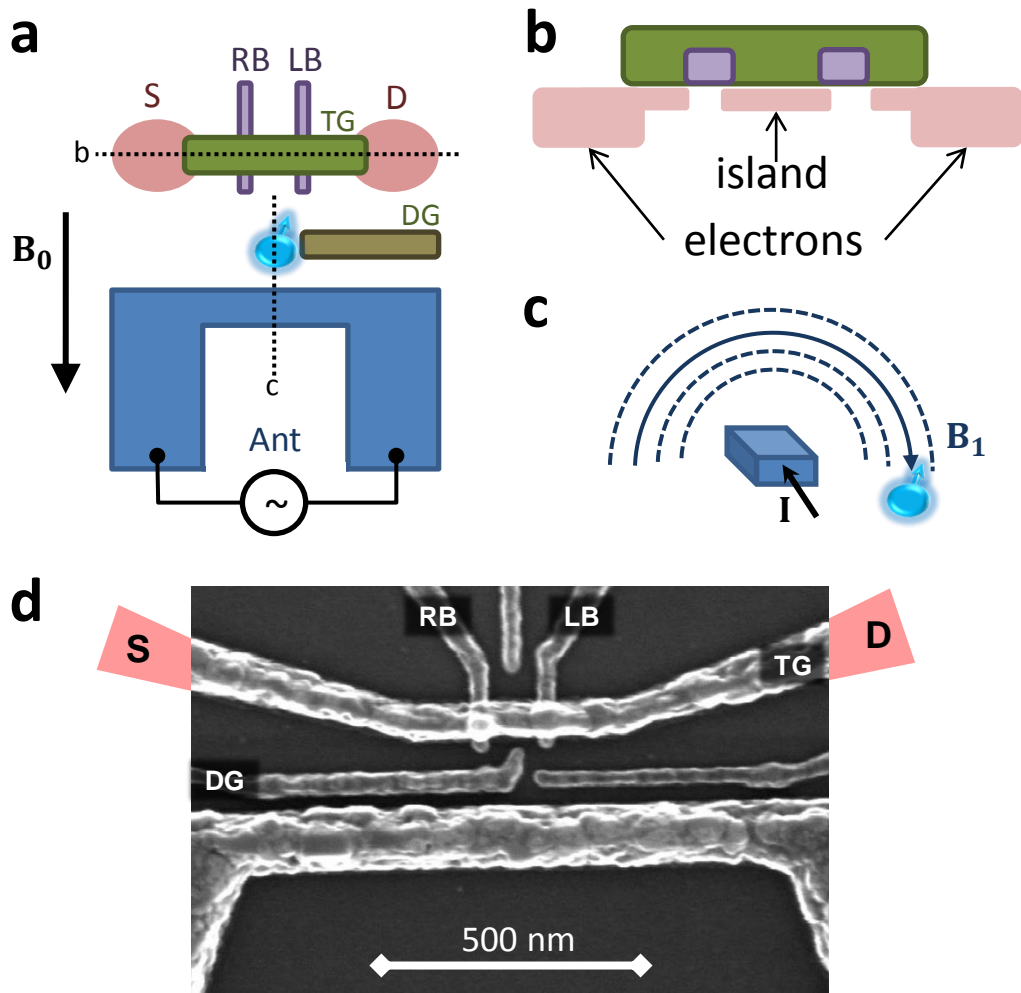


Figure 1.6: Qubit device schematic with main components. **a** Top overview of the qubit device. **b** Cross sectional view of the SET, showing the SET island. The tunnel barriers underneath LB and RB are electrostatically defined by applying a negative barrier voltage relative to TG. This potential repels the electrons underneath the barriers, creating the island. **c** Current flowing through the short-circuited termination of the spin-resonance antenna generates a magnetic field at the donor site which is perpendicular to the static magnetic field. **d** Scanning electron microscope image of a real device identical to the ones used for measurements. All the gates analogous to **a** are labeled.

The P donor atom

Donor atoms are introduced in semi-conductor substrates to provide reservoirs of charge carriers in the semi-conductor. This is commonly done in the electronics industry, as part of the fabrication process of the components in every modern electronic device. This task however becomes very challenging for our qubit devices, which require that only one (or a few at maximum) donor atom be incorporated within a $\sim 30 \times 30$ nm window. There are two approaches to this task:

The bottom-up approach uses a combination of scanning tunneling microscopy and molecular beam epitaxy to place individual P atoms with atomic precision on the silicon substrate [51]. After placing the atom, an extra layer of silicon is grown to seal the atom in the substrate. One of the main disadvantages of this approach is that the low thermal budget prevents the use of anneals and oxidation steps after the donors have been incorporated.

The top-down approach involves a technique called *ion implantation*, which is the same technique used commercially for doping, modified by using nanoscale masks and very low implantation energies [52]. With this method, very high quality oxides and gates can later be fabricated to complete the device. The disadvantage is the lack of atomic precision and not knowing exactly how many donors get implanted, however to operate our spin qubit devices, atomic precision of the location of the P atom is not needed. All the devices used in the experiments described in this thesis were fabricated using the top-down approach.

After the donor atom has been implanted, we fabricate a set of metal gates on the surface of the substrate ([Figure 1.6](#)) in order to perform the readout and control of the donor electron spin. The electrochemical potential of the donor electron can be tuned by applying a voltage to the *donor gate* (DG). The SEM image in [Figure 1.6d](#) gives an impression of the dimensions of these devices. The donor is implanted ~ 10 nm below the surface oxide.

The charge detector

The gates labeled S (source), D (drain), TG (top-gate), LB (left-barrier) and RB (right-barrier) in [Figure 1.6a–b](#) make up a single electron transistor (SET) [53] used for charge sensing. A standard metal-oxide-semiconductor field-effect transistor (MOSFET), used in most modern electronic devices, has a source and drain made of highly doped silicon (i.e. regions with many available charge carriers in the semiconductor), separated by a gap (the channel) above which there is a metal gate. By applying a small S-D voltage bias and applying a large enough voltage to the gate (greater than the turn-on voltage), a stream of electrons will flow through the gap generating a current between S and D. An SET is a very similar device, with the addition of the barrier gates which create tunnel-gaps in the stream of electrons, creating an electron *island* between the barriers (depicted graphically in [Figure 1.6b](#)). If it is small enough, the SET island will have a quantised electrochemical potential ladder (see [Figure 1.7a](#)); as we vary

1.2. Our qubit of choice: P-Si single-spins

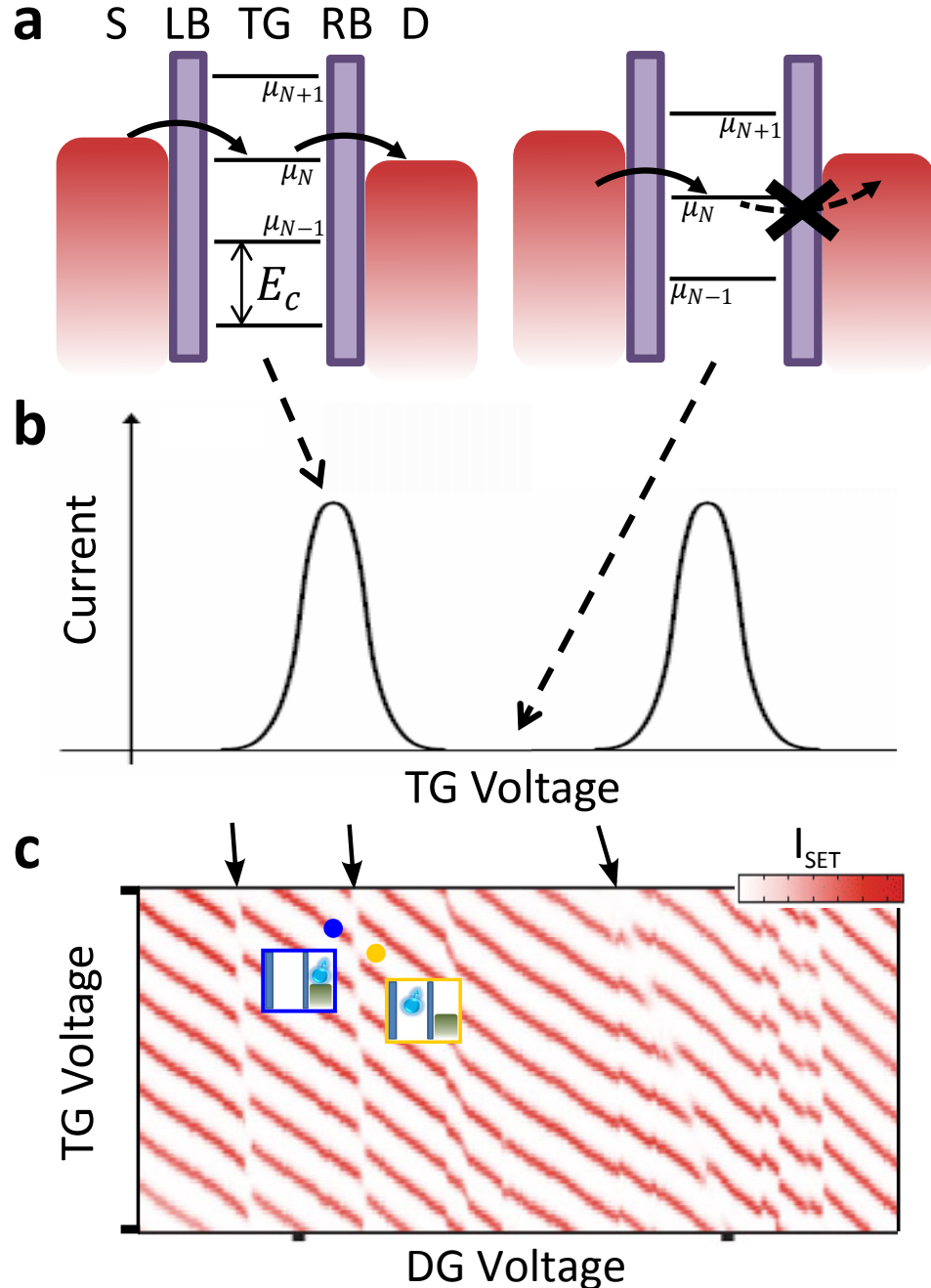


Figure 1.7: Basic operation of the SET. **a** The quantised potential ladder of the SET island can be shifted by sweeping the TG voltage. Electrons can flow from S to D by tunneling through the barrier, only when one of the island chemical potentials (μ) are inside the S-D window. **b** Resulting Coulomb peaks of output current, obtained when the TG is swept. If the device is tuned to the top of a Coulomb peak, an electron tunneling from the nearby donor to the island will cause a shift in que island's chemical potential, large enough to block the current. **c** Charge stability diagram highlighting some of the donor charge transitions (arrows). The charge detector can be tuned such that there is a large current when the donor is ionised (blue dot) or zero current when the donor is loaded (yellow dot). Figure extracted from Reference [31].

the voltage on TG, the energy levels of the ladder move accordingly; when an energy level finds itself in the S-D bias window, electrons are allowed to tunnel from source to island to drain, causing a current to flow. When there is no island energy level in the bias window, an electron that tunneled from source to island will not have enough energy to tunnel to the drain, therefore the current is blocked; this is known as *Coulomb blockade*. If we plot the S-D current as function of TG voltage, we see peaks of current (*Coulomb peaks*) separated by gaps of zero current (see [Figure 1.7b](#)). The distance between peaks is the *addition energy or charging energy* (E_c). The width of the peaks are a function of the S-D bias window, the probability of an electron tunneling through the barrier (known as *lifetime broadening*) and the temperature (see [Section 1.4](#)).

In order to use the SET as a charge detector, the electron island needs to be located in the vicinity of the P atom (~ 50 nm away), such that the presence of an electron on the donor emits an electric field large enough to shift the island's electrochemical potential by at least half the width of a coulomb peak. By performing a 2D map of the current as a function of both TG and DG voltages — known as a *charge stability diagram*, donors can be easily identified by discontinuities in the Coulomb peak lines. These discontinuities — or *charge transitions* — mark the boundary voltages between ionisation and neutralisation of a donor. In [Figure 1.7](#) we show a sample charge stability diagram with several charge transitions. The charge detector is operated at the charge transition boundary, such that a high current is observed when the donor is ionised, while a very contrasting zero current is observed when the donor is neutral. This method was pioneered by our research group [29] and has been used to demonstrate single-shot readout of a single electron spin from a P donor, with exquisite fidelities [31].

The spin resonance antenna

The final element of our qubit device is an antenna (labeled Ant in [Figure 1.6](#)) that generates the oscillating magnetic fields needed for spin resonance. The antenna consists of two strips of metal fabricated on the chip, which are terminated by a short circuit in the vicinity of the P atom (~ 50 nm away). An analysis of the *Biot-Savart law* will aid in understanding what results from applying a signal to the antenna:

$$\mathbf{B} = \frac{\mu_0 I}{4\pi r^2} \int_L d\mathbf{l} \times \hat{\mathbf{r}}$$

Here μ_0 is the magnetic permeability of free space, I is current (with $d\mathbf{l}$ an infinitesimal current direction vector), r distance (with $\hat{\mathbf{r}}$ a unit vector with direction to point \mathbf{r}), and L is the length of the current-carrying wire.

This equation tells us that a current flowing across a wire will generate a magnetic field which is always perpendicular the direction of the current flow, thus rotating around the wire. From the graphical representation in [Figure 1.6c](#), we can see that the current across the short circuit termination of the antenna will generate a magnetic field with direction perpendicular

to the plane near the surface of the substrate. Therefore if the direction of B_0 is in plane with the substrate surface, then applying an oscillating signal to the antenna will generate a B_1 perpendicular to the static field, which is appropriate for magnetic resonance ([Subsection 1.2.2](#)). Note that Biot-Savart's law also tells us that the field is inversely proportional to the distance from the B_1 source to the spin, therefore it is advantageous to place the antenna as near as possible to the donor atom.

Another effect of the short-circuit termination is that it creates a *potential node*, which means that the electric fields vanish as they reach the loop. This effect is important because, as described in [Section 1.2.6](#), the charge detector is very sensitive to small changes in electric field, therefore any electric field noise radiated from the antenna will negatively affect the qubit readout capability.

Basic experimental spin-resonance techniques

The next few paragraphs will describe some of the basic experiments that are carried out when operating spin qubits. This explanation is generalised for all spin qubits with single-shot measurement capabilities. The most important experimental issue to grasp is that every single-shot measurement is a *quantum measurement* which can only result in one of two possible states ($|\uparrow\rangle$ or $|\downarrow\rangle$). The *probability* of obtaining one of the states is given by the projection of the spin (on the Bloch sphere) on the measurement axis z (e.g. if the spin is pointing in along the y axis, there is a 50% probability of measuring $|\uparrow\rangle$). If we want to extract this probability experimentally, we need to repeat the same experiment several times and take an average of all the measurements. From this we define the *spin-up proportion* (P_\uparrow) as the proportion of measurements that resulted in $|\uparrow\rangle$ out of many repetitions of the same experiment. In this section we will also assume that for each experiment, the qubit is always initialised $|\downarrow\rangle$.

The first step is to obtain the spin-resonance frequency spectrum, which should expose the Larmor frequency of the spin (ν_{res}). This can be done by turning on the oscillating magnetic and sweeping the frequency (ν_1) across the expected Larmor frequency, while making repeated measurements after each frequency increment. As long as $\nu_1 \neq \nu_{\text{res}}$ (*off-resonance*) it will have no effect on the spin, and the measured $P_\uparrow = 0$. When the frequency is *on-resonance*, the spin will start to rotate around the Bloch sphere and the measurement will result in $P_\uparrow \neq 0$. By plotting the resulting P_\uparrow as a function of frequency, we obtain a frequency spectrum with a *spin resonance peak* as shown in [Figure 1.8a](#).

Once the correct resonance frequency has been found, we can perform Rabi oscillations to evaluate how fast the spin nutates from the South pole to the North pole of the Bloch sphere, given our applied B_1 strength. This is done by turning on B_1 for very short periods of time, or *pulses*. The pulse length (t_p) is stepped, and repeated measurements are taken after every pulse length increment. Every pulse length increment will increase the rotation angle; at a pulse length π it will reach $|\uparrow\rangle$, after which it will keep rotating back towards $|\downarrow\rangle$. If we plot P_\uparrow as a function of pulse length (see [Figure 1.8b](#)), we obtain a sinusoidal Rabi oscillation, ranging

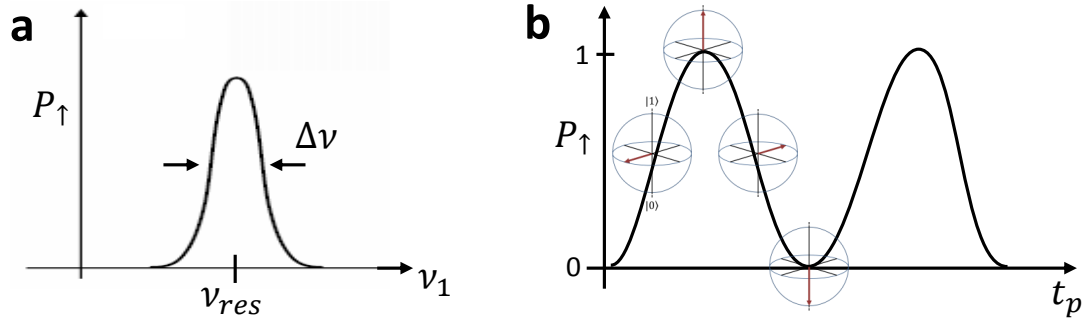


Figure 1.8: Spin resonance spectrum and Rabi oscillations. **a** Spin-up proportion measured when the oscillating field is turned on and swept in across the frequency. The width of the peak is a manifestation of the noise that we observe on the qubit. **b** Coherent oscillations of the qubit state. A graphical visualisation of the state in the Bloch sphere is depicted at different key rotation points.

from $P_{\uparrow} = 0$ to 1.

With these two experiments we have calibrated the resonance frequency and the appropriate pulse length to make any $n\pi$ rotation, giving us full control of our qubit.

1.3 Basic concepts in RF transmission lines

The design of the spin resonance antenna described in [Section 1.2.6](#) is one of the main topics in this thesis and will be discussed extensively in [Chapter 3](#). In this section we will define some important concepts related to radio frequency transmission lines, that are necessary to understand that chapter.

When electrical signals oscillate at radio frequencies (from kHz to hundreds of GHz), some properties of electromagnetism become much more relevant than for lower frequency signals. When a potential difference is applied between two conducting nodes, there will be an electric field generated between the nodes which, if there is a conducting medium between the nodes, will induce a current to flow from one node to the other. The flowing current has associated electric and magnetic fields given by Maxwell's equations. These *electromagnetic fields* travel in waves which have a length that is given by $\lambda = v/f$, where v is the propagation velocity and f is the frequency of oscillation. When this *wavelength* is comparable to the distance that the current is traveling, then the physics of wave propagation becomes very relevant to how the current is transmitted.

A *transmission line* (TL) is a medium through which electromagnetic (EM) waves can propagate. The most important concept in the description of EM wave propagation through a TL is the *characteristic impedance* (Z_0). The characteristic impedance is defined as the complex ratio of voltage to current of the traveling wave $Z_0 = V(t)/I(t)$ [54]. As long as the impedance is constant throughout the entire TL, the wave can propagate smoothly. If however there are discontinuities in the impedance of a transmission line, only part of the wave's total

amplitude will propagate through the discontinuity, while the other part will get reflected. The proportion of the wave amplitude that gets reflected is given by the *reflection coefficient* $\Gamma = (Z_2 - Z_1)/(Z_2 + Z_1)$, where $Z_{1(2)}$ is the impedance of the TL before(after) the discontinuity. This equation tells us that for a larger difference between the impedances at the discontinuity, a smaller proportion of the signal will propagate. When a transmission line has equal impedance along its entire length, it is known to be *impedance matched*, fulfilling the requirement for maximum signal propagation.

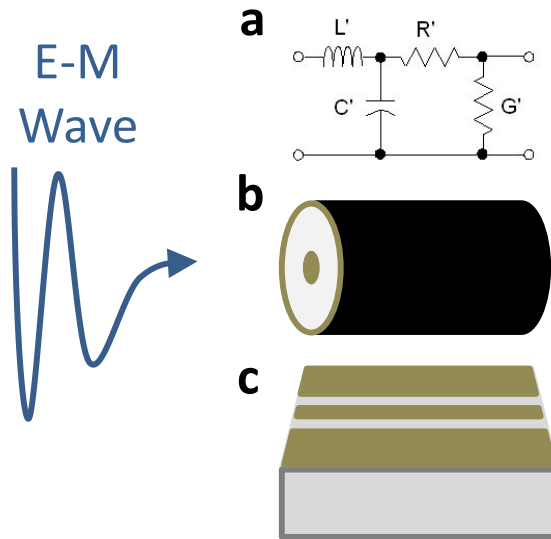


Figure 1.9: RF transmission lines. **a** Lumped element circuit model of a transmission line. **b** Coaxial line. **c** Coplanar line.

To characterise the behaviour of a TL as a function of frequency (ω), it is useful to model transmission lines using their *lumped element circuit* equivalent. Each section of a transmission line can be modeled through an equivalent electrical circuit made of resistors R , inductors L , conductors G and/or capacitors C . This turns a very difficult problem of analysing propagation using Maxwell's equations, into a much simpler circuit analysis problem. For example, an infinitesimal length of TL can be described by the circuit in Figure 1.9a where each of the elements (R' , L' , G' , C') are defined per unit length. Using this model, the characteristic impedance becomes $Z_0 = \sqrt{(R' + i\omega L')/(G' + i\omega C')}$. In a similar way, any features that break the homogeneity of a TL, such as bends, transitions or discontinuities, will also have an equivalent lumped element circuit. Therefore, transmission lines can exhibit frequency dependent attenuations or resonances. To get an idea of the frequencies at which these issues become relevant, consider again the TL model in Figure 1.9a. An RLC circuit exhibits a resonance at frequency $\omega_0 = 1/\sqrt{LC}$. For TL lengths comparable to the wavelength of the signal, the value of $1/\sqrt{LC}$ of the equivalent TL model will match the frequency of the signal. Therefore, these issues become important above tens of GHz, where wavelengths (in the order of cm) become comparable with our device sizes.

The most common way to characterise the frequency response of an RF TL, is through its *scattering parameters*, which describe the ratio between the amplitudes of transmitted and reflected EM waves, at different ports in the transmission line as function of frequency. Scattering parameters follow $S_{ij} = V_i/V_j$, corresponding to the transmission from the input port j to the output port i .

There are many different methods for implementing a transmission line, which have different advantages based on the application. In this thesis there are two relevant types ([Figure 1.9b-c](#)):

Coaxial lines consist of a conducting wire enclosed by a cylindrical conductor, with a dielectric filling the space between both conductors. This is the most common type of transmission line, and we use them to deliver signals from the instruments to our device.

Coplanar lines consist of two or three conducting strips on top of a dielectric block. These type of lines are useful for carrying signals along a circuit board or the chip that contains our device.

In [Chapter 3](#) we will build from these basic concepts to describe the methods we use to transmit high-frequency signals to our magnetic resonance antenna, in order to control our qubits.

1.4 Low temperature

The phosphorus donor in our system is surrounded by Si atoms in a lattice. Donors interact with the lattice by exchanging energy that is a function of the temperature. Up to now, we have been assuming that all the energies we have described are fixed and well defined, in order to make our explanations simpler for the reader. In reality, a particle that interacts with a lattice is always affected by thermal energy, which adds an uncertainty to our energy levels. This effect is known as *thermal broadening* and it causes the energy levels in our figures to become broadened by a probability distribution which depends on the mechanism that affects each system. In our spin-to-charge conversion process, the largest thermal broadening is that of the electron reservoir, which has a quasi-continuum density of states with a thermal broadening $\sim 4k_B T$, where k_B is the Boltzmann constant and T is the temperature. For our spin-to-charge conversion process to be effective, we need make sure that the thermal broadening is much smaller than the energy level spacing that we need to measure. The effects of temperature on the effectiveness of our measurement will be explored in further detail in [Section 2.5.2](#).

In order to operate our devices at adequate low temperatures, we use a *dilution refrigerator*, to reduce our qubit environment to temperatures below 100 mK (-273.05°C). These temperatures are achieved through a process of continually diluting two different helium isotopes (^3He into ^4He) [\[55\]](#), which through a quantum mechanical effect, absorbs energy which can be used for cooling. More details on the experimental setup needed to cool a device to those temperatures are given in [Section 2.3](#).

1.5 Important spin qubit characteristics

We will now define some qubit related concepts which will be used throughout this thesis, which allow us to characterise the performance of our qubits. In [Section 2.5](#) we will provide further detail on the experimental algorithms used to extract all of these qubit characteristics.

1.5.1 Spin lattice relaxation time

Spins can exchange energy with the surrounding lattice, and after a long enough time this spin-lattice coupled system will reach an equilibrium, which leaves the spin polarised preferentially in the ground state ($|\downarrow\rangle$). The spin energy splitting (E_Z) and the temperature of the lattice determine the spin ground state probability at equilibrium $P_{\downarrow}^{\text{eq}} = 1/(\exp(-E_Z/k_B T) + 1)$. A spin prepared in $|\uparrow\rangle$ will relax to equilibrium in a time given by the spin lifetime or spin-lattice relaxation time (T_1), such that $P_{\uparrow}(t) = (1 - P_{\downarrow}^{\text{eq}}) \exp(-t/T_1) + P_{\downarrow}^{\text{eq}}$. The spin lifetime is a function of many variables in both the spin and lattice systems, and can be quite demanding to calculate, but it can be measured relatively easy by preparing a spin $|\uparrow\rangle$ and measuring its state after increasing wait times, as will be described in detail in [Subsection 2.5.2](#).

T_1 sets a lower limit on the speed of the measurement equipment. If the delay between the qubit state preparation phase and the measurement phase is longer than T_1 , then by the time we are set to measure, the spin will have relaxed to the ground state and the measurement will be inaccurate.

1.5.2 Linewidths and coherence times

Our ability to control the qubit depends how well we can match the oscillating magnetic field frequency to the Larmor frequency of the spin (see [Subsection 1.2.2](#)). This means that any noise that affects the Larmor frequency will negatively affect our ability to track the spin. This noise is manifested as random rotations of a spin in the Bloch sphere around z , causing *dephasing*. Dephasing is the decoherence mechanism in spin qubits and its one of the most important topics that need to be addressed when characterising qubit performance.

Dephasing can be observed and characterised in a number of ways. The simplest one, because it does not require coherent control, is through the *linewidth* of the spin resonance peak. In the absence of noise or uncertainties, the spin resonance spectrum would have an infinitesimally narrow line at the exact resonance frequency. Noise modulates the spin precession frequency, therefore the spectrum measured will have a peak with finite width ($\Delta\nu$ in [Figure 1.8a](#)), corresponding to the amplitude of the noise. $\Delta\nu$ is not only a function of its environment, it also depends of the amplitude of the oscillating field [56]. When the field amplitude term dominates the observed $\Delta\nu$, the linewidth is said to be *power broadened*.

Another way to characterise dephasing noise is to evaluate the time it takes for the spin to “get lost” or *decohere*. If we prepare a spin in the x - y plane (by applying a $\pi/2$ rotation to an initialised spin), after some time we can apply another $\pi/2$ to bring the spin to $|\uparrow\rangle$.

This only works if the spin stays static (perpendicular to the control axis) between the two rotations. Noise however, will cause the spin to dephase randomly about the x - y plane. For very high noise, the spin will in a random position on x - y when we apply the second $\pi/2$, making the pulse ineffective. The measurement will result in $P_\uparrow = 0.5$. In this case we have completely lost coherence of the spin. **The time-energy version of Heisenberg's uncertainty principle ($\Delta E \Delta t \geq \hbar/2$) tells us that there is a limit to how far a spin can dephase after a finite wait time between $\pi/2$ pulses.** The postulate allows us to extract the amplitude of the noise from this experiment. If we start making measurements with very short wait times, the spin will still be coherent, resulting in $P_\uparrow = 1$. As we increase the wait time and start to lose coherence, the measurement results will decay towards $P_\uparrow = 0.5$. This decay time is known as the *free induction decay* (T_2^*) and it is intrinsically related to the linewidth by $\Delta\nu = 1/(\pi T_2^*)$. A graphical representation of the free induction decay measurement is shown in [Figure 1.10a](#).

Sources of decoherence

To get an idea of possible sources of dephasing, let's analyse our system's spin hamiltonian ([Equation 1.1](#)). Any noise that can couple to any of the terms on the quantization axis (z) will generate dephasing. Any magnetic noise with a z component is an effective noise on the $\gamma_e B_0 \mathbf{S}_z$ term. Possible sources of magnetic noise are equipment noise and nearby spins in the surrounding environment. The latter is one of the most studied sources of decoherence in solid state qubits. Spin- $\frac{1}{2}$ particles are magnetic dipoles, that radiate magnetic fields to their surroundings. When the spin flips, it inverts the polarisation of the field it emits. If these particles are in the vicinity of the qubit, it will feel an additional magnetic field equal to the sum of all the radiated fields from nearby spins [57]. Spins flip-flopping in time generate random variations of this field manifested as magnetic noise. One source of spin- $\frac{1}{2}$ particles is surrounding P donors. Additionally, an oxide (SiO_2) needs to be grown on the Si substrate and the gates for our nanostructure are fabricated on the oxide. Lattice mismatch at the interface of Si and SiO_2 can cause electron vacancies known as *charge traps*. If the spin of electrons in charge traps around the qubit is allowed to flip randomly, they will induce magnetic noise [58]. Another important source of magnetic noise comes from the Si lattice. Silicon has three stable isotopes (^{28}Si , ^{29}Si , ^{30}Si) out of which one of them (^{29}Si) has a spin- $\frac{1}{2}$ nucleus (the others are spin-0). The mechanism for magnetic noise from surrounding nuclear spins in the lattice is known as *spectral diffusion* and the effective magnetic fields generated by them are known as *Overhauser fields*. We will explore in the next subsection the relevance of ^{29}Si nuclei in our system.

Electric field noise can also be a source of dephasing. The *Stark effect* causes shifting of the spin resonance frequencies in the presence of an electric field. In our system, electric fields can cause Stark shifts by coupling to the hyperfine term in the hamiltonian ($A\mathbf{I} \cdot \mathbf{S}$) [59–61], or by modulating a term in γ_e known as the *g-factor* [62] ($\gamma_e = g\mu_B/h$, where μ_B is the Bohr magneton and h is the Planck constant). Electric noise can be radiated to our qubit

1.5. Important spin qubit characteristics

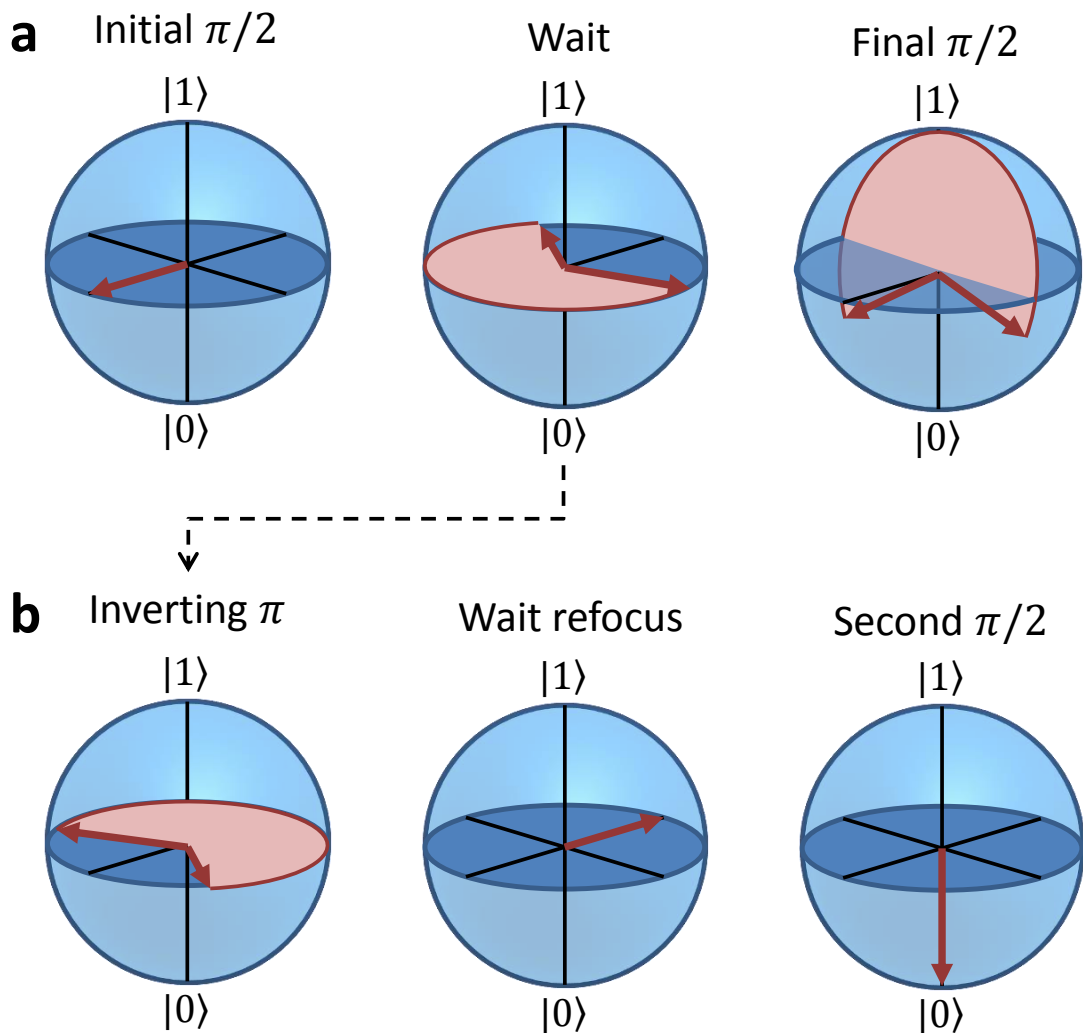


Figure 1.10: Coherence times measurements. **a** Pulse sequence to observe the free induction decay. After the wait time, the spin has decohered to an unknown state within the shaded (red) window. The result of a single-shot measurement can be any of the projections of the spin in the window. **b** Modified sequence to refocus a constant dephasing. The inversion pulse allows to regain coherence.

from the sources used to control our metallic gates. Additionally, if charge traps get filled and emptied at random intervals, they manifest as noise by changing the electric field environment of the qubit. Note that although the Stark effect allows electric noise to couple to our system, the ability to shift the hyperfine with electric fields is an important ingredient in our device architecture, because it can separate the ESR frequencies of two nearby donors in a two-qubit system, allowing us to address them individually [12].

Extending coherence

Dealing with decoherence is one of the most important tasks in quantum computing. Coherence must be maintained for long enough to perform all the needed operations. One way that coherence can be extended is by applying *dynamical decoupling* (DD), that can filter out the effects of the noise. These sequences are able to *refocus* a spin, when it undergoes relatively slow dephasing. In general, noise in solid-state systems decreases with frequency [63] — the largest noise amplitude is very slow in nature, which is exactly what DD is good for. The simplest DD sequence is the *Hahn echo* [64], which consists of applying a π pulse in the middle of the wait time of the previous free induction decay experiment (Figure 1.10b). Before the π pulse, the spin will have experienced some slow dephasing; the π pulse inverts the spin around the control axis; the same dephasing returns the spin to its original position, and coherence is restored. The Hahn echo cancels the very slow noise components, but there are always higher frequency components that ultimately cause a decay of coherence as the free precession times between pulses are increased. The longest decay achieved in a system using DD is commonly quoted as the *coherence time* of the qubit (T_2). If done carefully, DD sequences can be mixed with conventional qubit gate pulses to integrate them in quantum computations [65–67]. In Section 2.5.1 we will describe the dynamical decoupling sequences relevant to the qubit operations performed throughout this thesis.

A more intrinsic method to deal with decoherence is to remove noise from the environment of the qubit. From the previous section we learned that noise in our qubits can come from nearby ^{29}Si nuclei in the lattice. Natural silicon has $\sim 5\%$ concentration of ^{29}Si , however the material can be isotopically engineered to reduce this concentration (see Figure 1.11), thus removing the source of nuclear spin fluctuations [68]. In fact, a non-quantum computing related project established to redefine the kilogram, called the *Avogadro project* [69], has been engineering enriched silicon with the lowest ^{29}Si concentration ever made. As demonstrated in several ensemble measurements with this material [70–73], using isotopically purified Si as the substrate for our system can potentially extend our coherence times by many orders of magnitude (see Section 1.6). However, there is large skepticism with regards to the potential coherence times that could be measured for single spins, based on evidence of reduced coherence for bulk donors near a SiO_2 interface [74], and the hypothesis that gates from the nanostructure needed to measure single spins, will radiate significant electric field noise [75]. The effect of charge traps can be minimised by reducing the charge trap density through careful oxide growth; and working

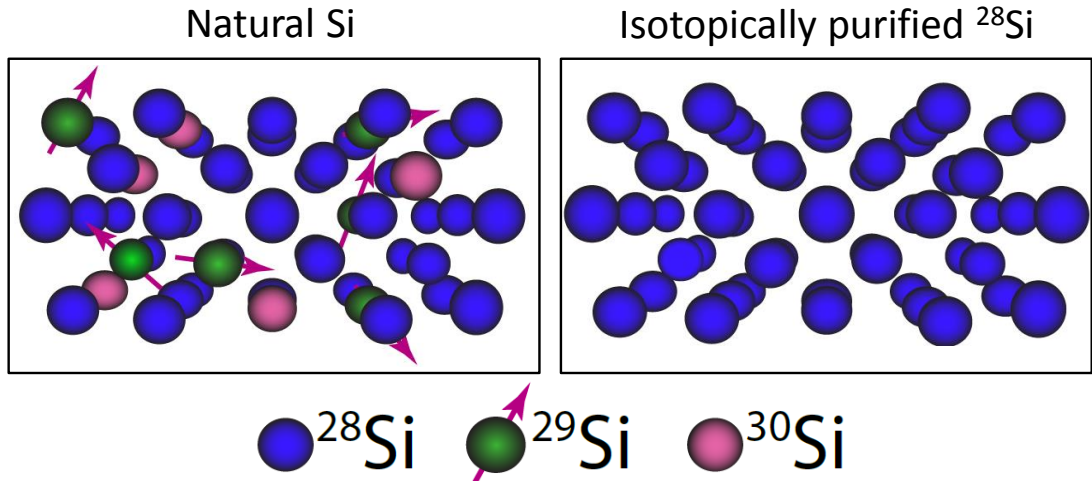


Figure 1.11: Isotopical purification of Si. The spins of the ^{29}Si isotopes are a source of decoherence for spin qubits in the substrate. Through isotopic purification, these spins can be removed, creating a noiseless environment for the qubit.

in a regime where the equilibrium polarisation of the spins $P_{\downarrow}^{\text{eq}} = 1/(\exp(-E_Z/k_B T) + 1) \approx 1$ (i.e. high B_0 and low T), such that the spins have a low probability of flipping. One of the main points in this thesis, is to measure the effects of isotopic purification on the coherence and fidelity of our single-spin qubit devices, and explore the relevance of these skeptical theories in our system (see [Chapter 4](#)).

1.5.3 Fidelities

Qubit fidelity is the ultimate measure of qubit performance. Maximising qubit fidelity involves analysing all the factors that affect initialisation, measurement and control of the qubit; understanding how they are affected and finding opportunities for optimisation in order to improve the performance of the qubit operation. Its a very complex process as many of the factors that affect fidelity are interrelated, and many solutions can have both advantageous and deleterious effects that need to be balanced.

In our qubits, the main factors that determine fidelity are the intrinsic environment, the equipment and setup, and the device nanostructure characteristics. We will now attempt to provide a glimpse of how all these factors are interrelated in affecting the fidelity, and how complicated it can get:

Environment Thermal broadening caused by interaction with the surrounding lattice (see [Section 1.4](#)) affects the initialisation and measurement fidelities: as E_Z becomes more comparable with the thermal energy $k_B T$, the measurement fidelities decrease. The lattice temperature also affects the lifetime T_1 (see [Subsection 1.5.1](#)), which affects the measurement fidelity: as our measurement acquisition time becomes more comparable to T_1 , measurement fidelity decreases.

The surrounding Si atoms can also be a source of magnetic noise (see [Subsection 1.5.2](#)), which affects the control fidelity: as $1/T_2^*$ becomes more comparable to the frequency spectrum of our control pulses, the control fidelity decreases.

Equipment We use state of the art equipment to provide control voltages and measure output currents. This equipment however still has limitations that affect our fidelity. First of all, our dilution refrigerator and experimental setup (which is described in detail in [Chapter 2](#)) relate to the environment effects, as they define our temperature limit. $E_Z = \gamma B_0$ means we need a magnet that provides B_0 fields larger than the temperature. However, larger fields present two deleterious effects: ν_e increases, which implies the use of higher frequency oscillating field generators, and the price and complexity of high-frequency experimental setups increases exponentially with frequency. Larger fields also cause T_1 to become shorter, which means we need to measure faster. Independent of the field, magnetic field sources (both static and oscillating) emit magnetic noise which can also be a limiting factor on fidelity.

The bandwidth of our measurement equipment limits how fast we can perform the measurements, which linked to T_1 , affects fidelity. In general, bandwidth and noise increase together (the RMS noise voltage of a resistor R as a function of the bandwidth Δf is $v_n = \sqrt{4k_B T R \Delta f}$), which means that increasing our bandwidth will decrease our ability to distinguish a current level from the noise (the ratio $(I_{\text{signal}}/I_{\text{noise}})^2$ is known as the *signal to noise ratio*).

Electric field noise, fed from our input voltage sources and emitted by the device gates, can also affect control fidelity. The Stark effect can couple electric fields to the hyperfine, converting the electric noise into an effective magnetic noise.

Device nanostructure The distance from the donor to the island plays an important role in the measurement fidelity. If they are too close, the tunnel rates between donor electron and island might be faster than the bandwidth of our measurement equipment. If they are too far, the change in electric field when the donor tunnels might not be enough for to obtain a large enough current contrast from the charge sensor (see [Section 1.2.6](#)).

The location and orientation of the spin resonance antenna is also relevant. It is desirable to have the antenna as near as possible to the donor in order to maximise B_1 , however stray electric fields radiating from the antenna will affect the potentials of the SET island, hindering its performance as a charge detector.

Another relevant energy level that affects fidelity is the addition energy E_c of the SET island, which determines the separation between Coulomb peaks. If the distance between the peaks is comparable to the peak width, we will lose I_{SET} contrast between donor charge states. E_c is defined by the size of the island, which is a function of the separation between the barrier gates and the width of the top gate.

Through specific experiments, we can quantify the measurement and control fidelities of our

system. In [Subsection 2.5.2](#) we will describe the details of these measurements and the analysis needed to extract the fidelities.

1.6 Putting some numbers in the equations

To gain a better understanding of our experimental requirements, we will now add realistic numbers to some of the equations presented in this introduction. Lets first look at the requirements for good electron measurement fidelity. The electron gyromagnetic ratio is $\gamma_e = 28 \text{ GHz/T} = 116 \text{ } \mu\text{eV/T}$ (using the free electron g-factor of 2). Dilution refrigerators can typically reach minimum electron temperatures of 200 mK; this in energy is $k_B T = 17 \text{ } \mu\text{eV}$. The addition energy of the SET island used in our system is $\sim 1.5 \text{ meV}$ [\[31\]](#). For high measurement fidelity we need the energy splittings to be much larger than the temperature (at least an order of magnitude), which means our SET is very good, and we need to apply static magnetic fields $B_0 > 10k_B T/\gamma_e \approx 1 \text{ T}$; our superconducting magnet can reach 6 T.

Lets now analyse some numbers relevant to electron qubit control. From the B_0 limit we obtain a lower bound of 28 GHz for the resonance frequency; we have a 0–50 GHz microwave source, which means we can use static fields up to 1.8 T. Electron spin lifetimes of 5 s were measured at 1.5 T in this system [\[31\]](#); which are very long compared to measurement times in the order 1 ms. Coherence times for P electrons in Si have been measured in bulk samples (i.e. not single spins) to be 300 μs in natural silicon and 10 ms in silicon with 0.08% ^{29}Si , both using Hahn echo [\[73\]](#); the record coherence so far is 450 ms with a Hahn echo, using isotopically purified Si from the Avogadro project [\[71\]](#). Coherence times set the limit of our gate operation times; according to DiVincenzo[\[10\]](#) fault tolerant quantum computation requires gate operation times to be 10^4 – 10^5 times shorter than coherence times. Assuming 0.08% purified Si bulk coherence times, this would mean we would need gate times in the order of 1 μs . To apply a π pulse in $t_\pi = 1 \mu\text{s}$, we need to apply $B_1 = f_{\text{Rabi}}/\gamma_e = 1/(2t_\pi\gamma_e) = 18 \text{ } \mu\text{T}$.

For nuclear measurement visibility, the relevant ratio is electron linewidth $\Delta\nu_e$ to hyperfine coupling A . A defines the separation between $\nu_{e\uparrow}$ and $\nu_{e\downarrow}$. If $\Delta\nu_e$ is comparable to A , the two nuclear spin states become harder to distinguish. The hyperfine coupling of bulk P in Si is 117 MHz [\[76\]](#), while $\Delta\nu_e$ in natural silicon is 5.6 MHz (and orders of magnitude smaller in purified Si) [\[73\]](#). This large difference reveals the potential for high fidelity readout of the nuclear spin. In contrast to the electron, the heavier nuclear gyromagnetic ratio of bulk P in Si is $\gamma_N = 17 \text{ MHz/T}$ [\[19, 77\]](#); as a consequence, the nucleus is much less sensitive to magnetic noise, which means it has the potential for much longer coherence times. Record coherence times of 39 minutes at room-temperature has recently been measured, in an ensemble of ionised P nuclei in purified silicon from the Avogadro project [\[70\]](#); this highlights the wonderful potential that the nuclear spin in our system has for qubit storage.

1.7 Thesis Outline

Chapter 2 gives extensive detail on the methods used to perform all the experiments described in the rest of the thesis. We will give a summary of the characteristics of the silicon chip, including implantation and nanostructure fabrication. We will describe all the equipment used and techniques employed to obtain our low electron temperatures; this section includes the novel design of filters aimed at diminishing high-frequency thermal radiation. We will give extensive detail on the electronic equipment, setup and manipulation used in these measurements to provide voltage inputs and acquire output signals efficiently. Finally, we will describe all the relevant experimental considerations that arise when attempting to operate a spin qubit.

Chapter 3 presents the design, simulation and implementation of a novel on-chip broadband nanoscale antenna for spin qubit control. This chapter serves as a guideline to microwave engineering design for physicists, presenting all the important issues related to achieving accurate simulations of microwave fields in nanostructures, and setting up experiments with minimum loss at those frequencies. It will also present an overview of the initial success obtained from this antenna design, in achieving the first ever demonstration of qubit operation from both the electron and nuclear spins of a single P atom in natural silicon.

Chapter 4 presents measurement results of single atom qubits from P donors in isotopically purified ^{28}Si . We have achieved record coherence times and high fidelity of both electron and nuclear qubits, along with an in depth characterisation of noise in our qubit's environment. The system's high fidelity has also allowed us to perform very accurate measurement of physical constants such as the electron g-factor, the nuclear chemical shift and the hyperfine interaction. Our unique experimental setup has also allowed to demonstrate real-time feedback control of the nuclear spin. Finally, this chapter will provide the theoretical background, experimental design and preliminary results of measurements aimed at demonstrating single-atom electron-nuclear entanglement in our system, through density matrix tomography and a test of the Bell inequalities.

Chapter 5 presents the first ever experimental demonstration of single-shot readout of the singlet-triplet states from a pair of exchange coupled electrons in a P-Si system. We analyse the two-qubit relaxation rates in different magnetic field regimes, through population models based on the singlet-triplet picture.

Chapter 6 includes the summary of the achievements of this thesis, along with an outlook for future experiments using this system.

Chapter 2

Experimental Methods

This chapter provides extensive detail on the experimental methods used to perform all the experiments described in the rest of the thesis. It presents a summary of the characteristics of the silicon chip, including implantation and nanostructure fabrication. It describes all the equipment used and techniques employed to obtain our low electron temperatures; this section includes the novel design of filters aimed at diminishing high-frequency thermal radiation. It also gives extensive detail on the electronic equipment, setup and manipulation used in these measurements to provide voltage inputs and acquire output signals efficiently.

The author acknowledges D.N. Jamieson, F.E. Hudson, K.W. Chan, K.Y. Tan for the implantation and fabrication of devices used for measurement in this thesis; K.M. Itoh for characterising and providing the isotopically purified silicon samples; J.T. Muhonen, A. Laucht and R. Kalra for helping build and characterise the filter boxes; and J.T. Muhonen for the electron temperature analysis

2.1 Introduction

Every scientific publication that presents ground breaking experimental results includes one or two paragraphs with an overview of methods employed for performing the measurements. These descriptions however, normally do not scratch the surface of what goes on behind the scenes of experimental science. This chapter aims at filling that gap of information, by providing details of all the important experimental techniques that the author was involved in designing and implementing. The chapter is broken down into four main sections: one section gives an overview of the device fabrication; another section describes the techniques employed to minimise the temperature of our qubit environment; next we provide details on how all the instruments work together, to control and measure our devices; and the final section details some the most important operations that we perform on our qubits.

2.2 Fabrication overview

The scope of this thesis does not include details on fabrication recipes or isotopic purification of silicon, yet it is still relevant to include the main characteristics of the materials and nanostructures used in the devices measured. The substrates used in the experiments described in [Chapter 3](#) and [Chapter 5](#) were high-purity, near intrinsic, natural isotope silicon ([Figure 2.1b](#)). For [Chapter 4](#), the substrate consisted of a 0.8 μm thick epitaxial layer of isotopically purified ^{28}Si , grown on top of a 500 μm thick natural silicon wafer ([Figure 2.1d](#)). The isotope composition of the ^{28}Si epilayer was measured by Fukatsu *et.al.* [78] using secondary ion mass spectroscopy, finding residuals of 730 ppm ^{29}Si and 30 ppm ^{30}Si .

Four different devices were employed in the measurements presented in this thesis. For experiments in [Chapter 3](#) and [Chapter 5](#) we used two devices from the same fabrication batch. For the results presented in [Chapter 4](#), we employed two devices (A and B) with slightly different characteristics. The differences between each of the devices will be highlighted in the relevant sections.

All our devices have were fabricated on (100) substrates with n_+ source/drain ohmic contacts obtained by phosphorus diffusion. A high-quality, 10 nm thick SiO_2 gate oxide was grown by dry oxidation at 800°C. Phosphorus donors were implanted through a 90x90 nm^2 aperture defined by electron-beam lithography in a PMMA mask. The fluence was chosen to obtain the maximum likelihood of having 3 P atoms in a 30x30 nm^2 area, subject to Poisson statistics. For the devices in [Chapter 3](#) and [Chapter 5](#) and Device A in [Chapter 4](#), P ions were implanted with 14 keV implantation energy. For Device B in [Chapter 4](#), P_2^+ molecular ions were implanted with 20 keV energy. Both types of implantation were designed for a target depth of 15 nm below the Si/SiO_2 interface. A 5 s, 1000°C rapid thermal anneal was performed to activate the donors and repair the implantation damage.

Aluminium gates to form the device nanostructure were defined with electron-beam lithography, thermal evaporation and lift-off. Exposure to a low-pressure oxygen plasma (0.15 mbar)

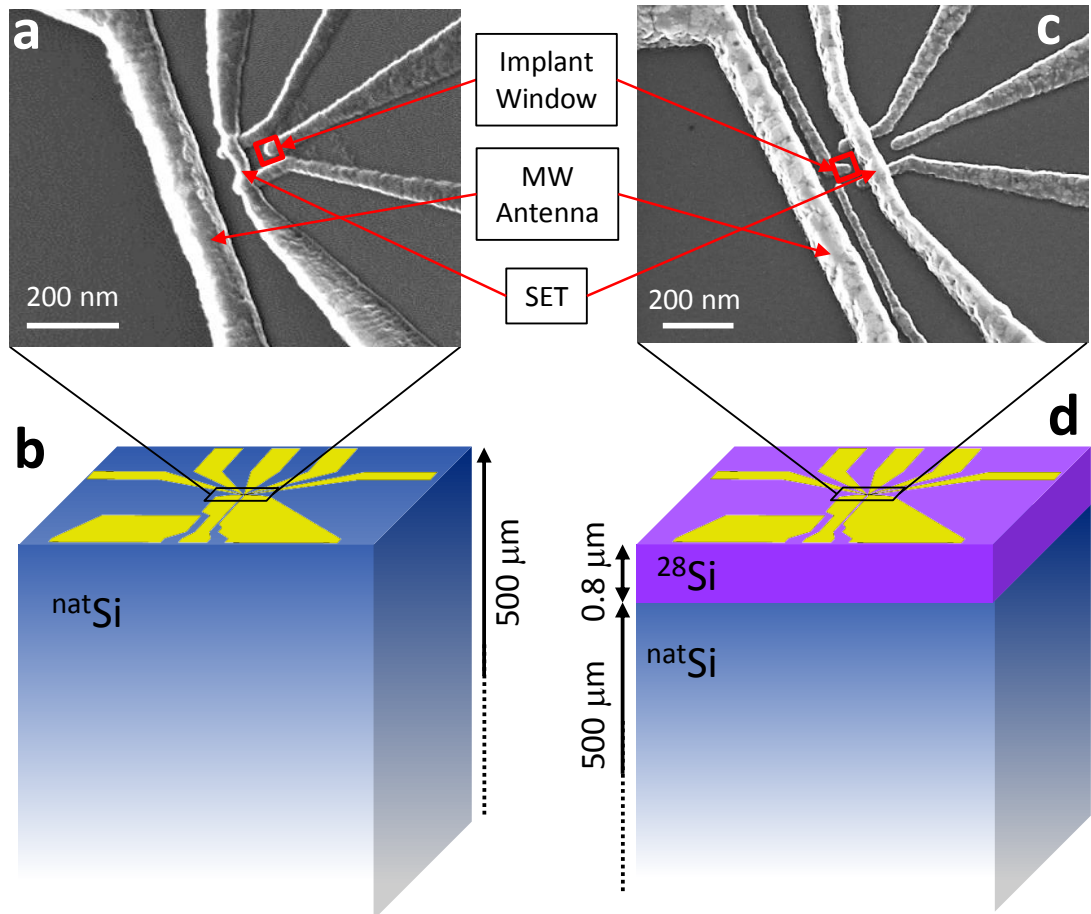


Figure 2.1: Device substrates and gate layouts. a-b.SEM of gate layout (a) and diagram of natural silicon substrate (b), this device architecture was used in experiments presented in [Chapter 3](#) and [Chapter 5](#). c-d.SEM of gate layout (c) and diagram of ^{28}Si epilayer (b), used in experiments presented in [Chapter 4](#).

for 3 min at a temperature of 150°C results in a few nanometre thick layer of oxide, which provides enough electric isolation to perform multi-layer gate fabrication [53]. A final 15 min forming gas anneal at 400°C with 95% N_2 and 5% H_2 was performed to reduce the interface trap density to the level of $2 \times 10^{10} \text{ cm}^{-2}\text{eV}^{-1}$.

We will present results from measurements done on devices with two different gate layout architectures. For the devices in [Chapter 3](#) and [Chapter 5](#), the gate layout is essentially the same as the one used in the measurements by Morello *et al.* [31], with the addition of the spin resonance antenna ([Figure 2.1a](#)). In [Chapter 4](#), we used a modified version of this gate layout, where the DG is positioned in between the antenna and the SET ([Figure 2.1c](#)). The improvements achieved from the latter architecture will be explored in detail in [Subsection 3.4.3](#).

2.3 Low temperature setup

As explained throughout [Chapter 1](#), temperature plays a very important role in the fidelities of our qubits. Dilution refrigerators like the one used in our setup (Oxford Kelvinox 100) are capable of reaching temperatures of < 30 mK, however transferring those low temperatures to operational qubits is a non-trivial task. The lowest temperatures in a dilution refrigerator occurs in the *mixing chamber*, where the He isotope dilution takes place. In order to effectively transfer these temperatures from the mixing chamber to the qubit we need materials with high *thermal conductivity*. The gates are connected through electrical lines to room-temperature equipment and, in order to carry the signals adequately, the lines have to be isolated, making them very difficult to cool down. Therefore for these lines, we need materials with low thermal conductivity to minimise the radiation of heat from room-temperature. The following table lists the thermal conductivity of some relevant materials (in increasing order):

Material	TC [W/(mK)]
Air	0.03
Copper-Nickel (55%-45%)	20
Stainless Steel	20
Phosphor-Bronze	60
Silicon	150
Aluminium	200
Copper	400
Silver	400

Our fridge has a copper mixing chamber and *cold finger* (see [Figure 2.2a](#)). To cool our device, we bolt to the cold finger a copper enclosure that contains the silicon chip. The chip is mounted using a mixture of polymethyl-methacrylate (PMMA) and silver paint — we adopted this method after finding that silver paint on its own left the chip too unstable for bonding. This setup provides good thermal contact between the mixing chamber and our qubit.

Any electrical line radiates thermal white noise — known as *Johnson-Nyquist noise* — given by $\overline{v_n^2} = 4k_B T R$ where k_B is the Boltzmann constant, T is the temperature and R is the resistance of the electrical line. Since Johnson-Nyquist noise is constant in frequency, filtering any unneeded frequencies can significantly reduce the amount of thermal noise radiated on to the qubit. Every conductor has an associated parasitic inductance, which appears in every connection on our filter circuits. For an RC filter, the series inductance between the capacitor and ground will cause the filter's attenuation to reduce at higher frequencies (the circuit acts as a low Q resonator). This effect can be minimised by making the ground connections as large in surface as possible, but it can never be completely avoided. [Figure 2.3a](#) shows the response of one of our RC filters, illustrating this behaviour above 1 MHz. For common room-temperature circuitry this is not a problem because these higher frequencies are normally outside the range of operation, but for low-temperature applications, noise at these high frequencies can significantly

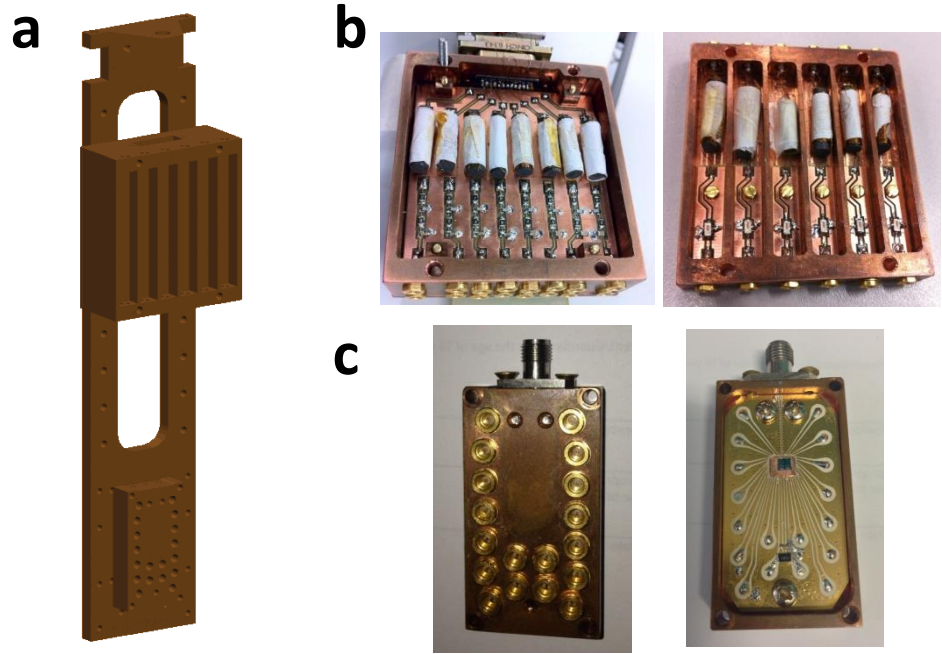


Figure 2.2: Low temperature components. a CAD model of cold finger with filter boxes and device enclosure mounted. b DC and AC filter boxes, open and unpotted, showing the anti-wound coil with Eccosorb coil and surface mount low pass filters on a PCB. c Copper enclosure with MMCX connectors. The inside contains the high-frequency PCB bonded to a chip mounted on the stage

contribute to thermal radiation.

Metal powder filters have been used for nearly three decades to filter high-frequency noise [79]. The attenuating effect of metal powder is attributed to *skin-effect damping*, caused by the large effective surface area of the oxidised metal grains. The amount of dissipation is proportional to the effective impedance, which is inversely proportional to the skin-depth $\delta = \sqrt{\rho/(\pi f \mu)}$ where ρ and μ are the resistivity and permittivity of the metal particles respectively. Therefore, the dissipation increases as frequencies increase. Typical cut-off frequencies for metal powder filters are in order of 1 GHz [80]. Another approach is to use *microwave absorbing* materials, such as *Eccosorb*, which have magnetic and electric properties such that the effective impedance seen by an incident electromagnetic wave is that of free-space [81]. These materials can be engineered to accommodate a wide range of cut-off frequencies and applications.

Our experimental setup requires three different types of lines: *DC lines*, which provide a constant voltage bias to the gates; *AC lines* (up to ~ 100 MHz), used for pulsing the donor potential and acquiring current outputs; and a high-frequency *fast line* used for transmitting signals up to 50 GHz to the control antenna. A unique feature in our latest device architecture (Figure 2.1c) is that we have fabricated separate gates for DC biasing and pulsing. Our previous setup (Figure 2.1a) used a single gate to control potentials that need to be biased and pulsed (e.g. the donor or SET island potentials), combining the signals at room temperature using a

2.3. Low temperature setup

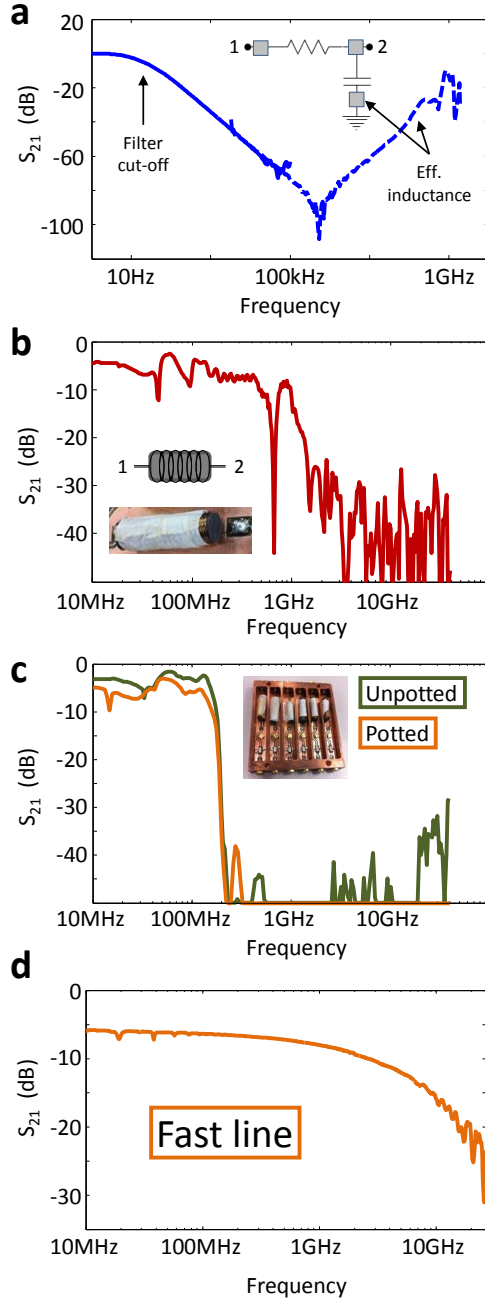


Figure 2.3: Frequency response (S_{21}) of components in our filter boxes. **a** Response of an RC filter without extra high-frequency filtering. The plot shows the overlap of measurements done with the lock-in technique and with the network analyser (see Figure 2.5). **b** Response of one of the anti-wound coils with Ecosorb core used in our boxes, showing the filtering effect > 1 GHz. **c** Response of the complete AC filter box before (green) and after (orange) potting the box with copper powder. **d** Response of the fast-line which goes down unfiltered, except for two attenuators used for thermalisation, which add up to 6 dB.

2.3. Low temperature setup

voltage summing circuit; the disadvantage is that the cold filters need to have cut-offs above the desired pulsing frequency, which feeds a significant part of the low-frequency noise spectrum from the DC voltage sources. In our latest setup, the gates nearest to our qubit are only connected to the DC sources and thus can be heavily filtered, while the pulsing is done through capacitively coupled gates located further away (see [Figure 2.4](#)).

For our DC and AC lines, we have designed a filter box consisting of a copper enclosure with an anti-inductive wound coil with 2 metres of phosphor bronze wire with an Eccosorb core (rods of MF-117, 1–18 GHz absorbtion), in series with a passive filter made with surface mount components on a printed circuit board (see [Figure 2.2b](#)). The enclosure is then potted with copper powder. The coil uses the core as a filter, as seen from the response in [Figure 2.3b](#) — the thermal coupling to the Eccosorb and copper powder increases with the length of the wire used in the coil. For the DC lines, the passive filter consists of a 20 Hz first order RC filter with 20 k Ω thin-film nichrome resistor and 470 nF ceramic (X7R or NP0) capacitor, in series with an 8 MHz RC filter (20 k Ω with 1 pF). For the AC lines, we used 80 MHz seventh-order integrated LC filters (Mini-Circuits LFCN-80). The selection criteria for filter components is based of the capacity of the component to maintain its value at mK temperatures — common component datasheets never include characterisation at these temperatures, so we based our choice on prior experience. The DC lines filter cut-off shifted slightly at 4 K to 150 Hz, and we saw no difference in cut-off of the AC lines filter at low temperatures. The filter-box was bolted to the cold finger and connected to room-temperature via copper-nickel twisted-pair wire (DC lines) and copper-nickel semi-rigid (EZ86) coaxial lines (AC lines). The lines from room-temperature to the filter boxes are thermalised at every temperature stage, by wrapping the flexible twisted pair wire around the copper rods connecting the fridge stages, or anchoring the coaxial lines with copper wire. [Figure 2.3c](#) shows the frequency response of the AC filter box before and after potting with copper powder, showing the desired effect of attenuating high-frequencies. As a side note, we initially attempted to implement these filter boxes with Eccosorb potting (instead of copper powder), but found that the thermal expansion of the material caused it to compress at low temperatures, severing the connection between our wires and enclosure connectors. These novel filters were implemented for the experiments in [Chapter 4](#); prior to that ([Chapter 3](#)) we used a setup with conventional copper powder filters and first order RC filters (150 kHz) inside the device enclosure.

The fast line cannot be filtered because we need to operate it using the entire spectrum, however we can use attenuators to create a thermal contact between the coaxial signal line and the ground shield, and we thermalise the shield to the fridge using copper anchors. The fast line coaxial is semi-rigid stainless steel (EZ86). [Figure 2.3d](#) shows the measured frequency response of the fast line. Note the 6 dB attenuation at low-frequencies due the installed thermalising attenuators. The accentuated loss at high-frequencies is dominated by the inevitable presence of lower frequency rated connectors at some of the connection nodes along the line.

From the filter box to the enclosure, it is indispensable to protect our cooled lines from

2.3. Low temperature setup

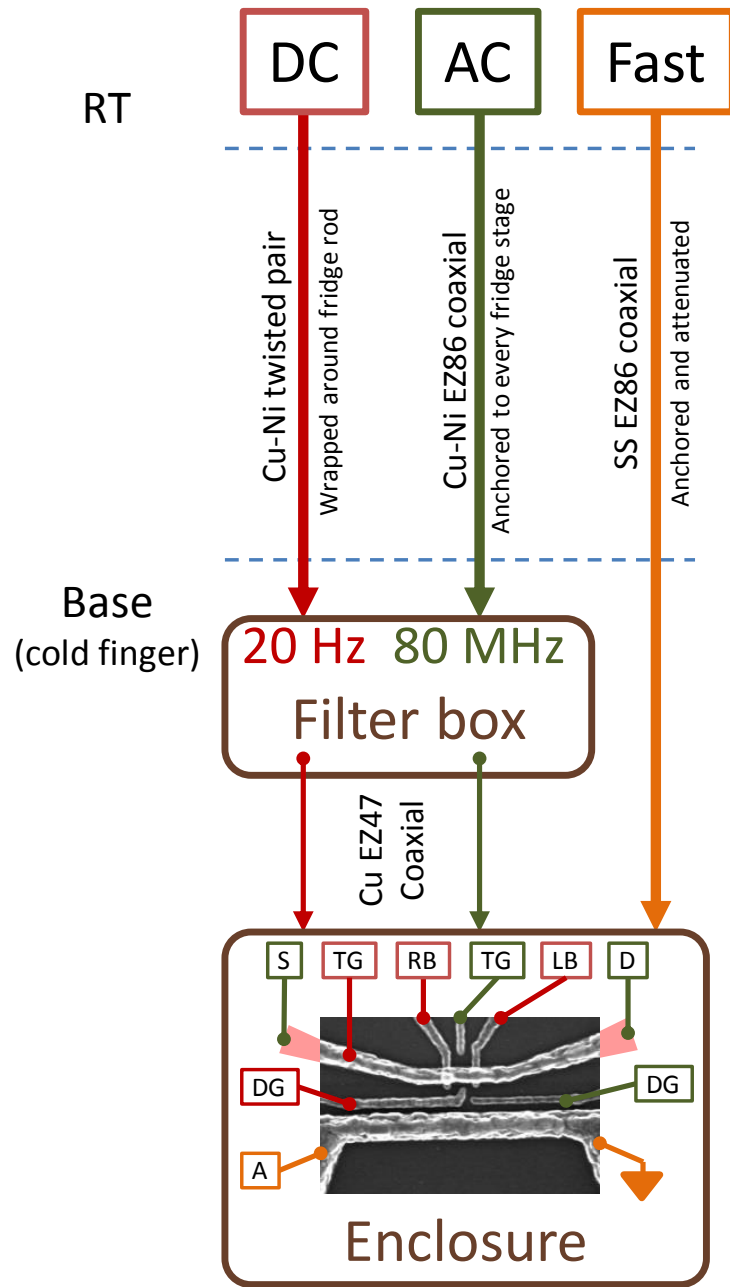


Figure 2.4: Schematic of the low temperature setup. Includes color coding of the lines according to their cut-off frequencies (described in the main text); the materials used in each type of line above and below the mixing chamber; and the device schematic, showing the type of line (color coded) connected to each of the gates.

2.3. Low temperature setup

external radiation (e.g. from the ~ 0.5 K radiation shield); we use thin semi-rigid (EZ47) copper coaxial lines with MMCX connectors. We migrated to MMCX connectors from SMA for two reasons: *size*, as we can now fit 18 connectors instead of 6 in the same enclosure size (see [Figure 2.2c](#)); *connectivity*, having pressure instead of screw type connectors makes the tasks of mounting the enclosure on the fridge simpler. The downside to MMCX is that the connectors start to wear out after a finite number of plug-ins, and we have found that they are not compatible between different brands (e.g. Huber-Suhner females do not match well with Jyebao males). Additionally, we tested flexible copper coaxial (LakeShore CC-SC-100) for these connections, and found them to be very unreliable and easy to break. As shown on [Figure 2.2c](#), the connectors in the enclosure link to a printed circuit board of high-frequency ceramic filled PTFE composite dielectric (Rogers 3010). The board contains impedance matched coplanar waveguides to the mounting stage, from which we contact the gates on the chip using Al wedge bonding. There is another coplanar waveguide on the board, impedance matched and designed for high-frequencies (50 GHz), from an SK connector to which we connect the fast line coaxial.

2.3.1 Filter response measurements

Frequency response measurements consist of applying a broadband input to the circuit, and comparing it to the spectrum of the output, the ratio is the S_{21} parameter (see [Section 1.3](#)). We used three different methods for the S_{21} measurements, depending on the frequency range we wanted to test. The most direct method is through a *network analyser*, which operates from 10 kHz to 6 GHz. For lower frequencies (between 1 Hz and 100 kHz) we use a *lock-in amplifier*, by feeding the lock-in signal to our circuit and measuring its output while sweeping the frequency. For > 6 GHz, we have access to a 50 GHz source, but no high-frequency signal acquisition instruments. We use a *microwave detector* which consists of a two-port rectifier with a high-frequency input (10 MHz to 33 GHz) and outputs a DC voltage that is a function of the input signal power. The range of linear output amplitude to input power behaviour is limited, so its best to calibrate it prior to operation. We feed the signal from the high-frequency source to the input of the circuit we want to measure, and acquire the output of the detector with a digital multimeter.

[Figure 2.5](#) shows schematics for all three S_{21} measurement methods.

2.3.2 Electron temperature measurements

To verify the effectiveness of the sophisticated filters we have built, we can perform measurements to obtain the effective temperature of our qubit, through a measurement of the width of the Coulomb peaks in our SET island. As described in [Section 1.2.6](#), the width of the peaks are a function of the S-D bias, lifetime and thermal broadening. If we minimise the S-D bias and lifetime broadening (by making the barriers as opaque as possible), the shape of the peak will be dominated by the temperature. We fit our measured Coulomb peaks to the rising and

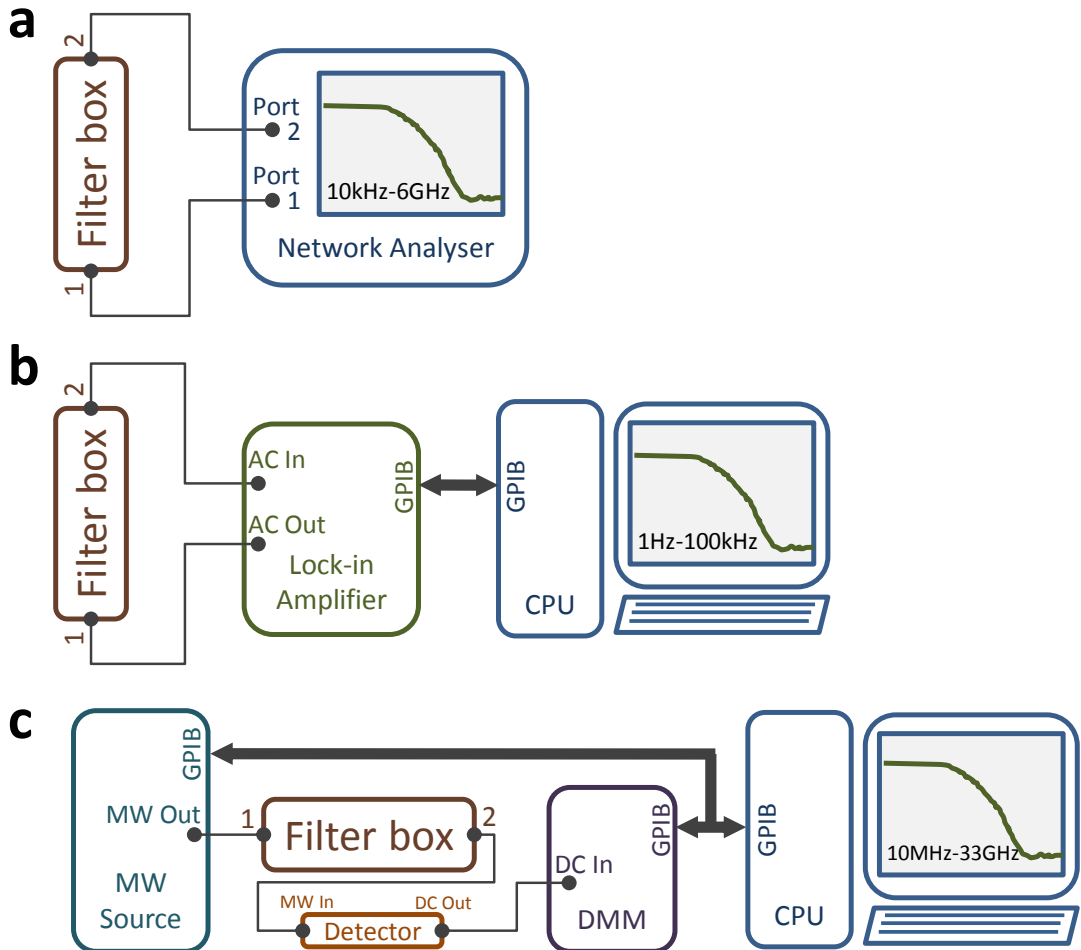


Figure 2.5: Schematics of different S_{21} measurement techniques used for different frequency ranges.
a Direct method using a network analyser. **b** Output/input voltage ratio using a lock-in amplifier. **c** Output/input power ratio using a MW source and a calibrated MW detector connected to a multimeter (DMM)

falling Fermi occupation energies, using (see Reference [82] for details):

$$I = \frac{1}{eI_{max}} (f(E_+, T) - f(E_-, T)) \quad (2.1)$$

$$\text{with } f(E, T) = \frac{1}{\exp(E/k_B T) + 1}$$

and $E_{\pm} = e(\alpha V_{TG} \pm V_{SD}/2)$

Here e is the electron charge, I_{max} is a free parameter corresponding to the peak height, α is the top-gate voltage to energy lever arm (free parameter) and the subscript TG(SD) correspond to top-gate(source-drain).

2.4. Room-temperature setup

From the fit in plot of the Coulomb peak in [Figure 2.6a](#) we extract an electron temperature of 70 mK. To verify this method, we perform Coulomb peak measurements while sweeping the refrigerator temperature, and confirm that the temperatures extracted from fits match the fridge temperatures (see [Figure 2.6b](#)). In comparison, our previous a setup using traditional copper powder filters and higher frequency RC filters, obtained electron temperatures of 200 mK [\[83\]](#), from which we highlight the significant improvement obtained by our novel low temperature experimental setup.

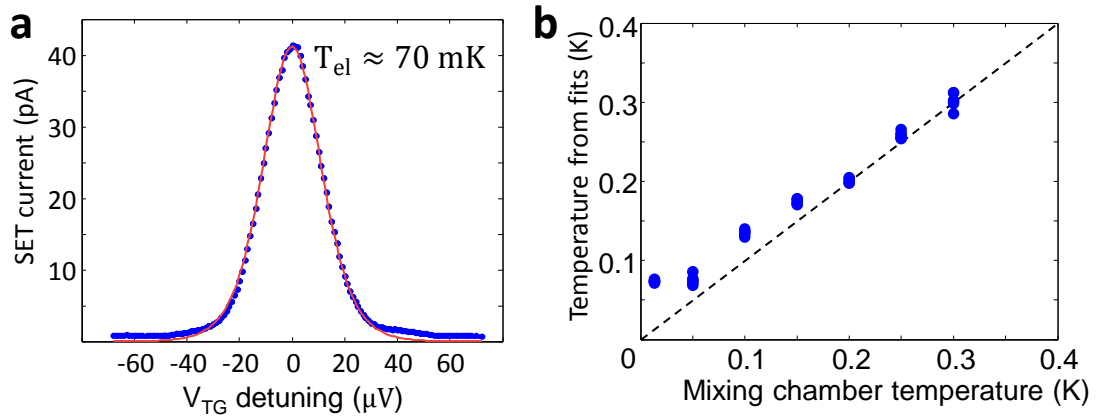


Figure 2.6: **Electron temperature extraction.** **a** A single coulomb peak measured (blue dots) with minimal S-D bias and lifetime broadening, fitted (red) using the [Equation 2.1](#). **b** Plot of temperature extracted from several measured coulomb peaks at different fridge temperatures.

2.4 Room-temperature setup

In this section we will describe our efforts to minimise input and output noise from instruments in our system; we will discuss our instrument setup and explain how we interconnect, control, synchronise and acquire data from our instruments. As a guide for this section, [Figure 2.7](#) shows a complete schematic of our instrument setup.

2.4.1 Noise

The currents to be measured from the SET are of order 1 nA. To measure such small currents, care needs to be taken to ensure both the input voltage sources and output signal amplifiers are as noiseless as possible; additionally, a significant resistance between common ground connections can cause *ground loops* which also feed noise into the system.

The DC biasing sources provide the largest voltage outputs in our system. We use Stanford Research Systems (SRS) isolated voltage sources (SRS SIM928); these have the advantages of being battery powered, which eliminates the 50 Hz noise present in rectifying sources. Additionally, having the output ground isolated from the instrument ground, prevents ground loops. The other input sources used for pulsing the gates and for high-frequency spin control are not

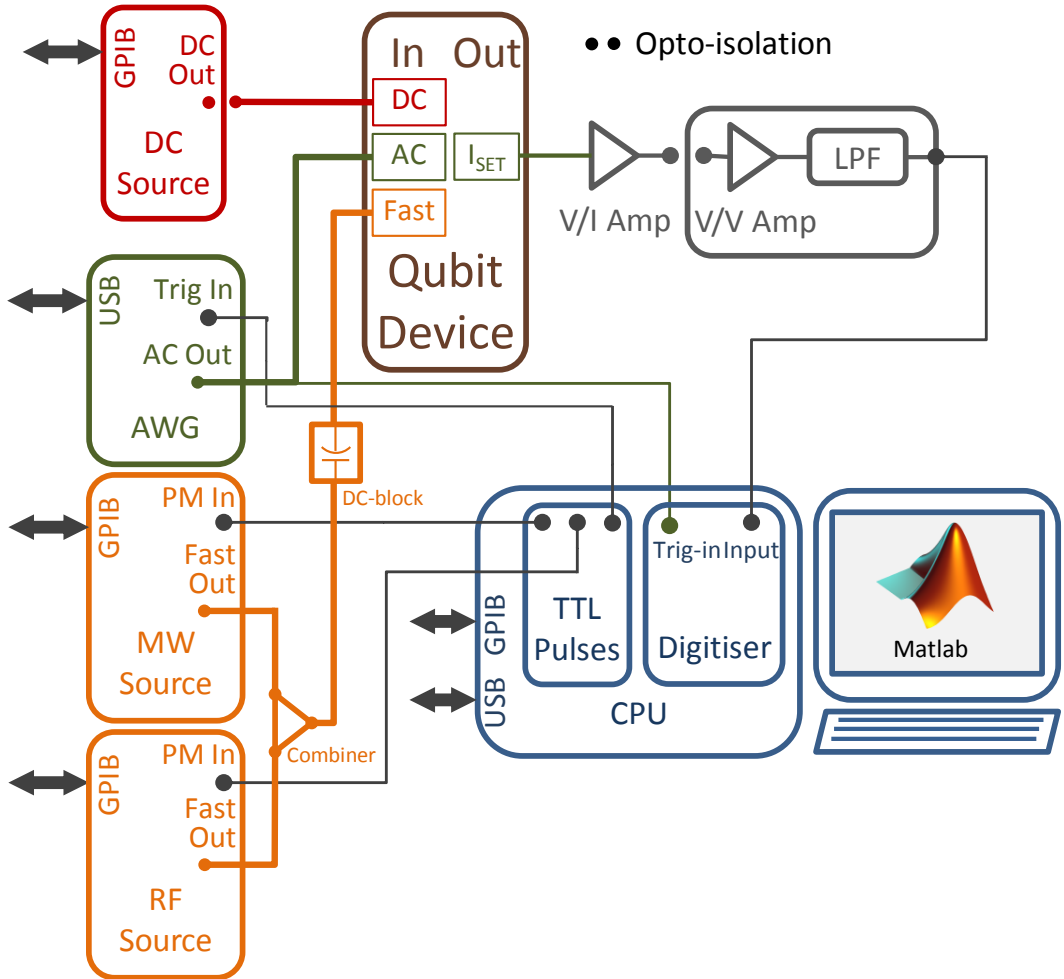


Figure 2.7: Schematic of the instrument setup. The input lines are color coded similar to Figure 2.4. The brand and model of all the instruments are enumerated in the main text.

isolated, but are connected with grounding straps to the fridge chassis. Additionally, we use a double DC block on the fast line at room-temperature, to provide low frequency isolation of the MW and RF signals.

Output currents are amplified and converted to voltages using a Femto DLCPA-200 transimpedance amplifier at room temperature; which in its low-noise setting can provide gains of 10^3 to 10^9 with bandwidths of 500 kHz to 1 kHz. The output of this amplifier is fed to an SRS SIM910 JFET low-noise voltage pre-amplifier with an isolated input to prevent ground loops from the rest of the acquisition instruments. Finally the signal is passed through an SRS SIM965 6th order Bessel filter, to provide additional sharper filtering of our signal before acquisition. With this setup we obtain current noise floors ranging from ~ 100 pA with 50 kHz bandwidth, to ~ 300 pA with 200 kHz.

Additional considerations

The effective input noise current for a transimpedance amplifier is given by [84]:

$$\langle i_n \rangle^2 = \langle i_{\text{amp}} \rangle^2 + \frac{4k_B T}{R_f} + \left(\frac{\langle v_{\text{amp}} \rangle}{R_f} \right)^2 + \frac{(\langle v_{\text{amp}} \rangle 2\pi F C_{in})^2}{3}$$

Here $i_{\text{amp}}(v_{\text{amp}})$ is the amplifier specified input current(voltage) noise, R_f is the feedback resistance, F is the bandwidth and C_{in} is the total input capacitance to the circuit.

The fourth term in the above equation implies that if the input capacitance is large enough, it can have a significant effect on the measured output noise of the amplifier. As described in [Section 1.3](#), every transmission line has some capacitance per unit length C' . For coaxial lines, C' depends of the radius of the coax — i.e. the separation between the center conductor and the shield — and the dielectric. For our system's typical coaxial line length ~ 2 m, the input capacitance are not negligible.

While preparing the experimental setup, we performed room-temperature output noise floor measurements for two different types of coaxial lines available in the fridge, connected to the input of the Femto DLCPA-200:

Cu-Ni EZ86 semi-rigid we found a factor 6 increase in noise floor after connecting the coax.

LakeShore stainless steel thin flexible we found a factor 14 increase in noise floor after connecting the coax.

The difference between them is not surprising, as the thin flexible cable has a smaller diameter, and needs to be thermalised by wrapping it around the anchors at the fridge stages, thus needing more cable length. More importantly, this experiment shows that there is a significant contribution to the noise by the capacitance of the coaxial cables in our setup; this is an important consideration for selecting the cables for the source and drain connections.

2.4.2 Instrument control

As we will describe in [Section 2.5](#), qubit operations require careful pulsing of different gates in our device, along with time sensitive signal acquisition. In order to achieve this successfully, all the signal generation and acquisition instruments need to be carefully synchronised. All instruments are connected to a mainframe computer from which we use Matlab for instrument control and data analysis. The following list contains all of our dynamic instruments with their main features.

Lecroy ArbStudio This arbitrary waveform generator (AWG) allows loading of any desired waveform. Waveforms are loaded through a vector of voltage levels, and the AWG will output the sequence of levels at the predetermined sampling ratio. It has 4 channels, a maximum sampling rate per channel of 250 MS/s, a minimum pulse length of ~ 10 μ s,

2.4. Room-temperature setup

and accepts sequences of up to 2 Mpts/ch. It connects to the computer via USB and it is controlled by Matlab through .NET commands.

SpinCore PulseBlasterESR-PRO This logic pulse generator outputs a programmable sequence of 3.3 V amplitude pulses of any desired length. It can receive programming commands where the output state of each channel and the time length are defined for each instruction in the sequence. It has 21 programmable channels (4 on BNC connectors), pulse lengths from 2 ns to 9 s with a rise time of < 1 ns, and accepts sequences of up to 4096 instructions. It connects to the computer via PCIe and has a Matlab library of commands.

Agilent E8257D PSG This microwave analog generator outputs signals of 250 kHz to 50 GHz frequency and -110 to 20 dBm output power. It has pulse, frequency and phase modulation. It connects to the computer and is controlled via GPIB. For lower-frequency NMR, we also use a similar RF signal generator (Agilent M5182B MXG) with lower frequency outputs (9 kHz to 6 GHz) and digital IQ modulation.

AlazarTech ATS9440 This digitiser samples signals and stores them in memory for analysis, and has a graphical computer interface to use as an oscilloscope. It has a maximum sampling rate of 125 MS/s, 4 channels, variable triggering levels, and an input range from ± 100 mV to ± 1 V. It connects to the computer via PCIe and has a Matlab software development kit of commands.

The flexibility of programming waveforms with any voltage level makes the ArbStudio a perfect instrument for controlling the gates coupled to the potentials of the donor and SET island. We use the PulseBlaster to synchronise the ArbStudio pulse lengths and to provide the pulse modulation and phase modulation pulses for the MW and RF sources. Having a broadband antenna for spin control means we can use the same fast line to apply both ESR and NMR pulses. We connect the MW and RF sources to the same line by using a broadband (DC-50 GHz) power combiner (Agilent 11667C).

The digitiser triggers from the output of the ArbStudio, at the change from the control to readout phase. This setup allows us to program a repetitive sequence of control and readout phases, and set the digitiser to acquire as many shots as needed to obtain an accurate measurement of the qubit state. Having a digitiser with a fast interface to the mainframe computer allows us to perform real-time feedback control. Data acquired from the digitiser is loaded in real-time into a Matlab variable, so we can perform analysis inside the measurement loop, and adjust the following control sequence conditional on the previous measurement result.

Controlled rotations around the x or y plane are done by phase shifting the output of the oscillating signal source. Depending on the capabilities of the source, this can be done in one of two ways: analog modulation or vector modulation. For analog modulation, a variable voltage is applied to the Ext1 input gate of the source and the phase at the output is proportional to the modulation voltage. In practice, we apply a TTL pulse (from the PulseBlaster) and

calibrate the modulation depth of the signal generator to obtain 180° shift between the *on* and *off* pulses. A vector source has two separate signals I and Q, 90° out of phase, which are mixed to obtain the output of the source. The amplitude of each signal can be controlled by applying voltages to input gates on the source, and the resulting phase at the output will be: $\theta = \tan^{-1}(V_Q/V_I)$, with $\sqrt{V_Q^2 + V_I^2}$ normalised to a instrument specific value (0.5 V) in order to keep the output power constant. The advantage of using a vector source is that phase shifts can be applied orders of magnitude faster than with analogue modulation, however the cost of a vector generator is more than double of that of an equivalent analogue generator. All of the experiments presented in this thesis were performed using analogue phase modulation.

2.4.3 The superconducting magnet

Static magnetic fields were supplied using a superconducting magnet with a 105 mm bore. The magnet is controlled using a 100 A power supply (Oxford Instruments IPS120-10), from which a maximum field of 6 T can be induced. Between the nodes connecting the superconducting magnet and power supply leads, there is a superconducting filament fitted with a resistive *switch heater*. When this heater is turned on, the filament is forced to have a finite resistance, therefore the magnet coil current can be induced by the power supply. Once the current is set to the desired value, the switch heater can be turned off, short-circuiting the magnet leads through the superconducting filament. The power supply can then be turned off, leaving the current to cycle through the lossless superconductor, in what is known as the magnet *persistent mode*. In practice the superconducting coil is not lossless — it will have small residual resistances at the joints and an effective flux motion resistance. Specifications for our magnet state a 1 part in 10,000 per hour of current decay in persistent mode. Some extra theoretical detail on switch heaters, flux motion resistance and other superconducting magnet related phenomena can be found in Reference [85].

For our electron qubit measurements, the decay in persistent mode can be significant. A field of 1.5 T implies an electron spin resonance frequency of ~ 42 GHz (from Equation 1.2). At this field, our magnet is specified to decrease by 70 kHz per minute. ESR linewidths in our devices are on the order of 1 kHz (for experiments in Chapter 4) to 10 MHz (Chapter 3). For some of our measurement times of hours, the specified magnet decay in persistent mode is unacceptable. An alternative way to operate the magnet is with the switch heater *on*, such that the power supply is always providing the necessary current, preventing any decay. For the experiments in Chapter 3, the magnet was always operated with the switch heater *on*. However, using this operation mode will feed noise from the power supply to the magnet coil. For experiments in Chapter 4, we found that this static field noise was limiting the coherence of our qubit. By operating the magnet with the switch heater *off*, but the power supply current *on*, we found that the magnet decay decreased by an order of magnitude, while maintaining adequate noise levels. The decay rates we measured experimentally were 10 kHz per minute for persistent mode, and 1 kHz per minute for switch heater *off* and power supply *on*.

2.5 Relevant qubit experiments

In Subsection 1.2.6 and Section 1.5 we introduced the theory and explained some basic experiments that allow us to characterise our qubits. In this section we will expand the details of the experimental techniques used to perform the most relevant qubit operations.

2.5.1 Qubit readout and control

The principle of qubit readout and the SET operation were described in Subsection 1.2.3 and Section 1.2.6. In this section we will give some extra detail on how the SET is tuned in order to find a readout location in gate space and perform single-shot readout. We will only describe details relevant to the analysis of this thesis, further details of the single-shot electron spin readout protocol has been published by Morello *et al.* [31]. Additionally, if the reader is not familiar with the basic theory and operation of quantum dots, Reference [86] gives relevant descriptions to the topics in this section. By operating our SET as a traditional transistor (i.e. with the barrier gates at the same potential as the top gate), we obtain turn-on voltages of $V_{G(ON)} \approx 0.8$ V and obtain currents of $I_{SD} \approx 2$ nA with a gate voltage $V_G \approx 2$ V and source drain bias $V_{SD} \approx 100$ μ V (channel resistance $R_{ch} = 50$ k Ω). We operate our SET as a charge detector by leaving the top gate $V_{TG} \approx 2$ V and lowering the voltage on the barrier gates to form a dot (the SET island) which exhibit Coulomb peaks of $I_{SET(peak)} \approx 1$ nA height. In this regime, the width of the peak (ΔE_{peak}) is dominated by the SD bias. From the size of our SET, we obtain a quantum dot with an $E_c \approx 1$ meV. A large E_c to ΔE_{peak} ratio is desirable in order to increase the chances of observing a charge transition with maximum charge transfer signal (see Figure 1.7). The *lever-arm* of the quantum dot — defined as the ratio $\Delta V_{TG}/\Delta \mu_E$ — is $\alpha_l \approx 0.07$ V/eV.

Figure 2.8a shows a sample 2D charge stability diagram (see Section 1.2.6, with two clear charge transitions. We define three *donor potential pulses*, which are voltage pulses applied to the DG, at the levels highlighted with dots in Figure 2.8a: *load pulse*, (LP, white) where the donor is fixed in the neutral state, *readout pulse*, (RP, green) where the SET island Fermi level is between the two spin energies of the donor, and *empty pulse* (EP, blue) where the donor is fixed in the ionised state. Figure 2.8b shows sample readout traces taken by Morello *et al.* [31] by performing the donor potential pulse sequence LP-RP-EP. A clear current “blip” is observed in the current trace of the charge detector, when a $|\uparrow\rangle$ electron tunnels from the donor to the SET island, and is replaced after a short time by a $|\downarrow\rangle$ electron.

Another important definition we need to make is the *control sequence*, which consists of a sequence of *on-off* pulses applied to the spin resonance antenna, with an oscillating signal at an appropriate spin resonance frequency. A complete qubit operation consists of donor potential pulses and control sequences, interleaved in a way that allows us to initialise, manipulate and readout the spin qubit.

For an electron qubit operation, we apply the donor potential pulse sequence LP-RP (Fig-

2.5. Relevant qubit experiments

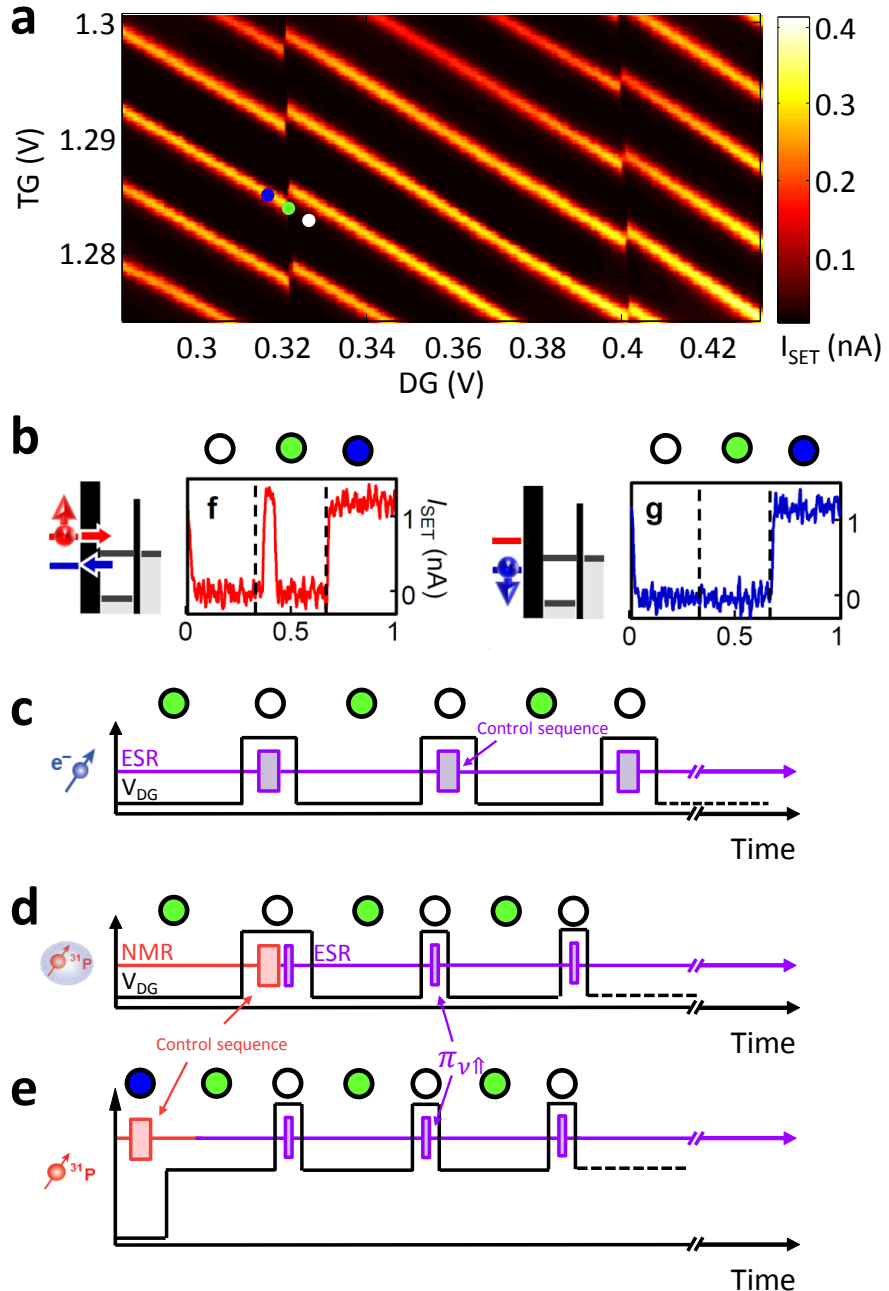


Figure 2.8: Charge detection, electron spin readout and control. **a** Charge stability diagram showing two charge transitions. **b** (extracted from [31]) Sample single shot readout traces using a three level pulse scheme. **c-e.** Pulse schemes for qubit control measurements: electron (c), neutral nucleus (d), ionised nucleus (e).

ure 2.8c). The RP serves to readout and initialise the spin for the next measurement. The LP serves to detune μ_E from E_F , so that the donor is fixed in the neutral state while the control sequence is applied. As explained in [Section 1.2.6](#), in order to extract P_\uparrow we need to repeat several measurements of the same control and readout sequence. Plots of electron control in this thesis were obtained through 100-200 single-shot repetitions per data point. Note that there are two different ESR control frequencies depending on the state of the nuclear spin (see [Subsection 1.2.2](#)), therefore every measurement is doubled to probe both frequencies. We select the results from the frequency that was active at the time of measurement.

As explained in [Subsection 1.2.3](#), nuclear spin readout is achieved by performing a nuclear readout sequence, which consists of mapping the nuclear spin to the electron spin by attempting a π pulse on the $\nu_{e\uparrow}$ frequency. We perform the nuclear readout sequence by applying the donor potential sequence LP-RP with the π pulse applied during the LP. In practice we can obtain higher nuclear readout visibility by implementing a readout phase with several nuclear readout sequences. We will explore the nuclear readout fidelity further in [Section 2.5.2](#). The nuclear spin can be controlled in both the neutral or ionised state. For the D^0 state ([Figure 2.8d](#)), the sequence begins with a LP during which we apply the nuclear control sequence, followed by the nuclear readout sequences. Note that the entire sequence always ends with a RP which initialises the electron spin, therefore we always control the nucleus with $\nu_{N\downarrow}$. For the D^+ state ([Figure 2.8e](#)), we apply the control sequence during an EP, followed by a RP to initialise the electron spin, before going into the nuclear readout phase. Note that there is no nuclear initialisation, however — due to the fact that nuclear readout is a QND measurement (see [Subsection 1.2.3](#)) — the state that we obtain after a single-shot measurement will be preserved as the initial state for the next control sequence. Therefore instead of obtaining P_\uparrow , for nuclear control experiments we extract the *nuclear spin-flip probability* (P_f).

Control sequences

In [Section 1.2.6](#) and [Subsection 1.5.2](#) we introduced some of the basic qubit control sequences we perform and we explained how we can extract qubit characteristics from them. We perform these sequences in the control phase of the complete qubit operation cycle described above. The following list contains all the control sequences relevant to this thesis. *On* times are noted as pulses as defined in [Subsection 1.2.2](#) and the *off* times τ allow for free precession time between pulses:

Spin resonance lines obtained by monitoring P_\uparrow (for the electron) or P_f (for the nucleus) as we sweep the oscillating field frequency around the expected spin resonance frequency $\nu = \gamma B_0$.

Rabi oscillations having identified the correct resonance frequency, we perform a sweep of the duration τ_R of a pulse which will rotate the spin by an angle $\theta = 2\pi\tau_R/\gamma B_1$. The result of the sweep are sinusoidal Rabi oscillations with a frequency $f_{\text{Rabi}} = \gamma B_1$.

2.5. Relevant qubit experiments

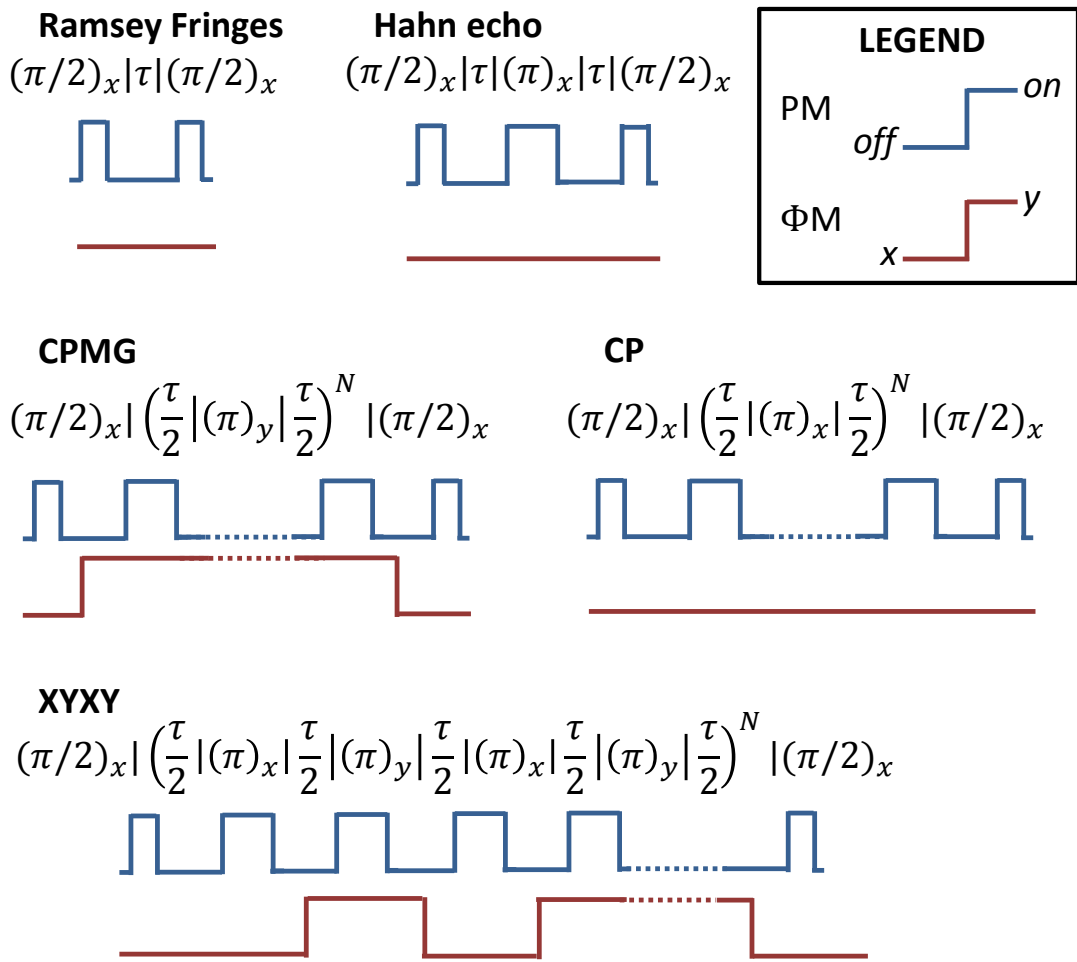


Figure 2.9: Control sequence diagrams. Timing diagrams of pulses needed to perform each of the control sequences described in this section. Blue pulses are applied to the pulse modulation (PM) external input of the signal generator connected to the spin resonance antenna. The PM input receives a TTL signal and turns the RF output *on* (at high input) and *off* (at low input). Red pulses are applied to the phase modulation (ΦM) input. The signal generator is calibrated to obtain 180° phase shift between pulse levels (see Subsection 2.4.2)

Ramsey fringes in Subsection 1.5.2, we explained how we could measure the free-induction decay of a qubit, by using the sequence $\pi/2_x - \tau - \pi/2_x$. There, we assumed that B_1 was in perfect resonance with the qubit rotating frame. If B_1 is slightly detuned from the qubit resonance, P_\uparrow or P_f will oscillate at the detuning frequency $\Delta\nu_1$, forming an interference pattern known as *Ramsey fringes*. The decay of the oscillations' envelope yields the pure dephasing time T_2^* . In practice it is useful to set a detuning $\Delta\nu_1 > 1/T_2^*$, to make sure that the observed decay comes from the free induction decay and not from detuning.

Hahn echo [64] obtained by applying the control sequence $\pi/2_x - \tau/2 - \pi_x - \tau/2 - \pi/2_x$. The π_x pulse cancels the effect of random variations of the instantaneous qubit frequency that are static over the timescale of a single experimental run, and yields the qubit coherence time T_2^H . In bulk experiments, this measurement is realised by detecting the magnetisation of the spins after the π_x pulse. Magnetisation will be maximum — generating the echo — after $\tau/2$, with the echo shape forming a peak with a half-width given by T_2^* . Therefore, measuring the echo shape can be useful in cases where T_2^* is too short to measure with Ramsey fringes. In our single-spin system, we can extract the echo shape by performing a Hahn echo sequence, taking several projective measurements with a fixed initial precession time (τ_1) and varying the second free precession time (τ_2) around τ_1 .

Carr-Purcell-Meiboom-Gill (CPMG) [87] obtained by repeating N ($\in \mathbb{N}_1$) refocusing pulses $\pi/2_x - (\tau/2 - \pi_y - \tau/2)^N - \pi/2_x$. This dynamical decoupling sequence is often used to extend the timescale over which a quantum coherent state can be preserved. The π_y pulses make it immune up to fourth-order to imperfections in the pulse lengths [88]. The decay measurement can be performed in two ways: by fixing N and varying τ , or by fixing τ and varying N . We use this sequence to probe the qubit noise at different frequencies, as will be explained in further detail in Chapter 4. A variant of CPMG is the Carr-Pucell (CP) [89] sequence, where the π_y pulses are replaced with π_x . This sequence loses the immunity to pulse errors, we therefore use it to extract the control fidelity of our qubits (see Section 2.5.2). A final variant of these dynamical decoupling sequences, XYXY [90] alternates the refocusing pulses between π_y and π_x in the same sequence, and the sequence length must have a multiple of four pulses ($\pi/2_x - (\tau/2 - \pi_x - \tau - \pi_y - \tau/2)^{2N} - \pi/2_x$). This sequence demonstrates control of the qubit over the entire Bloch sphere. From each of these sequences we can extract extended coherence times T_2^{CPMG} , T_2^{CP} and T_2^{XYXY} .

Figure 2.9 shows a diagram of the pulses needed at the control signal generator's modulation inputs ports in order to perform each of these sequences.

2.5.2 Qubit fidelities

As introduced in Subsection 1.5.3, the qubit fidelity is the ultimate measure of performance. We will define separates fidelities for the main operations we perform: initialisation, measurement

and control. Due to the different nature of the measurement between the electron and nuclear qubits, the definition and method for extracting the measurement and initialisation fidelities (F_m and F_i) are different. The control fidelity methods apply for both. We will define two types of control fidelity based on the limiting mechanism: intrinsic (F_c) and effective (F_{ec}).

Electron initialisation and measurement fidelities

There are two main sources of measurement errors for our electron qubit. The first is a function of the tunnel rates of the donor charge transition. Quantum tunneling events can occur at different times based on a probability distribution. When a tunneling event occurs at a time faster than our detection speed (or slower than our detection time), there will be an error in our detection. This error can be minimised by increasing the acquisition bandwidth (and increasing the length of the RP). The downside is that increasing the bandwidth leads to a decreased signal-to-noise ratio — the RMS noise voltage of current amplifier load R_L as a function of the bandwidth Δf is $v_n = \sqrt{4k_B T R_L \Delta f}$. The second source of error is thermal broadening. [Figure 2.10a](#) shows a graphical representation of this effect, which results in a non-zero probability of a spin-down tunneling to the SET (measurement error) or a spin-up tunneling to the donor (initialisation error) at the readout level. We denote these thermal measurement and initialisation fidelities as F_{tm} and F_{ti} respectively.

To extract electrical errors, we use the method designed by Morello *et al.* [31], where a histogram is made of the maximum SET current per single-shot, constructed from a large number of single-shot readout acquisitions after loading an electron with equal probability of $|\uparrow\rangle$ and $|\downarrow\rangle$. In their work, they describe a numeric model — which has now been expanded theoretically by D’Anjou and Coish [91] — which can be used to fit to the histogram, and extract peak current values for the separate states N_\uparrow and N_\downarrow (see [Figure 2.10b](#)). From these we can extract the electrical fidelity in measuring a spin-up ($F_{e\uparrow}$) and spin-down ($F_{e\downarrow}$). $F_{e\downarrow}$ only depends on our setting of the current threshold level with respect to the noise floor, and we generally set our current threshold such that we can assume $F_{e\downarrow} \approx 1$.

A Rabi oscillation measurement contains convoluted information of the electrical and thermal errors. A perfect Rabi oscillation will range from $P_\uparrow = 0$ to 1, however this range will be degraded in the presence of errors, causing the reduced oscillations illustrated in [Figure 2.10c](#). We denote the baseline and maximum of the range as $P_{\uparrow base}$ and $P_{\uparrow max}$ respectively. For measurements where a new electron is loaded, an initialisation error implies that the operation — as long as there are no further errors — will produce the opposite of the expected result. Including these errors in our averaged outputs will result in $P_{\uparrow base} = (1 - F_{ti})F_{e\uparrow} > 0$ and $P_{\uparrow max} = F_{ti}F_{e\uparrow} < 0$. Similarly, incorrect detection of $|\downarrow\rangle$ or $|\uparrow\rangle$ will cause our averaged output to further increase $P_{\uparrow base}$ by $F_{ti}(1 - F_{tm})F_{e\uparrow}$ or decrease $P_{\uparrow max}$ by $(1 - F_{ti})(1 - F_{tm})F_{e\uparrow}$ respectively. There is an additional complication in calculating the total $P_{\uparrow base}$ and $P_{\uparrow max}$, due to the fact that we only load a new electron when we measure $|\uparrow\rangle$. Having a probability that varies depending on the outcome of the previous measurement, implies our process in *non-Markovian*,

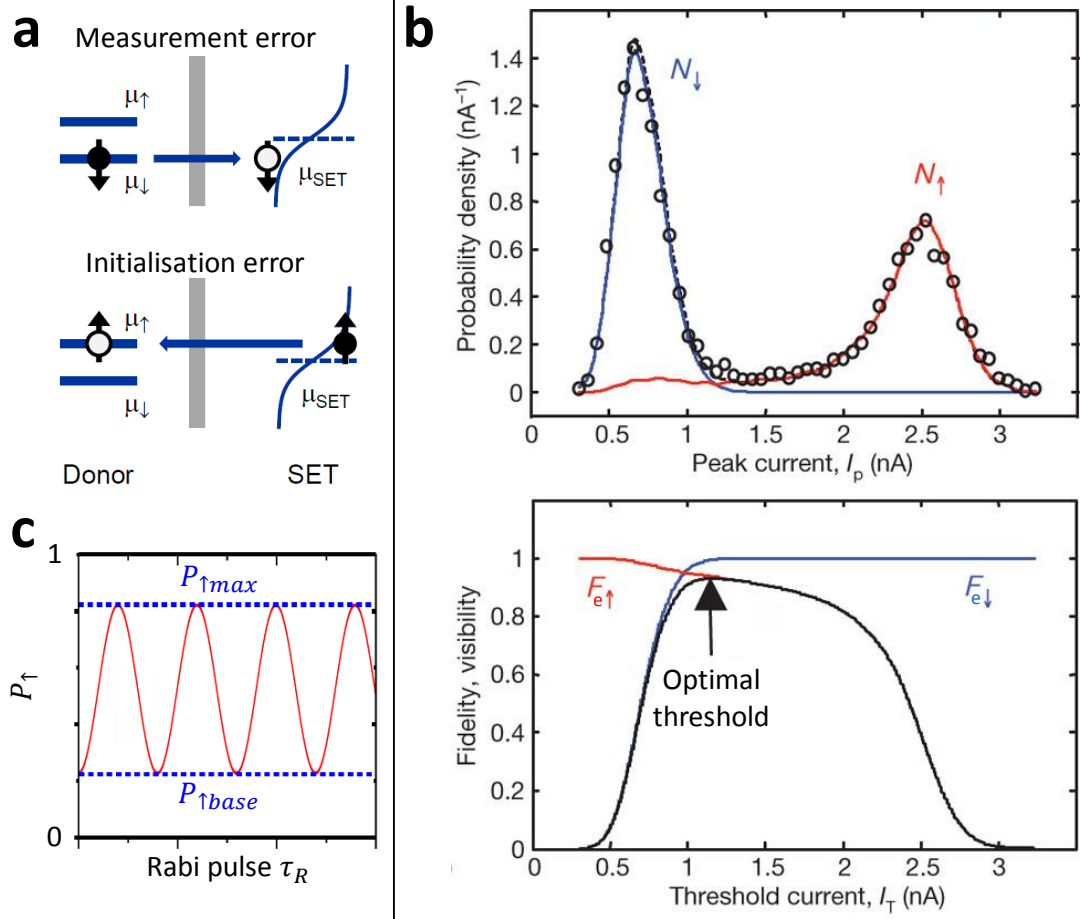


Figure 2.10: Electron qubit initialisation and measurement fidelities. **a** Mechanisms that cause errors due to non-zero temperature. **b** (extracted from [31]) Above: Histogram of peak current showing two well defined peaks corresponding to each electron spin state. The fits come from a numerical simulation of the experiment. Below: Errors extracted from the fits as a function of SET current threshold. From this plot the optimal threshold and maximum visibility are extracted. **c** Resulting Rabi oscillations when initialisation and measurement errors are accounted for.

and the probability must be derived recursively using the following expressions:

$$\begin{aligned} P_{\uparrow base}(0) &= ((1 - F_{ti}) + F_{ti}(1 - F_{tm})) F_{e\uparrow} \\ P_{\uparrow base}(i) &= P_{\uparrow base}(i-1) P_{\uparrow base} + [1 - P_{\uparrow base}(i-1)](1 - F_{tm}) F_{e\uparrow} \\ &= P_{\uparrow base}(i-1) ((1 - F_{ti}) F_{tm} + (1 - F_{tm})) F_{e\uparrow} \end{aligned}$$

$$\begin{aligned} P_{\uparrow max}(0) &= (F_{ti} + (1 - F_{ti})(1 - F_{tm})) F_{e\uparrow} \\ P_{\uparrow max}(i) &= P_{\uparrow max}(i-1) P_{\uparrow max}(0) + [1 - P_{\uparrow max}(i-1)] \\ &= 1 - P_{\uparrow max}(i-1) (1 - F_{ti}) F_{tm} F_{e\uparrow} \end{aligned}$$

This model can be used to obtain values for F_{ti} and F_{tm} that fit to $P_{\uparrow base}$ and $P_{\uparrow max}$ extracted from a Rabi oscillation measurement, using the previously calculated value of $F_{e\uparrow}$. After extracting and separating the thermal and electrical fidelities, the total initialisation and measurement fidelities can be calculated. We can set the read phase length long enough (compared to the tunnel rates), such that initialisation errors only come from the thermal effects, therefore $F_i = F_{ti}$. To calculate F_m , we take the average of the fidelity of measuring a spin-up (F_\uparrow) and the fidelity of measuring an electron spin-down (F_\downarrow). $F_\uparrow = F_{e\uparrow}$ since this fidelity is not affected by thermal effects; $F_\downarrow = F_{tm}$ since we work in the regime where $F_{e\downarrow} \approx 1$. We can now obtain:

$$F_m = \frac{F_\uparrow + F_\downarrow}{2} = \frac{F_{e\uparrow} + F_{tm}}{2} \quad (2.2)$$

Nuclear initialisation and measurement fidelities

For the nuclear spin qubit, fidelities are much simpler. To begin with, in a QND measurement (see [Subsection 1.2.3](#)) the initial state always corresponds to the previous measured state (assuming measurement intervals shorter than the nuclear spin lifetime T_1), therefore $F_i = F_m$. Since the measurement of the nucleus consists of the average of several conditional π -rotations and measurements of the electron, the resulting P_\uparrow from single-shot readout will have a distribution around $P_{\uparrow base}$ and $P_{\uparrow max}$. Extracting the measurement visibility (F_{vm}) involves measuring a histogram of P_\uparrow values for several measurements of $|\uparrow\rangle$ and $|\downarrow\rangle$, and calculating the error from the overlap of the distributions. This error can be reduced by increasing the nuclear readout sequence repetitions (N_s), as the standard deviation of the P_\uparrow distributions follows $\sigma_{P\uparrow} \propto 1/\sqrt{N_s}$.

Another contributing factor to the measurement fidelity is the possibility of a nuclear quantum jump (due to a relaxation process) during the measurement. Note that this mechanism also affects the electron fidelity, but in our experiments it is negligible in comparison with the other mechanisms described in the previous subsection. From the exponential decay of the nuclear T_1 (see [Subsection 2.5.3](#)) we can extract the probability of a nuclear flip (P_{fm}) within our measurement time (t_m). The total measurement fidelity is then:

$$F_m = F_{vm}(1 - P_{fm}) \text{ with } P_{fm} = 1 - \exp\left(\frac{-t_m}{T_1}\right) \quad (2.3)$$

Control fidelities

The *intrinsic* control fidelity is limited by the coherence and operation times of the qubit. A π pulse applied to our qubit has a frequency spectrum — or *excitation profile* — which is a function of the length and shape of the pulse. The area of the excitation profile in relation to the intrinsic linewidth (see [Subsection 1.5.2](#)) of the spin transition determines the precision of the pulse. F_c is then a function of our measured intrinsic coherence and gate speeds. The excitation profile is the Fourier transform of the π pulse, therefore it becomes wider as the pulse gets shorter. A

shorter pulse — and therefore a higher F_c — can be achieved by increasing the power of the resonance signal (increasing B_1), which increases the Rabi frequency (see [Section 2.5.1](#)). To extract F_c from experiments, we use a model which simulates Rabi oscillations in the presence of spectral line detuning [83], by numerically integrating Rabi spin-up proportions (P_{Rabi}), over the intrinsic linewidth ($\Delta\nu$), which we assume to be Gaussian shaped:

$$P_{\uparrow}(t_p) = \sum_{d=-5\sigma_{\nu}}^{5\sigma_{\nu}} P(d) \times P_{\text{Rabi}}(t_p, d) \Delta d \quad (2.4)$$

With:

$$\begin{aligned} P(d) &= \frac{1}{\sqrt{2\pi\sigma_{\nu}}} \exp\left(\frac{-d^2}{2\sigma_{\nu}^2}\right) \\ P_{\text{Rabi}}(t_p, d) &= \frac{f_{\text{Rabi}}^2}{f_{\text{Rabi}}^2 + d^2} \sin^2(\pi t_p \sqrt{f_{\text{Rabi}}^2 + d^2}) \\ \sigma_{\nu} &= \frac{\Delta\nu}{2\sqrt{2\ln(2)}} = \frac{1}{2\sqrt{2\ln(2)\pi T_2^*}} \end{aligned}$$

Here t_p is the Rabi pulse length, f_{Rabi} is the Rabi oscillation frequency and $\Delta\nu$ is the full width at half maximum (FWHM) of the Gaussian peak. The intrinsic control fidelity is then the reduced spin-up proportion of a π pulse using this model:

$$F_c = P_{\uparrow}(t_{\pi}) \text{ where } t_{\pi} = 1/(2f_{\text{Rabi}}) \quad (2.5)$$

We also define the *effective* control fidelity, which is limited by how precisely the instruments can calibrate and output the spin resonance pulses. To extract F_{ec} we apply the method described by Morton *et al.* [92], which compares the coherence decay between two similar dynamical decoupling sequences: CPMG and CP (see [Section 2.5.1](#)). The fundamental difference between the two sequences is that CPMG is fourth-order immune to pulse errors while CP is not. We first perform CPMG and extract the coherence as a function of the number of pulses ($T_2^{\text{CPMG}}(N)$) for a fixed τ . We then perform CP under the same conditions. If we assume Gaussian distributed pulse errors, the decay observed will have a pulse error component $P_{\uparrow}(N) \propto \exp(-(\sigma_p N/2)^2)$, where σ_p is the standard deviation of the pulse error distribution and we define it as the mean rotational error in radians. The total CP decay can then be fit to:

$$P_{\uparrow}^{\text{CP}}(N) = \exp\left(-\left(\frac{N}{T_2^{\text{CPMG}}(N)}\right)^n\right) \exp(-(\sigma_p N/2)^2) \quad (2.6)$$

The only free parameter in this fit is σ_p . We can then extract the effective control fidelity, defined as the probability of flipping the spin with a π pulse:

$$F_{ec} = \frac{1}{2} \left(\cos(\sigma_p) + 1 \right) \quad (2.7)$$

2.5.3 T_1 measurement

As described in [Subsection 1.5.1](#), a spin in an excited state can exchange energy with the surrounding lattice phonons to relax to the ground state, with a probability given by the spin lattice relaxation time T_1 . For electron spins, we measure T_1 by loading a fresh electron onto the donor and waiting some time (τ_w) before reading it out. As we increase τ_w , the loaded $|\uparrow\rangle$ electrons will decay to the ground state with increasing probability ($P_{\uparrow}(\tau_w) = (1 - P_{\downarrow}^{\text{eq}}) \exp(-\tau_w/T_1) + P_{\downarrow}^{\text{eq}}$ as per [Subsection 1.5.1](#)). To perform this measurement, we apply the donor potential sequence LP-RP-EP, with the LP having a variable length τ_w .

The QND nature of the nuclear measurements allows us to just monitor its spin state to observe quantum jumps of the nuclear spin state. As we will discuss further in [Chapter 3](#) and [Chapter 4](#), the lifetimes of the nucleus are in the order in tens of minutes.

2.5.4 Fitting functions

This section provides a summary of the basic fitting functions relevant to the data analysis in this thesis. In this section we use the variables $c_1, c_2 \in [0, 1]$ as normalising parameters .

For the **ESR spectral lines**, we measure P_{\uparrow} as a function of the ESR signal frequency ν_{ESR} . We use a peak fitting function to extract the resonance frequency ν_e and the peak width $\Delta\nu$ from the FWHM of the fit. The spectral lines can be measured in the intrinsic or power broadened regimes (see [Subsection 1.5.2](#)). In the **intrinsic** regime, the line shape should follow the exponent of the free induction decay, which is commonly **Gaussian**. The peak is fitted to:

$$P_{\uparrow}(\nu_{\text{ESR}}) = c_1 \exp\left(\frac{-(\nu_{\text{ESR}} - \nu_e)^2}{2\sigma_{\nu}^2}\right) + c_2 \quad (2.8)$$

For a Gaussian peak, its FWHM is not equal to the variance:

$$\Delta\nu = 2\sqrt{2\ln(2)}\sigma_{\nu}$$

In the **power broadened** regime, the peak has a **Lorentzian** shape [\[56\]](#):

$$P_{\uparrow}(\nu_{\text{ESR}}) = c_1 \frac{\frac{\Delta\nu}{2}}{(\nu_{\text{ESR}} - \nu_e)^2 + (\frac{\Delta\nu}{2})^2} + c_2 \quad (2.9)$$

If **Rabi oscillations** do not have a significant decay due to spectral line detuning, the measured spin-up (for ESR) or spin-flip (for NMR) probability P as a function of pulse length t_p , can be fitted by a simple **sine** function, to extract the Rabi frequency f_{Rabi} :

$$P(t_p) = \frac{c_1}{2} \sin(2\pi f_{\text{Rabi}} t_p) + \frac{c_2}{2} \quad (2.10)$$

For **Ramsey fringes**, we measure P as a function of the free precession time τ_p . Through this measurement we can extract a constant frequency detuning $\Delta\nu_{\text{det}}$ and the free induction

decay time T_2^* and decay exponent n . The fit is the product of an **exponential decay** and a **cosine** function:

$$P(\tau_p) = \frac{c_1}{2} \exp\left(-\left(\frac{\tau_p}{T_2^*}\right)^n\right) \cos(2\pi\Delta\nu_{det}\tau_p) + \frac{c_2}{2} \quad (2.11)$$

For echo experiments (e.g. Hahn or dynamical decoupling), the **echo shape** is obtained by measuring P_\uparrow as a function of the final precession time τ_2 (see [Section 2.5.1](#)). The echo is a **Gaussian peak** and from half of its FWHM we can also extract T_2^* :

$$P_\uparrow(\tau_2) = c_1 \exp\left(\frac{-(\tau_2 - \tau_1)^2}{2\sigma_\nu^2}\right) + c_2 \quad (2.12)$$

With:

$$T_2^* = \sqrt{2 \ln(2)} \sigma_\nu \quad (2.13)$$

Echo decays are obtained by measuring P as a function of the free precession time τ_p . From these we extract the echo sequence coherence time T_2^S and exponent n , after fitting to an **exponential decay**:

$$P(\tau_p) = c_1 \exp\left(-\left(\frac{\tau_p}{T_2^S}\right)^n\right) + c_2 \quad (2.14)$$

The electron \mathbf{T}_1 is extracted from a measurement of P_\uparrow as a function of the wait time in the load phase τ_w . The plot decays as a simple **exponential**:

$$P \uparrow (\tau_w) = c_1 \exp\left(\frac{-\tau_w}{T_1}\right) + c_2 \quad (2.15)$$

In [Chapter 5](#), we also extract T_1 from a model of **rate equations** with state populations. In those experiments we are able to measure the time evolution τ_w of the system eigenstate populations. The details of the model parameters will be explained in the chapter, but the basic principle of a rate equation model consists in constructing a system of differential equations, where for each of the n states S_k we have an equation of the form:

$$\frac{dS_k}{d\tau_w} = \sum_{i=1}^n \Gamma_{ik} S_i - S_k \sum_{i=1}^n \Gamma_{ki} \quad (2.16)$$

Where Γ_{kj} is the rate of population transfer (e.g. the relaxation rate) from S_k to S_j . The model is solved numerically by defining initial conditions (i.e. all the population proportions at $\tau_w = 0$) and calculating the population evolution over small time steps.

In order to obtain measurement fidelities in [Chapter 5](#), we need to fit two histograms of current blip detection times (t_b). For one case we use a **Normal distribution** to extract the

mean detection time μ_d and the standard deviation of the detection bandwidth σ_d :

$$\text{Counts} = c_1 \exp\left(-\frac{(t_b - \mu_d)^2}{2\sigma_d^2}\right) \quad (2.17)$$

For the second histogram we use an **exponential** fit to extract the tunnel rate Γ_t :

$$\text{Counts} = c_1 \exp(-\Gamma_t t_b) \quad (2.18)$$

If the electron temperature T_{el} is known, we can obtain the donor potential to DG **lever-arm** α_{DG} by sweeping V_{DG} across a donor charge transition and fitting the change in I_{SET} to a **Fermi distribution**:

$$I_{\text{SET}} = c_1 \frac{1}{\exp\left(\frac{\alpha_{\text{DG}} V_{\text{DG}}}{k_B T_{\text{el}}}\right) + 1} + c_2 \quad (2.19)$$

2.6 Conclusions

In this chapter we have given a detailed description of the experimental setup and the fundamental qubit measurement techniques. We described the measures we took to cool our qubit to minimum temperatures of 70 mK and the measurement setup that allowed us to reduce our measured noise to 100 pA. We described how we interconnected our available instruments to perform carefully synchronised qubit operations and measurements and subsequently we gave a detailed description of the qubit operation algorithms that are needed to obtain all the results we will present in the following chapters of this thesis.

Chapter 3

Controlling qubits with microwaves

The intense interest in spin-based quantum information processing has caused an increasing overlap between the two traditionally distinct disciplines of magnetic resonance and nanotechnology. In this chapter we discuss rigorous design guidelines to integrate microwave circuits with charge-sensitive nanostructures, and describe how to simulate such structures accurately and efficiently. We present a new design for an on-chip, broadband, nanoscale microwave line that optimizes the magnetic field used to drive a spin based quantum bit (or qubit), while minimizing the disturbance to a nearby charge sensor. We employed this antenna in the first ever experimental demonstration of single-atom qubits from P donors in Si. We present the characteristics measured through the electron and nuclear qubit operations. From the experiments, we extract the parameters that relate the qubit operation to the strength of electric and magnetic fields produced by the antenna, and we find very good agreement with the values expected from electromagnetic simulations.

Parts of this chapter have been published in:

J.P. Dehollain, J.J. Pla, E. Siew, K.Y. Tan, A.S. Dzurak, A. Morello. “Nanoscale broadband transmission lines for spin qubit control”. *Nanotechnology* vol. 24, no. 1, 015202 (2013)

J.J. Pla, K.Y. Tan, **J.P. Dehollain**, W.H. Lim, J.J.L. Morton, D.N. Jamieson, A.S. Dzurak, A. Morello. “A single-atom electron spin qubit in silicon”. *Nature* vol. 489, no. 7417, pp. 541-545 (2012)

J.J. Pla, K.Y. Tan, **J.P. Dehollain**, W.H. Lim, J.J.L. Morton, F.A. Zwanenburg, D.N. Jamieson, A.S. Dzurak, A. Morello. “High-fidelity readout and control of a nuclear spin qubit in silicon”. *Nature* vol. 496, no. 7445, pp. 334-338 (2013)

The author acknowledges E. Siew for the S_{21} measurements of the on-chip antenna; and J.J. Pla for leading the measurement and analysis of the single atom qubit experiments presented in this chapter

3.1 Introduction

In Chapter 1 we presented our approach to building a quantum computer, using single spins from phosphorus donors in silicon. Prior to commencing the work described in this thesis, the furthest experimental development for this system had been the successful demonstration of high-fidelity single-shot readout of a single electron spin from a P donor in Si [31]. The next natural step is to integrate a mechanism for spin control into our system. The theory of how this is to be implemented has been described in Subsection 1.2.2, including some examples of successful demonstrations of single-spin control. However, unsuccessful attempts at merely replicating methods such as the one used by Koppens *et al.* [24] have taught us that for our system, the problem requires closer inspection.

The techniques used in the past for single-spin control [21–25] tend to work well at relatively low frequencies (< 1 GHz) or when the spin under study and the method used to detect it are reasonably robust against heating and stray electric fields. In contrast, our system needs to operate at frequencies up to ~ 50 GHz (see Section 1.6) and the charge detector for single-shot readout is very sensitive to heat and electric fields. Previous discussion on this issue are limited to unsuccessful attempts at integrating high-frequency (> 10 GHz) microwaves with single spins confined in GaAs quantum dots [93, 94]. This task requires the fusion of two traditionally separate disciplines: microwave engineering and nanotechnology.

In the first sections of this chapter we will explain and assess a set of useful design rules that can be applied to maximize the chance of success of high-frequency spin resonance experiments in nanostructures. We illustrate the pros and cons of different designs tailored for our system, these guidelines however, can be applied to most single-spin systems. We start with the broad microwave engineering framework [54] to design a planar transmission line (TL) terminating in a loop close to the spin qubit. We then present a novel on-chip transmission line for broadband localized B_1 field generation (Figure 3.1). We describe a methodology for carrying out electromagnetic field simulations on structures with large dimensional range, from millimetre down to nanometre size. We then use this tool to test the proposed transmission line and compare its performance with other designs.

In the second half of the chapter, we will describe how this broadband antenna was used to successfully operate single-atom spin-qubits from P donors in Si. We will present the characteristics of both an electron and nuclear spin qubits, from which we can extract magnetic and electric field values to compare with our simulations.

3.2 Design guidelines for the optimal planar loop

The main spin-control structure consists of a short-circuit terminated coplanar transmission line (see Section 1.3, forming an *antenna* with a *loop* that generates oscillating magnetic fields at the qubit location (see Section 1.2.6)). The design of efficient TLs involves ensuring that the entire length of the TL is adequately *impedance and mode matched*; meaning that transitions between

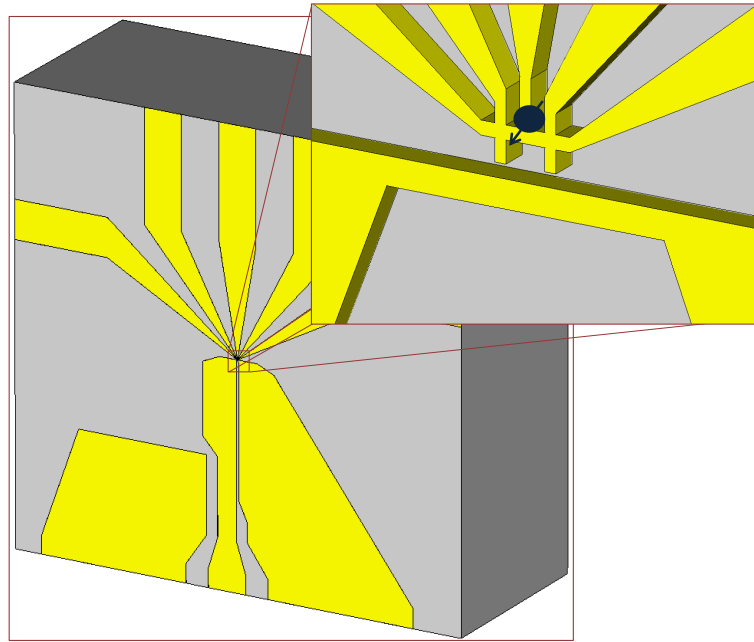


Figure 3.1: Broadband antenna model. Optimized design for an on-chip broadband microwave transmission line for the control of a spin qubit. The inset shows a close-up of the nanoscale part of the structure, consisting of a short-circuit termination of the transmission line and a spin readout device. The dark sphere with arrow indicates the assumed location of the spin qubit. Alternative transmission line designs will be analyzed, while maintaining the same spin readout device structure.

TL types (e.g. from coaxial to PCB waveguide), should be designed such that the impedance of the line and the mode of propagation are continuous, in order to minimise transmission losses (a general description of impedance is given in [Section 1.3](#), while the relevant modes of propagation will be defined in the following sections). From the device architecture and characteristics described in different sections of [Chapter 1](#), we can highlight the following constraints for our antenna design:

1. The electron spin Zeeman splitting (E_Z) must be larger than the thermal broadening, which for our systems requires a minimum resonance frequency $\nu_0 \approx 30$ GHz (see [Section 1.6](#)).
2. The amplitude of the oscillating magnetic field B_1 produced by the loop should be maximized, to allow fast rotations of the spin. From [Section 1.6](#) we calculated a lower bound $B_1 > 18$ pT. We note that, for the purpose of calculating the B_1 value relevant to spin resonance, the rotating wave approximation usually holds. A linearly polarized oscillating field should be decomposed into two counter-rotating components, only one of which contributes to the spin rotation. Therefore, the B_1 values obtained from a microwave simulator must be halved for the purpose of calculating e.g. a Rabi frequency.
3. Electric fields radiated from the transmission line should be minimized at the location

of the spin qubit and readout device, since they can lead to unwanted effects such as photon-assisted tunneling [24], disrupt the operation of charge sensing devices (see Sub-section 3.6.3), and contribute to the local heating of the nanostructure.

Given the constraints above, we will focus on simulations and design guidelines appropriate for spin resonance experiments in the 20–60 GHz range. However we note that a broadband planar loop that works well at $\nu > 30$ GHz will also exhibit good performance at MHz frequencies, since the losses and mode mismatches become less critical as the frequency is lowered. This is of relevance to the case where both electron spin resonance ($\nu > 30$ GHz) and nuclear magnetic resonance ($\nu \approx 100$ MHz) experiments can be performed on the same system, as in our case of dopant atom qubits [18].

3.2.1 Topologies of planar transmission lines

We consider here two main topologies of coplanar transmission lines: *coplanar stripline* (CPS) and *coplanar waveguide* (CPW). The fundamental difference between the two is that the CPS is a *balanced* TL, meaning that it consists of two conductors, each having the same impedance to the surrounding ground planes. A CPS can carry microwaves in two modes: an *odd* mode, where the potentials of the conductors oscillate in opposite phase, and an *even* mode, where both conductors oscillate together with respect to the ground potential. The even mode is generally undesired, but can be excited in the presence of discontinuities and mismatches. In contrast, the CPW is an *unbalanced* TL, consisting of a single conductor, while the ground planes act as return lines. It is also important to consider a planar TL topology known as *microstrip*, which consists of a single planar conductor, with a ground plane underneath the dielectric. Microstrip modes can be excited when coplanar lines are designed on a substrate that needs to sit on a conductive plate, and care needs to be taken to make sure the coplanar modes dominate the propagation of the signal.

Coaxial cables — which we assume are going to be used to carry the microwave to the sample — are unbalanced transmission lines. Therefore we analyze the most typical situation in which a coaxial cable is first coupled to a CPW fabricated on a printed circuit board (PCB). The CPW will have to be impedance-matched to the coaxial cable that delivers the microwave. The characteristic impedance of planar transmission lines is mainly a function of the width and thickness of the metal strips, the gap between coplanar strips and the thickness of the dielectric. Various transmission line analysis textbooks [95, 96] provide equations to calculate the impedance of many different planar transmission line types and configurations.

Referring to the drawings in Figure 3.2, we analyze four possible configurations of lines and loops. Where a CPS is employed, we describe how to realize the conversion from unbalanced to balanced mode, known as a *balun*.

Figure 3.2a is the simplest solution, consisting of a transition between the CPW on the board to a CPS on the chip, realized by bond wires. This design can match the line impedances, but it does not provide a well-controlled unbalanced to balanced line transition. It is crucial to

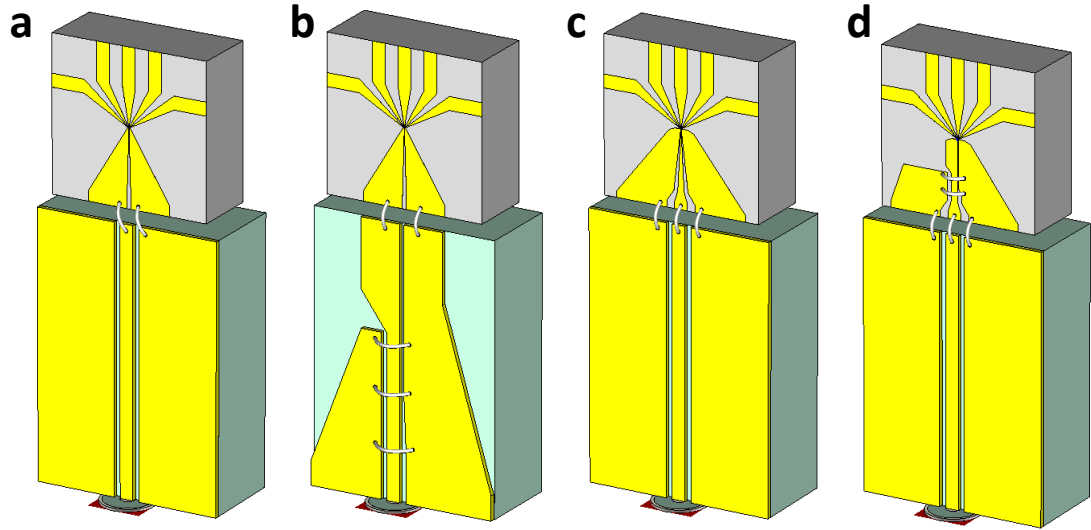


Figure 3.2: Four planar loop designs. **a** A simple CPW on a PCB directly bonded to an on-chip CPS. **b** On-chip CPS with a CPW to CPS transition on PCB. **c** CPW matched to the termination. **d** Novel on-chip balun for maximized current at the loop.

recognize that for these planar loops, the desired node of the electric field (see [Section 1.2.6](#)) only occurs for a perfect odd-mode transmission. Accidentally exciting an even mode will cause an *anti-node* of the electric field at the end of the line. This is a realistic danger for a CPW-CPS transition as crude as that shown in [Figure 3.2a](#). An on-chip CPS was used successfully by Koppens *et al.* [24] to drive the magnetic resonance of a single spin in a GaAs quantum dot at $\nu < 1$ GHz, but contacting the CPS was done directly with a microwave probe instead of using bond wires.

[Figure 3.2b](#) shows an improved design, where a CPW-CPS balun is first fabricated on the PCB, then the CPS on the board is bonded to the CPS on the chip. Here the conversion to a balanced line occurs in a more controlled way as compared to [Figure 3.2a](#), and is less likely to excite an even mode of transmission. However, some risk still exists due to the use of bond wires to connect to the CPS on the chip; the effects of bond wires will be explored further in [Subsection 3.4.3](#). Planar baluns come in many forms and complexities. We chose the CPW to CPS transition presented by Chiou *et al.* [97] and analyzed by Mao *et al.* [98], which combines simple design, broadband operation and low insertion loss.

[Figure 3.2c](#) shows a design based solely on CPWs, both on the PCB and on the chip. The CPW on chip terminates with short circuits on both sides. This type of design was used for instance by Fuchs *et al.* [25] to drive the ESR of a nitrogen-vacancy centre in diamond at $\nu = 0.49$ GHz. Due to the absence of mode conversions, this design will have the widest range of operating frequencies and the lowest insertion loss. However, the nature of the CPW short implies that the current is divided equally amongst two loops, therefore only half of the signal received at the short can be exploited to generate a magnetic field at the qubit location.

3.2. Design guidelines for the optimal planar loop

Finally, in [Figure 3.2d](#) we propose a novel planar loop design, which consists of a short-circuited, on-chip CPW to CPS transition. In this design we keep the matched CPW structure at the interface between PCB and chip, and make the transition to CPS on the silicon chip. To achieve this, the transition needs to be scaled to accommodate the limited dimensions.

In realistic experimental conditions, many parameters can influence the performance of the transmission lines. The chip will normally be mounted in a metallic enclosure for thermal and electromagnetic shielding. Delivering microwaves into the enclosure can excite cavity modes which can severely perturb the behaviour of the transmission lines. Therefore, the dimensions of the enclosure must be designed to minimize cavity modes. From microwave engineering textbooks [96], it is known that for CPW and CPS, keeping $c/(a + 2b) > 1.75$ and $d/a > 2.5$ (a, b, c, d are defined in [Figure 3.3](#)) ensures the enclosure will not affect the impedance of the transmission line by more than 1.5%. Microstrip modes are minimized by making $a + 2b$ shorter than the thickness of the dielectric.

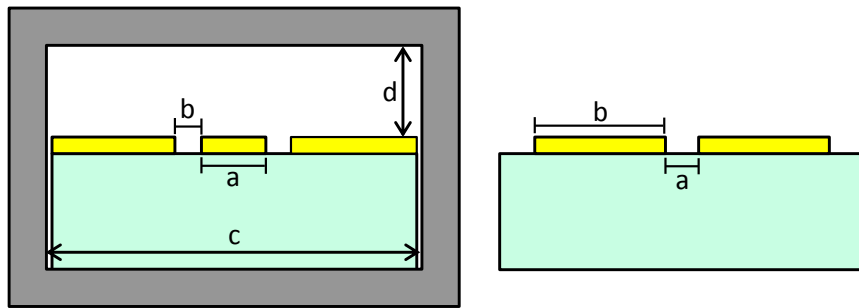


Figure 3.3: Conventions for the dimensions of coplanar TLs. CPW (left), CPS (right) and enclosures (shown in CPW image). For CPW: a is the width of the centre metallic strip, b is the pitch between the signal strip and the ground plates. For CPS: a is the pitch between the balanced strips, b is the width of each metallic strip. For enclosures: c is the width, d is the height from the top the transmission line.

The shape and length of the wire bonds connecting the PCB and chip will also have an important effect on the signal losses at higher frequencies. Bond wires have an effective inductance which increases as they get longer and thinner. With the help of simulations, we analyze this effect in more detail in [Subsection 3.4.3](#).

With regards to the design of the balun included in the topologies in [Figure 3.2b](#) and [Figure 3.2d](#), we follow the method used by Mao *et al.* [98], where the CPW to CPS transition is divided into five sections. Each section tapers, crops and/or expands the transmission line to gradually make the transition keeping impedance variations small and fluid. The length of each section and the angle of the discontinuities needs to be optimized to minimize losses. When scaling the transitions to fit our PCB and chip dimensions, we ran a parametric sweep of simulations to optimize each transition section. The discontinuities at each section of the transition can excite the even mode of propagation, which can increase losses in the transmission line. This effect can be suppressed by connecting the ground planes with bond wires or air

bridges where the discontinuities occur.

3.2.2 Choice of simulation methods for tapered structures

Modeling and simulation of the structures described in this chapter is carried out using the Microwave Studio software package, from Computer Simulation Technology (CST-MWS) [99]. The first step is to choose of a suitable solver, based upon three requirements:

1. In most spin qubit device structures, the spin is buried at some depth below the surface on which the planar loop is fabricated. Therefore the electromagnetic simulation — the goal of which is to obtain the magnetic and electric field at the qubit location — must be carried out with a volume-based method.
2. We are interested in obtaining broadband results, since the operating frequency of the spin qubit might vary over a wide range, depending on the applied magnetic field.
3. All the structures described in [Figure 3.2](#) are sharply tapered, with edge lengths shrinking from millimetres to nanometres. The electromagnetic solver must handle correctly such wide range of structures sizes.

The first requirement reduces our choice of available mesh types to hexahedral and tetrahedral. CST-MWS uses the finite integration method (FIM) [100] to support both these mesh types with time-domain and frequency-domain solvers. The chosen method should provide accurate results, in the least amount of simulation time.

FIM in the time-domain is a leap frog algorithm similar to the finite-difference time-domain method [101]. It is useful for obtaining broadband results, as a single time domain simulation can be transformed to obtain an arbitrarily wide frequency response. However, this method requires a structured grid and only supports hexahedral meshing in CST-MWS. This means that for an accurate representation of our structure, the mesh around the small features will generate a great amount of unneeded mesh points at the large features. Simulation time for this scheme increases linearly on the number of mesh points and the minimum distance between mesh points.

In the frequency-domain, FIM solves a set of Maxwell's equations for the entire volume, in one simulation. This makes the algorithm independent of the grid structure, which allows support for the more flexible tetrahedral meshing. Simulation times only depend on the total number of mesh points. The disadvantage of this scheme is that each simulation solves for only one frequency point, therefore it is necessary to run several simulations in order to obtain a broadband result.

Attempting to accurately represent our tapered structure with hexahedrons will result in an unmanageably large mesh. Therefore the best option is to use the frequency domain solver with tetrahedral meshing. The immense difference in simulation times makes it worth running

3.2. Design guidelines for the optimal planar loop

many simulations in the frequency domain, instead of one simulation with the time domain solver using hexahedral meshing.

Once the solver and mesh type have been selected, the next key step is to produce a mesh that adequately represents all the materials, corners and edges of the structure, with the minimum number of mesh points. CST-MWS can be configured to automatically create an initial mesh and run a mesh adaptation algorithm. The software will sequentially run a simulation and modify the mesh until a convergence is reached on scattering parameters (S-parameters) error. The algorithm adapts the mesh to increase its density at the electrically relevant locations (i.e. corners and edges). However, the automated meshing scheme fails to accurately adapt the mesh to accommodate the large feature size range in our sharply tapered structure. It is therefore necessary to manually divide the model into different sections and assign different meshing densities to each section (see [Figure 3.4](#)). With the mesh adjusted to both feature size and electrical relevance, we can obtain accurate results with minimal mesh points.

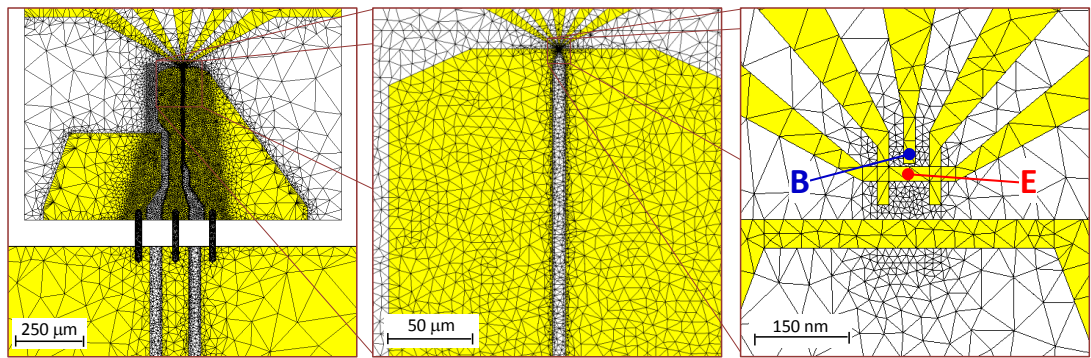


Figure 3.4: Tetrahedral mesh used for simulations. Mesh density is increased sequentially, adjusting to the sharp tapering of the structure. The rightmost inset shows the locations of the probes for all our simulation results: the magnetic field probe is at the donor site location (blue); the electric field probe is at the charge detector (red).

Boundary conditions must be set for each of the planes that define the limits of the modeling space. Boundary conditions can be defined to either minimize reflections (*open space*), or behave like a perfect metallic object (*electric*). To simplify simulations, we model a smaller PCB than what would typically be used in an experimental setup, and we set the boundary conditions to open space on the front and lateral sides of the structure. On the back side the boundary condition is set to electric, to observe the effects of microstrip modes in our transmission lines. These boundary conditions give accurate results as long the guidelines for enclosure size discussed in [Subsection 3.2.1](#) are followed.

Electric and magnetic field probes can be placed anywhere in the three dimensional space of the structure. As shown in [Figure 3.4](#), the electric field probe is placed at the location of the charge detector (i.e. the SET island); while the magnetic field probe is placed 20 nm underneath the DG (i.e. where the donor spin to be controlled is assumed to be located). We extract only the component of oscillating magnetic field that is perpendicular to the static magnetic field.

3.3. General model characteristics

Weiland *et al.* [102] provides a more detailed explanation of the simulation parameters described in this section.

3.3 General model characteristics

All the models we present, as shown on [Figure 3.2](#), comprise of a modeled coaxial input port, a PCB with a planar transmission line, and a Si chip with a planar antenna next to a spin readout device (SRD) similar to the one used by Morello *et al.* [31]. We always assume 1 mW (0 dBm) of power at the coaxial input port of the simulated structure. We modeled the PCB using the characteristics of the Rogers RO3010 laminate with a thickness of 640 μm and 35 μm copper (Cu) cladding. The planar transmission line on the PCB bridges the coaxial port and the chip. It is connected via bond wires to the planar antenna, which is assumed to be fabricated in 100 nm thick aluminium (Al), on top of a silicon (Si) chip with a surface of $1.2 \times 1.2 \text{ mm}^2$ and a thickness of 500 μm . As shown in [Figure 3.1](#), the loop is located at the centre of the chip surface, with a minimum width of 100 nm at the short circuit. The loop is separated from the SRD by 130 nm, and from the donor gate 190 nm. The conductivity of the Cu lines is increased by two orders of magnitude as compared to the room-temperature (RT) textbook values, to account for the use of the device at cryogenic temperatures [103, 104]. The conductivity of the Al thin-films is increased by a factor 4 as compared to its RT value, based on independent resistance measurements of a coplanar loop similar to the one described here, at RT and 4.2 K. We assume the structure is always placed in a magnetic field large enough to suppress the superconductivity in Al. The bonding pads of all Al strips have a minimum area of $100 \times 100 \mu\text{m}^2$. Unless otherwise stated, the bond wires have 25 μm diameter and a length of approximately 200 μm . The following table shows the relevant dimensions of all the planar transmission line types we present, using the conventions from [Figure 3.3](#):

Type of TL	Input		Termination	
	a (μm)	b (μm)	a (μm)	b (μm)
CPW on PCB	100	60	100	60
Balun on PCB	100	60	30	300
CPW on chip	100	60	1.6	1
CPS on chip	30	300	1	10
Balun on chip	100	60	7	90

3.4 Simulation Results

After describing our modeling methods, we now present the results of our simulation, starting with a general characterisation of the electro-magnetic transmission through our lines, followed by an analysis in performance of our designs. To finish this section we will present some parametric simulations that unveil the significance of some of the elements in our models, that

3.4. Simulation Results

are often overlooked in these experimental setups.

3.4.1 Electric and magnetic fields along the transmission line

We will begin with a characterization of the electric and magnetic field profiles along the short circuited coplanar transmission line shown in Figure 3.1. Figure 3.5a shows the amplitude of the perpendicular component of the magnetic field B_1 generated around the loop. B_1 clearly decays with distance from the short, which shows the importance of placing the loop as close as possible to the spin qubit.

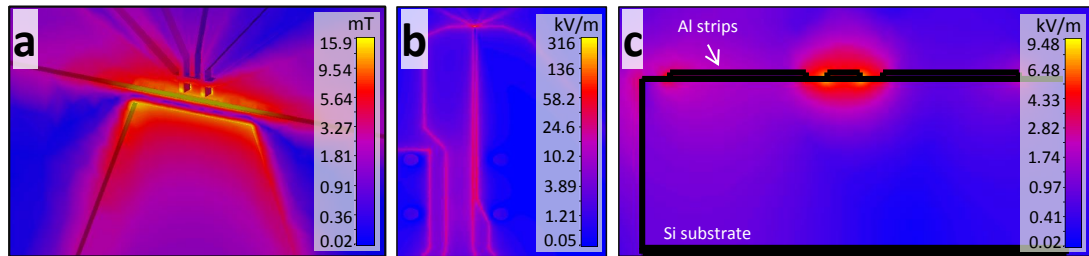


Figure 3.5: Characterization of the planar transmission lines. **a** 2D plot of the component of the magnetic field amplitude perpendicular to the surface of the chip. **b** 2D plot of the absolute value of the electric field. **c** Electric field at the input of the on-chip CPW. The field is mainly radiated from the centre Al conductor to the coplanar ground planes. The fields in all figures are calculated at 50 GHz.

The voltage difference between signal and ground lines generates an electric field, which decreases to zero (Figure 3.5b) as it approaches the voltage node at the short-circuit. However, the resonant stub behaviour of the on-chip line (explained later in Subsection 3.4.2) causes an additional electric field to be emitted at the end of the line. This electric field can be responsible for a degradation of the performance of the SRD, and heating of the electron layer nearby.

Figure 3.5c shows that the transmission through the on-chip line is dominated by the CPW mode, as desired. The field being radiated from the centre conductor to the back plate is negligible compared to that radiated to the coplanar planes.

The metal gates of the spin readout device couple capacitively to the loop, causing an increase in the electric field radiated by the loop. Simulating our structure without and with a SRD shows an electric field increase of ~ 1.5 orders of magnitude over the whole frequency range. In contrast, the magnetic field only increases by $\sim 30\%$ in the presence of the SRD.

The surface current monitor allows us to estimate the current flowing through the loop. We find that 80 μ A of current flowing through the planar loop will generate 0.1 mT of magnetic field at the spin location.

The skin depth effect can reduce the effective conductivity of transmission lines, therefore increasing signal loss in transmission. The skin depth δ can be calculated as $\delta = \sqrt{2\rho/\omega\mu}$ where ρ is the resistivity of the conductor, ω is the angular frequency of the current and μ is the absolute permeability of the conductor. The fields in the conductor decay by an amount

3.4. Simulation Results

proportional to $1/e^\delta$ [54]. Therefore having a conductor of thickness $> 4\delta$ ensures more than 98% of the electric field has decayed, with no significant reduction in the effective conductivity of the line. Between 20 and 60 GHz, the skin depth of an aluminium line at cryogenic temperatures — and B_0 above the critical field — ($\rho = 7 \text{ n}\Omega/\text{m}$) is 172 nm to 300 nm. The on-chip transmission lines modeled have conductor widths that comfortably exceed the skin depth limits, however the 100 nm thickness of the Al clad could potentially affect the transmission. Results from simulations of a similar model with a 1 μm thick on-chip transmission line, show there is no appreciable difference in transmission parameters or field amplitudes.

3.4.2 Performance comparison between CPS/CPW topologies

The four planar transmission line models presented in Subsection 3.2.1 were simulated and the results are compared in Figure 3.6. The S_{11} parameter, which represents the reflected power, is a useful measure of the broadband performance of the lines. An ideal short-circuited transmission line should be fully reflective, yielding $S_{11} = 0 \text{ dB}$ at all frequencies. $S_{11} < 0 \text{ dB}$ indicates radiative losses, and we indeed observed that the behaviour of S_{11} correlates with the electric field radiated by the line towards the SRD.

The simulations show that the fully-CPW structure shown in Figure 3.2c is the closest to having the ideal behaviour $S_{11} \approx 0 \text{ dB}$ from 0 to 60 GHz and, accordingly, the smallest electric field radiated at the SRD. This is not surprising, since this design is matched in impedance and propagation throughout. However, as mentioned before, this comes at the price of roughly halving the strength of B_1 available at the spin qubit location.

The on-chip balun design of Figure 3.2d generates the highest B_1 fields through most of the spectrum. It radiates adequately low electric fields, comparable to the CPW at low frequencies, but shows a resonance at around 60 GHz, where the electric field increases accordingly. This phenomenon, known as “stub resonance”, is caused by the discontinuity between the PCB and the Si chip, which makes the on-chip section of the transmission line behave like a short-circuited resonator [54]. A short-circuited line acts as a parallel R-L-C circuit when its length equals a quarter wavelength ($\lambda/4$). In this type of resonator, a $\lambda/4$ standing wave is formed by having a minimum of the current at the input and a maximum at the loop. The on-chip line modeled here has a length of 550 μm , thus the resonance should be observed at $\lambda = 2.2 \text{ mm}$. Frequency and wavelength in microwaves relate to each other through the propagation velocity, given by $v = c'/\sqrt{\epsilon_{eff}}$, where ϵ_{eff} is the effective dielectric constant of the medium through which the wave is traveling. Due to the fact that waves in planar lines travel at the interface of two different media (in this case vacuum, $\epsilon_r = 1$, and silicon, $\epsilon_r = 11.9$), obtaining ϵ_{eff} for our on-chip balun is non-trivial. Assuming an ideal planar line, half of its field travels in the substrate (filling factor of 50%), and its effective dielectric constant is the average between the two media. With this assumption we can estimate $\epsilon_{eff} \approx 6.45$, and a stub resonance at $f = v/\lambda = 53.7 \text{ GHz}$. The stub resonance observed in the simulations is shifted to a higher frequency due to the low inductance of the bond wires interfacing the PCB and chip. In Subsection 3.4.3, these effects

3.4. Simulation Results

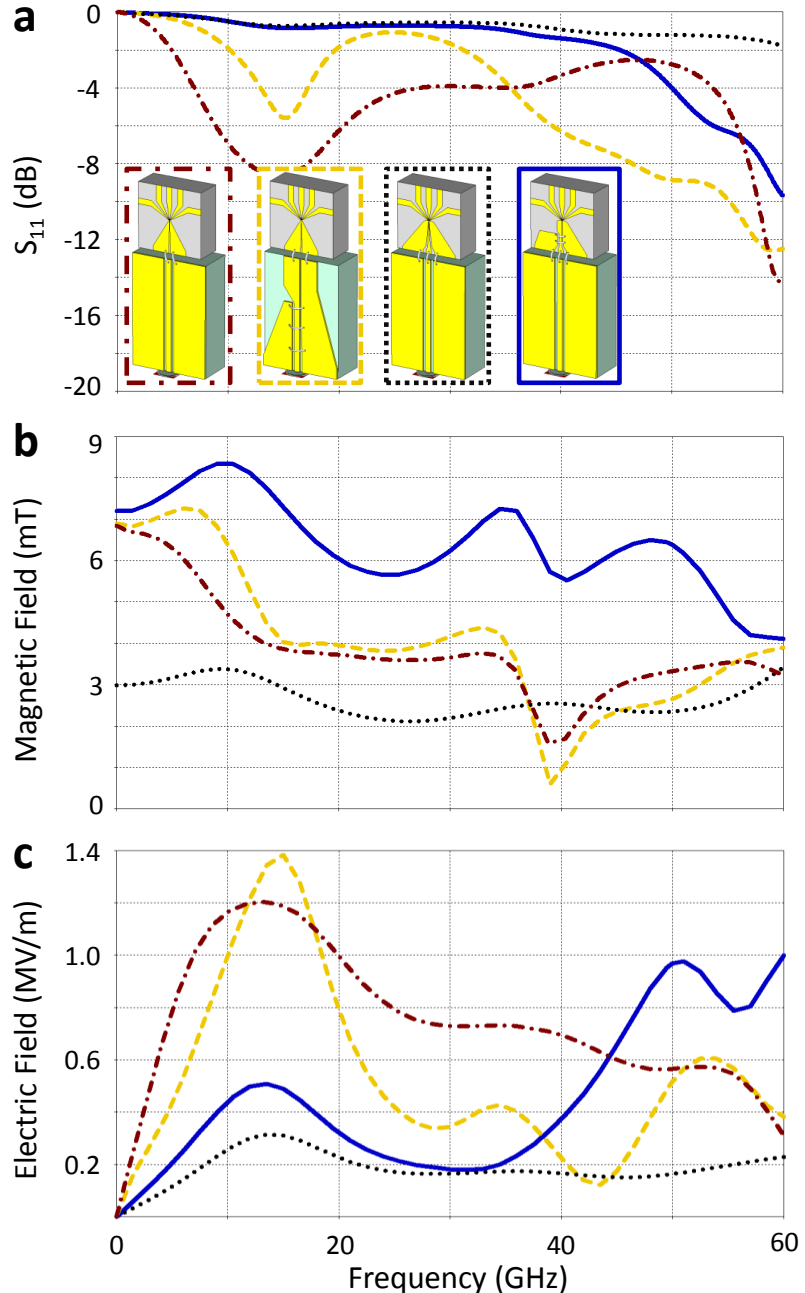


Figure 3.6: Simulation results comparing antenna designs. Frequency response of four planar loop designs: On-chip CPS with no transitions (red); On-chip CPS with PCB balun (yellow); On-chip CPW (black); On-chip balun (blue). **a** S_{11} parameter. **b** Magnitude of the perpendicular component of the magnetic field at the donor site. **c** Absolute electric field at the charge detector, in this case the SET island.

3.4. Simulation Results

are analyzed in further detail.

The design with propagation and mode mismatch (Figure 3.2a) shows the poorest performance at high frequencies, radiating more than two times the amount of electric field compared to other designs.

3.4.3 Further optimization

As explained in the previous section, the discontinuity between the PCB and the chip causes a stub resonance at high frequency. Bond wires have an effective inductance that increases with length and decreases with thickness [105]. In Figure 3.7 we show that with very long bond wires the resonance is very pronounced at the frequency calculated in Subsection 3.4.2. Shorter bond wires push the resonance to higher frequencies. This behaviour suggests that the bond wires can be modeled as an inductance in parallel with the R-L-C equivalent circuit of the on-chip resonating stub. Therefore, minimizing the effective inductance from the bond wires helps remove the resonant effect.

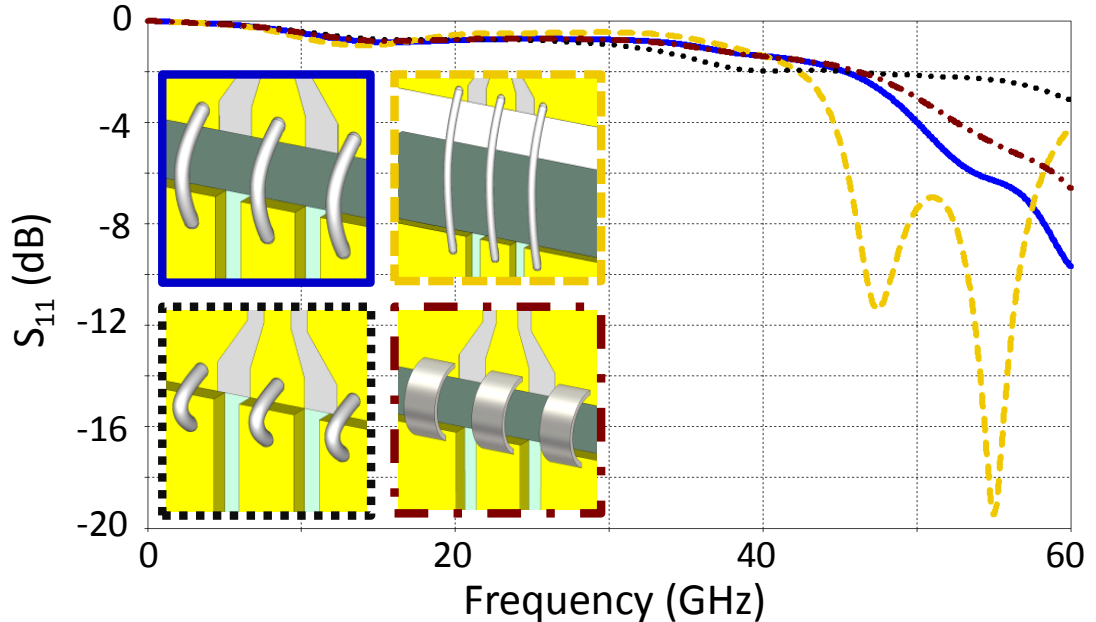


Figure 3.7: Comparison of S_{11} parameters for different bond wire lengths and types. 200 μm bond wire (blue); 500 μm bond wire (yellow); 150 μm bond wire (black); 200 μm ribbon bond 70 μm wide by 10 μm thick (red)

Using very short bond wires can completely remove the resonant effect, but bond lengths of less than 200 μm can be challenging to realize. A more viable solution is to use ribbon bonds, which have a much smaller effective inductance than standard bond wires. If ribbon bonds are not available, a good practice is to bond as many wires as possible in the space available on the bond pads.

3.4. Simulation Results

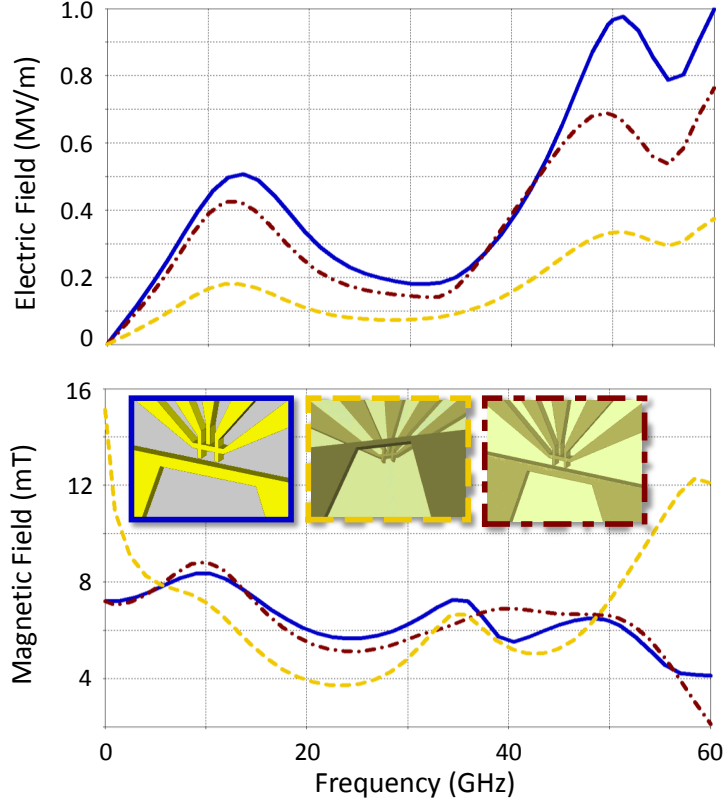


Figure 3.8: Qubit placement inside or outside the loop. The standard model with the qubit located outside the loop (blue); model with the transmission line elevated with calixarene, with the qubit located inside the loop (yellow); standard model with a thin film of calixarene surrounding the transmission line and gates (red).

We have seen in Figure 3.5b that the electric field is mainly radiated towards the outside of the loop. Therefore, placing the spin readout device on the inside of the loop should decrease the electric field observed by the qubit, while maintaining high oscillating magnetic fields. In the experiment performed by Koppens *et al.* [24], the SRD was indeed positioned on the inside of the loop, by separating the transmission line and the device with a thin film of dielectric. We can adjust our model to show results for this setup. We model a 100 nm coating of a material with $\epsilon_{eff} = 7.1$ (i.e. calixarene [106]) on top of the Si substrate and lay the planar loop on top, with the magnetic probe 50 nm inside the loop. We show in Figure 3.8 the simulated B_1 and electric field amplitudes of the shorted on-chip balun with and without the dielectric. The results suggest that using the dielectric layer to place the device inside the loop does improve the magnetic to electric field ratio at frequencies below 20 GHz and above 40 GHz. We also find that by adding the dielectric alone, without modifying the position of the loop, a shielding effect causes a reduction of the electric field at the SRD, without affecting the amplitude of the magnetic field.

3.4. Simulation Results

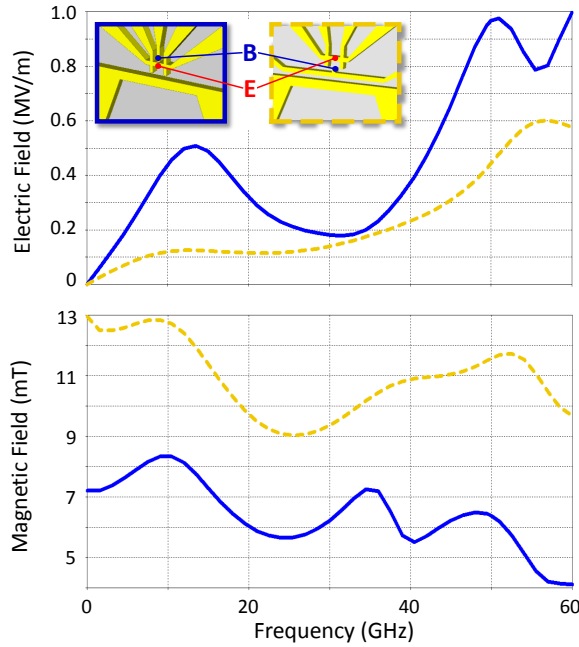


Figure 3.9: Improved performance for new device architecture. Performance comparison between the standard model (blue) and a model with an improved gate layout with the DG placed on the opposite side of the SRD (yellow). This architecture was used in the devices presented in [Chapter 4](#).

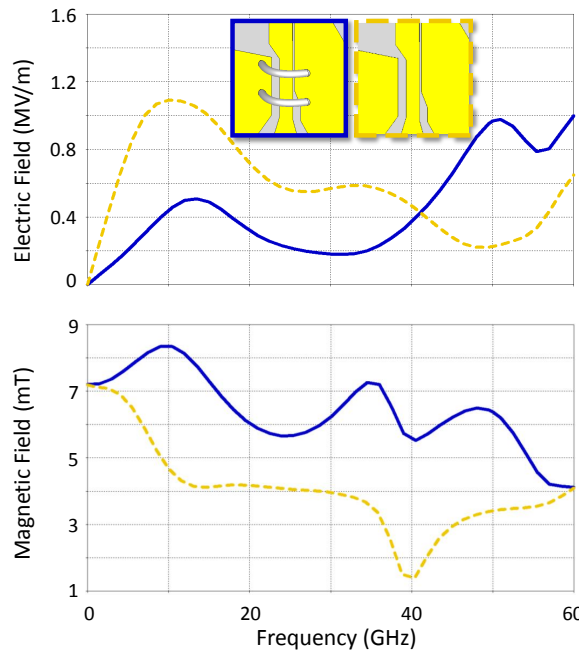


Figure 3.10: Importance of ground bridges at discontinuities. Electric and magnetic fields obtained from the model with (blue) and without (yellow) the bond wires bridging the ground plates of the on-chip CPW.

For the devices in Chapter 4, we have updated the device architecture in order to improve the B_1 to E ratio. We have modified the gate layout such that the DG is placed on the same side of the SRD as the antenna (see inset in Figure 3.9), which both increases the distance from the loop to the SRD to 230 nm (i.e. lower E) and decreases the distance to the donor spin to 150 nm (i.e. higher B_1). The results shown in Figure 3.9 show that we can expect a factor ~ 3 improvement in B_1 to E ratio with this new gate layout.

We explained at the end of Subsection 3.2.1 the importance of bridging the ground plates of a CPW at discontinuities, in order to suppress the excitation of even modes of propagation. The simulation results in Figure 3.10 show how removing the bond wires that bridge the ground planes leads to a some deterioration of the frequency response.

3.5 Operating the first single spin qubits in Si

With all the useful insight into the non-trivialities of implementing a single-spin control antenna, we proceeded to fabricate a qubit device and setup a qubit operation experiment as described in detail in Chapter 2. Figure 3.11a shows an image of our fabricated device with the spin resonance antenna. The operation principles of all the elements of this device were discussed in Subsection 1.2.6 and qubit operations mentioned in this section are all described in Section 2.5.

3.5.1 Electron qubit

The first hints of success came from the observation of the ESR spectral lines shown in Figure 3.11b. The two measurements in the figure were taken ~ 10 minutes apart and show a shift of the resonance peak corresponding to a quantum jump of the nuclear spin state (see Subsection 1.2.2). For the field $B_0 = 1.79$ T, the peaks are close to the expected $\nu_e = g\mu_B B_0 = 50$ GHz. From the separation between peaks we extract the hyperfine $A \approx 114$ MHz, close to the bulk value of 117.52 MHz [76]. We attribute the slight difference in value to a Stark shift of the hyperfine coupling, caused by the strong electric fields produced at the donor site by the gated nanostructure surrounding it, as well as possible strain from the proximity of the donor to the Si/SiO₂ interface. As we will discuss in the next chapter, this hyperfine shift can vary significantly between devices. The linewidth $\Delta\nu = 7.5 \pm 0.5$ MHz, is extracted by averaging many measurements and fitting the data to Equation 2.8.

Having characterised the ESR spectrum, we proceed to demonstrate coherent control through the Rabi oscillations shown in Figure 3.11c. We can observe a few clear oscillations with a range $\Delta P_\uparrow \approx 0.2$. Confirmation that these are Rabi oscillations comes from the dependence of the Rabi frequency with the applied microwave amplitude: $f_{\text{Rabi}} = \gamma_e B_1$ with $P_{\text{ESR}}^{1/2} \propto B_1$. The largest Rabi frequency attained was 3.3 MHz ($B_1 \approx 0.12$ mT), corresponding to a π rotation in ~ 150 ns.

We characterise the coherence of this qubit by operating it using the Hahn echo and XYXY control sequences (see Section 2.5.1). We fit the shape of the Hahn echo peak in Figure 3.11d to

3.5. Operating the first single spin qubits in Si

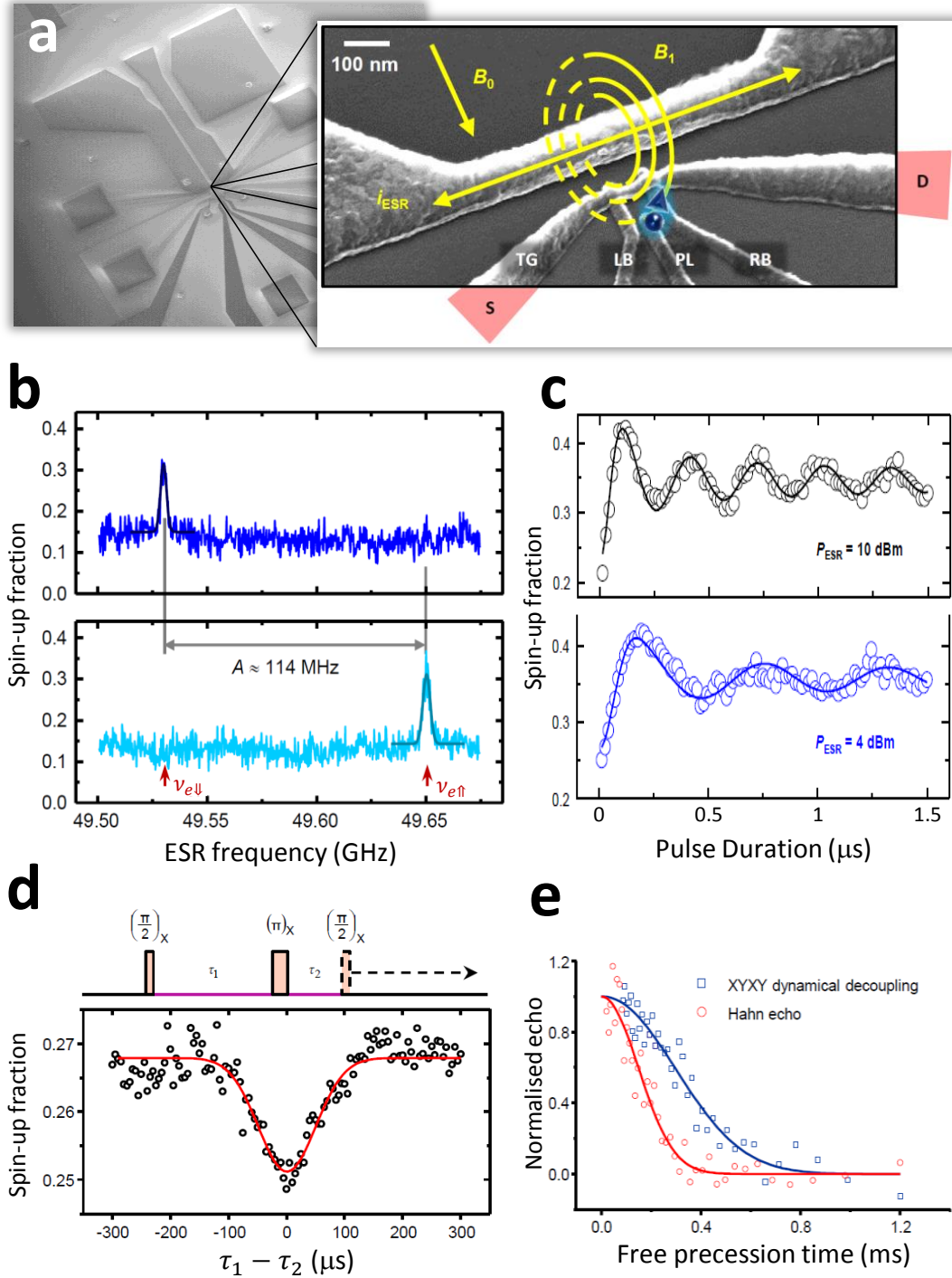


Figure 3.11: Qubit device and electron spin qubit operation. **a** Scanning electron microscope image of the on-chip device with an zoom inset showing the nanoscale features of the device. **b** Electron spin resonance peaks showing a well defined separation for each nuclear state. **c** Rabi oscillations at two different powers. The Rabi frequency clearly decreases with power. **d** Pulse sequence and data from a Hahn echo shape measurement ($\tau_1 = 10 \mu\text{s}$). Red line is a fit to a Gaussian peak. **e** Extended coherence measurements. Echo decays for Hahn echo (red circles) and XYXY (blue squares).

a Gaussian (Equation 2.12) to extract $T_2^* = 55 \pm 5$ ns. This measured free induction decay time corresponds to an intrinsic linewidth $\Delta\nu_{\text{ESR}} = 1/(\pi T_2^*) = 6 \pm 1$ MHz, which agrees well with our measured value. By fixing $\tau_1 = \tau_2 = \tau$, increasing τ and monitoring the echo amplitude we extract $T_2^H = 206 \pm 12$ μ s from the red plot in Figure 3.11e, which agrees very well with the measured bulk value [107]. The exponent from the fit $n = 2.1 \pm 0.4$ suggests the main source of decoherence is ^{29}Si induced spectral diffusion [108] which is not surprising given that it is a ^{29}Si sample. The blue plot in Figure 3.11e shows we have extended coherence times to $T_2^{\text{XYXY}} = 410 \pm 20$ μ s (with $b = 2.1 \pm 4$). As well as delivering a factor of 2 improvement in T_2 , the XYXY sequence demonstrates the ability to perform controlled rotations about two orthogonal axes on the Bloch sphere (X and Y), permitting arbitrary one-qubit gates for universal quantum computing [34].

In Subsection 2.5.2 we described the experiments and analysis that needs to be done in order to extract the qubit fidelities. Due to the fact that our Rabi oscillations decay quickly, we need to deconvolute the effects of initialisation and measurement errors from the effects of control errors in order to extract the separate fidelities. To do this, we use a modified version of Equation 2.4 to simulate our Rabi oscillations:

$$P_\uparrow(t_p) = c_1 + c_2 \sum_{d=-5\sigma_\nu}^{5\sigma_\nu} P(d) \times P_{\text{Rabi}}(t_p, d)$$

We fit to our data by leaving c_1 , c_2 and f_{Rabi} as free parameters, and fixing $\sigma_\nu = 3.2$ MHz from our measured linewidth. Initialisation and measurement error effects are then deconvoluted by solving:

$$\begin{aligned} c_1 &= P_{\uparrow\max} \\ c_2 &= P_{\uparrow\max} - P_{\uparrow\text{base}} \end{aligned}$$

Finally we extract the electrical visibility through the histogram shown in Figure 3.12. Having obtained all the needed fidelity parameters, we use the method described in Section 2.5.2 to obtain $F_m = 77 \pm 2\%$ and $F_i > 90\%$. By setting $c_1 = 0$, $c_2 = 1$ and using Equation 2.5 we extract $F_c = 60 \pm 3\%$. For this qubit the intrinsic control fidelity dominates and therefore $F_{ec} = F_c$.

3.5.2 Nuclear qubit

The measurement algorithm for single-shot readout of the nuclear spin state was explained in detail in Subsection 2.5.1. In order to maximize the probability of flipping the electron spin in each shot, we replace the electron π pulse with a fast adiabatic passage by applying a frequency chirp centered about the ESR transition [76, 109]. Figure 3.13a shows repeated

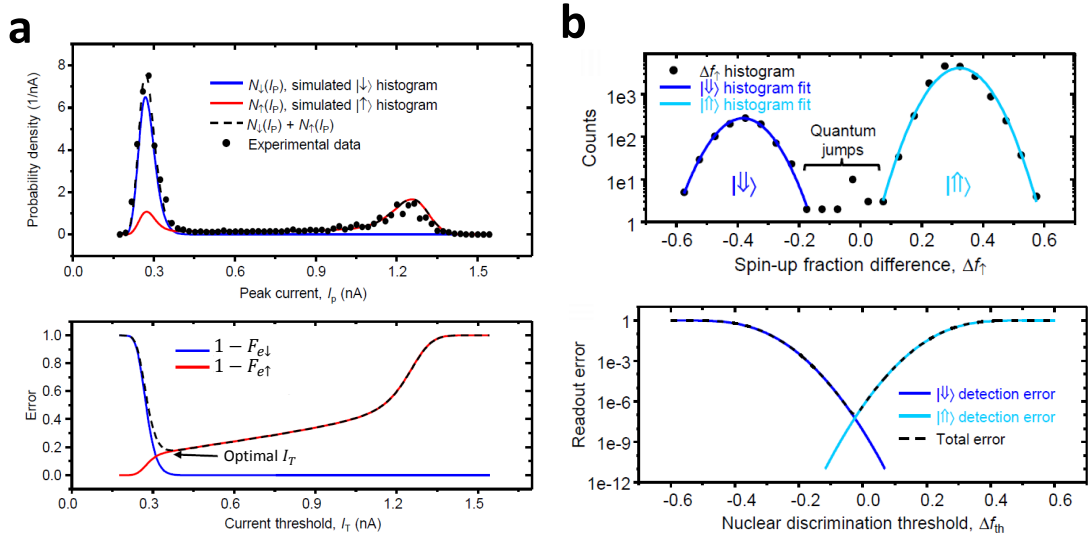


Figure 3.12: Measurement fidelity histograms for e and N qubits. **a** Electron qubit fidelity from electrical effects. Histogram of peak current per shot with fits from which the error can be plotted as a function of I_T . **b** Nuclear qubit measurement fidelity. Histogram of the electron spin-up fraction difference measured for each nuclear readout sequence. The two clear peaks correspond to each nuclear spin state. The error is extracted from the overlap of the fits to the Gaussian peaks.

electron spin measurements (P_{\uparrow}) at each nuclear spin state frequency ($\nu_{e\uparrow}$ and $\nu_{e\downarrow}$) over several minutes, averaging 250 electron spin measurements (total measurement time $t_m = 260$ ms) at each point. If the quantity $\Delta P_{\uparrow} = P_{\uparrow}(\nu_{e\uparrow}) - P_{\uparrow}(\nu_{e\downarrow})$ is positive, we assign the nuclear state $|\uparrow\rangle$, and vice versa. A histogram of ΔP_{\uparrow} (Figure 3.12b) shows two well-separated Gaussian peaks, corresponding to the two possible nuclear orientations. The widths of the peaks result from a combination of effects including: thermal broadening (caused by microwave-induced heating), charge fluctuations (which alter the device biasing) and an imperfect adiabatic passage. From this histogram we extract $1 - F_{vm} \approx 1 \times 10^{-7}$ (see Section 2.5.2).

We observe that the nuclear spin state remains unchanged for several minutes before exhibiting a “quantum jump” to the opposite state [110]. From Figure 3.13a, it is evident that the nuclear spin is predominantly polarized in the $|\uparrow\rangle$ state. We attribute this phenomenon to an electron-nuclear spin flip-flop process, in which the energy difference $E_{\uparrow\downarrow} - E_{\downarrow\uparrow}$ (i.e. between states $|\uparrow\downarrow\rangle$ and $|\downarrow\uparrow\rangle$) is released to the phonon bath. The spin-phonon coupling may arise from the modulation of the hyperfine coupling caused by lattice deformation [111]. The same mechanism was invoked to explain the ~ 100 s decay time of spin polarization stored in a P ensemble [112]. Since $E_{\uparrow\downarrow} - E_{\downarrow\uparrow} \gg k_B T$ in our experiment, this process acts only in the direction $|\uparrow\downarrow\rangle \rightarrow |\downarrow\uparrow\rangle$ (i.e., only spontaneous emission of phonons occurs), and should not be responsible for the observed nuclear spin jumps from $|\uparrow\rangle$ to $|\downarrow\rangle$. The mechanism for this latter quantum jump is not yet understood, but it is clear from the data that it occurs over a much longer timescale. Owing to this, the $|\downarrow\rangle$ lifetime $T_{1\downarrow} = 65 \pm 15$ s will be the limiting factor for our measurement fidelity. Using this value of T_1 with the values quoted above for F_{vm} and t_m ,

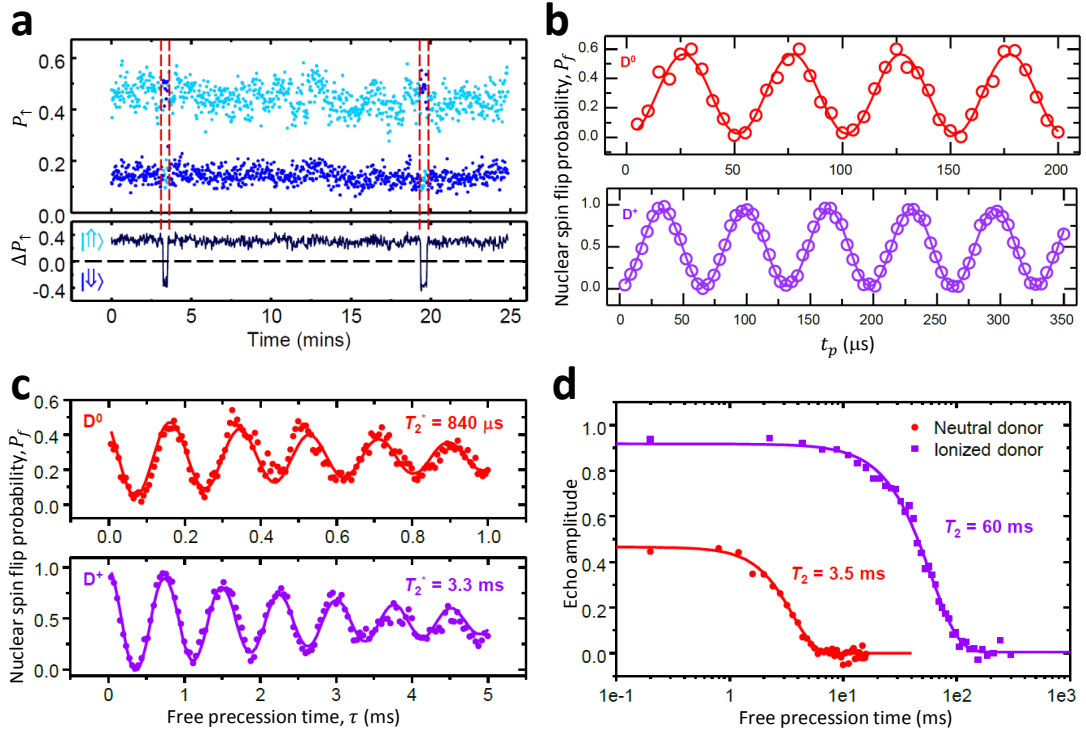


Figure 3.13: Operation of the nuclear spin qubit. **a** Nuclear readout showing quantum jumps and nuclear spin polarization. **b** Neutral (red) and ionised (purple) nuclear Rabi oscillations. **c** Ramsey fringe measurement revealing the free induction decay time T_2^* . **d** Hahn echo decays revealing extended coherence time T_2 .

Equation 2.3 yields $F_m = 99.84 \pm 0.04\%$, the highest for any solid-state qubit and comparable to readout fidelities in trapped ion systems [113].

The weak magnetic moment of the nucleus increases its immunity to environmental noise, therefore we expect control measurements to exhibit higher fidelities and longer coherence times than the electron. Furthermore, the nucleus in the D^0 state can be affected by noise felt by its bound electron, through the hyperfine interaction; therefore the bare nucleus (in the D^+ state), should exhibit the most robust characteristics. Figure 3.13b shows Rabi oscillations for both of the donor charge states. In contrast to the electron, we observe several oscillations without any decay, which implies a much improved control fidelity. The Rabi oscillation contrast is nearly perfect for D^+ , while we see a significant reduction for D^0 due to imperfect electron initialisation, most likely due to an additional thermal broadening and electric field noise induced by the broadband antenna (discussed further in Subsection 3.6.3). The highest Rabi frequencies obtained were $f_{\text{Rabi}} \approx 20 \text{ kHz}$. These plots are the result of 200 averaged measurements at each t_p (with 250 electron measurements per nuclear readout).

With our improved control fidelity we are able to perform the Ramsey fringe control sequence described in Section 2.5.1. Figure 3.13c shows interference oscillations which decay with a time constant $T_2^* = 840 \pm 100 \mu\text{s}$ for D^0 and $T_2^* = 3.3 \pm 0.3 \text{ ms}$ for D^+ . Figure 3.13d shows extended

coherence measurements with a Hahn echo sequence which reveal $T_2(D^0) = 3.5 \pm 0.1$ ms (with $b = 2.2 \pm 0.2$) and $T_2(D^+) = 60 \pm 1$ ms (with $b = 1.7 \pm 0.1$). The exponents are again consistent with spectral diffusion as the dominant source of noise. The relatively long free induction decay times imply a linewidth much narrower than the excitation profiles, which means the intrinsic control fidelity is very close to unity. Through the use of dynamical decoupling we can extract the effective control fidelity, by comparing CP and CPMG echo decays, as explained in [Section 2.5.2](#). With this method we estimate $F_{ec} \approx 99.9\%$. The limiting factor to obtain a more precise measurement was the timescale over which these measurements were obtained (~ 70 hours), but we highlight the magnificent fidelities achieved for this nuclear spin qubit.

3.6 Benchmark of antenna simulations with experiments

Now that we have demonstrated that our spin resonance antenna can be successfully used to control single atom spin qubits, we can use some of our measurement results to extract values that we can directly compare with our simulation results. In the device we used for experiments, we did not manage to make the short bond to bridge the ground lines of the on-chip TL, therefore we will use the simulation results in [Figure 3.10](#) (yellow) for experimental benchmarking in this section.

3.6.1 Stub resonance of the on-chip CPW/CPS balun

As a first experimental benchmark of the reliability of our modeling and simulation techniques, we made an S_{11} measurement using a 10 MHz to 50 GHz Agilent PNA microwave network analyzer. Instead of bonding the planar line to a PCB, we have used a microwave probe station, which terminates in a 3-terminal probe that can be placed directly on the chip at various locations (see inset [Figure 3.14](#)). This allows us to study the stub resonance of the on-chip balun structure, by varying the distance between the edge of the chip and the contact point of the probe. To simulate this setup accurately, we removed the PCB structure from the model shown in [Figure 3.2d](#) and connected short bond wires from the coaxial port to the on-chip line, at each different microwave probe locations. [Figure 3.14](#) shows a very good agreement between the measured and simulated S_{11} values.

3.6.2 Oscillating magnetic field at the spin qubit

From the electron spin control measurements presented in [Subsection 3.5.1](#), we can extract the value of oscillating magnetic that is reaching our qubit. The frequency of the Rabi oscillations is given by $f_{Rabi} = (g\mu_B B_1)/h$. From the fit to the power-dependence in [Figure 3.15](#) we can extrapolate $f_{Rabi} = 1.2$ MHz at 0 dBm power from the source, yielding an oscillating magnetic field at the donor $B_1 = 43$ μ T. This experiment was performed at a spin resonance frequency $\nu_{ESR} = 30$ GHz.

3.6. Benchmark of antenna simulations with experiments

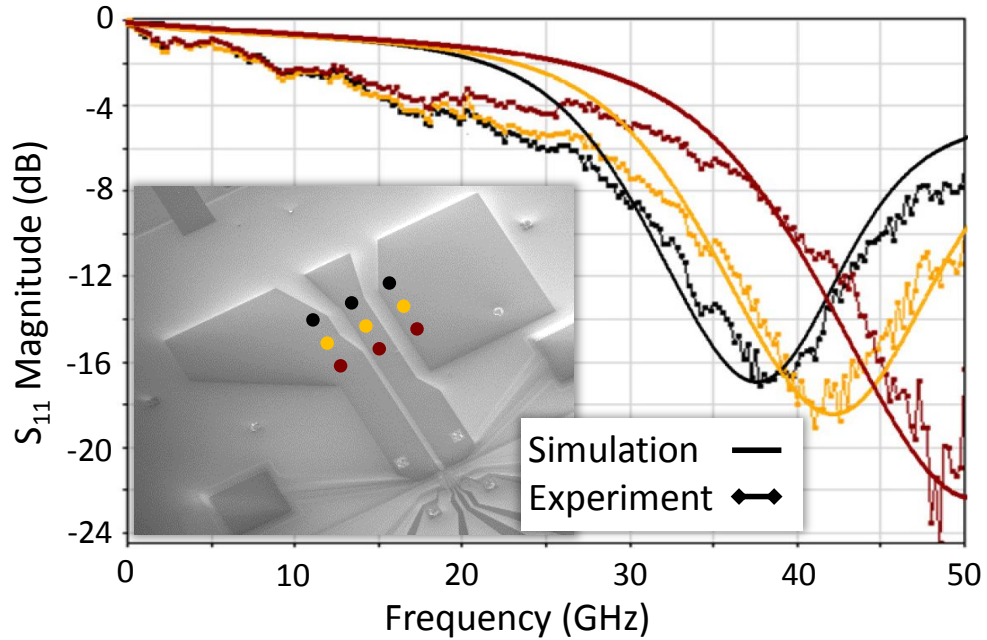


Figure 3.14: S_{11} measurements. Measurements are made at different locations along the on-chip transmission line, with a three-point probe. The locations are highlighted in the inset SEM image of the antenna, and the colors of the dots correspond to the colors in the graph. Simulated (solid lines) and experimental (dots) S_{11} parameters for the on-chip balun.

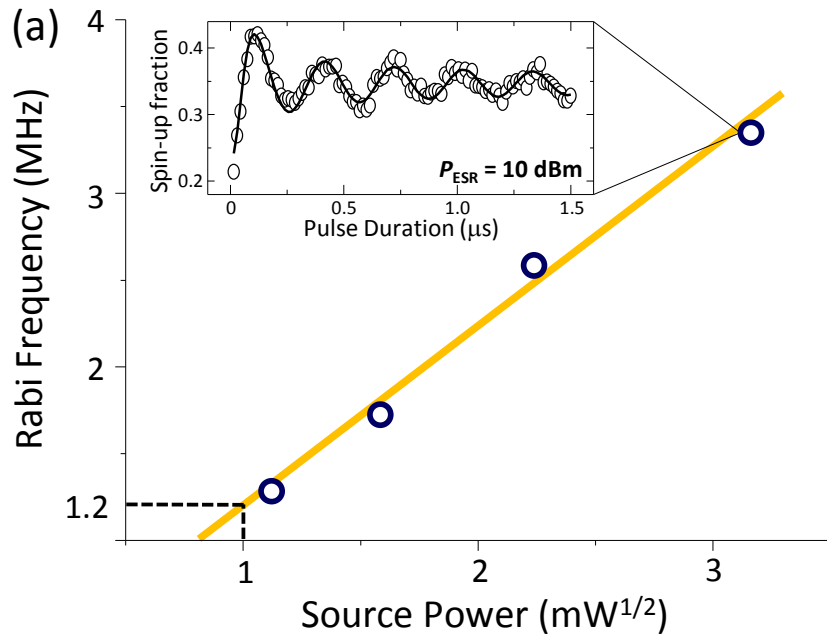


Figure 3.15: Power-dependence of the electron Rabi frequency. Data taken at 30 GHz. B_1 is extracted from the linear fit of the Rabi frequency at $1 \text{ mW}^{1/2}$ highlighted in the figure. Inset shows a sample electron spin Rabi oscillation measured at 10 dBm of power from the microwave source.

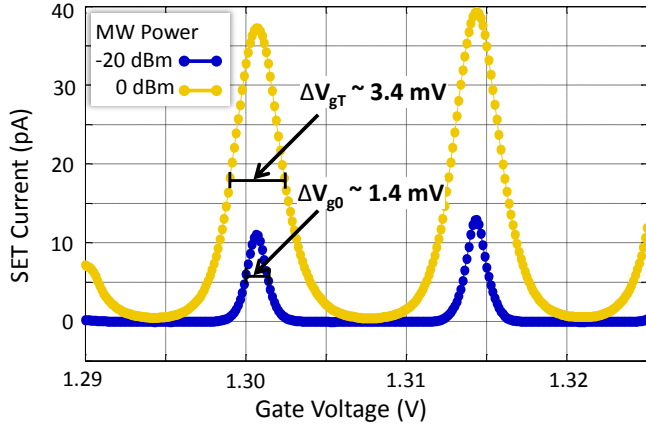


Figure 3.16: SET island coulomb peak broadening with applied signals to the spin resonance antenna. SET current as a function of gate voltage, in the presence of a continuous-wave microwave excitation at 30 GHz. Notice the broadening of the Coulomb peaks at high microwave power. The microwave powers quoted in the figure are the output powers at the source. The power at the chip is approximately 30 dB lower due to loss along the coaxial line. The electric field radiated by the loop is extracted from the width of each of the peaks labeled on the figure.

In these experiments, the loss of the coaxial line connecting the source to the device was ~ 30 dB at 30 GHz, as seen from the S_{21} measurement in Figure 2.3d. Rescaling the simulations results in Figure 3.10 to a power of -30 dBm at the PCB, and accounting for the rotating wave approximation (Section 3.2), our simulations predict 63 μT of B_1 at the donor (Figure 3.6b). We consider this to be a very good agreement between the simulations and the experiment, and highlight the fact that the microwave simulation is quite successful in predicting surface currents and magnetic fields, even in a structure that shrinks to sub-micron dimensions.

3.6.3 Electric field radiated to the spin readout device

The use of an electrostatically-induced SET [53] as the spin readout device allows us to estimate the magnitude of the electric field produced by the planar loop at the location of the SET island [82]. The width of these peaks in units of gate voltage ΔV_g is a function of temperature, source-drain voltage bias and transparency of the potential barriers around the SET island. Because the SET island has a floating potential, an oscillating electric field E_l produced by the loop will contribute an additional Coulomb peak broadening ΔV_{gE} . A simple parallel-plate capacitor model between the gate and the SET island yields the relation $E_l = \Delta V_{gE}/d$, where d is the distance between gate and SET island. In this case, $d \approx 8$ nm represents the thickness of the insulating SiO_2 layer.

A scan of the SET current as a function of the gate voltage shows broadening of the Coulomb peaks when a microwave excitation is applied to the loop (Figure 3.16). The peak broadening ΔV_{gE} can be extracted from Figure 3.16 by writing $\Delta V_{gE} = \sqrt{\Delta V_{gT}^2 - \Delta V_{g0}^2}$, where ΔV_{gT} (ΔV_{g0}) is the width of the Coulomb peak with (without) the microwave excitation. This

3.7. Conclusions

calculation yields $E_l \approx 380$ kV/m from the data in [Figure 3.16](#), taken at 30 GHz and 0 dBm power at the source.

Rescaling the results in [Figure 3.10](#) for a microwave source to device loss of ~ 30 dB (see [Subsection 3.6.2](#)), we obtain a prediction of $E_l \approx 20$ kV/m. This large discrepancy suggests that there could be additional mechanisms causing Coulomb peak broadening when the microwave excitation is applied, and/or that the simulation does not capture all the factors that influence the electric field patterns. For instance, additional thermal broadening of the Coulomb peaks could arise from radiated heat due to the sizeable current flowing through the loop. Additional electric fields could arise from cavity modes excited in the metallic enclosure used in this experimental setup.

3.7 Conclusions

We have presented an extensive study on the integration of microwave transmission lines in nanostructures, for the purpose of optimizing the design of magnetic resonance experiments aimed at single spins.

We have discussed a variety of topologies and explained the pros and cons of each one, supported by microwave simulation techniques that are specifically suited to deal with dimensions shrinking from millimetre to nanometre scale. We have then described a new structure that combines a good control of microwave transmission modes with a maximized value of the magnetic field available to drive coherent control of a spin qubit.

This structure has been employed to achieve coherent control of single-atom spin qubits in silicon. We were able to clearly demonstrate full control of the electron qubit, but the control fidelities and coherence times fall short of the requirement for large-scale quantum computation [10]. The nuclear qubit showed more than adequate measurement and control fidelities, as well as long coherence times, displaying its great potential for use as a quantum memory [18] in quantum computing architectures. The experiments show that the simulation describes accurately the magnetic field produced by the microwave loop, whereas the electric field modeling remains in need of better understanding.

We expect the design guidelines presented in this paper to be useful in assisting and facilitating the intense efforts towards performing new demonstrations of coherent spin control in nanostructures, where high values of oscillating magnetic fields at frequency $\gg 10$ GHz must coexist with charge-sensitive devices.

Chapter 4

Qubits in isotopically purified ^{28}Si

In previous chapters we laid the foundation and demonstrated the successful operation of spin qubits in Si. We now report new benchmarks for coherence times and control fidelities of both electron and nuclear spin qubits in our devices. For the latter we have set new standards for solid-state qubits with $T_2 > 30$ seconds and $F_c > 99.99\%$. We combine our novel experimental setup and device structure with a substrate made from isotopically engineered ^{28}Si . Bulk ensembles of spins in ^{28}Si exhibit exceptionally long coherence, but it has been suspected that this would be disrupted by the noise and disorder in a functional nanostructure. With a detailed noise spectroscopy analysis we show that — contrary to widespread belief — device-intrinsic phenomena, such as charge and spin noise from oxides and interfaces, do not play the limiting role in our devices. Our results open the gates for many exciting future experimental demonstrations such as electron-nuclear entanglement and two-qubit coupling; and reestablish silicon – the most important material in modern information technology – as an ideal platform for the future of quantum information.

A condensed version of this chapter has been submitted for publication in *Nature Nanotechnology*

The author acknowledges J.T. Muhonen and A. Laucht for assistance in measurements and data analysis.

4.1 Introduction

In [Section 1.2](#) we introduced the electron and nuclear spins of P donors in Si for use as qubits, showing how their operational attributes as well as their compatibility with the well established Si industry, make them a prime candidate for large scale quantum computing. In [Section 3.5](#) we presented the operation of the first spin qubits from a single P donor in Si. This was a very encouraging proof of principle result, however, the fidelities obtained for the electron spin qubit was well below the requirement for fault-tolerant large-scale quantum computation [[114](#), [115](#)]. We described in [Subsection 1.5.2](#) how a solid state environment typically causes strong interactions between the qubit and several uncontrolled degrees of freedom, such as the nuclear spins of surrounding atoms [[57](#)], or charge and spin fluctuators in defects, oxides and interfaces [[58](#)]. Nuclear spin fluctuations can be drastically reduced through the isotopic enrichment of ^{28}Si .

4.1.1 From bulk to a gated nanostructure

Experiments on bulk ensembles of P donors in highly enriched ^{28}Si crystals have demonstrated extraordinary coherence times for both electron and nuclear spins (see [Section 1.6](#)). Bulk experiments, however, are not necessarily a good proxy for the performance of individual qubits in functional quantum information processors, where the spins are addressed through gated nanostructures. Spin resonance experiments on donors in enriched ^{28}Si have raised the suspicion that the proximity to a Si/SiO₂ interface deteriorates the spin coherence. Schenkel *et al.* [[74](#)], compared bulk coherence experiments on samples with donors implanted at depths of 150 nm and 50 nm below a Si/SiO₂ interface, finding that their measured T_2 decreased by a factor 5 for the shallower donors. Furthermore, they found that by replacing the Si/SiO₂ interface with hydrogen passivation, the coherence times increased by a factor 2.5. This led them to conclude that the dominant decoherence mechanism for shallow donors near an interface was fluctuating magnetic fields due to spin flips of paramagnetic defects and/or the loading and unloading of charge traps at the interface and in the oxide (see [Subsection 1.5.2](#)). This work has caused a widespread belief that the benefits of a low nuclear spin concentration in the host material will be largely lost when the qubit is integrated in a nanoelectronic device, leading some colleagues to search for alternative solutions such as Si spin qubit systems that are to first order immune to electric or magnetic noise [[116](#)] (but not both simultaneously).

In spite of this, we were not deterred from moving forward with attempting to implement and operate a single atom spin qubit in isotopically purified ^{28}Si . Our main argument is that the experiments performed by Schenkel *et al.* [[74](#)] were performed at relatively high temperatures (5.2 K) and low magnetic fields (~ 0.3 T) compared to our experiments. In our lower temperature (100 mK) and higher field (1.5 T) regime, any paramagnetic center is fully polarized, and its spin fluctuations exponentially suppressed [[58](#)]. Furthermore, although charge fluctuations can still occur, our devices exhibit an order magnitude lower charge trap density [[117](#)], significantly reducing the probability of having charge fluctuators near our donor spins. Finally, a

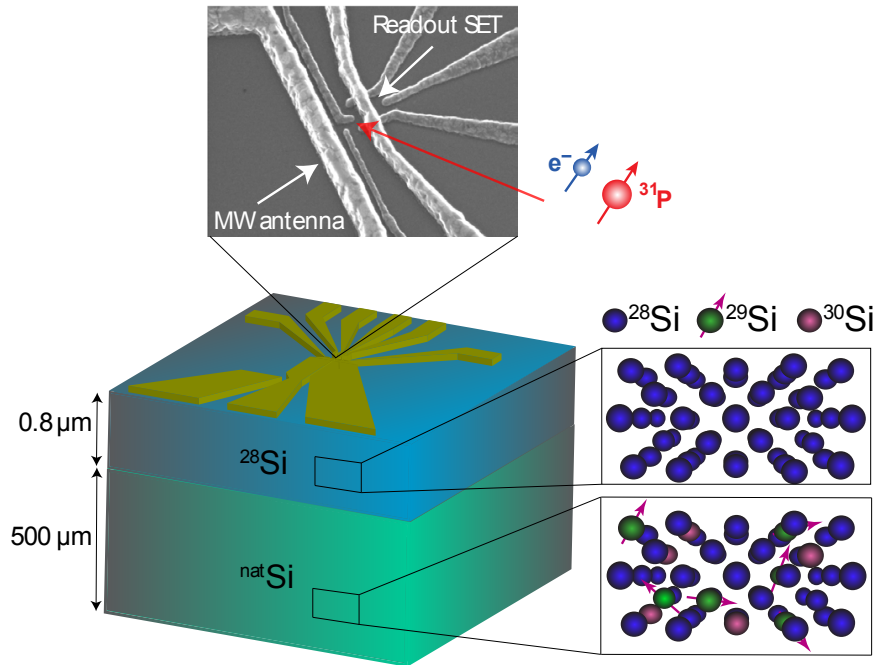


Figure 4.1: Device schematic. Summary of all the main novel features in the devices used in this chapter, including the ^{28}Si epilayer substrate and SEM of gate layout with donor location.

few of our colleagues have spent a significant amount of time attempting to match theoretical models to the results obtained by Schenkel *et al.* [74] without much success; therefore any further experimental insight in this topic would be much appreciated by the community, even if it is a result that shows significant deleterious effects on the qubits.

4.1.2 A new generation

With our motivation intact, we proceeded to implement the next generation of spin qubits. As should be clear from previous chapters, the best experimental conditions for our qubit system are low temperatures, low-noise/high-bandwidth measurements, high magnetic fields (both B_0 and B_1) and a low-noise environment. From the experiments in Section 3.5 we made a few modifications to optimise our qubit operation conditions. The main ingredient for the next generation devices was the substrate, moving from natural silicon to isotopically enriched ^{28}Si with 800 ppm residual ^{29}Si concentration (see Section 2.2). By implementing the low temperature techniques described in Section 2.3, we were able to reduce the electron temperature by a factor ~ 2 . Finally, by modifying the gate layout — such that the donor is placed between the antenna and the SET, instead of on the far side of the SET — and practising better high-frequency TL techniques from the insights acquired from Subsection 3.4.3, we estimate an increase in the B_1 to electric field ratio in from the spin resonance antenna in

our system by a factor ~ 3 .

We have successfully operated both electron and nuclear spin qubits in these devices. In the following sections, we will present all our efforts to perform in depth characterisation of the qubits and their environment. We have measured two devices, A and B, which differ slightly in their gate layout and ion-implantation parameters (see [Section 2.2](#)). All the measurements were performed in high magnetic fields $B_0 = 1.62$ T for Device A and $B_0 = 1.5$ T for Device B. All the details of the experimental techniques necessary to perform the measurements described in this section have been introduced in [Section 2.5](#).

4.2 The electron qubit

4.2.1 ESR spectrum

We initially identify a donor qubit by measuring the electron spin resonance spectrum ([Subsection 1.5.2](#)). Once we have found the correct resonance frequencies, we can attempt to measure the inhomogeneous broadening, from which we can estimate T_2^* , giving us initial insights into the coherence in the system. To obtain the inhomogeneous broadening, the linewidth measurement needs to be performed at low enough power, such that it is not dominated by power broadening (see [Subsection 1.5.2](#)). Additionally, we need to make sure that the excitation profile of our pulse (see [Section 2.5.2](#)) is not broader than the intrinsic linewidth. This can be achieved by making the control pulse longer, but the pulse length is limited by our observed magnet drift ([Subsection 2.4.3](#)) — the linewidth measurement time must be short enough, such that the magnet drift is not comparable to the linewidth. Another well known way to reduce the excitation profile width is to use pulse shaping. [Figure 4.2](#) shows the ESR lines measured at -50 dBm source power — the minimum power at which we could obtain accurate data — with two different pulse shapes. The peak measured with the square pulse (left) is best fit with a Lorentzian function ([Equation 2.9](#)) — which suggests that it is still power broadened [56] — from which we extract $\Delta\nu_s = 3.8 \pm 0.2$ kHz. By using a Gaussian shaped excitation (right) we were able to measure a narrower $\Delta\nu_G = 1.75 \pm 0.06$ kHz, with best fit from a Gaussian function ([Equation 2.8](#)). These ESR line widths and shapes can be corroborated with the T_2^* measurement — which will be shown in the following subsections. Nevertheless, these measurements imply a ~ 4000 fold narrower linewidth compared to the 7.5 MHz obtained in our previous measurements ([Subsection 3.5.1](#)), which already promises great fidelities for our ^{28}Si nanoelectronic device.

The values of $\Delta\nu$ we observed are substantially smaller than those measured in bulk ensembles, even in ultra-pure ^{28}Si sourced from the Avogadro Project [71] which contain < 50 ppm residual ^{29}Si . With 800 ppm residual ^{29}Si in our epilayer, the expected number of ^{29}Si nuclei in the 2.5 nm Bohr radius of the electron wave function is less than 3. This brings us in a very peculiar regime where the ‘spin bath’ is a small and discrete system, and comparisons with ensemble-averaged experiments are not meaningful. In addition, a single-atom experiment is

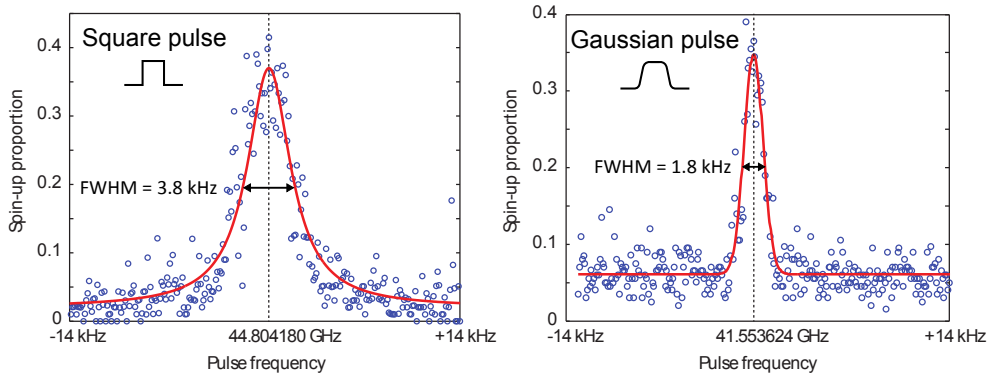


Figure 4.2: Direct measurement of electron spin resonance linewidths. The ESR measurements were performed with -50 dBm of MW source power and 500 μ s pulse width. Device A was measured using square-shaped pulses, while Device B was measured using Gaussian-shaped pulses. Solid lines are a Lorentzian fit (left) and a Gaussian fit (right), with parameters as quoted in the figures.

intrinsically immune from inhomogeneities in the g -factor and the hyperfine coupling.

Another important characteristic we can extract from the ESR spectrum is the hyperfine coupling. The two measured devices had significantly different hyperfine constants ($A \approx 116.6$ MHz for Device A and 96.9 MHz for Device B), probably resulting from a combination of different donor depths, electric fields [60, 61] or strain [118]. We made no attempt to actively tune A , but we note that the observed difference corresponds to $> 10,000$ times the linewidth of the spin resonance transition. Engineering and controlling A over the observed range would therefore allow very precise individual addressing of individual qubits in a large register.

4.2.2 Coherent measurements

The coherent operation of the electron qubit is shown in Figure 4.3a. The Rabi oscillations continue for over 500 μ s before any signs of decay. This is a tremendous improvement over the previous results in ^{nat}Si , where the Rabi oscillations decayed in less than 1 μ s. The Rabi map in Figure 4.3b shows the power dependence of the frequency of the oscillations. We obtain these exquisite Rabi fidelities at relatively low MW source power, therefore we do not have the need to push them further (at the risk of damaging the device). However, if we extrapolate our power dependence of the Rabi frequency to the maximum power used in the previous devices, we obtain a factor ~ 2.5 improvement in gate operation times, highlighting the effects of our gate layout upgrade. The Ramsey experiment (Figure 4.3b) yields a pure electron dephasing time $T_2^* = 250 \pm 110$ μ s (with $n = 1.8 \pm 0.8$) on Device A — a 5,000-fold improvement over the ^{nat}Si value of 55 ns, and comparable to the values obtained with nitrogen-vacancy (NV) electron spins in isotopically purified ^{12}C diamond [119, 120]. The corresponding ESR linewidth is $\Delta\nu = 1/(\pi T_2^*) = 1.3 \pm 0.6$ kHz, which validates our previous linewidth measurement. The $n \approx 2$ decay exponent of the Ramsey oscillations corresponds to a Gaussian lineshape in the frequency domain. This exponent is consistent with a single spin in a dilute spin bath [121],

4.2. The electron qubit

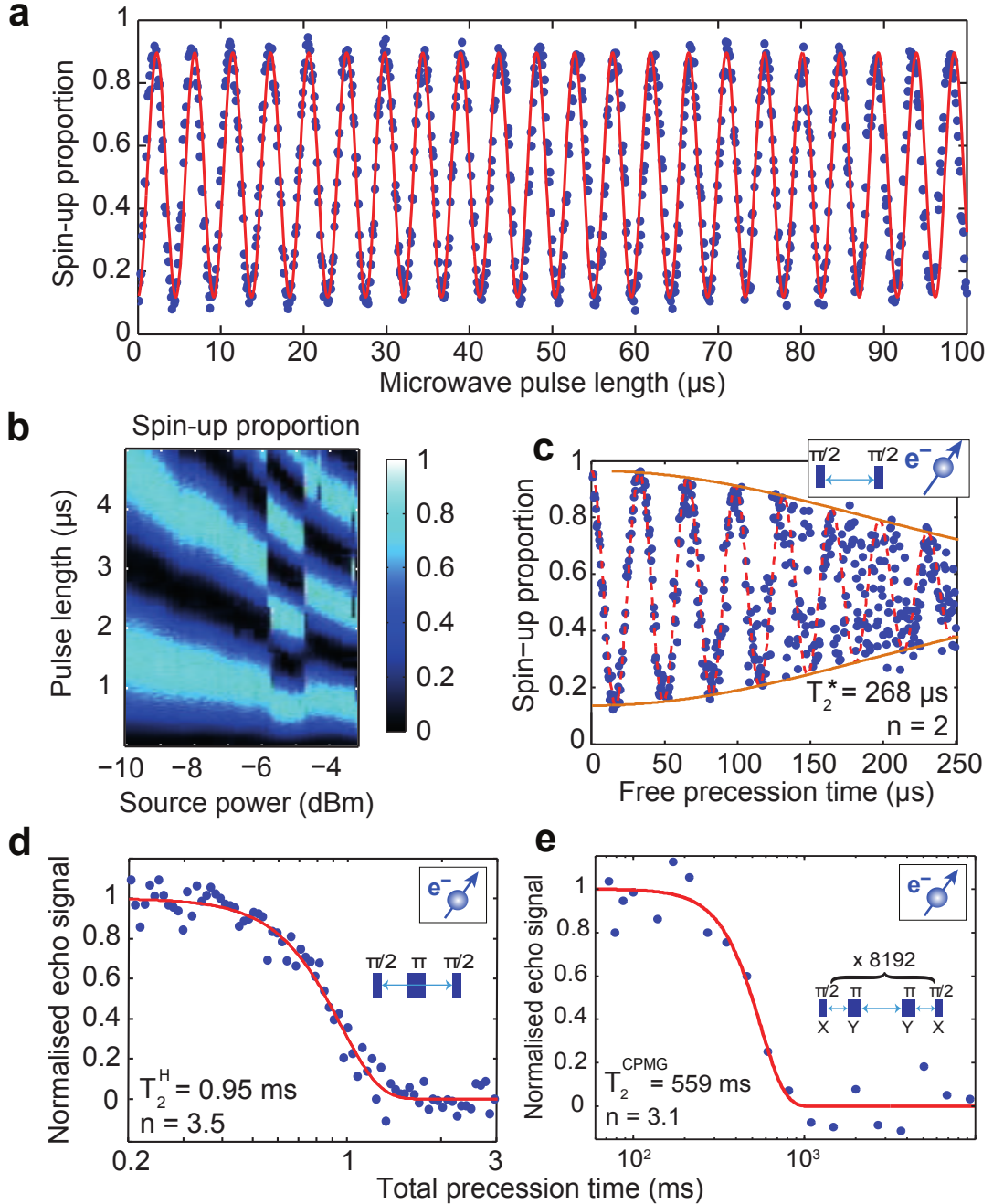


Figure 4.3: Electron qubit coherence. **a** Long-lasting Rabi oscillations of the electron qubit, showing no decay up to $100 \mu\text{s}$. **b** 2D plot of Rabi oscillations at varying microwave powers. The jumps in the plot are caused by flips of the P nucleus between $|\uparrow\rangle$ and $|\downarrow\rangle$. Rabi nutation pulses are applied at both $\nu_{e\uparrow\uparrow}$ and $\nu_{e\downarrow\downarrow}$, but the resulting Rabi period is different in the two cases because of small variations in the frequency response of the microwave antenna and the transmission line. **c** Ramsey fringes. **d** Hahn echo decay. **e** Longest qubit coherence times obtained with CPMG.

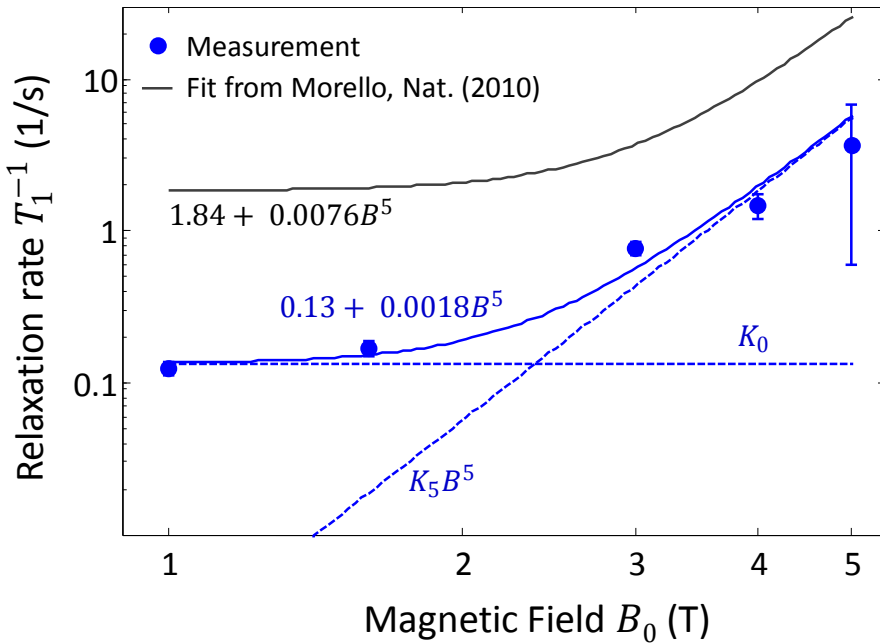


Figure 4.4: Field dependence of the electron lifetimes. Comparison between T_1 measurements on ^{nat}Si vs ^{28}Si devices

however as we will analyse Subsection 4.4.2, we are doubtful that our coherence is currently limited by the spin bath. With a Hahn echo sequence we measured electron coherence times $T_2^H \approx 1$ ms in both devices (Figure 4.3c), only a factor 5 longer than in ^{nat}Si [83]. However, using the CPMG dynamical decoupling technique we extended the electron spin coherence to $T_2^{\text{CPMG}} = 0.56$ s in Device B (Figure 4.3d).

4.2.3 T_1 measurements

As discussed in detail by Morello *et al.* [31] the spin-lattice relaxation for P donors in Si in the low temperature limit follows $T_1^{-1} = (g\mu_B/k_B)K_5B_0^5$, where K depends on characteristics of the host material such as crystal lattice deformation, g -factor anisotropy, valley excited state energies and material density and sound velocities [122]. Additionally, they observed in their experiments that the relaxation rates could become B_0 independent at low fields ($T_1^{-1} = K_0$), which they attributed to spin flip-flops between the donor electron qubit and other nearby donor electrons, through dipolar coupling. Our measured field dependence of the spin-lattice relaxation rates is plotted in Figure 4.4. The results obtained by Morello *et al.* [31] are plotted on the same graph for comparison. We observe a factor 4 decrease in the K_5 term of the relaxation rate fit. As both devices are very similar in terms of interfaces and donor concentration and depth, the difference must be related to the isotopic purification of the host material. An in depth characterisation of the materials is outside the scope of this thesis, however, our results agree qualitatively with bulk measurements performed by Tyryshkin *et al.* [123], where the

observed a factor ~ 2.5 decrease in relaxation rate from natural Si to ^{28}Si . We also observe a field independent term $K_0 = 0.13 \pm 0.07 \text{ s}^{-1}$. This term — being a function of the relative location of donors nearest to our qubit — is sample dependent due to the probabilistic nature of our implantation process, therefore no comparison can be made with previous results. It is however, the limiting factor of our maximum measured $T_1(1 \text{ T}) = 8.0 \pm 0.9 \text{ s}$.

4.2.4 Fidelities

The electron qubit measurement and initialisation fidelities F_m and F_i were extracted from the Rabi oscillation shown in Figure 4.5a, using the method described in Section 2.5.2. F_m is limited by the interplay of measurement bandwidth and electron tunnel times, and by the occurrence of false spin-up counts due to thermal effects. With our reduced electron temperature we have achieved a fidelities $F_m, F_i \approx 97\%$. While performing the lower field T_1 measurements, we observed no noticeable decrease in Rabi contrast at $B_0 = 1 \text{ T}$. This confirms our low electron temperatures, but suggests that the limiting factor to our Rabi contrast is not thermal. We plan to perform a systematic analysis of this issue in the near future.

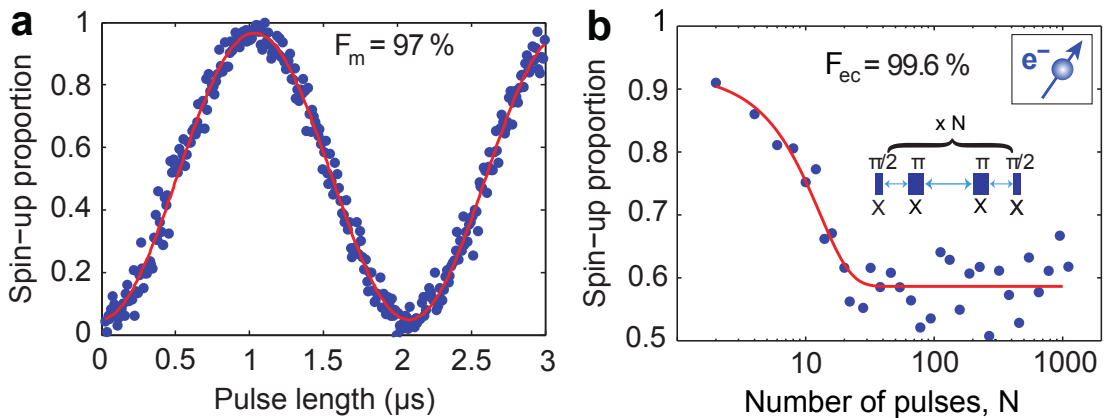


Figure 4.5: **Electron fidelity measurements.** **a** High contrast Rabi oscillation used to extract the measurement fidelity. **b** CP decay used to extract the effective control fidelity.

In the $^{\text{nat}}\text{Si}$ device presented in the previous chapter, the control fidelity was limited by the intrinsic spectral diffusion caused by the surrounding ^{29}Si nuclei. In our isotopically purified substrate the ESR linewidth is two orders of magnitude smaller than the excitation pulse spectrum, which yields $F_c > 99.9999\%$. Therefore, the observed control errors arise solely from variation in pulse parameters due to technical limitations of the room-temperature electronic set-up. The latter can be estimated by comparing the coherence decay obtained from CPMG and CP, as explained in detail in Section 2.5.2. With this method (CP data shown in Figure 4.5b) we obtained $F_{ec} = 99.6 \pm 0.3\%$.

In spite of the nanoelectronic device skepticism, we have achieved electron qubit fidelities which are now approaching the limits needed for fault tolerant large scale quantum computation. Furthermore, we highlight that the limiting factor is not currently fundamental but

instrumental, which means these fidelities can be easily be pushed further with equipment upgrades.

4.3 Nuclear qubit

4.3.1 Measurement fidelity and lifetimes

As seen from the previous device results presented in [Subsection 3.5.2](#), the nuclear qubit F_m (see [Section 2.5.2](#)) is very close to unity and depends mainly on the $T_{1\downarrow}$ lifetime. With our much improved electron fidelity, we can perform high-fidelity readout of the nuclear qubit (see inset [Figure 4.6](#)) with 50 single-shot readouts of the electron state, which is a factor 5 less than in the ^{29}Si devices. In these particular devices, longer electron tunnel rates (sample dependent from the probabilistic implantation) means our total readout time is still $t_m = 250$ ms. From [Figure 4.6](#) we extract nuclear lifetimes $T_{1\downarrow} = 2900 \pm 1100$ s from which we extract a measurement fidelity $F_m = 99.991 \pm 0.005\%$. The longer lived $|\uparrow\rangle$ exhibited quantum jumps at a rate $T_{1\uparrow} = 7900 \pm 2900$ s.

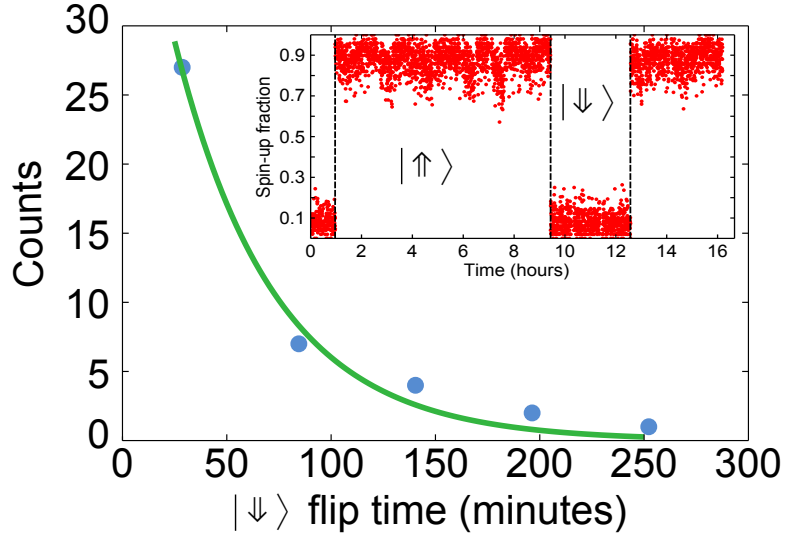


Figure 4.6: Nuclear readout and lifetimes. Histogram of nuclear flip times from the $|\downarrow\rangle$ state. From the exponential fit we extract the lifetime quoted in the main text. The inset shows sample nuclear readout data taken over 16 hours, showing a few nuclear quantum jumps. With 50 electron reads per point, the visibility is close to unity.

4.3.2 Coherent measurements and control fidelity

Coherent operation of the nuclear qubit in both the neutral (D^0) and ionised (D^+) states is demonstrated through the Rabi oscillations, Ramsey fringes and Hahn echo measurements shown in [Figure 4.7](#). The Rabi oscillations are similarly impressive as in the previous measurements in ^{29}Si , we just highlight that the range of the oscillations for the D^0 are improved to

4.3. Nuclear qubit

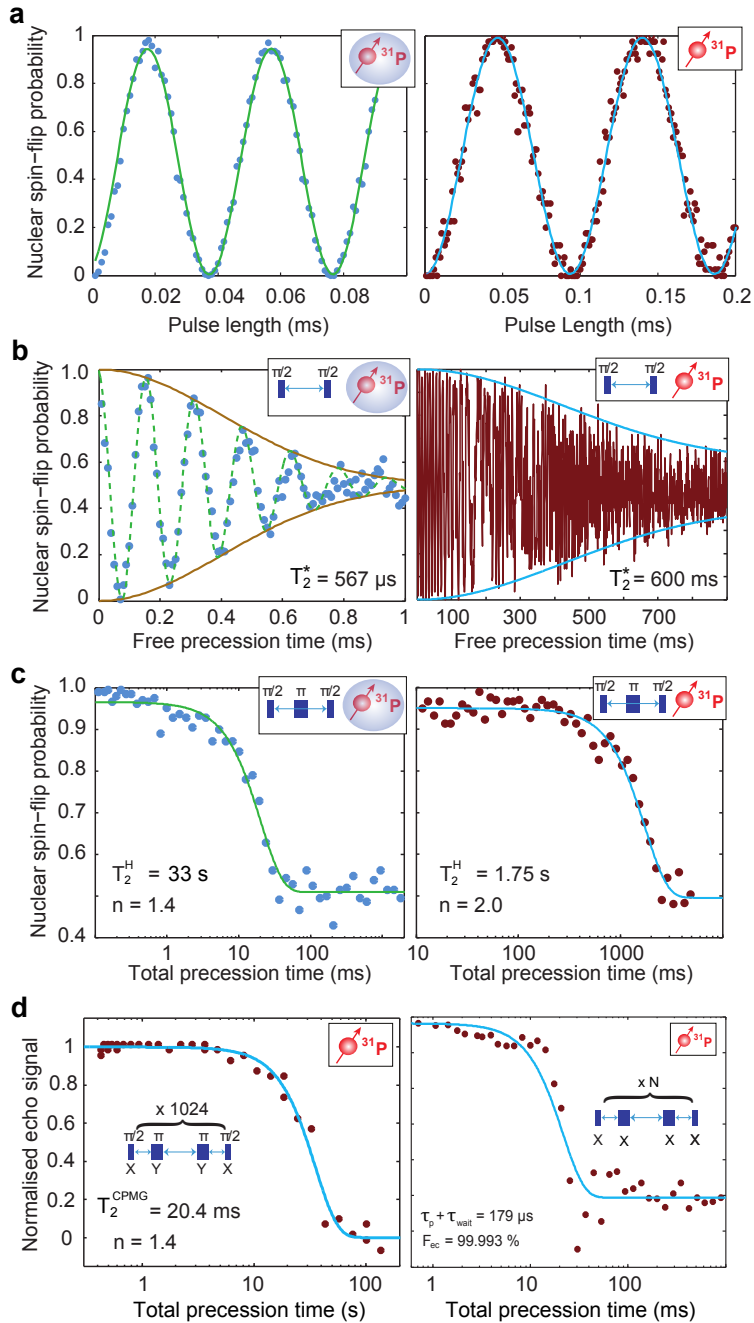


Figure 4.7: Nuclear control and coherence times. a-c. Rabi oscillations, Ramsey fringes and Hahn echo decay (respectively) for the D^0 (left) and D^+ (right) nuclear qubit. d. Dynamical decoupling measurements on the D^+ nucleus: record coherence for a qubit in solid state (left) and CP decay used to extract the control fidelity (right).

near perfect, as a consequence of our improved electron initialisation fidelity. The D^0 qubit shows a similar dephasing time to the electron qubit, $T_2^*(D^0) \approx 500 \mu\text{s}$. The Hahn echo decay was found to be very different between devices A and B, with values $1.5 \pm 0.5 \text{ ms}$ and $19 \pm 2 \text{ ms}$, respectively. As observed in our previous measurements as well as in bulk experiments [70], the nuclear spin coherence improves dramatically by removing the electron from the P atom. The D^+ Ramsey decay times reached the value $T_2^*(D^+) \approx 0.6 \text{ s}$, which would correspond to an NMR linewidth $\Delta\nu \approx 0.5 \text{ Hz}$ (which we did not attempt to measure directly). The simple Hahn echo sequence preserves the qubit coherence beyond 1 second, $T_2^H(D^+) = 1.8 \pm 0.2 \text{ s}$. The highlight of these measurements was an extended coherence with CPMG dynamical decoupling beyond 30 s, $T_2^{\text{CPMG}}(D^+) = 33 \pm 3 \text{ s}$. This currently represents the record coherence for any *single* qubit in solid state. By comparing a CPMG measurement with the CP measurement shown in Figure 4.7e, we extract $F_{ec}(D^0) > 99.9\%$ and $F_{ec}(D^+) > 99.99\%$.

4.3.3 Nuclear initialisation using real-time feedback

In Subsection 2.4.2 we described an instrument setup that allows us to acquire and analyse data in real-time (i.e. the result of a single-shot electron or nuclear readout is available before the start of the next measurement sequence). This feature allows us to perform feedback, adjusting our next measurement based on the previous measurement result. To demonstrate this principle, we used feedback to initialise the nucleus, in order to perform coherent measurements on the $\nu_{N\uparrow}$ transition of nuclear qubit. Our spin to charge conversion mechanism (see Subsection 1.2.3) allows us to initialise the electron spin state exclusively $|\downarrow\rangle$. In order to perform an NMR measurement on the $\nu_{N\uparrow}$ transition, we need to flip the electron spin before the start of the nuclear control sequence. If the nuclear state is unknown at the end of a sequence, we do not know which ESR transition to use to flip the electron at the beginning of the next one, therefore after every sequence we initialise the nucleus by analysing the single-shot readout acquisition and applying a nuclear π pulse conditional on the result of the readout. A diagram of the feedback procedure and pulse sequences is shown on Figure 4.8, along with a sample Hahn

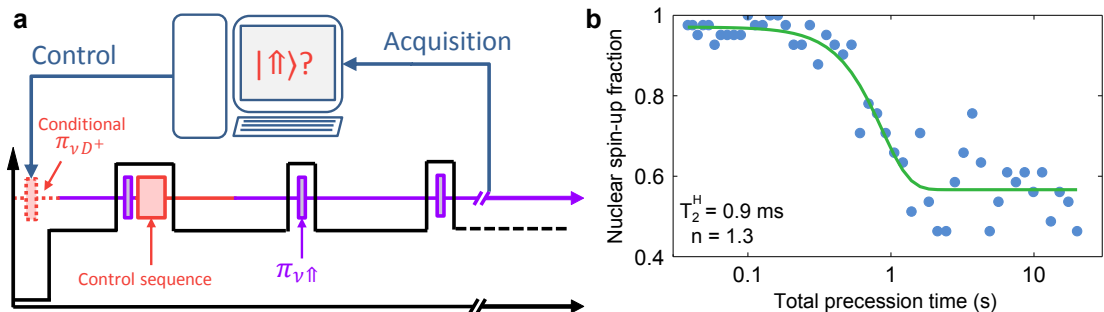


Figure 4.8: Nuclear initialisation with feedback. **a** Schematic of feedback process used to initialise the nucleus at the start of each control sequence. A nuclear π pulse is applied only if the the result of the readout of the previous sequence is $|\downarrow\rangle$. **b** Hahn echo measurement performed for on the neutral nucleus using $\nu_{N\uparrow}$. Measurement performed on Device A.

echo measurement performed on the $\nu_{N\uparrow}$ transition. We note that the nuclear spin can also be initialised without the use of feedback, by applying the sequence $\pi_{\nu_{e\downarrow}} - \pi_{\nu_{N\uparrow}}$ [124].

4.3.4 High-precision spectrum characterisation

In Section 2.5.1 we explained that oscillations in a Ramsey fringe experiment arise from the detuning between the frequency of B_1 and the qubit resonance. Therefore, this measurement can be used to calibrate the resonance frequency, with precision limited by $1/T_2^*$. In our long lived system we can obtain precisions of $\sim \pm 15$ kHz for ν_{ESR} and $\sim \pm 1$ kHz for ν_{NMR} . In this section we will use these calibration capabilities to extract some important parameters of our system's spectrum.

The exact ESR and NMR frequencies, obtained without adopting the high-field approximation, are:

$$\begin{aligned}\nu_{e\uparrow} &= \frac{B_0\gamma_- + \sqrt{(B_0\gamma_+)^2 + A^2} + A/2}{2} \\ \nu_{e\downarrow} &= \frac{B_0\gamma_- + \sqrt{(B_0\gamma_+)^2 + A^2} - A/2}{2} \\ \nu_{N\uparrow} &= \frac{B_0\gamma_- - \sqrt{(B_0\gamma_+)^2 + A^2} + A/2}{2} \\ \nu_{N\downarrow} &= \frac{-B_0\gamma_- + \sqrt{(B_0\gamma_+)^2 + A^2} + A/2}{2}\end{aligned}$$

The simplest parameter to extract is the hyperfine $A = \nu_{N\uparrow} + \nu_{N\downarrow}$. It can be extracted by subtracting the ESR frequencies as well, but the NMR Ramsey measurement gives higher precision.

By solving the following system of equations we can extract γ_e and γ_N :

$$\begin{aligned}\nu_{e\uparrow} + \nu_{e\downarrow} &= B_0(\gamma_e - \gamma_N) + \sqrt{(B_0(\gamma_e + \gamma_N))^2 + A^2} \\ \nu_{N\uparrow} - \nu_{N\downarrow} &= -B_0(\gamma_e - \gamma_N) + \sqrt{(B_0(\gamma_e + \gamma_N))^2 + A^2}\end{aligned}$$

Unfortunately, we do not have an external means to accurately calibrate B_0 , making its precise value unknown. However, measurements of γ_N have been performed previously in bulk P-Si systems [19, 77]. Moreover, due to the insensibility of the P nucleus to its environment, we can assume that the value of γ_N is an intrinsic property of the P:Si system, although it may depend on the charge state of the donor. This allows us to make a precise calculation of the electron g -factor $g = \gamma_e/\mu_B$ and B_0 .

Another important parameter we can extract is the nuclear chemical shift δ_N , defined as the proportion in change of γ_N between D^0 and D^+ ($\delta_N = (\gamma_N^+ - \gamma_N)/\gamma_N$). We can do this by performing the Ramsey fringe measurement on the bare nucleus to obtain the single-spin transition frequency $\nu_N^+ = \gamma_N^+ B_0$, and extract γ_N^+ using B_0 obtained from above.

We performed a set of measurements to obtain all the relevant transition frequencies, being

careful to complete the whole set of measurements in a timescale short enough such that our magnet decay (see [Subsection 2.4.3](#)) did not affect the results. We only performed these measurements on Device A. Using the known value of $\gamma_N = 17.2323(9)$ MHz/T [\[19\]](#), we compiled the following table, including comparisons to previous measurements:

Parameter	Extracted Value	Previous Measurements
A	116.6246(14) MHz	Bulk (1959): 117.52 MHz [76] Bulk (2011): 117.5239359(10) MHz [19] Single-spin: 114.30(1) MHz [83] Device B: ~ 96.9 MHz
g -factor	1.9985946(2)	Bulk: 1.99875(10) [76] Single-spin: 1.9987(6) [83]
γ_N^+	17.2327(15) MHz/T	Bulk: 17.228(2) [77]
δ_N	20(100) ppm	Bulk: 710(10) [77]

4.4 In search of the sources of decoherence

We have been successful in demonstrating an immense improvement in coherence times, however we are still well short of the values measured in bulk experiments [\[70–72\]](#), which means that there is some residual source of decoherence in our devices that does not appear in bulk experiments. We now present some experiments designed with the aim of narrowing down the possible sources of decoherence in our system.

4.4.1 B_1 source *on-off* ratio

From discussion with colleagues in the trapped-ions community, it was suggested that in systems with such high ratio of coherence to gate time as ours, one of the limiting factors for coherence times could be driven spin rotations during the free-precession period of a refocusing sequence, due to the *on-off* ratio of the source of oscillating magnetic field. The pulse modulation (PM) input of the signal generator acts as a switch that turns the output *on* or *off* when the PM signal is above or below a threshold respectively. In practice, it does not completely shut off the output, but it applies a very large attenuation. This attenuated signal could still be large enough to cause significant spin rotations over long time periods.

Our signal generators specify a minimum PM *on-off* ratio of 80 dB. When we perform electron coherence time measurements, we operate at source powers (P_s) that produce a Rabi frequency $f_{\text{Rabi}} \approx 500$ kHz. The Rabi frequency follows the relation $f_{\text{Rabi}} \propto \sqrt{P_s}$, therefore with 80 dB less power the spin will rotate at $f_{\text{Rabi}}(-80 \text{ dB}) \approx 50$ Hz. This is equivalent to a $\pi/2$ length of ~ 5 ms, which is very comparable to our electron $T_2^H \approx 1$ ms.

To test this issue experimentally, we applied the sequence $\pi_x - \tau_w$, measuring the electron spin after the wait time τ_w , which we increased after every measurement. As seen from [Figure 4.9](#), we observe no appreciable change in the measured P_\uparrow up to $\tau_w = 500$ ms, which suggests

that the practical *on-off* ratio from our generator is much lower than the 80 dB minimum in the specifications.

We performed a similar experiment on the nuclear qubit, by just waiting in the PM *off* state and measuring P_f , and again found $P_f \approx 0$ up to $\tau_w = 30$ s.

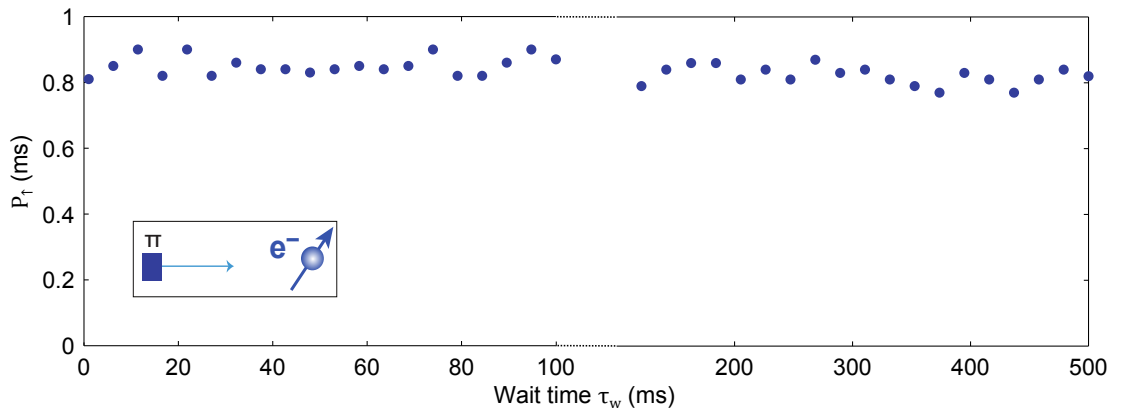


Figure 4.9: Effects of the signal generator on-off ratio. Measurement of the electron spin state after preparing it $|\uparrow\rangle$ and observing its evolution. The MW signal generator is kept on, but the output is suppressed by keeping the PM input low.

4.4.2 Noise spectroscopy using DD

We can obtain invaluable insight into the investigation of the microscopic origin of spin decoherence in our nanoelectronic device, through an analysis of the spectral properties of the noise power $S(\omega)$ that modulates the transition energies in our qubits.

Theory and method

Dynamical decoupling is a well known method in the spin resonance community to cancel out low frequency noise. By applying π -pulses with regular intervals (τ) one effectively averages out noise at frequencies much lower than $1/2\tau$. For random noise with a mean of zero, noise at much higher frequencies also averages to zero. As a result, it can be very useful to think about dynamical decoupling (DD) pulsing schemes as band-pass spectral filters for the noise [125–128], with passband frequency centred at $\omega_p = \pi/\tau$. Therefore, by choosing different τ we shift the center frequency of the filter, i.e. which portion of the noise spectrum couples the qubit. The benefits of dynamical decoupling are easily understood by considering a colored noise, e.g $S(\omega) \propto 1/\omega$. Adding more π -pulses, thus reducing τ , shifts ω_p to higher frequency where the noise is weaker. For the same reason, dynamical decoupling is ineffective in the presence of frequency-independent (white) noise.

To understand how DD acts as a bandpass filter, start by considering pure dephasing noise

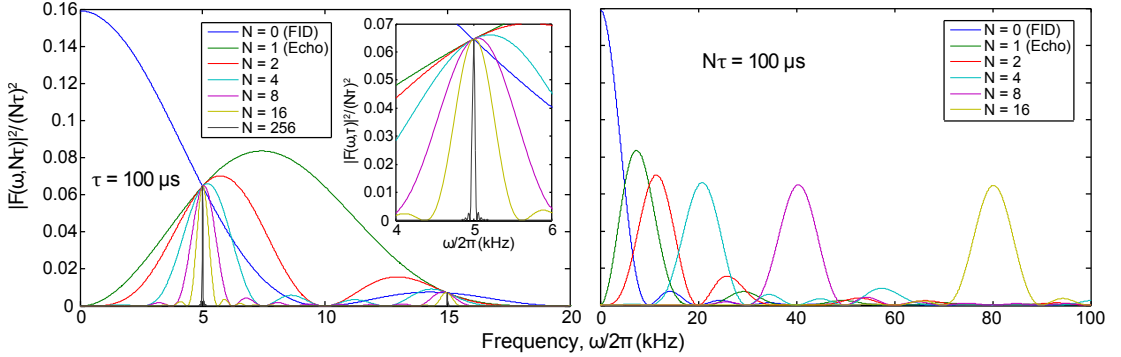


Figure 4.10: The filter function. Noise filter function of the CPMG sequence, plotted with fixed interval between the pulses (left) and with fixed total evolution time (right). The left plot is normalized with $(N\tau)^2$, as the height of the peak grows with the square of the total evolution time. (The width of the peak scales roughly as $(N\tau)^{-1}$.) In the right plot no normalization is needed as the area under the curve stays constant.

with a Hamiltonian:

$$\mathcal{H} = \frac{\hbar}{2} (\Omega + \beta(t)) \sigma_z$$

Where Ω is the Larmor frequency ($\hbar\Omega$ is the energy splitting of the qubit states) and $\beta(t)$ is time-dependent noise (in angular frequency units). It can be shown [128–130] that the echo decay is of the form:

$$P(N\tau) \propto \exp \left(- \int_0^\infty S(\omega) |F(\omega, N\tau)|^2 d\omega \right) \quad (4.1)$$

With:

$$S(\omega) = \int_{-\infty}^\infty \exp(-i\omega t) \langle \beta(t) \beta(0) \rangle dt$$

The total evolution time is $N\tau$ where N is the number of pulses (the pulses are assumed to be instantaneous). We define $S(\omega)$ as the noise power in the energy splitting of the qubit states (in angular frequency units), as opposed to making assumption on its physical nature (magnetic, electric, etc.) and adding a coupling constant in Equation 4.1. $|F(\omega, N\tau)|^2$ is a pulse sequence dependent function known as the *filter function*, since it determines which parts of the noise spectra contribute to the decoherence process. It has an analytical expression for the case of π -pulses applied at regular intervals [126]:

$$|F(\omega, N\tau)|^2 = \frac{8}{\pi} \frac{1}{\omega^2} \frac{\sin^4(\omega\tau/4) \sin^2(\omega N\tau/2)}{\cos^2(\omega\tau/2)}.$$

This function has the shape of a bandpass filter whose passband characteristics are dependent on N and τ . We illustrate this in Figure 4.10, by plotting the function with a constant interval between the pulses (left) and with a constant total evolution time (right). The left

figures shows how in the high N limit, the filter function becomes a series of narrow peaks, thus is can be used to sample the noise amplitude at a set of single particular frequencies. The right figure shows how — if τ is varied — the frequency of the passband shifts, which allows us to sample difference frequencies in the spectrum. Notably, if one keeps the total free evolution time of the qubit constant, the integral over the filter function (“the bandwidth”) is the same for all regular interval π -pulsing schemes. Hence, if the dephasing noise has a fully flat (white) spectral density, the refocusing pulses will make no difference to the decoherence time, whereas for strongly frequency dependent noise DD can be very effective. It is interesting to point out that these noise spectrum expressions imply that the exponent n of the measured echo decay will also depend on the shape of the dephasing noise within the passband of the filter, giving exponential decay ($n = 1$) for white noise, gaussian decay ($n = 2$) for $1/\omega$ noise and so on, i.e., $S(\omega) \propto \omega^{-(n-1)}$. In a Hahn echo measurement, different passbands of the filter are probed as τ is increased, therefore the decay may be composed of different exponential slopes,

It was recently pointed out [129, 130] that in the limit where N is large, the echo decay has a simple analytic form:

$$P(N\tau) \propto \exp \left(-N\tau \frac{4}{\pi^2} \sum_{k=0}^{\infty} \frac{1}{(2k+1)^2} S(\omega_k) \right) \quad (4.2)$$

Where $\omega_k = (2k+1)\pi/\tau$. Hence, as proposed by Alvarez and Suter [130] measuring the decay time T_2^S at multiples of some minimum frequency ω_0 allows one to map out the noise spectral density including the higher harmonics of the filter function. Note that taking only the first term ($k = 0$) of Equation 4.2 leads to the simple delta filter form:

$$P(N\tau) \propto \exp \left(-N\tau \frac{4}{\pi^2} S(\pi/\tau) \right) \quad (4.3)$$

In the case of frequency independent noise (S constant) Equation 4.2 reduces to (use $\sum_{k=0}^{\infty} 1/(2k+1)^2 = \pi^2/8$):

$$P(N\tau) \propto \exp \left(-\frac{N\tau S}{2} \right) \quad (4.4)$$

The experimental method for extracting the normalised noise spectral density is as follows:

1. Choose a range of spectrum to measure ω_0 to ω_{max} , with $\omega_{max} = (2k_{max} + 1)\omega_0$. The lower bound must satisfy $\omega_0 > \pi/T_2^H$, in order to meet the high N limit condition.
2. For all values of ω_k in the range, perform an equal pulse interval dynamical decoupling sequence (e.g. CPMG) in the fixed τ variable N mode (see Section 2.5.1), with $\tau = \pi/(2k+1)\omega_0$. Extract the echo decay time $T_{2(k)}^S$.
3. Starting from $k = k_{max}$ and stepping back to $k = k_0$, compute all the power spectral density terms using:

$$S(\omega_{max}) = \frac{\pi^2}{4T_{2(max)}}$$

For $k \neq k_{max}$:

$$S(\omega_k) = \frac{\pi^2}{4T_{2(k)}} - \sum_{i=1}^{k_{max}-k} \frac{1}{(2k+1)^2} S(\omega_{i+k})$$

Results

In Figure 4.11 we show $S(\omega)$ extracted using the method described above, performed on the electron qubit. At frequencies $\omega/2\pi > 3$ kHz the noise spectrum appears flat, $S(\omega) \approx 10$ (rad/s)²/Hz in Device A, corresponding to $T_2^S \approx 0.2$ s (from Equation 4.4). Assuming that the noise is of magnetic origin, this corresponds to a longitudinal magnetic field noise $b_n = \hbar\sqrt{S(\omega)/(g\mu_B)} = 18$ pT/ $\sqrt{\text{Hz}}$. It is interesting to notice that substituting the simple band-pass formula here (Equation 4.3), we would recover the equation for sensitivity obtained by viewing the electron qubit as an a.c. magnetic field sensor $\eta_{a.c.} = \pi\hbar/(2g\mu_B\sqrt{T_2})$ [131].

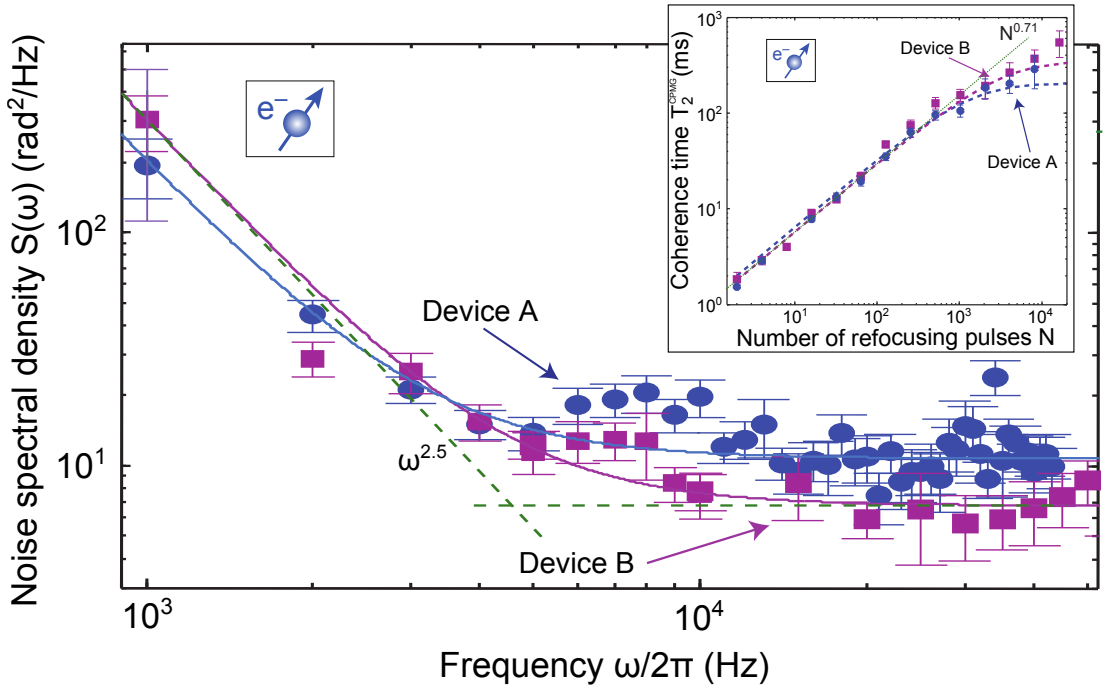


Figure 4.11: Measured noise spectra in our devices. Noise power spectral densities for Device A (dots), and Device B (squares). Solid lines are fits of the form $C_2/\omega^{2.5} + C_0$, with the following parameters: $C_2 = 6 \times 10^{11}$, $C_0 = 10$ for Device A; $C_2 = 9 \times 10^{11}$, $C_0 = 6$ for Device B. The dashed lines show the two terms separately for Device B. Inset shows electron coherence times T_{2e}^{CPMG} from CPMG pulse sequences as a function of the number N of refocusing pulses. Lines are theoretical predictions assuming the noise spectral density from the fits in b. The excellent agreement between the calculated lines and the data at low N proves that the $S(\omega) \propto \omega^{-2.5}$ dependence continues well below the 1 kHz measured in b. With $S(\omega) \propto \omega^{-\alpha}$, the coherence time should be proportional to $N^{\alpha/(\alpha+1)}$ [132], yielding $N^{0.71}$ for $\alpha = 2.5$, which is shown in the figure as a guide to the eye.

Working from the premise that this white noise may come from broadband radiation of the spin resonance antenna, we performed extensive modeling of the magnetic and electric fields radiated by the antenna, using the techniques described in detail in [Section 3.2](#). The MW antenna is designed to minimise electric fields at the qubit location (see [Section 1.2.6](#)). In practice, imperfections in the propagation along the antenna result in nonzero electric fields at its termination (see [Section 3.4](#)). The electric field couples to the qubit energy levels by Stark-shifting the hyperfine constant A [59–61] and/or the g -factor of the electron spin [62]. Additionally, the antenna should ideally produce purely transverse oscillating magnetic field $B_1 \perp z$, as any longitudinal (i.e. $\parallel B_0$) component of the magnetic field will directly modulate the qubit Larmor frequency and cause decoherence. However, as shown in [Figure 4.12a](#) our device geometry does allow for some nonzero longitudinal field component. [Figure 4.12b](#) presents simulation results for our device model, showing the absolute electric field and the longitudinal component of magnetic field, for the frequency range at which we performed the noise spectroscopy.

The measurement results on Device A show a noise floor of $S(\omega) \approx 10 \text{ rad}^2/\text{s}$, which converted to amplitude spectral density and to magnetic field gives $b_n = \hbar\sqrt{S(\omega)}/(g\mu_B) = 18 \text{ pT}/\sqrt{\text{Hz}}$ for $g = 2$. The finite-elements modeling shows that, at $\sim \text{kHz}$ frequencies, 1 mW of power result in a longitudinal magnetic field component $B_z \approx 1 \text{ mT}$. Since the magnetic field is proportional to the square root of the power, we deduce that the equivalent noise power P_n at the MW antenna input which produces $b_n = 18 \text{ pT}/\sqrt{\text{Hz}}$ is:

$$P_n = \left(\frac{b_n}{1 \text{ mT}} \right)^2 \times 1 \text{ mW} = 3.2 \times 10^{-19} \text{ W} = -155 \text{ dBm} \quad (4.5)$$

During the measurement of Device A we had a total of 6 dB attenuation along the signal line (the losses of the coaxial cable are negligible at kHz frequencies), thus -155 dBm at the chip corresponds to $P_n^s = -149 \text{ dBm}$ noise power at the source. The power radiated down by the attenuators themselves would give maximum 2% correction to this value as they are thermalised to the pot (1.5 K) and mixing chamber (0.02 K). If we assume that the noise power is Johnson-Nyquist noise produced by a resistor R at $T = 300 \text{ K}$, $P_n^s = 4k_B T R$ per unit of frequency, we find:

$$R = \frac{10^{-14.9} \times 10^{-3}}{4k_B T} = 76 \Omega.$$

This value is remarkably close to the 50Ω impedance presented by the output of the microwave source, especially considering that the exact conversion between P_n and b_n involves the large uncertainty of the donor location.

Having identified the source of broadband noise that limits the ultimate qubit coherence, we added a further 7 dB attenuation at the 1.5 K stage of our dilution refrigerator before measuring Device B. This has the effect of reducing the amount of room-temperature thermal radiation that reaches the qubit. As expected, Device B exhibits a reduced white-noise floor,

4.4. In search of the sources of decoherence

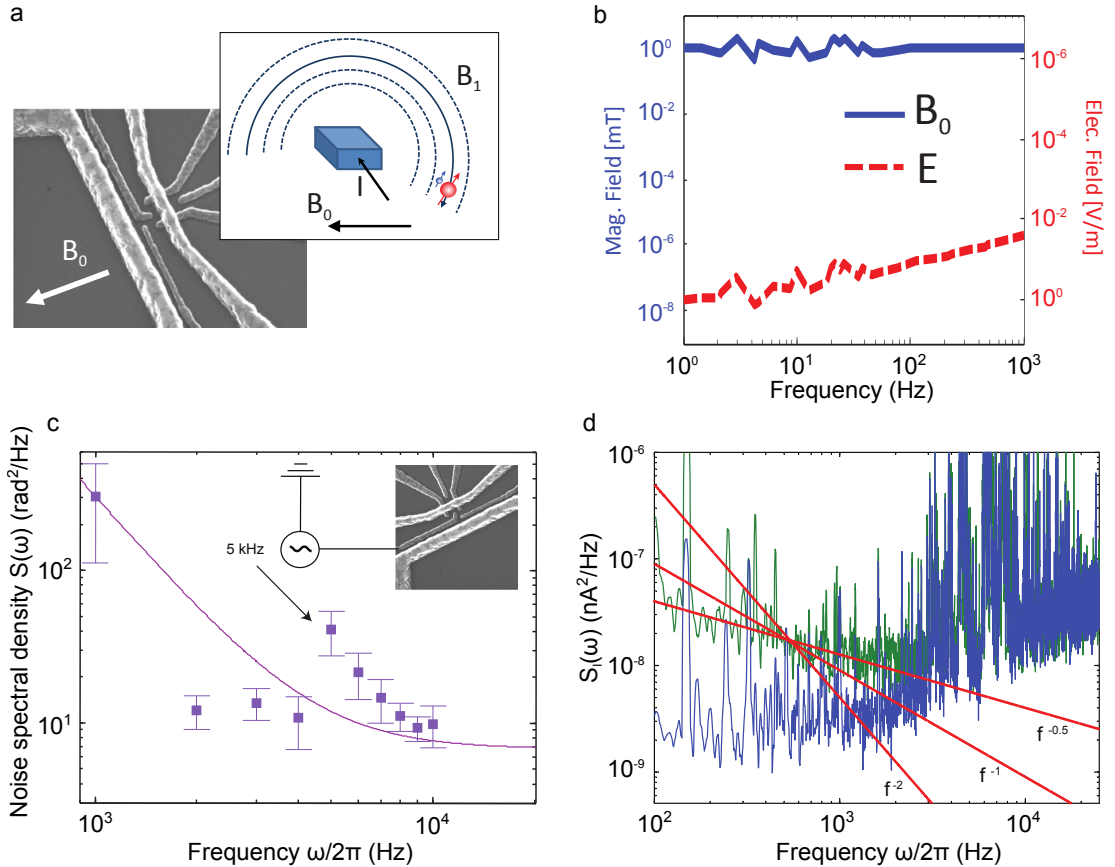


Figure 4.12: Noise spectrum analysis. **a** Schematic of B_1 field generated from antenna, showing that there is a longitudinal component of the oscillating field which is parallel to B_0 . **b** Simulation results for the longitudinal magnetic field component (B_0) and electric field (E), at low frequencies. **c** Noise spectroscopy measurement while applying a 5 kHz voltage signal to the gate shown in the SEM image. The noise signal was a sine-wave with 100 μ V amplitude (200 μ V_{p-p}). A clear peak appeared in the noise spectra at 5 kHz. Solid line is the same as plotted in Figure 4.11. **d** Power spectral density of current traces taken while the SET was tuned to be either maximally sensitive to charge fluctuations (green) or minimally sensitive (blue). The data has been numerically smoothed. The difference at low frequencies is from the charge noise in our device and follows $1/\omega^\alpha$ dependency, with $\alpha \approx 0.5$. Lines are guides to the eye. At higher frequencies (above ~ 2 kHz) the noise is dominated by the room-temperature transimpedance amplifier and the two curves coincide.

$S(\omega) \approx 6 \text{ (rad/s)}^2/\text{Hz}$ and $b_n = 14 \text{ pT}/\sqrt{\text{Hz}}$ (see [Figure 4.11](#)). However, the white-noise floor reduction does not correspond with the numerical amount expected on the basis of the additional attenuation. This could be due to a different donor location in Device B, such that the B_z component is larger than for Device A.

Both devices exhibit a colored noise spectrum below 3 kHz, approximately $S(\omega) \propto \omega^{-2.5}$ (see inset [Figure 4.11](#)). We attribute this low-frequency noise to instability of the external magnetic field B_0 , based on several arguments. In [Subsection 4.1.1](#), we presented arguments that rule out the possibility of spin-fluctuations from nearby paramagnetic traps. However, we left open the possibility of electric field induced decoherence from charge fluctuations in nearby traps. We will now describe three experimental observations which give evidence to eliminate the possibility of decoherence from charge fluctuations.

First, we verified that the qubit is sensitive to electric field noise, by repeating the noise spectroscopy experiment in the presence of an oscillating voltage at 5 kHz, applied to an electrostatic gate above the qubit location. As seen in [Figure 4.12c](#), a clear peak in $S(\omega)$ appeared at the expected 5 kHz frequency, confirming the effectiveness of the method. However, the amplitude of the signal we had to apply in order to distinguish it from the background was of the order of 100 μV , which corresponds to an equivalent electric field on the order of $\sim 2 \text{ MV/m}$, which is orders of magnitude larger than the charge noise we would expect in our device.

Second, in an effort to study the frequency dependence of the intrinsic charge noise in our device we measured few long traces of the output of our current amp with the SET in two different charge states: tuned to a slope of a Coulomb peak where the current through the SET is maximally sensitive to any charge variations in its surroundings; and in a non-conductive region (Coulomb blockade) where no signal can originate from the device, and therefore the measured noise comes only from the amplifier chain. Comparing the spectra of these two traces we can extract the low frequency charge noise of our device (at higher frequencies the noise floor of the amplifier is the limiting factor). As shown in [Figure 4.12d](#), the low-frequency charge noise follows a $1/\omega^\alpha$ dependence with $\alpha \approx 0.5$. This is in stark contrast with the measured spectrum of the noise acting on the qubit with $\alpha = 2.5$, adding further evidence that our observed noise $< 3 \text{ kHz}$ is not due to charge noise.

Third, [Figure 4.11](#) shows devices A and B exhibit nearly identical low-frequency noise magnitude. The typical trap density in our devices $\sim 10^{10} \text{ eV/cm}^2$ [117] implies an average of one trap every $\sim 100 \text{ nm}$. It is therefore extremely unlikely that donors in two different devices should couple to exactly the same fluctuating charge environment. Conversely, noise from the external magnet would obviously appear with the same strength in both devices, measured with the same setup. In any case, the main message we learned from the noise spectroscopy measurements is that the *ultimate* limit to the qubit coherence, as obtained with dynamical decoupling, is currently set by thermal noise from the microwave antenna, and not by any noise processes intrinsic to the nanoelectronic device.

4.5 An unlikely accident

While measuring Device A, we attempted to connect a new instrument to our setup. As we connected the instrument to the power supply, there was a static discharge that gave our device a “shock”. After this discharge the SET still functioned as normal and we could still perform ESR, however we could no longer perform NMR and we noticed that, in order to get equivalent ESR frequencies, we now had to increase the MW source power by ~ 20 dB. From these observations we suspected that the short circuit termination of the spin resonance antenna might have been damaged by the shock, causing the termination to become open circuit. Under these conditions, the node and anti-node of electric and magnetic fields would interchange, causing the magnetic field to tend to zero at low frequencies (i.e. NMR). At high frequencies however, the capacitive coupling between the tightly spaced coplanar lines could allow the signal to get through and generate a larger magnetic field. We proceeded to compare our device EM simulation (see [Chapter 3](#)) with a model in which we removed the short-circuit termination, and the results — shown on [Figure 4.13a](#) — confirm our expectations, showing ~ 70 dB decrease in B_1 at NMR frequencies (~ 50 MHz), while at ESR frequencies (~ 45 GHz) a less significant decrease ~ 30 dB is not too distant from our observations from the Rabi measurements. The SEM image shown on [Figure 4.13c](#), taken after we extracted Device A from the dilution refrigerator gives visual confirmation of this unlikely accident.

The opening of the antenna termination has the added effect of increasing the low frequency electric field radiated by the antenna. This effect was observed experimentally through an increase in the white noise level sensed by the qubit, as can be seen from the spectroscopy measurement in [Figure 4.13d](#). In the previous section, we observed through the 5 kHz tone measurement ([Figure 4.12c](#)) that an electric field ~ 2 MV/m would produce a noise power $S \approx 40$ $(\text{rad/s})^2/\text{Hz}$. The $S \approx 300$ $(\text{rad/s})^2/\text{Hz}$ white noise floor measured in [Figure 4.13d](#) would then correspond to an electric field noise of $E_n \approx 4$ MV/m. [Figure 4.13b](#) shows that for a 0 dBm input, simulations predict ~ 10 MV/m of electric field. From our previous calculations ([Equation 4.5](#)) we estimate that the noise power coming from the source is equivalent to -149 dBm, which we can use to scale our simulations to obtain an equivalent electric field noise $E_n = 4 \times 10^6 \times 10^{-149/20} = 0.1$ V/m. As in [Subsection 3.6.3](#), there is a large discrepancy between measurement and simulation of electric fields, which reinforces our suggestion that there are mechanisms that generate electric fields in our system, which are not being captured by our EM simulations.

4.6 Towards electron-nuclear entanglement

The quantum computing architecture that we have been following [[13](#)] envisions the use of the electron qubit for fast gate operations, while the nucleus is used for longer term storage of quantum information (see [Section 1.2](#)). The process of coherently transferring the spin between electron and nucleus requires entangling operations between them. In this section we will

4.6. Towards electron-nuclear entanglement

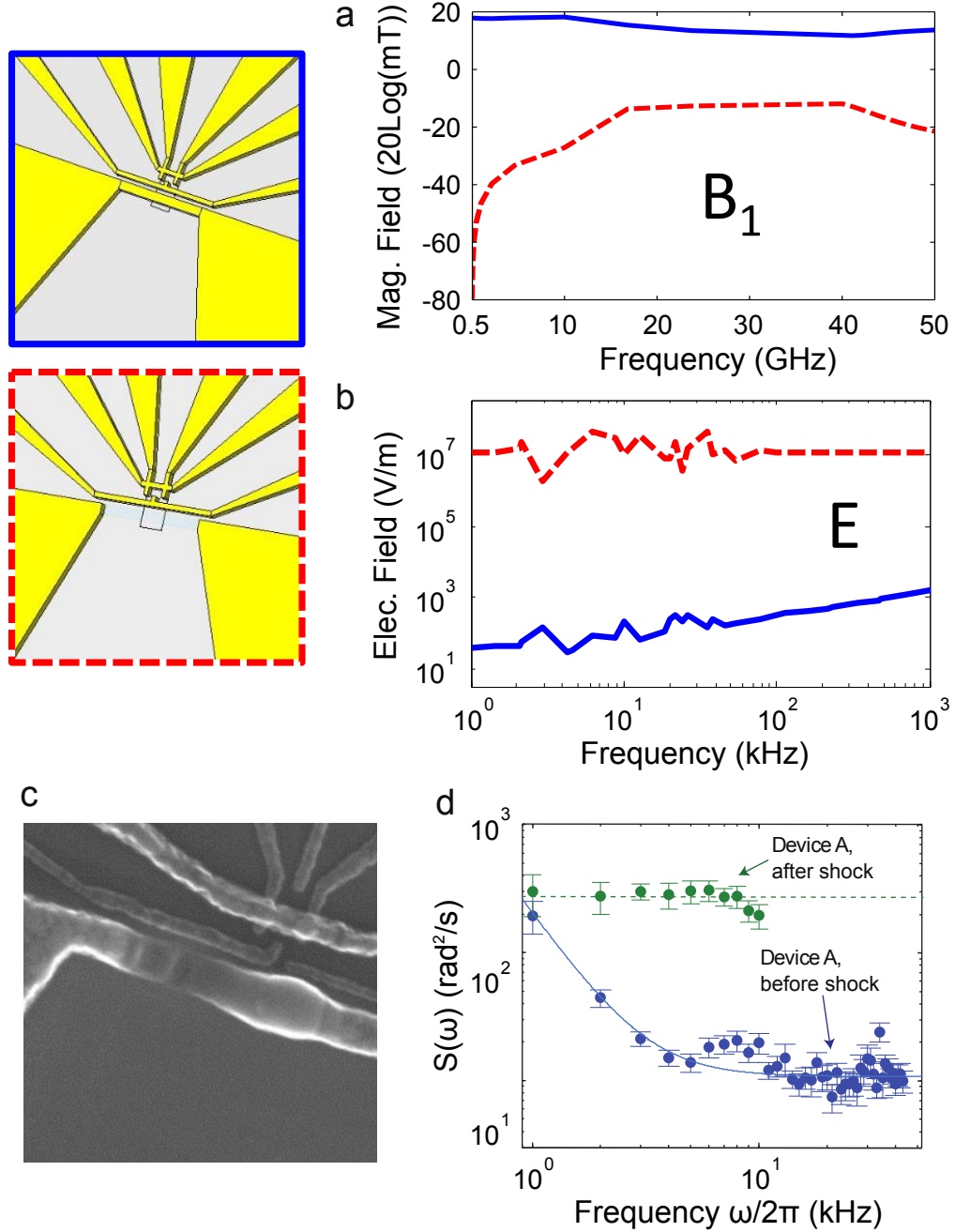


Figure 4.13: Damaged antenna measurements. a-b. EM simulations of the fields from the spin resonance antenna to the qubit. Solid lines are the original results, while dashed lines are results for a model where the short-circuit termination of the antenna has been removed. c SEM image of Device A — taken after completing all measurements on it — showing clear damage to the spin resonance antenna. d Noise spectrum showing the effect of the increased low frequency electric field, dominating the qubit coherence after the device shock.

provide a method to characterise the electron-nuclear entanglement in our system.

4.6.1 Basic theory

A two-qubit state (this can be generalised for N -qubit states) can be coherently prepared in a superposition state in which the outcome of the measurement of one qubit cannot be predicted, but the state of the second qubit collapses to a known state after measurement of the first qubit. The existence of these *entangled states* are a unique feature of quantum mechanics that has no classical analogue.

The degree of correlation between the measurement of the qubits determines the degree of entanglement, and for a two-qubit system there are four *maximally* entangled states known as the *Bell states*:

$$\begin{aligned} |\Phi^+\rangle &= \frac{1}{\sqrt{2}}(|\downarrow\downarrow\rangle + |\uparrow\uparrow\rangle) \\ |\Phi^-\rangle &= \frac{1}{\sqrt{2}}(|\downarrow\downarrow\rangle - |\uparrow\uparrow\rangle) \\ |\Psi^+\rangle &= \frac{1}{\sqrt{2}}(|\downarrow\uparrow\rangle + |\uparrow\downarrow\rangle) \\ |\Psi^-\rangle &= \frac{1}{\sqrt{2}}(|\downarrow\uparrow\rangle - |\uparrow\downarrow\rangle) \end{aligned}$$

Entangled states on spin pairs that have distinguishable conditional transitions (e.g. the electron-nuclear spin system from a P donor), can be easily prepared by applying a short pulse sequence. For example, with our spin system initialised in the $|\downarrow\uparrow\rangle$ state, applying the sequence $\pi/2_{\nu_{e\uparrow}} - \pi_{\nu_{N\downarrow}}$ will prepare $|\Phi^+\rangle$.

There are two general measurements to demonstrate that a system is in an entangled state. The first — known as the *violation of Bell's inequalities* [133] — is based on correlation measurements, applied in a specific way to ensure that there is no possibility of the existence of local hidden variables that could alter the outcome of the correlation measurements. This type of entanglement demonstration is beyond the scope of this thesis, as a method has not yet been established to perform these measurements on our system.

The second measurement to demonstrate entanglement is *density matrix tomography*. A simple quantum measurement on a qubit cannot distinguish between a mixed state or a coherent superposition state — e.g. the same measurement outcome will result from a spin that has been in $|\uparrow\rangle$ for $T_1 \ln(2)$ or from a spin that is coherent anywhere along the xy plane. The density matrix (ρ) gives a full description of state, containing the probabilities of the state being in any of the possible permutations of the eigenstates of the system.

4.6.2 Density matrix tomography in the P-Si system

For a single qubit, the density matrix can be expressed as a function of the projection of the qubit state on each of the axes of the Bloch sphere: $\rho = \mathbf{I}_2 + 1/2 \sum_{i=x,y,z} P_i \sigma_i$, where \mathbf{I}_2 is the

2×2 identity matrix, P is probability and $\sigma_{x,y,z}$ are the well known *Pauli matrices* — which are operators that project the spin onto each of the axes. We can measure $P_{x,y,z}$ by rotating the qubit, such that the sought projection gets mapped onto the measurement axis z — therefore we can obtain P_y by applying $\pi/2_x$ and P_x by applying $\pi/2_y$ before measurement [134].

For two-qubit density matrix tomography, a similar method to the single qubit case can be applied, requiring the ability to measure the two-spin state. This method has been used to demonstrate entanglement in trapped ion systems [135] and superconducting qubits [136] where both qubits can be measured simultaneously, and in NV-centre systems [137] where the two nuclear spin system is measured through an ancilla electron spin. However in our system, the nuclear spin must be read through the electron, therefore there are no mechanisms available to directly measure the two-spin system.

Instead, we can apply a method based on z axis rotations of the qubit system space, through which the elements of the density matrix can be extracted. We will start by defining the z axis rotations. On a single spin, these rotations consist of a controlled dephasing of the spin along the xy plane. Although these z rotations are not directly available operations in our system, they can be implemented in a number of ways. The most robust of these is the *geometric phase gate* [138], which takes advantage of the fact that a driven spin rotation accumulates a *Berry phase* [139]. By applying two π rotations using different phases ($\pi_x - \pi_{-x+\theta}$), the spin will return to its previous position with respect to the z projection, but will have accumulated a phase θ on the xy plane. On the 4-dimensional space of the two-spin system, the z rotations are impossible to visualise, but can be mathematically expressed as an operator which adds a different phase to each of the diagonal elements of the 4-dimensional matrix. This can be achieved by applying e.g. $\pi_x - \pi_{-x+\theta_e}$ on $\nu_{e\uparrow\uparrow}$, followed by $\pi_x - \pi_{-x+\theta_N}$ on $\nu_{N\downarrow\downarrow}$, yielding the following phase gate operator:

$$U_{\text{pg}} = \begin{pmatrix} \exp(-i\theta_e) & 0 & 0 & 0 \\ 0 & 1 & 0 & 0 \\ 0 & 0 & \exp(i(\theta_e - \theta_N)) & 0 \\ 0 & 0 & 0 & \exp(i(\theta_N)) \end{pmatrix}$$

The next step is to measure the y projection of each “coherence” in our system. We define a coherence as a superposition between two levels in the system. In our electron-nuclear four-level system (see Subsection 1.2.1), there are four coherences corresponding to the electron and nuclear control transitions (see Subsection 1.2.2), plus two entangling coherences: the flip-flip ($|\downarrow\downarrow\rangle \leftrightarrow |\uparrow\uparrow\rangle$) and the flip-flop ($|\downarrow\uparrow\rangle \leftrightarrow |\uparrow\downarrow\rangle$). When we perform an electron spin readout, we are measuring the z projection of the electron qubit. This measurement can be expressed mathematically as $P_\uparrow = 0.5 \langle \psi_{eN} | \sigma_{ze} | \psi_{eN} \rangle + 0.5$, where $|\psi_{eN}\rangle$ is the two-spin (electron-nuclear) quantum state that is being measured, and $\sigma_{ze} = \sigma_z \otimes \mathbf{I}_2$ is the electron spin z projection operator ($\sigma_z = \begin{pmatrix} 1 & 0 \\ 0 & -1 \end{pmatrix}$ is the known Pauli matrix). If we want to make a measurement of the y projection of one of the electron transitions, we need to apply a $\pi/2_x$ rotation on the

desired electron transition. The operator for this rotation in the two-spin system is the one-spin rotation operator applied conditionally on the state of the second spin — e.g. if we want to apply the rotation using $\nu_{e\downarrow}$ the operator is given by:

$$U_{e\downarrow}^{\pi/2} = \begin{pmatrix} \cos(\pi/4) & -i \sin(\pi/4) \\ -i \sin(\pi/4) & \cos(\pi/4) \end{pmatrix} \otimes |\downarrow\downarrow\rangle\langle\downarrow\downarrow| + \mathbf{I}_2 \otimes |\uparrow\uparrow\rangle\langle\uparrow\uparrow|$$

Let us now consider an arbitrary two-spin state $|\psi_{eN}\rangle = a|\uparrow\uparrow\rangle + b|\uparrow\downarrow\rangle + c|\downarrow\uparrow\rangle + d|\downarrow\downarrow\rangle$, with $|a|^2 + |b|^2 + |c|^2 + |d|^2 = 1$. Its density matrix is given by:

$$\rho = |\psi_{eN}\rangle\langle\psi_{eN}| = \begin{pmatrix} |a|^2 & ab^* & ac^* & ad^* \\ a^*b & |b|^2 & bc^* & bd^* \\ a^*c & b^*c & |c|^2 & cd^* \\ a^*d & b^*d & c^*d & |d|^2 \end{pmatrix}$$

If we perform the phase gate operation on this state, followed by the y projection measurement described above, the result will yield:

$$\begin{aligned} P_\uparrow &= \frac{1}{2} \langle U_{e\downarrow}^{\pi/2} U_{pg} \psi_{eN} | \sigma_{ze} | U_{e\downarrow}^{\pi/2} U_{pg} \psi_{eN} \rangle + \frac{1}{2} \\ &= \frac{1}{2} (|a|^2 - |c|^2 + bd^* i \exp(-i\theta_N) - b^* di \exp(i\theta_N)) + \frac{1}{2} \end{aligned}$$

By observing the evolution of P_\uparrow as θ_N is increased, there will be oscillations with amplitude given by the off-diagonal elements of the projected coherence. Furthermore, the offset of the oscillations gives information on the diagonal matrix elements, which can be used to form a solvable equation system (which must include $|a|^2 + |b|^2 + |c|^2 + |d|^2 = 1$), once all the coherences have been projected and measured. In order to obtain all the projections, any coherence can be mapped onto an electron transition by applying π pulses on the appropriate transitions to transfer the population from one coherence to another — e.g. if we want to map the flip-flip coherence onto $\nu_{e\downarrow}$, we apply a π pulse on $\nu_{N\uparrow}$, thus transferring the population of $|\uparrow\uparrow\rangle$ to $|\uparrow\downarrow\rangle$. With this method, all the projections can be measured, obtaining the following results on our

arbitrary state:

$$\begin{aligned}
 P_{\uparrow}(e \Downarrow) &= \frac{1}{2} (|a|^2 - |c|^2 + bd^*i \exp(-i\theta_N) - b^*di \exp(i\theta_N)) + \frac{1}{2} \\
 P_{\uparrow}(e \Uparrow) &= \frac{1}{2} (|b|^2 - |d|^2 + ac^*i \exp(-i(2\theta_e - \theta_N)) - a^*ci \exp(i(2\theta_e - \theta_N))) + \frac{1}{2} \\
 P_{\uparrow}(N \Downarrow) &= \frac{1}{2} (|a|^2 - |b|^2 + cd^*i \exp(-i(\theta_e - 2\theta_N)) - c^*di \exp(i(\theta_e - 2\theta_N))) + \frac{1}{2} \\
 P_{\uparrow}(N \Uparrow) &= \frac{1}{2} (|d|^2 - |c|^2 + ab^*i \exp(-i\theta_e) - a^*bi \exp(i\theta_e)) + \frac{1}{2} \\
 P_{\uparrow}(\text{flip-flip}) &= \frac{1}{2} (|b|^2 - |c|^2 + ad^*i \exp(-i(\theta_e + \theta_N)) + a^*di \exp(i(\theta_e + \theta_N))) + \frac{1}{2} \\
 P_{\uparrow}(\text{flip-flop}) &= \frac{1}{2} (|a|^2 - |d|^2 - bc^*i \exp(-i(\theta_e - \theta_N)) - b^*ci \exp(i(\theta_e - \theta_N))) + \frac{1}{2}
 \end{aligned}$$

From all these projections we can extract every element of the density matrix. For a practical example, we can apply our tomography operations to the maximally entangled $|\Phi^+\rangle$ Bell state. The resulting measurements yield:

$$\begin{aligned}
 P_{\uparrow}(e \Downarrow) &= 0.75 \\
 P_{\uparrow}(e \Uparrow) &= 0.25 \\
 P_{\uparrow}(N \Downarrow) &= 0.75 \\
 P_{\uparrow}(N \Uparrow) &= 0.25 \\
 P_{\uparrow}(\text{flip-flip}) &= 0.5 + 0.5 \cos(\theta_e + \theta_N) \\
 P_{\uparrow}(\text{flip-flop}) &= 0.5
 \end{aligned} \tag{4.6}$$

As expected, the only oscillating (off-diagonal) component is of the flip-flip coherence yielding $ad^* = a^*d = 0.5$, and from the offsets we solve $|a|^2 = 0.5$, $|b|^2 = 0$, $|c|^2 = 0$ and $|d|^2 = 0.5$. The density matrix is the same if we compute it directly:

$$\rho = |\Phi^+\rangle \langle \Phi^+| = \begin{pmatrix} 0.5 & 0 & 0 & 0.5 \\ 0 & 0 & 0 & 0 \\ 0 & 0 & 0 & 0 \\ 0.5 & 0 & 0 & 0.5 \end{pmatrix}$$

In [Figure 4.14](#) we show the result of a simulation of the tomography sequence on $|\Phi^+\rangle$ taking 100 phase increments with different values for the increment size $\Delta\theta_e$ and $\Delta\theta_N$, and plotting the expected value of the y projection as a function of the increment index. A clear oscillation of the flip-flip coherence is observed, and the fourier transform of the oscillation confirms that the oscillation frequency corresponds to $\Delta\theta_e + \Delta\theta_N$, as expected from [Equation 4.6](#).

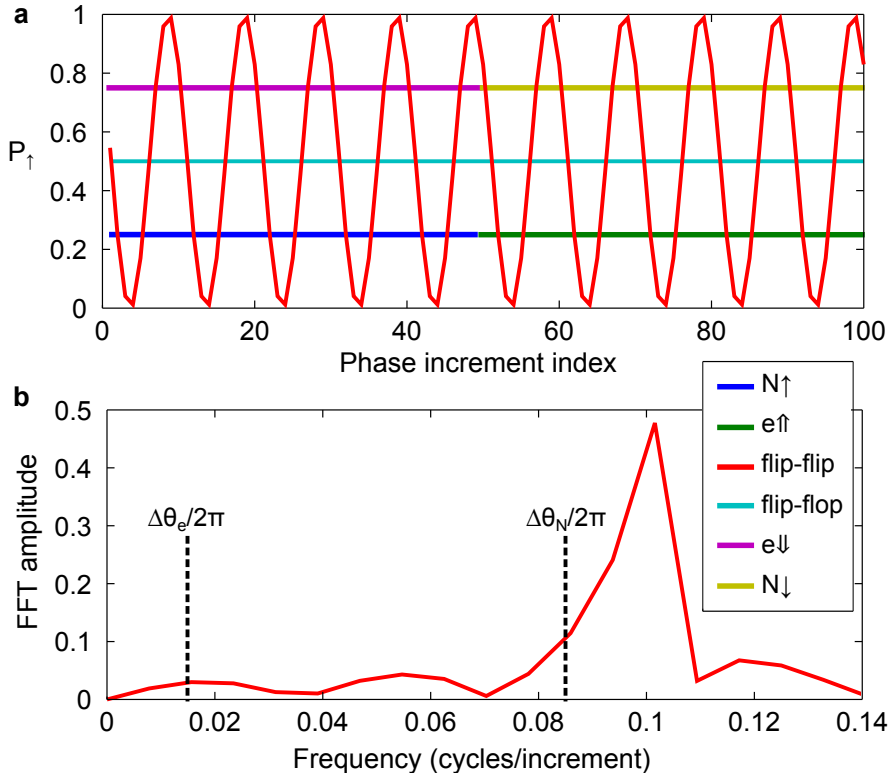


Figure 4.14: **Density matrix tomography simulations.** **a** Simulated measurement outcome for each of the two-spin system coherences, plotted as a function of the increment in phase. We have chosen the phase increments $\Delta\theta_e$, $\Delta\theta_N$ such that $\Delta\theta_e/2\pi = 0.015$ and $\Delta\theta_N/2\pi = 0.085$. **b** Fourier transform of the flip-flip coherence extracted from the measurement, showing a clear peak at 0.1 cycles per increment. This matches the expected value $\Delta\theta_e/2\pi + \Delta\theta_N/2\pi$.

4.6.3 Experimental considerations

The entire tomography sequence is lengthy enough that T_2^* could start to play a role and affect the measurement fidelity. It is important to characterise the dephasing of every transition and consider the amount of time that is spent on them during each of the pulses in the sequence. We have shown in this chapter the characterisation of the dephasing of the individual electron and nuclear transitions, but the flip-flip and flip-flop have not yet been characterised.

Preliminary attempts at the tomography sequence show very inconsistent results, which suggests that characterisation of the dephasing is important, and that the pulse sequence will probably need to involve refocusing at the adequate transitions, in order to extend the coherences and obtain successful experimental results.

4.7 Conclusions and future work

The results presented in this chapter conclusively show that the exceptional quantum coherence exhibited by spins in isotopically pure ^{28}Si can be preserved and exploited in a top-gated

nanoelectronic device, fabricated with standard Metal-Oxide-Semiconductor methods. The proximity of an amorphous interface and gated nanostructures does not appear to significantly affect the control fidelity and the coherence time, which reaches here a new record for solid-state single qubits with $T_2 > 30$ s in the $^{31}\text{P}^+$ spin.

These results have provided invaluable insight which will allow us make important improvements for future generation devices. The effect of longitudinal component of B_1 — found in Subsection 4.4.2 to be the limiting factor coherence times — can be eliminated by rotating the sample orientation by 90° on the device surface plane. This involves a healthy amount of MW engineering in order to implement a CPW 90° bend on the enclosure’s RF board. This method should uncover longer limits to coherence times and through noise spectroscopy we should get further insight into new coherence limiting mechanisms. Another important insight is that we do not need to push our MW source to its power extremes in order to obtain high electron fidelities. Based on this, we can consider modifying our on-chip balun antenna to the on-chip CPW design, which we showed in Subsection 3.4.2 to exhibit the best E-M ratio and the flattest frequency response.

These single spin devices still have potential to be exploited for several measurements which can provide important contributions for the future of quantum computing and fundamental physics. Electron-nuclear entanglement measurements are ready to be performed and are next in line in the measurement agenda for these devices. A more accepted method by the quantum computing community to characterise the fidelity of qubits is *randomised benchmarking* [140], which consists in applying successive gate operations — chosen randomly from a set known as the *Clifford group* [141] — and observing the decay of the experimental vs. expected results as the gate number is increased. We had not performed this measurement due to instrument limitations — it requires a vector MW source to enable fast phase variations — however, it is in the near-term pipeline of future measurements. The QND nature of the nuclear spin readout should in principle allow us to perform *weak measurements* [142] of the nuclear spin. Weak measurements together with real-time feedback techniques — such as the one we demonstrated in Subsection 4.3.3 — have been used to perform interesting measurements, such as the stabilization of Rabi oscillations [143] and qubit manipulation through the backaction of a weak measurement [144].

Seminal work being carried out in parallel to the experiments presented in this thesis, is the demonstration of single-spin qubits from electrostatically induced quantum dots in silicon [145]. These devices are also made with industry compatible MOS technology, with the added advantage of utilising gates to confine the single electron spin. It is generally accepted that these type of devices have the greatest potential in terms scalability of silicon quantum computation, as the use of gates to confine electrons allow for much simpler qubit localisation and addressability. Latest measurements on these devices, fabricated on ^{28}Si , show coherence times and fidelities comparable to the ones presented in this chapter.

Looking beyond the single-qubit level, we note that the most promising proposals for 2-qubit

4.7. Conclusions and future work

logic gates and long-distance coupling involve rather weak interactions, either through exchange coupling [44], or in a circuit quantum electrodynamics architecture [38]. The extremely narrow linewidths observed here will facilitate multi-qubit operations based on magnetic resonance, since the individual resonances will remain resolvable over a very broad range of inter-qubit couplings, greatly relaxing the need for atomically precise donor placement. In the following chapter we will present an important experimental milestone towards the implementation of 2-qubit logic gates: single-shot readout and relaxation measurements on a pair of exchange coupled P donors.

The work in this chapter represents a fundamental advance in control and understanding of spin qubits in solid state, and shows a clear path forward to integrating them with functional electronic devices.

Chapter 5

Readout of coupled electrons in P-Si

In this chapter we present the experimental observation of a large exchange coupling $J \approx 300 \text{ } \mu\text{eV}$ between two P electron spins in silicon. The singlet and triplet states of the coupled spins are monitored in real time through our spin to charge conversion technique, detecting ionization from tunnel-rate-dependent processes in the coupled spin system, yielding single-shot readout fidelities above 95%. The triplet to singlet relaxation time $T_1 \approx 4 \text{ ms}$ at zero magnetic field agrees with the theoretical prediction for J -coupled P dimers in silicon. The time evolution of the 2-electron state populations gives further insight into the valley-orbit eigenstates of the donor dimer, valley selection rules and relaxation rates, and the role of hyperfine interactions. These results pave the way to the realization of 2-qubit quantum logic gates with spins in silicon, and highlight the necessity to adopt gating schemes compatible with weak J -coupling strengths.

This chapter has been submitted for publication in *Physical Review Letters*

The author acknowledges J.T. Muhonen for assistance in measurements; A. Saraiva for laying out the valley-orbit theory; T.F. Watson, M.G. House and X. Hu for enlightening discussions

5.1 Introduction

This thesis has been mainly focusing on demonstrations of single qubit operations. In order to complete a universal set of quantum logic gates for circuit-based quantum computing, entangling two-qubit operations are also needed [15]. These have been demonstrated in several physical qubit platforms [9], including spins in semiconductors [39, 146, 147]. Conversely, an entangling quantum logic gate for a pair of spin qubits in silicon is still awaiting experimental demonstration. As introduced in [Subsection 1.2.4](#), several coupling mechanisms can be used for this purpose, but the simplest and most appropriate for two-qubit gates is the exchange interaction J .

Although there have been old and recent observations of exchange interaction between pairs of donors in silicon [42, 43], its application to quantum information processing requires the ability to dynamically control it, and to measure the instantaneous quantum state of the qubits. In this chapter we report the time-resolved observation of large exchange coupling $J \approx 300$ μeV between the electrons of a P donor pair. We employ our charge detector to perform single-shot readout of the spin singlet $|S\rangle$ and triplet $|T\rangle$ states of the two-electron system (as defined in [Equation 1.4](#)). We exploit the significant difference in the size of the orbital wavefunctions for $|S\rangle$ and $|T\rangle$ states to perform high-fidelity tunnel-rate-selective readout (TR-RO) [32], as introduced in [Subsection 1.2.3](#). We apply these techniques to measure the valley and spin relaxation times, and its dependence on the external magnetic field B_0 .

5.2 Experiment background

The device from which we obtained the results in this chapter ([Figure 5.1a](#)) was fabricated as part of the same batch of ${}^{\text{nat}}\text{Si}$ devices as those from which we obtained the results in [Chapter 3](#). The initial objective of the experiment was to test and characterise the experimental setup described in [Chapter 2](#), by comparing with the qubit characteristics of similar devices operated in previous experimental setups.

The first thing we noticed during our initial measurements was that the charge stability diagrams (see [Section 1.2.6](#)) were very hysteretic, and our DG lever-arm (see [Subsection 2.5.1](#)) was about an order of magnitude smaller than in previous measured devices. The hysteretic behaviour became absent if we performed the charge stability diagram measurement using one of the barrier gates instead of the DG. These observations lead us to conclude that there must have been some damage to the DG, although we were never able to confirm the nature of the damage. We did however, constantly observe in our charge stability diagrams, two nearby charge transitions — highlighted in [Figure 5.1b](#) — which is our first hint of having exchange coupled donors in our system. Donors that ionise at similar potentials have a high probability of also being spatial neighbours.

5.2. Experiment background

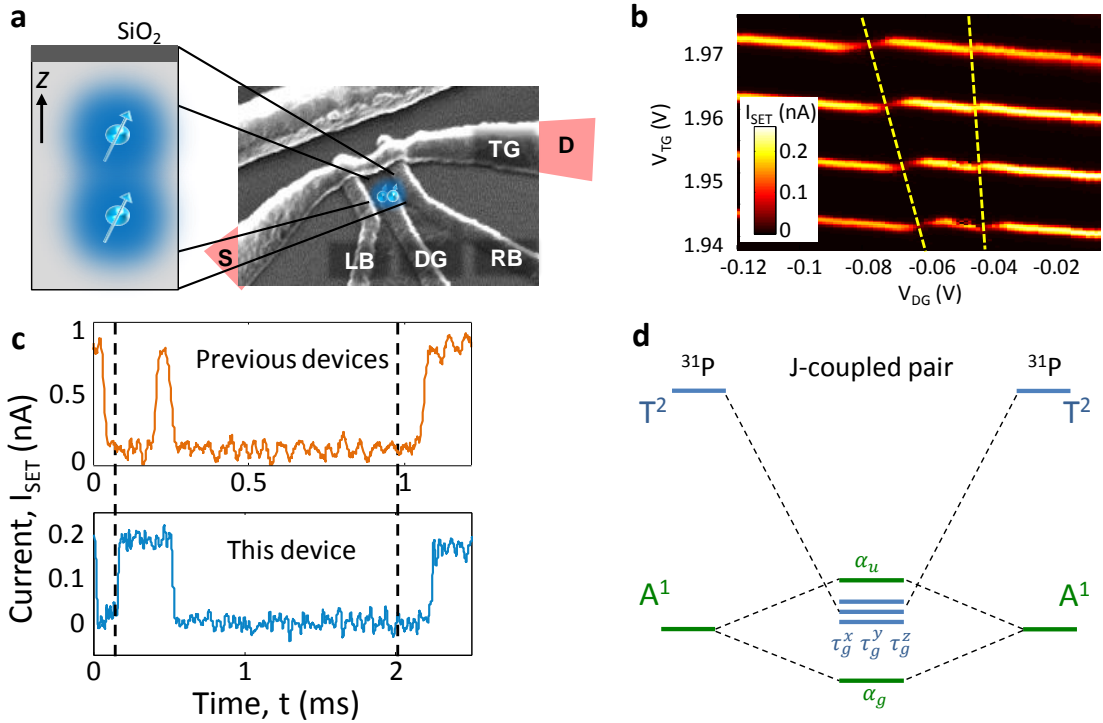


Figure 5.1: Device layout and initial measurements. **a** SEM image of a device identical to the one measured. The device is from the same batch of devices as Chapter 3. Inset shows two nearby donor electrons with overlapping wavefunctions. As explained in the main text, experiments suggest that donors are aligned predominantly along the z axis. **b** SET charge stability diagram showing two nearby charge transitions (highlighted with dashed lines). **c** Sample excited state readout traces comparing previous measured devices with the one measured here. There is an evident asymmetry between tunnel times of the excited and ground state. **d** Diagram showing the expected modification of the valley-orbit states for coupled P donors $\lesssim 6$ nm apart.

5.2.1 Initial readout measurements

The first step in the process of identifying a measurable P donor is to apply a large magnetic field B_0 and search for the current ‘‘blips’’, signature of electron spin readout (see Subsection 2.5.1). With $B_0 = 2$ T, we were able to successfully observe the readout signature, however we noticed that — unlike our previous measured devices — there was a very large asymmetry between the tunnel rates of the excited state the ground state. This is visually evident by comparing the two current traces in Figure 5.1c. In previous devices (top) a clear gap can be observed between the start of the read pulse (RP) and the start of the current blip; the length of the gap and the length of the blip are similar, indicating similar tunnel rates of the $|\uparrow\rangle$ and $|\downarrow\rangle$ states. In contrast, this device shows no apparent gap between the start of the RP and the onset of the blip, which suggests that the excited state tunnels much faster than the ground state.

This tunnel rate asymmetry has been previously observed in a quantum dot system, while loading and unloading the second electron of the dot [32]. In this case, the excited and ground state corresponded to the $|T\rangle$ and $|S\rangle$ states of the two electron spin system in the dot. In

the spin-antisymmetric singlet, both electrons are allowed to occupy the ground state orbital, whereas for the spin-symmetric triplet, the Pauli exclusion principle forces one of the electrons to occupy an excited orbital. In general, excited orbital wavefunctions have a greater spatial extent than ground state orbitals, therefore the overlap between the nearby electron reservoir and the $|T\rangle$ wavefunction will be greater than for $|S\rangle$ [86], resulting in the tunnel rate asymmetry.

For single P donors in Si systems, loading a second electron onto a single P donor requires a charging energy $E_c \approx 40$ meV [51, 148], which is generally higher than our V_{DG} operating range (we avoid V_{DG} greater than the SET turn-on voltage, to prevent inducing a 2DEG under the DG). However, the two electron spin system from nearby exchange coupled donors would have the same tunnel rate asymmetry effect. In a single donor, we need B_0 to split the $|\uparrow\rangle$ and $|\downarrow\rangle$ states. However, for a two-spin system, the energy splitting occurs intrinsically due to the necessary occupation of different orbital states. Therefore the first obvious test in our system was to turn off the field and repeat the readout measurements. As we will see from the following measurement results, we found that we could still observe an energy splitting at $B_0 = 0$ T.

Our objective for the rest of this chapter is to convince the reader that we were indeed observing time-resolved signatures of exchange coupled P donors, by presenting several novel measurements and introducing various theoretical concepts and predictions which show great agreement with our measurements.

5.3 Spins and valleys in exchange coupled P-Si donors

Before presenting further measurement results it is necessary to introduce some theory regarding the energy configuration of a system of exchange coupled donors. The band structure of Si, with its non-zero momentum conduction band minimum, along with the lattice cubic symmetry, result in the presence of six *valleys* [11]. The {1s} orbital of a single P donor in Si has a valley-orbit ground state A^1 (1-fold degenerate), and excited states T^2 (3-fold degenerate) and E (2-fold degenerate) [149]. In particular, the 3-fold degeneracy of T^2 arises from it being an antisymmetric combination of pairs of valleys $\pm x, \pm y, \pm z$, where all valleys have the same energy. The A^1 to T^2 splitting is ≈ 11.7 meV, making the excited valley-orbit states unimportant for most aspects of single-qubit physics.

As donors come close together and their wavefunctions begin to overlap, the hybridization of the valley-orbit states results in “bonding” / “antibonding” eigenstates, whose energy is split according to the wavefunction overlap. The Bohr radius of the T^2 states is about twice that of A^1 , resulting in a much larger splitting of the resulting coupled states. It has been estimated [150] that for interdonor separation $\lesssim 6$ nm there is an inversion in the hierarchy of states that originate from single-donor A^1 and T^2 . The energy of the bonding combination of T^2 states (τ_g) crosses below that of the antibonding A^1 (α_u), whereas the overall ground state always remains the bonding A^1 combination (α_g) (see Figure 5.1d). Therefore, in this configuration the spin-singlet state occupies the α_g valley-orbit eigenstate, while the spin-triplets

can occupy any of the three $\tau_g^{x,y,z}$ states, distinguished by their valley composition. We denote all the available triplet states as $|T_{+,0,-}\rangle^{x,y,z} = |\alpha_g \tau_g^{x,y,z}| \otimes |T_{+,0,-}\rangle$, where $|\dots\rangle$ stands for the Slater determinant.

To fully understand the dynamics of our system, some additional aspects of the physics of donors and dots in silicon need to be considered here. First, at ~ 6 nm, the difference in electrostatic energy between the ground and first excited state orbitals can be tens of meV, however at this short interdonor distances there are strong correlations between $|S\rangle$ and $|T\rangle$ that reduce the singlet triplet splitting to hundreds of μeV [43]. Second, the 2-electron $\tau_g^{x,y,z}$ states are not degenerate. Consider for example a donor pair oriented along z , as in [Figure 5.1a](#). Since the transverse effective mass in Si is smaller than the longitudinal one [151], states composed of valleys perpendicular to the orientation of the pair have stronger tunnel coupling, hence $\tau_g^{x,y}$ are lowered in energy further than the τ_g^z state ([Figure 5.1d](#)). Similarly, α_g is not an equal-weight combination of all 6 valleys, but has a predominant component of valleys perpendicular to the dimer axis. Finally, the spin state of the donor pair is read out through electron tunneling into the island of an SET formed at a (001) interface. In electrostatically defined quantum dots — such as our SET island — the electric field induced electron confinement splits the valleys into two Γ ($k_{z,-z}$) and four Δ ($k_{x,-x,y,-y}$) valleys, with Γ tens of meV lower in energy than Δ [151]. As a consequence, the SET island only couples to states of the donor dimer with nonzero $\pm z$ valley composition. These Si-specific aspects are revealed in the time-resolved experiments described below.

5.4 Exchange coupling estimation

With the DG voltage (V_{DG}) set near a donor charge transition, the device is tuned in the charge sensing regime described in [Subsection 2.5.1](#). The 2D plot shown in [Figure 5.2](#) is obtained by monitoring I_{SET} while performing the donor pulse sequence LP-RP-EP. After each set of measurements, the voltage V_{DG} at the RP is stepped, such that the donor electrochemical potential μ_D goes from higher to lower than the SET island Fermi energy E_F . A well-defined “tail” — where excess current occurs at the start of the read-phase — indicates the presence of an energy-split pair of electron states. In this region, we observe the blips of current characteristic of single-shot spin readout. The data in [Figure 5.2](#) was taken in the absence of magnetic field ($B = 0$ T). Therefore, the observed splitting cannot be the Zeeman energy E_z of a single spin (see [Subsection 1.2.1](#)). We postulate that the measurement constitutes the observation of the $|S\rangle$ and $|T\rangle$ states of a pair of P donors, split by an exchange interaction $J = \mu_T - \mu_S$, where μ_T and μ_S are the $|T\rangle$ and $|S\rangle$ electrochemical potentials at $B = 0$. To extract the value of J we first convert V_{DG} to a shift in μ , by fitting a Fermi distribution function ([Equation 2.19](#)) to the shape of $I_{\text{SET}}(V_{\text{DG}})$ for $0.1 < V_{\text{DG}} < 0.5$ V in the read-phase after the decay of the “tail” (inset [Figure 5.2](#)). Using the method described in [Subsection 2.3.2](#) we obtained a value for the electron temperature $T_{el} = 125 \pm 25$ mK in this system. The length of the readout “tail”

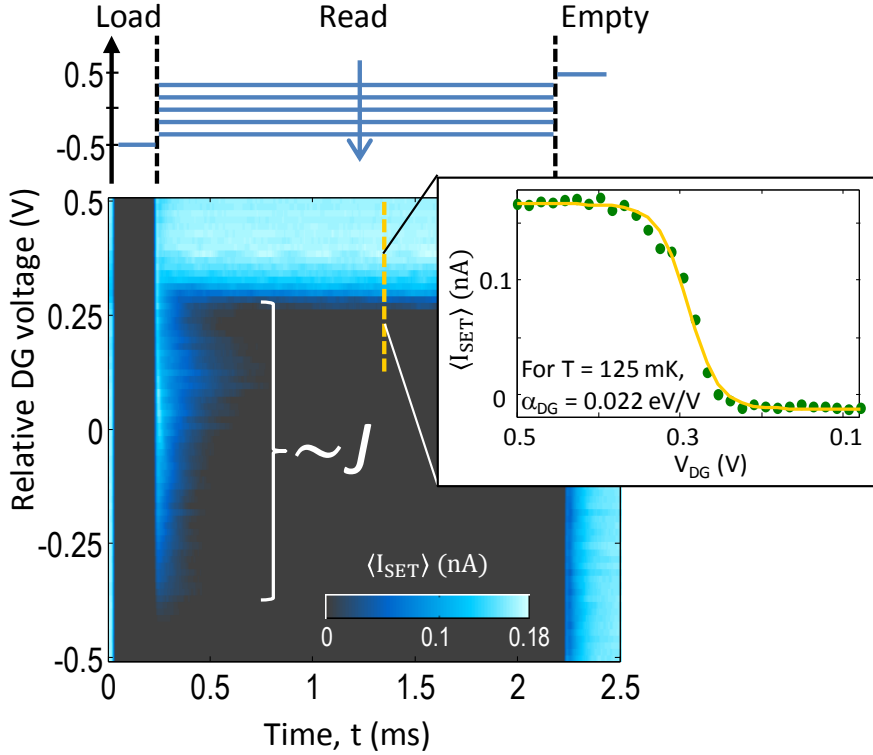


Figure 5.2: Exchange coupling estimation. Measurement performed using the pulsing protocol sketched at the top of the figure. The tail of current of length J correspond to the regime where the Fermi energy of the SET island is between the excited and ground state of the system. Inset shows a fit to the data along the dotted line, from which the donor gate lever-arm α_{DG} can be extracted.

$\Delta V_{DG} = 0.6 \pm 0.1$ V can be converted into the value of $J = 345 \pm 100$ μeV . This value of J is expected to correspond to donors < 8 nm apart [35, 36, 43], furthermore it is in the range of values were the α_u - τ_g inversion is expected to be [43].

5.5 Tunnel-rate selective readout

In our standard energy-selective readout scheme, we set the E_F in between the excited μ_T and ground μ_S state potentials such that only $|T\rangle$ allows an electron to tunnel to the SET island, and we discriminate between $|S\rangle$ and $|T\rangle$ by the absence or presence of a current blip respectively. For an exchange coupled pair in the valley inversion regime, $|T\rangle$ can occupy any of the three available valley-orbit excited states $\tau_g^{x,y,z}$, only one of which (τ_g^z) couples to the SET island. Therefore the accuracy of the energy-selective readout technique is compromised, as it cannot discriminate between $|S\rangle$ and $|T\rangle^{x,y}$ (i.e. neither of them will show a blip during the RP).

In Subsection 1.2.3, we introduced the concept of tunnel-rate-selective readout (TR-RO) [32], a technique catered to systems with a large tunnel rate asymmetry. With this technique, E_F

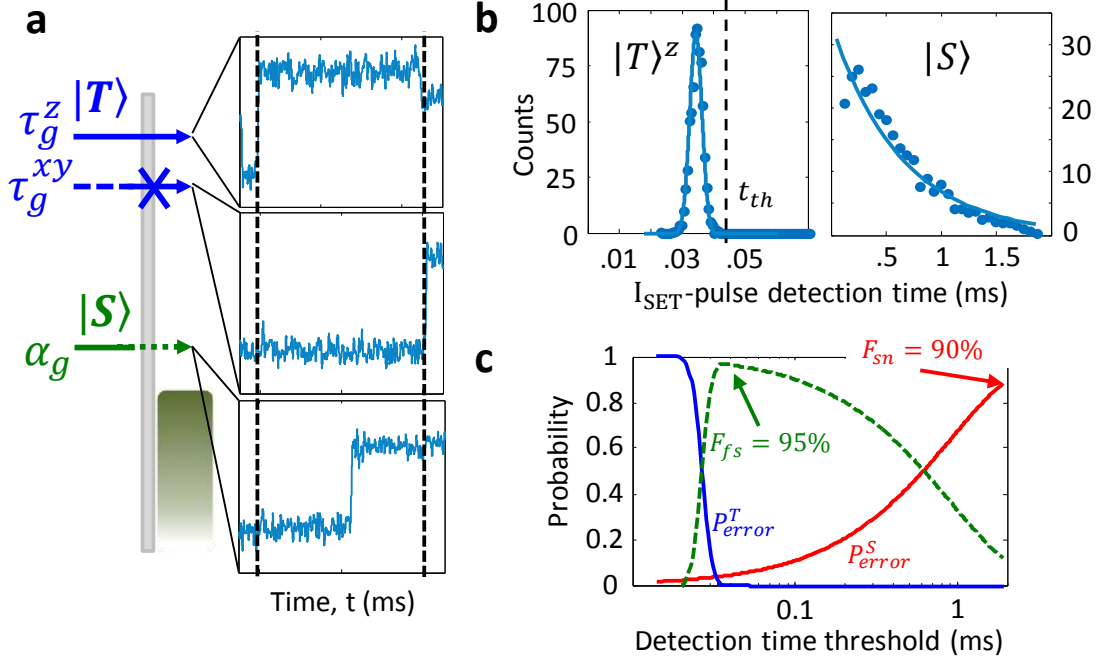


Figure 5.3: TR-RO readout scheme and fidelities. **a** Diagram of electrochemical potentials and tunnel rates for all the states in the two-donor system. $|T\rangle^z$ and $|S\rangle$ tunneling is asymmetric due to the difference in spatial extent of their wavefunctions, while $|T\rangle^{x,y}$ is not allowed to tunnel due to valley incompatibility with the SET island. Insets on the right shows sample readout traces for each state. **b** Histograms of tunnel rates taken from a data-set of 1000 readout traces. Both histograms are constructed from the same data-set, but use different bin resolution to highlight different tunneling processes. Histogram on the left shows the peak corresponding our detection bandwidth, it is fitted with a normal distribution (Equation 2.17) with $\mu_d = 27 \mu\text{s}$ and $\sigma_d = 3.2 \mu\text{s}$. Histogram on the right shows an exponential decay (Equation 2.18 with $\Gamma_t = 1100 \text{ s}^{-1}$) corresponding to the $|S\rangle$ tunnel time. The first point of the histogram is omitted to exclude the fast-tunnel events. **c** Measurement fidelities for discriminating between fast and slow-tunneling events (F_{fs}), and between slow and no-tunneling (F_{sn}), extracted from fits to the histograms (see main text for details).

is tuned below μ_S (and thus below μ_T as well), as depicted in Figure 5.3a. Discrimination is achieved by setting a time threshold to the onset of a tunnel event (blip of current). To accommodate our system, we apply a modified version of TR-RO, in which we define three types of tunneling events: fast-tunneling, slow-tunneling and no-tunneling. We identify a fast(slow)-tunneling event by the presence of a current blip before(after) a time threshold t_{th} , while no-tunneling corresponds to the absence of a current blip within our read pulse window (t_{RP}). We can then assign fast-tunneling to $|T\rangle^z$, slow-tunneling to $|S\rangle$ and no-tunneling to $|T\rangle^{x,y}$. Figure 5.3a show a diagram of this state discrimination, with sample current traces showing a clear distinction between tunneling events.

We can assess the fidelity of this readout technique by constructing a histogram of tunnel times from a large sample of readout measurements. In Figure 5.3b, we show two histograms, constructed with the same data-set, using different bin resolutions to distinguish between time scales. The histogram on the left shows our fast-tunneling events. The tunnel rate for these

events is faster than our detection bandwidth, therefore the histogram is dominated by our detection bandwidth, showing a peak which we fit to a normal distribution ([Equation 2.17](#)). The histogram on the right is fitted to an exponential decay ([Equation 2.18](#)) corresponding to the tunnel rate of the slow-tunneling events. We can then construct expressions for the error probabilities in detecting a triplet (P_{error}^T) or a singlet (P_{error}^S), as a function of the detection time threshold t_{th} :

$$P_{\text{error}}^T = 1 - \frac{1}{2} \left(1 + \text{erf} \left(\frac{t_{\text{th}} - \mu_d}{\sqrt{2\sigma_d^2}} \right) \right)$$

$$P_{\text{error}}^S = 1 - \exp(-\Gamma_t t_{\text{th}})$$

Here, $\text{erf}(x) = 2/\sqrt{\pi} \int_0^x \exp(-t^2) dt$ is the error function, and parameters are as defined in [Equation 2.17](#) and [Equation 2.18](#). The error probabilities are plotted as a function of the detection threshold in [Figure 5.3c](#). We define the measurement fidelity in discriminating between fast and slow-tunneling events as (green dashed line):

$$F_{\text{fs}} = 1 - (P_{\text{error}}^T + P_{\text{error}}^S)$$

We find a fidelity $F_{\text{fs}} = 95\%$ for $t_{\text{th}} = 44$ μs . Furthermore, if we assume $P_{\text{error}}^T(t_{\text{RP}}) \approx 0$, the measurement fidelity for discriminating between slow and no-tunneling events is given by:

$$F_{\text{sn}} = P_{\text{error}}^S$$

We find $F_{\text{sn}} = 90\%$ for our readout window $t_{\text{RP}} = 2$ ms. We have assumed that the fidelity in identifying a current blip (based on the current signal-to-noise ratio) is much higher than the tunnel time discrimination fidelity.

5.6 Relaxation measurements

This novel readout technique — here demonstrated in Si for the first time — allows us to follow in real time the evolution of the state populations, as they relax from the highest excited state to the ground state. This allows us extract information on the spin and valley-orbit energy configuration of our system. The method is the same as the T_1 measurement described in [Subsection 2.5.3](#) and depicted in [Figure 5.4a](#), however with TR-RO we can now obtain readout proportions of $|T\rangle^z$ (blue dots in [Figures 5.4](#) and [5.5](#)), $|S\rangle$ (green squares) and $|T\rangle^{x,y}$.

This type of population evolution can be simulated through a model of rate equations, which we introduced through [Equation 2.16](#). We use the following model to obtain fit our data in

5.6. Relaxation measurements

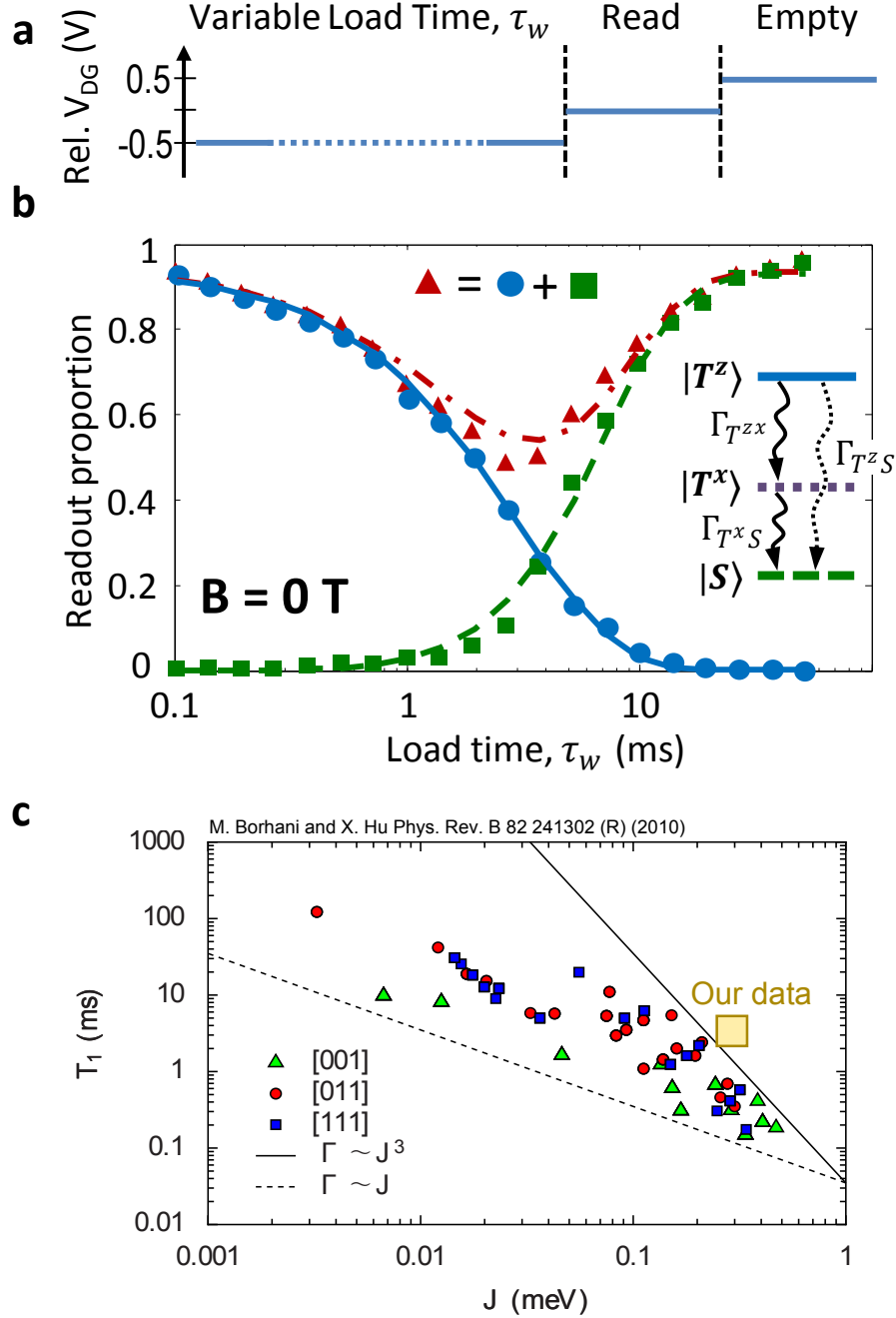


Figure 5.4: Relaxation measurements and fits. **a** Gate pulsing scheme for relaxation measurements. **b** Spin relaxation at $B_0 = 0$. Dots: fraction of fast tunneling events (using t_T) identified as $|T\rangle^z$. Squares: slow tunneling events, identified as $|S\rangle$, excluding those with no observed tunneling in the read-phase ($|T\rangle^x$). Solid lines are fits to the model in Equation 5.1. The triangles correspond to $T^z + S$. **c** (Figure adapted from Reference [152]) Theoretical prediction of relaxation times as a function of J for dimers along different lattice orientations. Measured values from our data have been highlighted in the figure.

[Figure 5.4b](#), where we include for simplicity only the $|T\rangle^x$ shelving state:

$$\begin{aligned}\frac{dT^z}{d\tau_w} &= -(\Gamma_{T^{zx}} + \Gamma_{T^z S}) T^z \\ \frac{dT^x}{d\tau_w} &= \Gamma_{T^{zx}} T^z - \Gamma_{T^x S} T^x \\ \frac{dS}{d\tau_w} &= \Gamma_{T^z S} T^z + \Gamma_{T^x S} T^x\end{aligned}\tag{5.1}$$

Here T^z , T^x , S are the populations of the corresponding states, $\Gamma_{T^{zx}}$ is the relaxation rate from $|T\rangle^z$ to $|T\rangle^x$ and $\Gamma_{T^{z(x)}S}$ is the $|T\rangle^{z(x)}$ to $|S\rangle$ relaxation rate. We include the parameters $c_T \equiv T^z|_{\tau_w=0}$ and $c_S \equiv S|_{\tau_w=\infty}$ ($\in [0, 1]$) that multiply the corresponding populations to account for initialization and measurement imperfections. A least-squares fit to the data in [Figure 5.4b](#) yields $\Gamma_{T^{zx}}^{-1} = 2.9 \pm 0.2$ ms, $\Gamma_{T^x S}^{-1} = 4.1 \pm 0.4$ ms, $c_T = 0.94 \pm 0.02$, and $c_S = 0.93 \pm 0.02$. The model also yields $\Gamma_{T^z S} \ll \Gamma_{T^x S}$ (an accurate value of $\Gamma_{T^z S}$ could not be extracted). This latter observation is again consistent with having a dimer along z , for which it is predicted that – in the high J regime – the valley composition of the ground state α_g will have five times less contribution from the valleys which are longitudinal to the dimer orientation [150]. Finally, the near-unity value of c_{T^z} confirms that the system is preferentially initialized in $|T\rangle^z$, as expected on the basis of the spatial extent of τ_g states, and the valley selection rules discussed above. We note that we could not obtain any improvement in the fit by including $|T\rangle^y$ as an additional shelving state. Furthermore, with the increased number of parameters the uncertainties become very large.

In this picture, $\Gamma_{T^{zx}}$ represents a valley relaxation rate, while the spin relaxation process is captured by $\Gamma_{T^z S}$. The value of $\Gamma_{T^z S}^{-1} \equiv T_1 \approx 4$ ms extracted from the data agrees well with the $|T\rangle \rightarrow |S\rangle$ relaxation times predicted by Borhani and Hu [152] specifically for P donor pairs in Si, in the presence of an exchange interaction $J \approx 300$ μeV ([Figure 5.4c](#)). The electron-nuclear hyperfine coupling A (assumed $\ll J$) mixes the J -split $|S\rangle, |T\rangle$ states and provides a new channel for spin-lattice relaxation which is ~ 3 orders of magnitude faster than a single-spin flip at an equivalent value of the Zeeman splitting ($E_Z \approx 300$ μeV corresponds to $B_0 \approx 2.5$ T on a single spin, where $T_1 \approx 1$ s [31]). The $|T\rangle \rightarrow |S\rangle$ relaxation is predicted to slow down at lower J , giving $T_1 \gg 1$ s for $J \approx 1$ μeV . For $J < A = 117$ MHz ≈ 0.5 μeV this relaxation channel becomes suppressed. Therefore our measurements clearly indicate that 2-qubit coupling schemes which do not require large values of J [44, 153] will have the additional benefit of preserving the long spin lifetime of the individual qubits.

Applying a magnetic field B_0 splits the $|T\rangle$ states by E_Z ([Figure 5.5a](#)). For $J \approx 300$ μeV , $E_Z < J$ when $B \lesssim 2.5$ T. In this regime, we found no B -dependence of $\Gamma_{T^{zx}}$ (data not shown), agreeing with theory which expects orbital relaxation to be field independent up to ~ 10 T [154]. Additionally, our data was not conclusive enough to extract any notable information on the spin relaxation. At $B_0 = 2.5$ T, $E_Z \gtrsim J$ ([Figure 5.5a](#)), the spin ground state inverts to $|T_-\rangle$ and there are several relaxation channels as sketched in [Figure 5.5b](#). We neglect the single-spin

relaxation channels between triplet states, for which $\Gamma^{-1} \approx 1$ s at 2.5 T [31], and we neglect all of the possible channels between τ_g^z and α_g which we showed — in the $B_0 = 0$ T case — are also much slower. The rate equation model then becomes:

$$\begin{aligned}\frac{dT_+^z}{d\tau_w} &= -\Gamma_{T^{zx}} T_+^z \\ \frac{dT_+^x}{d\tau_w} &= \Gamma_{T^{zx}} T_+^z - \Gamma_{T_+^x S} T_+^x \\ \frac{dT_0^z}{d\tau_w} &= -\Gamma_{T^{zx}} T_0^z \\ \frac{dT_0^x}{d\tau_w} &= \Gamma_{T^{zx}} T_0^z - \Gamma_{T_0^x S} T_0^x \\ \frac{dS}{d\tau_w} &= \Gamma_{T_+^x S} T_+^x + \Gamma_{T_0^x S} T_0^x - \Gamma_{ST_-^x} S \\ \frac{dT_-^z}{d\tau_w} &= -\Gamma_{T^{zx}} T_-^z \\ \frac{dT_-^x}{d\tau_w} &= \Gamma_{ST_-^x} S + \Gamma_{T^{zx}} T_-^z\end{aligned}\tag{5.2}$$

For this model, we assume that each $|T_{+,0,-}\rangle^z$ loads with equal probability. We obtain a very good fit to the data in [Figure 5.5c](#) with $\Gamma_{T^{zx}}^{-1} = 5.2 \pm 0.4$ ms, $\Gamma_{ST_-^x}^{-1} = 146 \pm 25$ ms, $\Gamma_{T_+^x S}, \Gamma_{T_0^x S} \gg \Gamma_{ST_-^x}$, $c_T = 0.72 \pm 0.04$, and $c_S = 0.50 \pm 0.03$. Since $\Gamma_{T^{zx}} \gg \Gamma_{ST_-^x}$ the $|S\rangle$ population that first increases ($|T_{+,0}\rangle \rightarrow |S\rangle$) then decreases ($|S\rangle \rightarrow |T_-\rangle$). As expected from the diagram in [Figure 5.5a](#), in this regime ($E_Z \gtrsim J$) the slowest relaxation comes from the energetically close $|S\rangle$ and $|T_-\rangle$.

When $B \gtrsim 4$ T, $\Gamma_{ST_-^x}$ becomes the fastest rate (see [Figure 5.5a](#)), and at $B = 5.5$ T ([Figure 5.5d](#)) only $\Gamma_{T^{zx}}^{-1} = 1.13 \pm 0.13$ ms, with $c_T = 0.92 \pm 0.05$, can be reliably extracted from the data. Interestingly, we observe a constant population of $|S\rangle$ for $\tau_w \gtrsim 1$ ms. This reveals a subtle feature of the spin relaxation mechanism of Borhani and Hu [152]: the hyperfine interaction A mixes states having the same total value of the electron (m_e) and nuclear (m_N) spin quantum number. The transition $|S\rangle \rightarrow |T_-\rangle$ yields $\Delta m_e = -1$, thus requires $\Delta m_N = +1$, and becomes forbidden if the P nuclei are in the state $|\psi_N\rangle = |\uparrow\uparrow\rangle$. We interpret the long-time plateau of S as a manifestation of this spins selection rule. The plateau height should depend on the probability that $|\psi_N\rangle = |\uparrow\uparrow\rangle$, which is unknown and uncontrolled in this experiment, but we may assume that the nuclei randomly populate all possible states over the time necessary to acquire a set of data as in [Figure 5.5](#).

There are noticeable fluctuations in the value of $\Gamma_{T^{zx}}$ between each of the relaxation measurements presented. These fluctuations are independent of the B_0 regime, and we believe they are due to different electric field environments caused by the need to perform small gate tuning adjustments between measurements. It is well known that electric fields can influence both the valley splitting and the exchange coupling [11]. The hysteretic behaviour of our DG did not allow us to perform a more systematic analysis of the tunability of J or the valley splitting.

5.6. Relaxation measurements

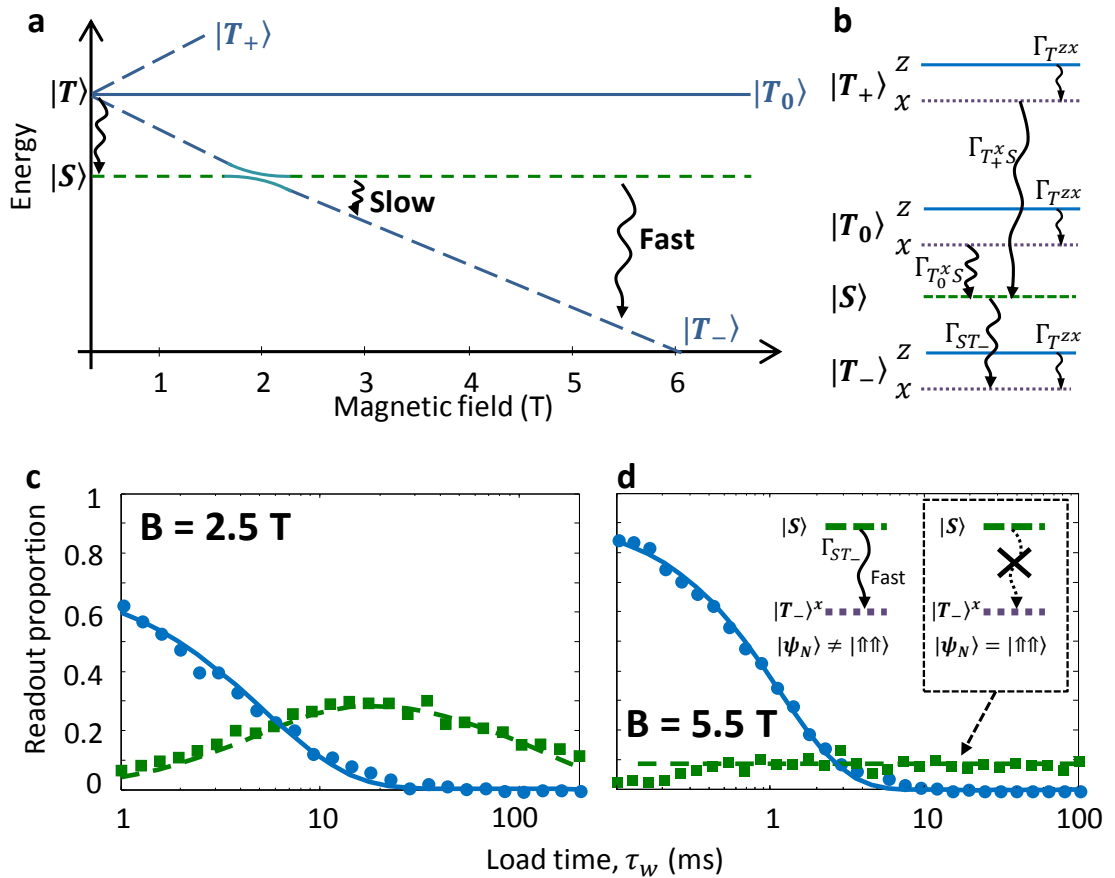


Figure 5.5: Relaxation in different B_0 -field regimes. **a** Spin energies as a function of B_0 , showing the expected spin relaxation in the different regimes we measured. **b** Full diagram of spin and valley-orbit energies for the $E_z > J$ regime. All the available relaxation channels are depicted and labeled. Longer relaxation channels between spin triplet states and between τ_g^z and α_g are ignored. **c** $B = 2.5 \text{ T}$, where $E_z \gtrsim J$ and $\Gamma_{ST_-^x}$ can be observed. **d** At $B = 5.5 \text{ T}$, $E_z \gg J$ and $\Gamma_{ST_-^x}$ becomes too fast to resolve. The long-time plateau (green dashed line) of S is due to spin selection rules sketched in the inset and described in the main text. Solid lines on both relaxation plots are fits to Equation 5.2.

5.7 Conclusions

The time-resolved observation of singlet and triplet states of an exchange-coupled P donor pair reported here provides a physical basis for the construction of large-scale donor-based quantum computer architectures [13].

The theory of valley-orbit physics for strong exchange coupling in donor pairs in Si has only come to surface in the few months prior to the analysis of this data. It is astounding that our experiments have been able to confirm this theory with the degree of detail shown here.

The short $|T\rangle \leftrightarrow |S\rangle$ relaxation times $T_1 \approx 4$ ms in this experiment arise from the interplay of a large exchange coupling $J \approx 300$ μeV with the hyperfine interaction $A = 117$ MHz ≈ 0.5 μeV . Therefore, our results indicate that the best regime to operate J -mediated 2-qubit logic gates is where $J \lesssim A$, as described in recent proposals [44, 153].

Chapter 6

Conclusions and future work

“One small step for a man, one giant leap for mankind”

-Neil Armstrong

I hope I live to see my small steps, along with those of all the people from this wonderful community, turn into a giant leap for the positive evolution of mankind.

6.1 Summary of achievements

Prior to the work presented in this thesis, silicon had always been a “potential candidate” for quantum computation. Experimental demonstrations of its low spin-noise qualities in industry compatible nanoelectronic devices had been scarce and well below the fidelity standards of other qubit systems. The experimental results presented here have put Si spin qubits on the same page as its top peers.

High-fidelity single-shot electron spin readout had already been demonstrated, but there was a gap of knowledge in how to effectively implement a mechanism that would allow to perform coherent control of single-spin qubits. Our initial contribution was to fill that gap, by acquiring microwave engineering skills and developing methods to perform electro-magnetic simulations on our nano-scale structures. We designed a novel on-chip antenna that maximises the radiation of oscillating magnetic fields needed to perform both electron spin resonance and nuclear magnetic resonance [155]. The implementation of this novel antenna lead to the first ever demonstration of the full operation of qubits from both the electron and nuclear spins of a single phosphorous donor implanted in a Si substrate and controlled by an industry compatible, gated nanostructure [83, 156]. Through the lessons learned from those devices about the limiting mechanisms of our qubit coherence and fidelities, we proceeded to upgrade our nanoelectronic qubit device and experimental setup, with the highlight of moving to an isotopically purified ^{28}Si substrate, providing a nuclear spin free environment for our qubits. With this system we were able to demonstrate exquisite control fidelities and coherence times — very fast approaching the fault tolerant limit — including a record > 30 s coherence on the nuclear qubit [157]. Finally, we made an important contribution to the understanding of the physics behind the dynamics of exchange coupled donors, through the demonstration of time resolved measurements of a two electron-spin system from a pair of exchange coupled P donors in Si [158].

This work propels a significant leap for silicon quantum computation, and lays the ground work for the next generation of wonderful experiments and advances.

6.2 Chapter 2 - Experimental methods

Our efforts to perform experimental demonstrations of spin qubits in Si start with a state of the art experimental setup. For the successful operation of these systems it is indispensable to work in very low temperature environments and to minimise any electrical noise from and to our instruments. Apart from describing all of the qubit control, data acquisition and analysis methods needed to understand this thesis, the highlight of this chapter was the design of a novel thermal filtering setup to reduce the electron temperature, and the implementation of an instrument setup that allows for fast acquisition and analysis of the experimental data.

6.3 Chapter 3 - Microwave control of qubits

The leap from single-shot electron spin readout to full operation of P donor qubits required an extensive study on the integration of microwave transmission lines in nanostructures. Electromagnetic simulations are not trivial for structures with dimensions shrinking from millimetre to nanometre scale. This chapter begins by exploring these non-trivialities. By comparing the performance of different spin resonance antenna structures, we chose to implement a novel design, consisting of an on-chip CPW to CPS — impedance and mode matched — balun. This design combines a good control of microwave transmission modes with a maximized value of the magnetic field available to drive coherent control of a spin qubit. We use the invaluable information that modeling and simulations provide, to describe a set of guidelines for the successful operation of spin resonance antennas, highlighting the most important — and often overlooked — implementation details.

We successfully implemented and demonstrated full operation of a single P donor qubit device in Si. We were able to coherently manipulate the donor bound electron as a qubit, with a maximum gate speeds $t_\pi = 150$ ns, maximum coherence times $T_2^{\text{XYXY}} = 410$ μs and fidelities $F_m = 77\%$ and $F_c = 60\%$. We were also able to perform high-fidelity QND readout of the P nuclear spin ($F_m = 99.8\%$) and coherent control — with gates times ~ 25 μs — of both the neutral ($T_2^{\text{H}} = 3.5$ ms) and ionised ($T_2^{\text{H}} = 60$ ms) nucleus. In the noise insensitive nucleus, the control fidelity significantly increased to $F_{ec} = 99.9\%$. These results completed the milestone of proof of principle for single spin qubits in Si, and paved the way for our next experiments which would see Si spin-qubits being established as a frontrunner in quantum computation.

6.4 Chapter 4 - Qubits in isotopically purified Si

The main objective of this chapter was to prove that single spin qubits controlled by a nanoelectronic device, could still reap the benefits of isotopically purified ^{28}Si . By having the ability to work at low temperatures and high magnetic fields, we were able to mitigate the previously observed deleterious effects of spin and charge noise from interface traps, and set new benchmarks of performance for qubit devices in solid state. Our electron qubit coherence times increased to $T_2^{\text{CPMG}} = 0.56$ s — a 3 order of magnitude improvement from the previous generation devices — with fidelities pushed to $F_m = 97\%$ and $F_{ec} = 99.6\%$. The nuclear qubit coherence was the highlight of these results, with a record breaking $T_2^{\text{CPMG}} = 33$ s.

Our analysis of the types of noise coupling to our qubit lead us to invaluable insight. We found two different noise regimes in our qubit environment, none of which are consistent with coherence limitations from either charge traps or the nuclear spin bath. We believe our qubit performance is currently limited by noise in our instruments, and we have identified opportunities to improve our experimental setup in order to push these coherence times and fidelities further, to a more device intrinsic regime.

In the last section of the chapter, we laid the ground work for a method to demonstrate

entangling operations between electron and nuclear qubits, which are an important feature of our quantum computing architecture.

6.5 Chapter 5 - Readout of J -coupled P donors

Sometimes great science appears in places where we do not expect to find it. A measurement of the tunneling characteristics of the electrons from one of our qubit devices, lead us to discover that we were observing the time-resolved signature of an exchange coupled P donor pair. Furthermore, by making use of a novel readout technique, energy relaxation measurements uncovered that our closely spaced donors were in a unique valley orbit regime, only predicted by theorists a few months prior to our data analysis. From our measurements we estimate the donors to have a coupling $J \approx 300$ μeV , with valley-orbit relaxation rates $\Gamma_{T_{zz}}^{-1} \approx 3$ ms and spin relaxation $\Gamma_{T_x S}^{-1} \approx 4$ ms. Our conclusion of the observation of a strongly J -coupled donor pair is based on a substantial amount of experimental evidence: (i) A single-shot electron spin readout signature at $B_0 = 0$ T; (ii) The tunnel rate asymmetry between excited and ground state, consistent with the spatial extent of the $|T\rangle$ and $|S\rangle$ orbitals; (iii) spin relaxation and J measurements agree with previous theory; (iv) Our observation of the valley-orbit $\alpha_u\tau_g$ inversion is consistent with theory for donors with J of hundreds of μeV and $\lesssim 6$ nm apart; (v) Relaxation characteristics in different B_0 regimes are as expected for a two-spin system.

The observation of the reduced T_1 for strongly coupled donor pairs confirms the need to use two-qubit gate operation schemes that work in the low- J regime. Additionally, the observation of valley-orbit effects for closely spaced donors implies that theoretical analysis of exchange and donor separation for applications such as two-qubit gates and spin transport, will need to be modified to take these issues into account.

6.6 Future work and outlook

In [Chapter 4](#) we identified several immediate opportunities for interesting measurements of spin qubits from P donors in Si. An adjustment in the orientation of the device and antenna design should push our qubit coherence times further and reveal important information about the device intrinsic limitations to coherence. Specifically, we are very interested in finding out at what point we will see interface related effects and how important they could be to a larger scale outlook in our QC architecture. Additionally, Randomised benchmarking provides a more robust and universally accepted characterisation of the fidelity of our qubits. The results from these measurements will give us better insight into the position of our qubits in the fault-tolerant large-scale QC realm.

In the mid-term, we need to finish ticking the boxes of the demonstration of all the elements in our QC architecture. Entangling electron-nuclear operations are only a stone-throw away after the work presented in [Section 4.6](#). With regards to two donor qubit operations, the

6.6. Future work and outlook

theoretical ground work has been laid out [44], with the fabrication and initial measurement of devices also underway. These measurements will benefit greatly from the insight obtained in [Chapter 5](#). The final piece of the puzzle is qubit transport. There has been a large amount of theoretical work [45–50] relevant to this topic, but experimental demonstrations are still in infancy. In particular, our research group is working on projects for long-distance coupling of qubits through resonators and quantum dots, and we are excitedly awaiting the outcome of those projects.

Once we have demonstrated that we can implement all the elements of a quantum computer with fault-tolerant fidelities, the next big challenge is to integrate all the elements and scale them into a functional quantum computer. One of the main challenges for our type of device architecture is individual qubit addressability. We have been able to fabricate a local antenna to address our individual qubit, but this antenna takes up a significant amount of chip space, and it is unlikely that it will be possible to reduce further, in order to have an antenna for each qubit. Instead, a more likely option is to use a global antenna — which would radiate a constant spin resonance field — and qubits can be addressed via local electrical gates, by tuning them in or out of resonance through Stark shifts of the hyperfine or of the g -factor. We showed in [Chapter 4](#) that our devices can have large shifts in the hyperfine, and work is currently underway to show that these shifts can be tuned systematically with electric fields, along with the demonstration of a new protocol for electrical control of our qubits under CW spin resonance excitation. Another big challenge is device matching. The qubit device architecture shown in this thesis relies on the ion implantation process, which is currently very probabilistic in terms of number of ions implanted and precise location of the ions. Although our devices show a very high yield of functionality ($\sim 80\%$), we showed in [Chapter 4](#) that Devices A and B had some very different characteristics. These differences will become hard to manage as we attempt scale up. New implantation technologies are being developed that could allow for more precise control of both donor numbers and positions. Another very viable option is to use qubits from confined electrons in quantum dots, instead of donors. There has been a very recent demonstration of high-fidelity coherent control of electron spin qubits, confined in a ^{28}Si quantum dot defined electrostatically by a gate stack fabricated with industry compatible MOS processes [145].

Quantum computing based on other systems and architectures such as superconductors and trapped ions have already shown significant advances in demonstrating the integration of all the elements in their QC architectures [9]. However, they now face the daunting engineering task of developing the technologies to fabricate large scale functional quantum computers. This is where we believe Si will show its true colours. Silicon-based technology already has a six decade head start in experience with large-scale device fabrication, which should make scaling up of qubits in Si relatively easy. Whichever the system, architecture and technology one chooses to look at, the last couple of decades have been very exciting and fun for quantum computing research, and in the next few decades to come, the excitement will surely carry on. We hope that this thesis will serve as incentive to fuel and spread the excitement.

References

- [1] Feynman, R. *International journal of theoretical physics* **21**(6), 467–488 (1982).
- [2] Schumacher, B. *Phys. Rev. A* **51**(4), 2738–2747 Apr (1995).
- [3] Shor, P. *Algorithms for quantum computation: discrete logarithms and factoring*, 124–134. Institute of Electrical and Electronics Engineers (1994).
- [4] Grover, L. K. *A fast quantum mechanical algorithm for database search*, 212–219. Association for Computing Machinery (1996).
- [5] Ambainis, A. *SIAM Journal on Computing* **37**(1), 210–239 Jan (2007).
- [6] Harrow, A., Hassidim, A., and Lloyd, S. *Physical Review Letters* **103**(15) Oct (2009).
- [7] Lanyon, B. P., Whitfield, J. D., Gillett, G. G., Goggin, M. E., Almeida, M. P., Kassal, I., Biamonte, J. D., Mohseni, M., Powell, B. J., Barbieri, M., and et al. *Nature Chemistry* **2**(2), 106–111 Jan (2010).
- [8] Raha, K., Peters, M. B., Wang, B., Yu, N., Wollacott, A. M., Westerhoff, L. M., and Merz, Jr, K. M. *Drug Discov Today* **12**(17-18), 725–731 Sep (2007).
- [9] Ladd, T. D., Jelezko, F., Laflamme, R., Nakamura, Y., Monroe, C., and O'Brien, J. L. *Nature* **464**(7285), 45–53 March (2010).
- [10] DiVincenzo, D. *Fortschritte der Physik* **48**(9-11), 771–783 (2000).
- [11] Zwanenburg, F. A., Dzurak, A. S., Morello, A., Simmons, M. Y., Hollenberg, L. C. L., Klimeck, G., Rogge, S., Coppersmith, S. N., and Eriksson, M. A. *Reviews of Modern Physics* **85**(3), 961–1019 Jul (2013).
- [12] Kane, B. E. *Nature* **393**(6681), 133–137 May (1998).
- [13] Hollenberg, L., Greentree, A., Fowler, A., and Wellard, C. *Physical Review B* **74**(4) Jul (2006).
- [14] Awschalom, D. D., Bassett, L. C., Dzurak, A. S., Hu, E. L., and Petta, J. R. *Science* **339**(6124), 1174–1179 March (2013).
- [15] Bennett, C. H. and DiVincenzo, D. P. *Nature* **404**(6775), 247–255 Mar (2000).

REFERENCES

- [16] Greenland, P. T., Lynch, S. A., van der Meer, A. F. G., Murdin, B. N., Pidgeon, C. R., Redlich, B., Vinh, N. Q., and Aeppli, G. *Nature* **465**(7301), 10571061 Jun (2010).
- [17] Hill, C., Hollenberg, L., Fowler, A., Wellard, C., Greentree, A., and Goan, H. *Physical Review B* **72**(4), 45350 (2005).
- [18] Morton, J., Tyryshkin, A., Brown, R., Shankar, S., Lovett, B., Ardavan, A., Schenkel, T., Haller, E., Ager, J., and Lyon, S. *Nature* **455**(7216), 1085–1088 (2008).
- [19] Steger, M., Sekiguchi, T., Yang, A., Saeedi, K., Hayden, M. E., Thewalt, M. L. W., Itoh, K. M., Riemann, H., Abrosimov, N. V., Becker, P., and et al. *Journal of Applied Physics* **109**(10), 102411 (2011).
- [20] Slichter, C. P. *Principles of magnetic resonance*, volume 1 of *Solid-State Sciences*. Springer, 3rd edition, (1990).
- [21] Rugar, D., Budakian, R., Mamin, H., and Chui, B. *Nature* **430**(6997), 329–332 (2004).
- [22] Jelezko, F., Gaebel, T., Popa, I., Gruber, A., and Wrachtrup, J. *Physical Review Letters* **92**(7), 76401 (2004).
- [23] Xiao, M., Martin, I., Yablonovitch, E., and Jiang, H. *Nature* **430**(6998), 435–439 (2004).
- [24] Koppens, F., Buijzer, C., Tielrooij, K., Vink, I., Nowack, K., Meunier, T., Kouwenhoven, L., and Vandersypen, L. *Nature* **442**(7104), 766–771 (2006).
- [25] Fuchs, G., Dobrovitski, V., Toyli, D., Heremans, F., and Awschalom, D. *Science* **326**(5959), 1520–1522 (2009).
- [26] van Wees, B., van Houten, H., Beenakker, C., Williamson, J., Kouwenhoven, L., van der Marel, D., and Foxon, C. *Physical Review Letters* **60**(9), 848–850 Feb (1988).
- [27] Wharam, D. A., Thornton, T. J., Newbury, R., Pepper, M., Ahmed, H., Frost, J. E. F., Hasko, D. G., Peacock, D. C., Ritchie, D. A., and Jones, G. A. C. *Journal of Physics C: Solid State Physics* **21**(8), L209–L214 Mar (1988).
- [28] Kastner, M. *Reviews of Modern Physics* **64**(3), 849–858 Jul (1992).
- [29] Morello, A., Escott, C., Huebl, H., Willems van Beveren, L., Hollenberg, L., Jamieson, D., Dzurak, A., and Clark, R. *Physical Review B* **80**(8), 81307 (2009).
- [30] Elzerman, J., Hanson, R., van Beveren, L., Witkamp, B., Vandersypen, L., and Kouwenhoven, L. *Nature* **430**(6998), 431–435 (2004).
- [31] Morello, A., Pla, J., Zwanenburg, F., Chan, K., Tan, K., Huebl, H., Möttönen, M., Nugroho, C., Yang, C., van Donkelaar, J., et al. *Nature* **467**(7316), 687–691 (2010).

REFERENCES

- [32] Hanson, R., van Beveren, L., Vink, I., Elzerman, J., Naber, W., Koppens, F., Kouwenhoven, L., and Vandersypen, L. *Physical Review Letters* **94**(19) May (2005).
- [33] Braginsky, V. B., Vorontsov, Y. I., and Thorne, K. S. *Science* **209**(4456), 547–557 Aug (1980).
- [34] Barenco, A., Bennett, C., Cleve, R., DiVincenzo, D., Margolus, N., Shor, P., Sleator, T., Smolin, J., and Weinfurter, H. *Physical Review A* **52**(5), 3457–3467 Nov (1995).
- [35] Koiller, B., Hu, X., and Das Sarma, S. *Phys. Rev. Lett.* **88**, 027903 Dec (2001).
- [36] Wellard, C. J., Hollenberg, L. C. L., Parisoli, F., Kettle, L. M., Goan, H.-S., McIntosh, J. A. L., and Jamieson, D. N. *Phys. Rev. B* **68**, 195209 Nov (2003).
- [37] Trifunovic, L., Pedrocchi, F. L., and Loss, D. *Phys. Rev. X* **3**, 041023 Dec (2013).
- [38] Hu, X., Liu, Y.-x., and Nori, F. *Phys. Rev. B* **86**(3) Jul (2012).
- [39] Petta, J. R. *Science* **309**(5744), 2180–2184 Sep (2005).
- [40] Maune, B. M., Borselli, M. G., Huang, B., Ladd, T. D., Deelman, P. W., Holabird, K. S., Kiselev, A. A., Alvarado-Rodriguez, I., Ross, R. S., Schmitz, A. E., and et al. *Nature* **481**(7381), 344–347 Jan (2012).
- [41] Taylor, J. M., Engel, H.-A., Dr, W., Yacoby, A., Marcus, C. M., Zoller, P., and Lukin, M. D. *Nature Physics* **1**(3), 177–183 Dec (2005).
- [42] Jérôme, D. and Winter, J. M. *Phys. Rev.* **134**, A1001–A1007 May (1964).
- [43] Gonzalez-Zalba, M. F., Saraiva, A., Heiss, D., Calderón, M. J., Koiller, B., and Ferguson, A. J. *arXiv:1312.4589* (2013).
- [44] Kalra, R., Laucht, A., Hill, C., and Morello, A. December (2013).
- [45] Greentree, A., Cole, J., Hamilton, A., and Hollenberg, L. *Physical Review B* **70**(23) Dec (2004).
- [46] Mehring, M. and Mende, J. *Physical Review A* **73**(5), 52303 (2006).
- [47] Friesen, M., Biswas, A., Hu, X., and Lidar, D. *Physical Review Letters* **98**(23) Jun (2007).
- [48] Oh, S., Shim, Y.-P., Fei, J., Friesen, M., and Hu, X. *Physical Review A* **87**(2) Feb (2013).
- [49] Craig, N. J. *Science* **304**(5670), 565–567 Apr (2004).
- [50] Raimond, J., Brune, M., and Haroche, S. *Reviews of Modern Physics* **73**(3), 565–582 Aug (2001).

REFERENCES

- [51] Fuechsle, M., Miwa, J. A., Mahapatra, S., Ryu, H., Lee, S., Warschkow, O., Hollenberg, L. C. L., Klimeck, G., and Simmons, M. Y. *Nature Nanotechnology* **7**(4), 242–246 Feb (2012).
- [52] Jamieson, D., Yang, C., Hopf, T., Hearne, S., Pakes, C., Prawer, S., Mitic, M., Gauja, E., Andresen, S., Hudson, F., et al. *Applied Physics Letters* **86**, 202101 (2005).
- [53] Angus, S., Ferguson, A., Dzurak, A., and Clark, R. *Nano Letters* **7**(7), 2051–2055 (2007).
- [54] Pozar, D. *Microwave engineering*. Wiley, New York, (1997).
- [55] Craig, N. and Lester, T. *Hitchhiker's Guide to the Dilution Refrigerator*. Marcus Lab, Harvard University, 2 edition, 8 (2004).
- [56] Allen, L. and Chapman, W. K. *Optical Resonance and Two-Level Atoms (Dover Books on Physics)*. Dover Publications, (2012).
- [57] Yao, W., Liu, R.-B., and Sham, L. *Phys. Rev. B* **74**(19) Nov (2006).
- [58] de Sousa, R. *Phys. Rev. B* **76**(24) Dec (2007).
- [59] Bradbury, F., Tyryshkin, A., Sabouret, G., Bokor, J., Schenkel, T., and Lyon, S. *Physical Review Letters* **97**(17) Oct (2006).
- [60] Rahman, R., Wellard, C., Bradbury, F., Prada, M., Cole, J., Klimeck, G., and Hollenberg, L. *Physical Review Letters* **99**(3) Jul (2007).
- [61] Mohiyaddin, F. A., Rahman, R., Kalra, R., Klimeck, G., Hollenberg, L. C. L., Pla, J. J., Dzurak, A. S., and Morello, A. *Nano Lett.* **13**(5), 1903–1909 May (2013).
- [62] Rahman, R., Park, S., Boykin, T., Klimeck, G., Rogge, S., and Hollenberg, L. *Phys. Rev. B* **80**(15) Oct (2009).
- [63] Paladino, E., Galperin, Y. M., Falci, G., and Altshuler, B. L. April (2013).
- [64] Hahn, E. *Physical Review* **80**(4), 580–594 Nov (1950).
- [65] Liu, G.-Q., Po, H. C., Du, J., Liu, R.-B., and Pan, X.-Y. *Nature Communications* **4** Aug (2013).
- [66] Zhang, J., Souza, A. M., Brandao, F. D., and Suter, D. *Physical Review Letters* **112**(5) Feb (2014).
- [67] Rong, X., Geng, J., Wang, Z., Zhang, Q., Ju, C., Shi, F., Duan, C.-K., and Du, J. *Physical Review Letters* **112**(5) Feb (2014).
- [68] Witzel, W. M., Carroll, M. S., Morello, A., Cywiński, L., and Das Sarma, S. *Phys. Rev. Lett.* **105**(18), 187602 Oct (2010).

REFERENCES

- [69] Becker, P., Pohl, H.-J., Riemann, H., and Abrosimov, N. *physica status solidi (a)* **207**(1), 49–66 Jan (2010).
- [70] Saeedi, K., Simmons, S., Salvail, J. Z., Dluhy, P., Riemann, H., Abrosimov, N. V., Becker, P., Pohl, H.-J., Morton, J. J. L., and Thewalt, M. L. W. *Science* **342**(6160), 830–833 Nov (2013).
- [71] Tyryshkin, A. M., Tojo, S., Morton, J. J. L., Riemann, H., Abrosimov, N. V., Becker, P., Pohl, H.-J., Schenkel, T., Thewalt, M. L. W., Itoh, K. M., and Lyon, S. A. *Nature Materials* **11**(2), 143–147 February (2012).
- [72] Steger, M., Saeedi, K., Thewalt, M. L. W., Morton, J. J. L., Riemann, H., Abrosimov, N. V., Becker, P., and Pohl, H.-J. *Science* **336**(6086), 1280–1283 (2012).
- [73] Abe, E., Tyryshkin, A. M., Tojo, S., Morton, J. J. L., Witzel, W. M., Fujimoto, A., Ager, J. W., Haller, E. E., Isoya, J., Lyon, S. A., Thewalt, M. L. W., and Itoh, K. M. *Phys. Rev. B* **82**, 121201 Sep (2010).
- [74] Schenkel, T., Liddle, J. A., Persaud, A., Tyryshkin, A. M., Lyon, S. A., de Sousa, R., Whaley, K. B., Bokor, J., Shangkuan, J., and Chakarov, I. *Applied Physics Letters* **88**(11), 112101 (2006).
- [75] Morton, J. J. L., McCamey, D. R., Eriksson, M. A., and Lyon, S. A. *Nature* **479**(7373), 345–353 Nov (2011).
- [76] Feher, G. *Physical Review* **114**(5), 1219–1244 Jun (1959).
- [77] Dreher, L., Hoehne, F., Stutzmann, M., and Brandt, M. S. *Physical Review Letters* **108**(2) Jan (2012).
- [78] Fukatsu, S., Takahashi, T., Itoh, K. M., Uematsu, M., Fujiwara, A., Kageshima, H., Takahashi, Y., Shiraishi, K., and Gösele, U. *Applied Physics Letters* **83**(19), 3897–3899 (2003).
- [79] Martinis, J., Devoret, M., and Clarke, J. *Physical Review B* **35**(10), 4682–4698 Apr (1987).
- [80] Mueller, F., Schouten, R. N., Brauns, M., Gang, T., Lim, W. H., Lai, N. S., Dzurak, A. S., van der Wiel, W. G., and Zwanenburg, F. A. *Review of Scientific Instruments* **84**(4), 044706 (2013).
- [81] <http://www.eccosorb.com.hk/technical-reference/electromagnetic-principles-and-applications>.
- [82] Beenakker, C. *Physical Review B* **44**, 1646–1656 Jul (1991).

REFERENCES

- [83] Pla, J. J., Tan, K. Y., Dehollain, J. P., Lim, W. H., Morton, J. J. L., Jamieson, D. N., Dzurak, A. S., and Morello, A. *Nature* **489**(7417), 541–545 September (2012).
- [84] Ramus, X. Application Report SBOA-122, Texas Instruments, (2009).
- [85] <http://www.americanmagnetics.com/tutorial.php>.
- [86] Kouwenhoven, L. P., Austing, D. G., and Tarucha, S. *Reports on Progress in Physics* **64**, 701–736 (2001).
- [87] Meiboom, S. and Gill, D. *Review of Scientific Instruments* **29**(8), 688 (1958).
- [88] Borneman, T. W., Hrlimann, M. D., and Cory, D. G. *Journal of Magnetic Resonance* **207**(2), 220233 Dec (2010).
- [89] Carr, H. and Purcell, E. *Physical Review* **94**(3), 630–638 May (1954).
- [90] Gullion, T., Baker, D. B., and Conradi, M. S. *Journal of Magnetic Resonance (1969)* **89**(3), 479–484 Oct (1990).
- [91] DÁnjou, B. and Coish, W. A. *Phys. Rev. A* **89**(1) Jan (2014).
- [92] Morton, J., Tyryshkin, A., Ardavan, A., Porfyrakis, K., Lyon, S., and Briggs, G. *Physical Review A* **71**(1) Jan (2005).
- [93] Simović, B., Studerus, P., Gustavsson, S., Leturcq, R., Ensslin, K., Schuhmann, R., Forrer, J., and Schweiger, A. *Review of Scientific Instruments* **77**, 064702 (2006).
- [94] Obata, T., Pioro-Ladrière, M., Kubo, T., Yoshida, K., Tokura, Y., and Tarucha, S. *Review of Scientific Instruments* **78**(10), 104704 (2007).
- [95] Simons, R. *Coplanar waveguide circuits, components, and systems*. John Wiley, New York, (2001).
- [96] Wadell, B. *Transmission line design handbook*. Artech House Antennas And Propagation Library. Artech House, (1991).
- [97] Chiou, H., Chang, C., and Lin, H. *Electronics Letters* **31**(24), 2113 –2114 Nov (1995).
- [98] Mao, S., Hwang, C., Wu, R., and Chen, C. *IEEE Transactions on Microwave Theory and Techniques* **48**(1), 23–29 (2000).
- [99] <http://www.cst.com>.
- [100] Weiland, T. *Archiv Elektronik und Uebertragungstechnik* **31**, 116–120 (1977).
- [101] Yee, K. *Antennas and Propagation, IEEE Transactions on* **14**(3), 302–307 may (1966).
- [102] Weiland, T., Timm, M., and Munteanu, I. *IEEE Microwave Magazine* **9**(6), 62–75 (2008).

REFERENCES

- [103] Berman, R. and MacDonald, D. *Proceedings of the Royal Society of London. Series A, Mathematical and Physical Sciences* **211**(1104), pp. 122–128 (1952).
- [104] Kumar, G., Prasad, G., and Pohl, R. *Journal of Materials Science* **28**(16), 4261–4272 (1993).
- [105] Gupta, K., Garg, R., and Chadha, R. *Computer-aided design of microwave circuits*. Artech Microwave Library. Artech, (1981).
- [106] Holleitner, A., Blick, R., and Eberl, K. *Applied Physics Letters* **82**, 1887 (2003).
- [107] Tyryshkin, A. M., Morton, J. J. L., Benjamin, S. C., Ardavan, A., Briggs, G. A. D., Ager, J. W., and Lyon, S. A. *Journal of Physics: Condensed Matter* **18**(21), S783–S794 May (2006).
- [108] Chiba, M. and Hirai, A. *Journal of the Physical Society of Japan* **33**(3), 730–738 Sep (1972).
- [109] Laucht, A., Kalra, R., Muhonen, J. T., Dehollain, J. P., Mohiyaddin, F. A., Hudson, F., McCallum, J. C., Jamieson, D. N., Dzurak, A. S., and Morello, A. *Appl. Phys. Lett.* **104**(9), 092115 Mar (2014).
- [110] Neumann, P., Beck, J., Steiner, M., Rempp, F., Fedder, H., Hemmer, P. R., Wrachtrup, J., and Jelezko, F. *Science* **329**(5991), 542–544 Jul (2010).
- [111] Pines, D., Bardeen, J., and Slichter, C. *Physical Review* **106**(3), 489–498 May (1957).
- [112] McCamey, D. R., Van Tol, J., Morley, G. W., and Boehme, C. *Science* **330**(6011), 1652–1656 Dec (2010).
- [113] Myerson, A., Szwer, D., Webster, S., Allcock, D., Curtis, M., Imreh, G., Sherman, J., Stacey, D., Steane, A., and Lucas, D. *Physical Review Letters* **100**(20) May (2008).
- [114] Knill, E. *Nature* **434**(7029), 39–44 Mar (2005).
- [115] Fowler, A. G., Mariantoni, M., Martinis, J. M., and Cleland, A. N. *Phys. Rev. A* **86**(3) Sep (2012).
- [116] Wolfowicz, G., Tyryshkin, A. M., George, R. E., Riemann, H., Abrosimov, N. V., Becker, P., Pohl, H.-J., Thewalt, M. L. W., Lyon, S. A., and Morton, J. J. L. *Nature Nanotechnology* **8**(8), 561–564 August (2013).
- [117] Johnson, B., McCallum, J., Willems van Beveren, L., and Gauja, E. *Thin Solid Films* **518**(9), 2524–2527 Feb (2010).
- [118] Huebl, H., Stegner, A., Stutzmann, M., Brandt, M., Vogg, G., Bensch, F., Rauls, E., and Gerstmann, U. *Physical Review Letters* **97**(16) Oct (2006).

REFERENCES

- [119] Balasubramanian, G., Neumann, P., Twitchen, D., Markham, M., Kolesov, R., Mizuochi, N., Isoya, J., Achard, J., Beck, J., Tissler, J., and et al. *Nature Materials* **8**(5), 383–387 May (2009).
- [120] Maurer, P. C., Kucsko, G., Latta, C., Jiang, L., Yao, N. Y., Bennett, S. D., Pastawski, F., Hunger, D., Chisholm, N., Markham, M., and et al. *Science* **336**(6086), 1283–1286 Jun (2012).
- [121] Dobrovitski, V., Feiguin, A., Awschalom, D., and Hanson, R. *Physical Review B* **77**(24) Jun (2008).
- [122] Hasegawa, H. *Phys. Rev.* **118**(6), 1523–1534 Jun (1960).
- [123] Tyryshkin, A. M., Lyon, S. A., Astashkin, A. V., and Raitsimring, A. M. *Phys. Rev. B* **68**, 193207 Nov (2003).
- [124] Waldherr, G., Wang, Y., Zaiser, S., Jamali, M., Schulte-Herbrüggen, T., Abe, H., Ohshima, T., Isoya, J., Du, J. F., Neumann, P., and et al. *Nature* **506**(7487), 204207 Feb (2014).
- [125] Uhrig, G. *Physical Review Letters* **98**(10) Mar (2007).
- [126] Cywiński, L., Lutchyn, R., Nave, C., and Das Sarma, S. *Phys. Rev. B* **77**(17) May (2008).
- [127] Biercuk, M. J., Doherty, A. C., and Uys, H. *Journal of Physics B: Atomic, Molecular and Optical Physics* **44**(15), 154002 Aug (2011).
- [128] Bylander, J., Gustavsson, S., Yan, F., Yoshihara, F., Harrabi, K., Fitch, G., Cory, D. G., Nakamura, Y., Tsai, J.-S., and Oliver, W. D. *Nat Phys* **7**(7), 565–570 May (2011).
- [129] Yuge, T., Sasaki, S., and Hirayama, Y. *Physical Review Letters* **107**(17) Oct (2011).
- [130] Álvarez, G. A. and Suter, D. *Physical Review Letters* **107**(23) Nov (2011).
- [131] Taylor, J. M., Cappellaro, P., Childress, L., Jiang, L., Budker, D., Hemmer, P. R., Yacoby, A., Walsworth, R., and Lukin, M. D. *Nat Phys* **4**(10), 810–816 Oct (2008).
- [132] Medford, J., Beil, J., Taylor, J. M., Rashba, E. I., Lu, H., Gossard, A. C., and Marcus, C. M. *Physical Review Letters* **111**(5) Jul (2013).
- [133] Bell, J. S. *Physics* **1**(3), 195–200 November (1964).
- [134] Steffen, M., Ansmann, M., McDermott, R., Katz, N., Bialczak, R., Lucero, E., Neeley, M., Weig, E., Cleland, A., and Martinis, J. *Physical Review Letters* **97**(5) Aug (2006).
- [135] Höffner, H., Hnsel, W., Roos, C. F., Benhelm, J., Chek-al kar, D., Chwalla, M., Krber, T., Rapol, U. D., Riebe, M., Schmidt, P. O., and et al. *Nature* **438**(7068), 643646 Dec (2005).

REFERENCES

- [136] Steffen, M. *Science* **313**(5792), 1423–1425 Sep (2006).
- [137] Pfaff, W., Taminiau, T. H., Robledo, L., Bernien, H., Markham, M., Twitchen, D. J., and Hanson, R. *Nat Phys* **9**(1), 29–33 Oct (2012).
- [138] Aharonov, Y. and Anandan, J. *Physical Review Letters* **58**(16), 1593–1596 Apr (1987).
- [139] Berry, M. V. *Proceedings of the Royal Society A: Mathematical, Physical and Engineering Sciences* **392**(1802), 4557 Mar (1984).
- [140] Knill, E., Leibfried, D., Reichle, R., Britton, J., Blakestad, R., Jost, J., Langer, C., Ozeri, R., Seidelin, S., and Wineland, D. *Physical Review A* **77**(1) Jan (2008).
- [141] Gottesman, D. In *Proceedings of the XXII International Colloquium on Group Theoretical Methods in Physics*, Corney, S. P., Delbourgo, R., and D., J. P., editors, 32–43 (International Press, Cambridge, MA, 1999).
- [142] Ashhab, S., You, J. Q., and Nori, F. *New Journal of Physics* **11**(8), 083017 Aug (2009).
- [143] Vijay, R., Macklin, C., Slichter, D. H., Weber, S. J., Murch, K. W., Naik, R., Korotkov, A. N., and Siddiqi, I. *Nature* **490**(7418), 77–80 Oct (2012).
- [144] Blok, M. S., Bonato, C., Markham, M. L., Twitchen, D. J., Dobrovitski, V. V., and Hanson, R. *Nat Phys* **10**(3), 189–193 Feb (2014).
- [145] Veldhorst, M., Hwang, J. C. C., Yang, C. H., Leenstra, A. W., de Ronde, B., Dehollain, J. P., Muñonen, J. T., Hudson, F. E., Itoh, K. M., Morello, A., and Dzurak, A. S. Submitted to *Nature Nanotechnology* (2014).
- [146] Shulman, M. D., Dial, O. E., Harvey, S. P., Bluhm, H., Umansky, V., and Yacoby, A. *Science* **336**(6078), 202–205 Apr (2012).
- [147] Nowack, K. C., Shafiei, M., Laforest, M., Prawiroatmodjo, G. E. D. K., Schreiber, L. R., Reichl, C., Wegscheider, W., and Vandersypen, L. M. K. *Science* **333**(6047), 1269–1272 Sep (2011).
- [148] Tan, K. Y., Chan, K. W., Mottonen, M., Morello, A., Yang, C., Donkelaar, J. v., Alves, A., Pirkkalainen, J.-M., Jamieson, D. N., Clark, R. G., and et al. *Nano Lett.* **10**(1), 1115 Jan (2010).
- [149] Kohn, W. and Luttinger, J. *Phys. Rev.* **98**(4), 915–922 May (1955).
- [150] Klymenko, M. V. and Remacle, F. *J. Phys.: Condens. Matter* **26**(6), 065302 Feb (2014).
- [151] Ando, T. *Rev. Mod. Phys.* **54**(2), 437–672 Apr (1982).
- [152] Borhani, M. and Hu, X. *Physical Review B* **82**(24) Dec (2010).

REFERENCES

- [153] Srinivasa, V., Xu, H., and Taylor, J. M. *arXiv:1312.1711 [cond-mat.mes-hall]* December (2013).
- [154] Murdin, B., Li, J., Pang, M., Bowyer, E., Litvinenko, K., Clowes, S., Engelkamp, H., Pidgeon, C., Galbraith, I., Abrosimov, N., and et al. *Nature Communications* **4**, 1469 Feb (2013).
- [155] Dehollain, J. P., Pla, J. J., Siew, E., Tan, K. Y., Dzurak, A. S., and Morello, A. *Nanotechnology* **24**(1), 015202 Jan (2013).
- [156] Pla, J. J., Tan, K. Y., Dehollain, J. P., Lim, W. H., Morton, J. J. L., Zwanenburg, F. A., Jamieson, D. N., Dzurak, A. S., and Morello, A. *Nature* **496**(7445), 334–338 Apr (2013).
- [157] Muhonen, J. T., Dehollain, J. P., Laucht, A., Hudson, F. E., Sekiguchi, T., Itoh, K. M., Jamieson, D. N., McCallum, J. C., Dzurak, A. S., and Morello, A. *arXiv:1402.7140 [cond-mat.mes-hall]* February (2014).
- [158] Dehollain, J. P., Muhonen, J. T., Tan, K. Y., Saraiva, A., Jamieson, D. N., Dzurak, A. S., and Morello, A. *arXiv:1402.7148 [cond-mat.mes-hall]* February (2014).